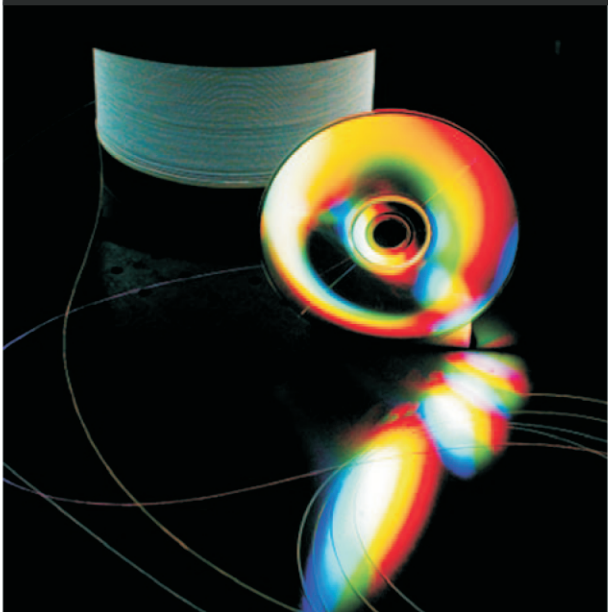

Deep-blue supercontinuum light sources based on tapered photonic crystal fibres

Simon Toft Sørensen
PhD Thesis
June 2013

DTU Fotonik
Department of Photonics Engineering

Deep-blue supercontinuum light sources based on tapered photonic crystal fibres

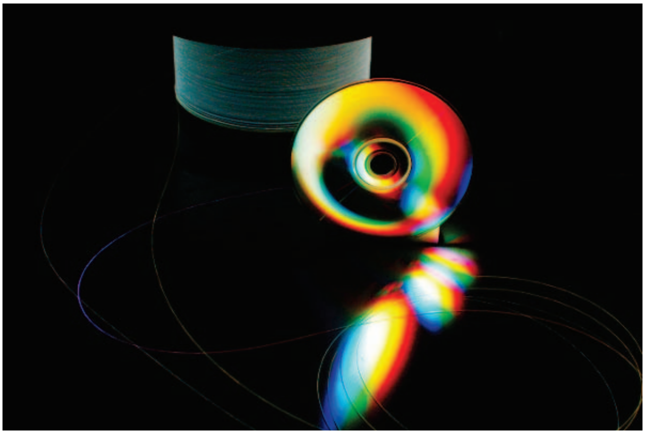

Simon Toft Sørensen

PhD Thesis

June 2013

DTU Fotonik
Department of Photonics Engineering

Technical University
of Denmark

NKT Photonics
the power of light

Abstract

The nonlinear pulse broadening phenomenon of supercontinuum generation in optical fibres is appreciated as one of the most striking in nonlinear physics. Thanks to the unique combination of high brightness and octave-spanning spectra, modern "white-light" supercontinuum lasers have found numerous applications in areas such as spectroscopy and microscopy.

In this work, we exploit the tremendous design freedom in air hole structured photonic crystal fibres to shape the supercontinuum spectrum. Specifically, the supercontinuum dynamics can be controlled by clever engineering of fibres with longitudinally varying air hole structures. Here we demonstrate supercontinuum generation into the commercially attractive deep-blue spectral region below 400 nm from an Yb laser in such fibres. In particular, we introduce the concept of a group acceleration mismatch that allows us to enhance the amount of light in the deep-blue by optimising the fibre structure. To this end, we fabricate the first single-mode high air-fill fraction photonic crystal fibre for blue-extended supercontinuum sources.

The mechanisms of supercontinuum broadening are highly sensitive to noise, and the inherent shot-to-shot variations in long-pulsed supercontinuum sources are a limiting factor for several applications. We investigate different approaches to quantify and lower the spectral noise. Specifically, we characterise the spectral noise in the framework of statistical higher-order moments, which provides insight into the nature of the noise across the spectrum. We further investigate the possibilities of reducing the spectral noise by modulating the pump with a weak seed, which makes the broadening dynamics increasingly deterministic rather than driven by noisy modulation instability. Particular attention is paid to the commercially relevant high power regime. Finally, we examine passive noise reduction in photonic crystal fibres with longitudinally varying air hole structures.

Resumé

Blå-forstærkede superkontinuum lyskilder baseret på taperede fotoniske krystal fibre

Den ekstreme pulsforbredning i optiske fibre, superkontinuum generering, er anerkendt som et af de mest spektakulære fænomener i den ulineære fysik. Takket være den unikke kombination af en høj lysstyrke og spektre der spænder over mere end en optisk oktav, har moderne superkontinuum "hvidlys" lasere fundet talrige anvendelser inden for bl.a. spektroskopi og mikroskopi.

I dette arbejde udnytter vi den enorme designfrihed i fotoniske krystal fibre, bestående af en mikrostruktur af lufthuller, til at forme superkontinuum spektret. Konkret kan dynamikken bag superkontinuum generering styres ved at variere mikrostrukturen af lufthuller på langs af fiberen. Ved at gøre dette, demonstrerer vi superkontinuum generation i det kommercielt attraktive mørkeblå bølgelængdeområde under 400 nm fra en Yb laser. Vi indfører desuden begrebet gruppe-accelerations tilpasning, der gør det muligt, at øge lyseffekten i den blå spektrale kant ved at optimere fiberstrukturen. Til dette formål fabrikerede vi den første single-mode fotoniske krystal fiber med høj luftfyldningsfaktor til blå-forstærkede superkontinuum kilder.

Forbredningsmekanismerne bag superkontinuum generering er meget følsomme over for støj, hvilket medfører store variationer fra puls til puls i superkontinuum kilder baseret på lange pulser. Dette er en klar begrænsning for adskillige potentielle anvendelser. Vi undersøger forskellige tilgange til at kvantificere den spektrale støj, samt til at sænke støjen ved at kontrollere forbredelsesmekanismerne. Konkret karakteriserer vi den spektrale støj med

statistiske højereordens momenter, der giver indsigt i karakteren af støjen over hele den spektrale båndbredde. Vi gransker desuden mulighederne for at reducere den spektrale støj, ved at modulere pumpen med en svag puls. Dette gør i højere grad forbredelsen deterministisk fremfor drevet af modulations instabiliteter. Vi fokuserer specielt på det kommercielt relevante høj-effekts regime. Derudover undersøger vi, om den turbulente superkontinuum forbredning kan tæmmes i fotoniske krystal fibre med longitudinalt varierende mikrostruktur.

Preface

This thesis is submitted for the degree of Doctor of Philosophy of the Technical University of Denmark. The research contained herein has been carried out over the three year period May 2010 to April 2013 as a part of the research project ”Intelligent tapers and seeding for taming the optical rogue wave and develop stable deep-blue supercontinuum light sources (ITRUS)” supported by the Danish Agency for Science, Technology and Innovation (Det Frie Forskningsråd for teknologi og produktion, projektnr. 09-070566). The majority of the work was performed at the main project partners DTU Fotonik, Department of Photonics Engineering at the Technical University of Denmark and NKT Photonics A/S in Birkerød, but also during a research stay in the Optoelectronics and Photonics research group at University of Franche-Comté, Besançon, in the summer 2011. The project was supervised by Prof. Dr. Ole Bang, DTU Fotonik, and Carsten L. Thomsen, Manager - Product Development at NKT Photonics A/S, but also partly by Prof. Dr. John M. Dudley during the research stay in Besançon.

I would, of course, like to take the full credit for all the good parts of this work and blame the faults, flaws and weaknesses on others. However, not only is this sort of behaviour generally frowned upon, it also greatly discredits the large team effort on which this work is based. Without all the dedicated help and support I have received, the outcome of this project would simply not have been possible. I am therefore indebted to several people. First and foremost, I wish to thank my supervisor Ole Bang for giving me the opportunity to work on this exciting project *and* for making it a truly enjoyable journey. This thesis would not have come to existence without his dedication and enthusiastic guidance, motivation and support. I must also thank my co-supervisor Carsten L. Thomsen for his support and guidance, but also for opening the doors for an exciting academic-industrial collaboration.

My (project) partners in crime, Casper Larsen and Uffe Møller, deserve special mentioning for superb teamwork and heaps of fun. In fact, the same goes for the many others who contributed to this work. Especially, Christian Jakobsen for always finding a way to fabricate our increasingly odd and demanding fibre designs, and Jeppe Johansen and Peter M. Moselund for discussions and indispensable help in the lab. But also my other co-authors and collaborators: Christian Agger, Thomas V. Andersen, Thomas Feuchter, Alex Judge (University of Sydney) and Michael Frosz (now at Max Planck Institute for the Science of Light, Erlangen). And Chris Brooks for last-minute proofreading this thesis. It is also my pleasure to thank John M. Dudley for hosting me in Besançon and making it a fun and enlightening experience (yes, I am infinitely beer indebted), and to Benjamin Wetzel for great collaboration during my stay. I am also very thankful to all the guys who showed me how to have a good time in France (without speaking French).

I further want to express a special thanks to everybody who participated in the OSA Student Chapter and PhD Club activities, and to all my friends and family for a seemingly infinite support.

Finally, I wish to acknowledge the Technical University of Denmark and the Danish Agency for Science, Technology and Innovation for financial support of this PhD project, and Otto Mønsteds Fond, Oticon Fonden, the French Embassy in Denmark (Programme de coopération scientifique et universitaire) and the Optical Society of America for indispensable financial support for conference participation and my research stay in Besançon.

The thesis was presented for public examination and debate on 27 May 2013 at the Technical University of Denmark. The evaluation committee consisted of Dr. Goëry Genty, Tampere University of Technology, Finland, Dr. John C. Travers, Max Planck Institute for the Science of Light, Erlangen, Germany, and Dr. Jesper Lægsgaard, Technical University of Denmark. A few minor corrections have been made to the original thesis.

Kongens Lyngby, June 2013

Simon Toft Sørensen

Contents

List of publications

Journal publications

This thesis is based on the following peer-review journal publications. It should be noted that Paper IV is not yet published.

Paper I
: S. T. Sørensen, A. Judge, C. L. Thomsen, and O. Bang, "Optimum fiber tapers for increasing the power in the blue edge of a supercontinuum—group-acceleration matching," Opt. Lett. **36**, 816–818 (2011).
`http://dx.doi.org/10.1364/OL.36.000816`

Paper II
: S. T. Sørensen, U. Møller, C. Larsen, P. M. Moselund, C. Jakobsen, J. Johansen, T. V. Andersen, C. L. Thomsen, and O. Bang, "Deep-blue supercontinnum sources with optimum taper profiles – verification of GAM," Opt. Express **20**, 10635-10645 (2012).
`http://dx.doi.org/10.1364/OE.20.01063`

Paper III
: U. Møller, S. T. Sørensen, C. Larsen, P. M. Moselund, C. Jakobsen, J. Johansen, C. L. Thomsen, O. Bang, "Optimum PCF tapers for blue-enhanced supercontinuum sources [Invited]," Opt. Fiber Technol. **18**, 304-314 (2012).
`http://dx.doi.org/10.1016/j.yofte.2012.07.010`

Paper IV
: S. T. Sørensen, C. Larsen, C. Jakobsen, C. L. Thomsen, O. Bang, "Single-mode high air-fill fraction photonic crystal fiber for high-power deep-blue supercontinuum sources," submitted to Opt. Lett. 29 April 2013.

Paper V

S. T. Sørensen, O. Bang, B. Wetzel, J. M. Dudley, ”Describing supercontinuum noise and rogue wave statistics using higher-order moments,” Opt. Comm. **285**, 2451-2455 (2012).
`http://dx.doi.org/10.1016/j.optcom.2012.01.030`

Paper VI

S. T. Sørensen, C. Larsen, U. Møller, P. M. Moselund, C. L. Thomsen, and O. Bang, ”Influence of pump power and modulation instability gain spectrum on seeded supercontinuum and rogue wave generation,” J. Opt. Soc. Am. B **29**, 2875-2885 (2012).
`http://dx.doi.org/10.1364/JOSAB.29.002875`

Paper VII

S. T. Sørensen, C. Larsen, U. Møller, P. M. Moselund, C. L. Thomsen, and O. Bang, ”The role of phase coherence in seeded supercontinuum generation,” Opt. Express **20**, 22886-22894 (2012).
`http://dx.doi.org/10.1364/OE.20.022886`

Paper VIII

U. Møller, S. T. Sørensen, C. Jakobsen, J. Johansen, P. M. Moselund, C. L. Thomsen, and O. Bang, ”Power dependence of supercontinuum noise in uniform and tapered PCFs,” Opt. Express **20**, 2851-2857 (2012). `http://dx.doi.org/10.1364/OE.20.002851`;
Erratum, Opt. Express **20**, 23318-23319 (2012).
`http://dx.doi.org/10.1364/OE.20.023318`

Conference contributions

The conference contributions with relation to this thesis are listed below in chronological order.

Conference I

S. T. Sørensen, A. Judge, C. L. Thomsen, and O. Bang, ”Group-Acceleration Matching in Tapered Optical Fibers for Maximising the Power in the Blue-Edge of a Supercontinuum,” in CLEO/Europe and EQEC 2011 Conference Digest, OSA Technical Digest (CD) (Optical Society of America, 2011), paper CD.P12.

Conference I

U. Møller, S. T. Sørensen, P. M. Moselund, J. Johansen, C. L. Thomsen, and O. Bang, ”Reduced Amplitude Noise in Supercontinuum Generated in Tapered PCFs,” in CLEO/Europe and EQEC 2011 Conference Digest, OSA Technical Digest (CD) (Optical Society of America, 2011), paper CD8.3.

Conference III

S. T. Sørensen, O. Bang, J. M. Dudley, ”Higher order moment description of supercontinuum noise and rogue wave statistics,” Rogue Waves: International Workshop, Dresden, Germany (2011).

Conference IV

U. Møller, S. T. Sørensen, C. Jakobsen, J. Johansen, P. M. Moselund, C. L. Thomsen, and O. Bang, ”Supercontinuum noise in tapered photonic crystal fibers,” Rogue Waves: International Workshop, Dresden, Germany (2011).

Conference V

S. T. Sørensen, U. Møller, C. Larsen, P. M. Moselund, C. Jakobsen, J. Johansen, T. V. Andersen, C. L. Thomsen, and O. Bang, ”Asymmetric Draw-Tower Tapers for Supercontinuum Generation and Verification of the Novel Concept of Group-Acceleration Matching,” in CLEO: QELS-Fundamental Science, OSA Technical Digest (Optical Society of America, 2012), paper QM4E.4.

Conference VI

S. T. Sørensen, O. Bang, B. Wetzel, J. M. Dudley, ”Higher-Order Moment Characterisation of Rogue Wave Statistics in Supercontinuum Generation,” in Nonlinear Photonics, OSA Technical Digest (Optical Society of America, 2012), paper JTu5A.22.

Conference VII

U. Møller, S. T. Sørensen, C. Larsen, C. Jakobsen, J. Johansen, P. M. Moselund, C. L. Thomsen, and O. Bang, ”Optimization of Tapered Photonic Crystal Fibers for Blue-Enhanced Supercontinuum Generation,” in Nonlinear Photonics, OSA Technical Digest (Optical Society of America, 2012), paper JW4D.1. **Postdeadline**.

Conference VIII

U. Møller, S. T. Sørensen, P. M. Moselund, C. Jakobsen, C. L. Thomsen, and O. Bang, ”High power supercontinuum generation in tapered photonic crystal fibers”, part of: 3rd International Workshop on Laser-Matter Interaction (WLMI 2012), Porquerolles.

Conference IX

U. Møller, S. T. Sørensen, C. Larsen, P. M. Moselund, C. Jakobsen, J. Johansen, C. L. Thomsen, and O. Bang, ”Tapered photonic crystal fibers for blue-enhanced supercontinuum generation,” part of: EOS Annual Meeting (EOSAM 2012), ISBN: 978-3-9815022-4-4, European Optical Society.

Conference X

S. T. Sørensen, C. Larsen, U. Møller, P. M. Moselund, C. Jakobsen, J. Johansen, T. V. Andersen, C. L. Thomsen, and O. Bang, ”Su-

percontinuum Generation in Uniform and Tapered Photonic Crystal Fibers," Presented at: The International OSA Network of Students (IONS) conference and SPIE Federation of Optics College and University Students (FOCUS), New York (2012).
Best Oral Presentation award by the American Physical Society (APS) Division of Laser Science (DLS).

Conference XI
S. T. Sørensen, C. Larsen, U. Møller, P. M. Moselund, C. L. Thomsen, and O. Bang, "Seeded Supercontinuum Generation - Modulation Instability Gain, Coherent and Incoherent Rogue Waves," in Frontiers in Optics Conference, OSA Technical Digest (online) (Optical Society of America, 2012), paper FTh1D.4.

Conference XII
C. L. Thomsen, F. D. Nielsen, J. Johansen, C. Pedersen, P. M. Moselund, U. Møller, S. T. Sørensen, C. Larsen, and O. Bang, "New horizons for supercontinuum light sources: from UV to mid-IR," in Proc. SPIE 8637, Complex Light and Optical Forces VII, 86370T (2013). **Invited**.

Conference XIII
S.T. Sørensen, C. Larsen, U. Møller, P. M. Moselund, C. L. Thomsen, and O. Bang, "Influence of Phase Coherence on Seeded Supercontinuum Generation," to be presented at CLEO/Europe and EQEC 2013, paper IF-P.10.

Conference XIV
S.T. Sørensen, C. Larsen, U. Møller, P. M. Moselund, C. L. Thomsen, and O. Bang, "Coherent and Incoherent Rogue Waves in Seeded Supercontinuum Generation," to be presented at CLEO/Europe and EQEC 2013, paper JSIII-P.6.

Conference XV
S.T. Sørensen, C. Larsen, C. Jakobsen, C. L. Thomsen, and O. Bang "Hole-Size Increasing PCFs for Blue-Extended Supercontinuum Generation," to be presented at CLEO/Europe and EQEC 2013, paper CD-P.45.

Scientific reports outside the scope of the thesis

The following journal and conference papers were published during the course of the project, but lie outside the scope of this thesis.

Paper IX
C. Agger, S. T. Sørensen, C. L. Thomsen, S. R. Keiding, and O. Bang, "Nonlinear soliton matching between optical fibers," Opt. Lett. **36**,

2596-2598 (2011).
http://dx.doi.org/10.1364/OL.36.002596

Paper X

C. Larsen, S. T. Sørensen, D. Noordegraaf, K. P. Hansen, K. E. Mattsson, O. Bang, ”Zero-dispersion wavelength independent quasi-CW pumped supercontinuum generation,” Opt. Comm. **290**, 170-174 (2013).
http://dx.doi.org/10.1016/j.optcom.2012.10.030

Conference XVI

C. Agger, S. T. Sørensen, C. L. Thomsen, S. R. Keiding, and O. Bang, ”Nonlinear matching of Solitons - Continued redshift between silica and soft-glass fibers,” in CLEO: QELS-Fundamental Science, OSA Technical Digest (Optical Society of America, 2012), paper QF1G.8.

Acronyms

CW	Continuous wave
DW	Dispersive wave
FWHM	Full-width at half-maximum
FWM	Four-wave mixing
GAM	Group acceleration mismatch
GNLSE	Generalised nonlinear Schrödinger equation
GV	Group velocity
GVD	Group velocity dispersion
HOM	Higher-order moment
IR	Infrared
MI	Modulation instability
NLSE	Nonlinear Schrödinger equation
PCF	Photonic crystal fibre
RIN	Relative intensity noise
SC	Supercontinuum
SPM	Self-phase modulation
UV	Ultraviolet
XPM	Cross-phase modulation
ZDW	Zero-dispersion wavelength

Chapter 1

Introduction

Supercontinuum (SC) generation is a spectacular phenomenon of extreme spectral broadening involving a plenitude of nonlinear physics [1,2]. Following the first observation of SC generation in bulk glass in the 1970s [3,4], the field was taken to optical telecom fibres [5,6]. However, the full potential of SC generation that pushed the technology from a mere laboratory curiosity to the development of today's commercial sources was first realised with the invention of the photonic crystal fiber (PCF) in the late 1990s [7–12], in which light can be manipulated by tailoring the PCF's air hole structure. Because of the unprecedented design freedom of the guiding properties that were impossible in bulk materials and standard optical fibres, the advent of the PCF spawned a renaissance of nonlinear optics in general and SC generation in particular [13]. Specifically, by design optimisation the zero-dispersion wavelength (ZDW) can be tuned into the visible [14]; the fibre can be made endlessly single-mode [15] or even guide light in air [16].

SC generation in PCFs is synonymous with soliton physics: when long pico or nanosecond pulses, or even continuous waves (CWs), are launched into the fibre, the process of modulational instability (MI) induces a temporal break-up that splits the pulse envelope into a distributed spectrum of solitons [17–23]. As it turns out, the subsequent soliton propagation and interactions are in fact the main driving mechanism behind the spectral SC broadening. Modulational instability is a universal physical phenomenon, in which a weak modulation of a wave experience an exponential growth [13, 24–26]. In the specific context of fibre optics, the modulation builds from quantum noise and results in large spectral shot-to-shot variations. A closer inspection of these variations led to the surprising observation of optical rogue waves [27]; statistically rare solitons with peak powers significantly above the mean. Because of their statistical nature, these optical rogue waves constitute an analogue to rogue phenomena found in such diverse systems as ocean waves, where they appear out of nowhere and cause serious damage on ships and oil rigs [28–30], finance [31] and biology [32].

It is thus clear that SC generation in PCFs provides an excellent platform for investigating important fundamental effects and their links with other physical systems. Amongst the numerous effects discovered in this context are soliton fission [33], Raman redshift cancellation by the presence of a second ZDW [34], and soliton trapping of dispersive waves (DWs) in gravitational wells [35–37]. The latter is principal for SC generation, where the long wavelength spectral "red" edge is comprised of solitons and the short wavelength spectral "blue" edge by trapped DWs. The trapping mechanism thus manifests itself as a lock between the two edges separated by upto multiple optical octaves: when the distributed spectrum of MI-generated solitons are redshifted by the Raman effect, they trap DWs across the ZDW and force them to blueshift so as to satisfy group velocity (GV) matching with the solitons [35, 38]. With a clever engineering of the GV landscape, the SC dynamics can therefore be harnessed to generate certain spectral qualities, such as an enhancement of the blue edge [38–40].

Commercial SC sources saw the light of day in 2003 (NKT Photonics A/S) and have since been established as a mature and reliable technology. As an example of their versatile applicability, Leica's new generation TCS SP8 X confocal microscope for fluorescence microscopy allows up to eight continuously tunable excitation lines to be picked simultaneously from a single SC sources. High-power commercial SC sources are typically based on long-pulsed fibre lasers, resulting in bright spectra with more than one optical octave of bandwidth. These sources are characterised by a low temporal coherence and high spatial coherence, making them suitable for a range of sophisticated spectroscopy and imaging techniques, such as optical coherence tomography [41–43] and fluorescence lifetime imaging [44,45]. Broadly speaking, the SC technology has great potential in fields where a single SC source can replace an array of lasers operating at different wavelengths, although the technology has also found applications in areas requiring ultrahigh precision, such as the development of ultra-stable optical clocks [46–50]. The potential of the SC field is highlighted by the immense growth over the last ten years, and it was recently estimated that the market for SC sources has an annual sales potential in excess of $150M [51]. The future of the fibre-based SC field seems to point to the development of cheap high-power SC sources based on (quasi) CW lasers [52–54], fully coherent SC sources in all-normal PCFs [55–61], and extending the SC spectrum into the infrared (IR) in nonsilica glasses with higher nonlinearities and/or low transmission loss in the mid-IR [62–65] or into the deep-blue and ultraviolet

(UV) with dispersion engineering [40, 66–69].

In this work we pursue two such goals: (1) to extend the SC into the deep-blue by manipulating the spectral development with dispersion engineering in tapered PCFs; and (2) to lower the spectral shot-to-shot noise by controlling either the initial MI dynamics by modulating the input pulse with a weak seed or the subsequent soliton-driven dynamics with tapered fibres. These goals are motivated by a direct commercial relevance: the entire visible part of the electromagnetic spectrum is very important for biological applications in, e.g. high resolution imaging with confocal microscopy and studies of ultrafast temporal responses with fluorescence lifetime imaging, as well as optical coherence tomography [41, 44, 45, 70]. However, most commercial sources are limited to 450-500 nm and hence cannot be used to access the biologically relevant deep-blue spectral region. Similarly, low shot-to-shot fluctuations are required in many applications where, e.g. the dynamics of a biological system is studied on a time scale comparable to the repetition rate of the light source, and in optical coherence tomography where low-noise femtosecond lasers remain the preferred choice over SC sources, despite their more attractive spectral properties. Indeed, the limited spectral shot-to-shot stability is currently one of the main drawbacks facing commercial long-pulsed SC sources.

1.1 Outline

This thesis compiles the main research results obtained during the author's PhD study. The thesis is divided into five chapters including this introduction and a summary, followed by an appendix with complementary information and the scientific journal publications Papers I-VIII published during the study (note: due to copyright ownership the full articles are not included in the online version of the thesis). The thesis should be considered a compliment to these eight scientific journal publications, and contains the necessary background information to make the thesis and publications self-contained. In addition to this background information, the thesis highlights the main results of Papers I-VIII in a coherent manner. This inevitably introduces a degree of repetition between the thesis and publications.

An introduction to nonlinear pulse propagation in microstructured optical fibres is presented in Chapter 2. The chapter is intended to establish a frame of reference to understand long-pulsed SC generation and the results presented in the following chapters. Specifically, Chapter 2 summarises the basic theory of linear and nonlinear fibre optics with a clear focus on SC generation.

In Chapter 3 we explain how dispersion engineering can be utilised to extend and enhance SC generation into the deep-blue in tapered PCFs. The chapter reviews the results of Papers I-IV plus additional unpublished results. In particular, we introduce the concept of group acceleration matching that allows us to optimise the blue edge of an SC. This is demonstrated with an array of experimental results, including the first PCF with longitudinally varying pitch and hole-size for deep-blue SC generation.

Chapter 4 discusses the noise properties of long-pulsed SC generation. Specifically, we characterise the noise properties with statistical high-order moments as described in Paper V, which provides direct insight into the nature of the noise across the spectrum. Following this, we numerically examine noise reduction by modulating the pump with a seed and experimentally by taming the SC dynamics with tapered fibres, similar to those used in Chapter 3. These results relate to Papers VI-VII and Papers III and VIII, respectively. Particular emphasis is given on the noise properties in the commercially relevant high-power regime, which has remained relatively unexplored.

Chapters 3–4 are concluded individually, and a final summary of the thesis is given in Chapter 5. Additionally, a description of the numerical modelling and the eight scientific journal publications are included as appendices.

Chapter **2**

Pulse propagation in nonlinear optical fibres

The interaction of light and matter has been extensively studied for decades. Today it is well established that light can cause matter to oscillate on an atomic or molecular level, which in turn re-emits light that interferes with the original light, and that this interaction is described by the Maxwell equations. Thanks to this understanding it is today possible to control light by engineering the medium in which it propagates. In optical fibres light is subject to *dispersion* and, if the intensity is sufficiently high, a *nonlinear* electronic response called the *Kerr effect*. That is, the refractive index depends on both the frequency and intensity of the light, which disperses the different frequencies of the light as it propagates and leads to the generation of light at new frequencies, respectively. Light can further interact with the molecular vibrations of the medium through the *Raman effect*.

The scope of this chapter is to give a condensed introduction to the physics of pulse propagation in nonlinear optical fibres, so as to make this thesis self-contained. Emphasis is given on the basic mathematical and physical background needed to understand the driving mechanisms in SC generation. An in-depth treatment is easily found elsewhere, see e.g. the book by Agrawal [71] and the 2006 review on SC generation by Dudley *et al.* [1].

2.1 Linear propagation

An electromagnetic field can be constrained by the physical boundaries of a waveguide, such a singlemode optical fibre, where guiding is achieved by surrounding the core region with a lower refractive index cladding. An electric field $\mathbf{E}(\mathbf{r}, t)$ propagating in the fundamental mode of an optical fibre can be mathematically described as

$$\mathbf{E}(\mathbf{r}, t) = \hat{x} \left\{ F(x, y) A(z, t) \exp\left[i(\beta_0 z - \omega_0 t) \right] \right\}, \tag{2.1}$$

where the field is assumed linearly polarised along the $\hat{x}$-direction. $F(x, y)$ is the transverse field distribution, $A(z, t)$ is pulse envelope and $\beta_0 = \beta(\omega_0)$ the propagation constant at pulse centre frequency ω_0, which specifies the phase change per unit length.

2.1.1 Dispersion

One of the key parameters of optical fibres is the dispersion, or the frequency dependence of the refractive index $n(\omega)$. Dispersion originates partly from the frequency dependence of the response of silica to electromagnetic waves, and partly from frequency dependencies associated with the geometry and confinement of the waveguide. These two components are referred to as *material* and *waveguide dispersion*, respectively. Dispersion is mathematically accounted for by Taylor expanding the propagation constant about the pulse centre frequency [71]

$$\beta(\omega) = n(\omega)\frac{\omega}{c} = \beta_0 + \beta_1(\omega - \omega_0) + \frac{1}{2}\beta_2(\omega - \omega_0)^2 + \cdots, \tag{2.2}$$

where c is the speed of light and the β_m coefficients are given by

$$\beta_m = \left. \frac{\partial^m \beta(\omega)}{\partial \omega^m} \right|_{\omega=\omega_0}. \tag{2.3}$$

The parameters β_1 and β_2 are particularly important in fibre optics. The *group velocity* v_g, i.e. the velocity with which the pulse envelope propagates, is directly related to β_1

$$v_g = \left(\frac{\partial \beta(\omega)}{\partial \omega} \right)^{-1} = \beta_1^{-1}. \tag{2.4}$$

The frequency dependence of v_g leads to pulse broadening of short pulses, and this *group velocity dispersion* (GVD) (or simply dispersion) is related to the GVD parameter β_2

$$D = \frac{\partial \beta_1}{\partial \lambda} = -\frac{2\pi c}{\lambda^2}\beta_2, \tag{2.5}$$

where λ is the wavelength. Dispersion parameters β_m of third and higher order are called higher-order dispersion.

The sign and magnitude of β_2 are crucial for most nonlinear processes in optical fibres. A region with $\beta_2 > 0$ ($D < 0$) is said to have *normal dispersion* and a region with $\beta_2 < 0$ ($D > 0$) *anomalous dispersion*. Normal dispersion means that the GV increases with wavelength, and that short wavelength "blue" components of a pulse travels slower than its longer wavelength "red" components. The opposite is true for regions with anomalous dispersion. The crossing point is called the *zero-dispersion wavelength* (ZDW). Efficient nonlinear conversion requires extended interaction with propagation of pulses at different wavelengths. The nonlinear interaction can thus be limited by temporal walk-off if the pulses (or frequency components) propagate with different GV, and accurate control of the dispersion is a clear prerequisite for manipulating nonlinear processes.

2.1.2 Photonic crystal fibres

Single-mode optical fibres consist of a small core surrounded by a cladding with a lower refractive index (Fig. 2.1(a)). They are typically made from fused silica glass and the index difference is controlled by dopants. Light is guided in the core due to *total internal reflection* at the boundary between the core and cladding. In contrast, *photonic crystal fibres* (PCFs) have a fundamentally different design with a complex cladding made of an array of air holes running along the length of the fibre, resembling the structure of a photonic crystal. In solid-core PCFs (Fig. 2.1(b)), the periodicity is broken by introducing a solid core, which enables light guidance in the core by a modified total internal reflection due to a lower (effective) refractive index of the air hole-surrounding relative to the core [9–11]. The first solid-core PCF was demonstrated in 1995 [7, 8], but the idea of guidance in single-material fibres was attempted as early as the 1970s [72]. In another class of PCFs light is guided in a hollow core by a photonic bandgab effect [73–75] (Fig. 2.1(c)).

PCFs can be drawn on conventional fibre draw-towers. The preform is typically made by stacking silica tubes in a close-packed array, where the core is shaped simply by placing a solid tube in the centre of the preform.

The cladding index of PCFs has a much greater wavelength dependence than that of conventional fibres, as the light distribution in the air and glass varies with wavelength. This enables endlessly single-mode operation [15], but also makes calculations of the fibre properties more difficult, and must be numerically determined with e.g. a finte-element solver. The design of the air holes allows a unique engineering of the dispersive and nonlinear properties [76], which offers unprecedented control of nonlinear processes. In particular, the success of PCFs lies in the easy tunability of the ZDW to

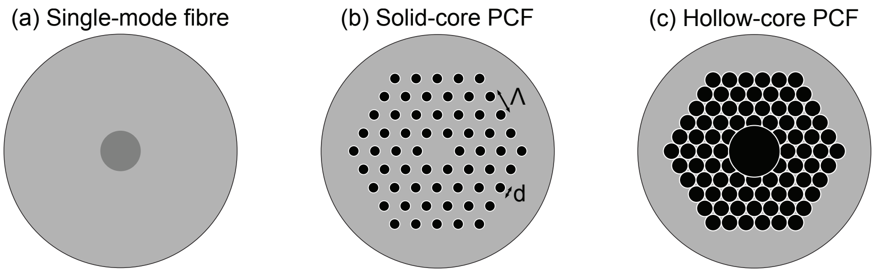

Figure 2.1: Schematic illustration of fibre cross-section of the fibre types discussed in the text. Grey areas are glass and black areas are hollow. The pitch Λ and hole size d are marked in (b).

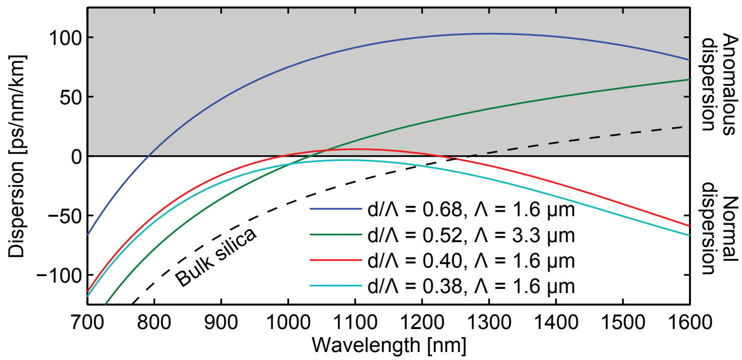

Figure 2.2: Dispersion profiles of solid-core PCFs with different hole size (d) and pitch (Λ). The dispersion of bulk silica is from [71].

match the wavelength of commercially available lasers. This is illustrated in Fig. 2.2, where the dispersion landscape is controlled to match the ZDW to a pump wavelength of either 800 or 1064 nm, and further to bring the second ZDW close to the pump or even have normal dispersion at all wavelengths. By controlling the waveguide dispersion it is thus possible to create fibres with properties very different from bulk silica.

Modal properties

Optical fibres can support a number of guided modes depending on the fibre design and wavelength; the modes differ in transverse amplitude profiles and propagation constant. Throughout this thesis we will only consider propagation in the *fundamental mode* of a solid-core PCF, which is characterised by the largest effective index and a symmetric intensity profile. In fibres with circular symmetry, the fundamental mode is two-fold degenerate with orthogonally polarized modes. The fibre properties considered here were calculated with the commercial finite-element solver COMSOL from a specified fibre geometry and appropriate choice of boundary conditions.

Attenuation

The attenuation in PCFs comes partly from the intrinsic material loss of the silica host material and partly from various sources of imperfections [10, 11, 71]. The PCF production causes imperfection in the form of structural defects and contaminations leading to additional extrinsic losses. PCFs are particularly exposed to water-related losses, where an overtone of OH-silica bond absorption causes attenuation at 1.38 μm [77]. The material loss of pure silica is low in the range 500-2000 nm, but increases towards the ultraviolet and mid-infrared due to electronic and vibrational resonances, respectively [78]. Scattering from surface roughness at the air-silica boundaries can be significant due to the large index contrast [79–81]. This becomes an increasing problem when the intensity of the guided mode is high at the boundaries, like for the small cores in the tapered PCFs considered in this thesis. Similarly, OH losses are known to increase with decreasing core size [82]. Confinement losses occur when a guided mode has a substantial evanescent field in the cladding, which can be mitigated by increasing the number of air hole rings. Appendix A includes a discussion on how to treat the dominating sources of attenuation when modelling SC generation, and attenuation in tapered PCFs is further discussed in Chapter 3.

2.2 Nonlinear propagation

From Maxwell's equations it can be shown that an electromagnetic field propagating in an isotropic medium with no free charges obeys the wave equation [71]

$$\nabla \times \nabla \times \mathbf{E}(\mathbf{r}, t) = -\frac{1}{c^2}\frac{\partial^2 \mathbf{E}(\mathbf{r}, t)}{\partial t^2} - \mu_0 \frac{\partial^2 \mathbf{P}(\mathbf{r}, t)}{\partial t^2}, \tag{2.6}$$

where μ_0 is the free space permeability and $\mathbf{P}(\mathbf{r}, t)$ is the electric polarisation. A high-intensity electromagnetic field can give rise to a nonlinear response of a dielectric medium, which in turn can generate light at new frequencies. This happens when the motion of the bound electrons becomes anharmonic. The nonlinear response of the induced polarisation to an electromagnetic field can be described by a Taylor expansion in the electric field when operating far from any resonances of the medium [71]

$$\mathbf{P}(\mathbf{r},t) = \epsilon_0 \left(\chi^{(1)} + \chi^{(2)}\mathbf{E}(\mathbf{r},t) + \chi^{(3)}\mathbf{E}(\mathbf{r},t)\mathbf{E}(\mathbf{r},t) + \cdots \right) \mathbf{E}(\mathbf{r},t), \quad (2.7)$$

where $\chi^{(n)}$ is the nth order *susceptibility.* The linear susceptibility $\chi^{(1)}$ is the dominating effect; its real and imaginary parts are related to the refractive index and attenuation, respectively. Due to the centrosymmetry of silica all even-order terms vanish. As a consequence, effects like second-harmonic and sum-frequency generation associated with the second order susceptibility $\chi^{(2)}$ do (normally) not occur in silica fibres.

The lowest-order nonlinear effects in silica fibres can hence be associated with $\chi^{(3)}$, which gives rise to the Kerr effect and Raman scattering. The former manifests itself as an intensity dependent modification of the refractive index, which leads to phenomena such as *self-phase modulation* (SPM), *cross-phase modulation* (XPM) and *four-wave mixing* (FWM) that are discussed in the following. In its simplest form, the intensity dependent contribution to the refractive index can be written as

$$\Delta n = n_2|E|^2; \qquad n_2 = \frac{3}{8n}\mathrm{Re}(\chi^{(3)}_{xxxx}), \quad (2.8)$$

where $|E|^2$ is the optical intensity and Re denotes the real part. Many of the components of $\chi^{(3)}$ can be zero for symmetry reasons, and for a linearly polarized field only the $\chi^{(3)}_{xxxx}$ component is non-zero. The nonlinearity can then be quantified through the nonlinear refractive index of silica $n_2 \approx 2.6 \cdot 10^{-20}$ m^2/W [71].

A propagation equation for the pulse envelope that includes dispersive and nonlinear $\chi^{(3)}$ effects can be derived from the wave equation Eq. (2.6). It assumes that the nonlinearity is small (i.e. that the nonlinear polarisation can be treated as perturbation) and that the bandwidth is less than $\sim$1/3 of the carrier frequency [83]. The result is the scalar *generalised nonlinear Schrödinger equation* (GNLSE) in the retarded time frame $\tau = t - z/v_g$ [83]

$$\begin{aligned}\frac{\partial A}{\partial z} &= i\sum_{m\geq 2}\frac{i^m\beta_m}{m!}\frac{\partial^m A}{\partial\tau^m} - \frac{\alpha}{2}A \\ &\quad + i\gamma\left(1 + i\tau_{\text{shock}}\frac{\partial}{\partial\tau}\right)\left(A(z,\tau)\int_{-\infty}^{+\infty} R(\tau')|A(z,\tau-\tau')|^2 d\tau'\right). \quad (2.9)\end{aligned}$$

The complex pulse envelope is normalised such that $|A(z,t)|^2$ gives the instantaneous power. The sum on the right hand side of Eq. (2.9) describes dispersion and α is the loss. The nonlinearties are quantified by the *nonlinear coefficient*

$$\gamma = \frac{n_2(\omega_0)\omega_0}{cA_{\text{eff}}}, \quad (2.10)$$

where the *effective area* of the mode $A_{\text{eff}} = (\int |\mathbf{E}|^2 dA)^2 / \int |\mathbf{E}|^4 dA$ depends on the modal distribution integrated over the xy plane [71, 84]. The time derivative in Eq. (2.9) describes the dispersion of the nonlinearity and is characterised by a time scale $\tau_{\text{shock}} = 1/\omega_0$ [1,71], which leads to effects like *self-steepening*. $R(t)$ is the nonlinear response function of silica

$$R(t) = (1 - f_R)\delta(t) + f_R h_R(t), \tag{2.11}$$

which comprises two effects: (1) the electronic response, which is assumed instantaneous and hence described by the delta function $\delta(t)$, and (2) the delayed Raman response $h_R(t)$ originating from phonon interactions [83]. $f_R = 0.18$ is the relative strength of the Kerr and Raman interactions.

When neglecting all terms except the GVD and instantaneous Kerr nonlinearity, the GNLSE reduces to the standard *nonlinear Schrödinger equation* (NLSE) [71]

$$\frac{\partial A}{\partial z} = -i\frac{\beta_2}{2}\frac{\partial^2 A}{\partial \tau^2} + i\gamma A|A|^2. \tag{2.12}$$

The NLSE is the simplest nonlinear equation for studying $\chi^{(3)}$ effects.

2.2.1 Numerical solutions

Analytical solutions to the GNLSE only exist in few highly simplified cases rendering numerical integration the obvious approach to the full problem. Numerical solutions to the GNLSE have been demonstrated to produce spectra and noise properties in good - occasionally excellent - agreement with experiments over a large range of input conditions, see e.g. [1]. The numerical modelling in this thesis is based on the particular implementation by Lægsgaard [85] that directly includes the frequency dependence of the effective area. The GNLSE is solved in the interaction picture [86] by an adaptive step-size fourth order Runge-Kutta solver. The implementation is detailed in Appendix A together with some useful tricks. The mode profile and effective area were calculated with the finite element mode solver COMSOL and will not be discussed here. It should be noted that Eq. (2.9) preserves the number of photons if loss is neglected, but energy is not preserved due to the photon-phonon energy transfer through the Raman effect [71].

It is often important to include a noise background in the simulations. This is commonly done with the *one photon per mode* model by injecting a fictitious field consisting of one photon with a random phase in each spectral discretisational bin. Additional noise sources are discussed in Chapter 4 and Appendix A.

The numerical results can be visualised in various ways. In the time domain, the pulse envelope is directly related to the instantaneous power

$P(t) = |A(t)|^2$, as mentioned above. The frequency domain envelope $\tilde{A}(\omega)$ is then simply given by the Fourier transform of $A(t)$. However, when comparing to experiments, it is often more convenient to show the power spectral density $\mathrm{PSD}(\omega) = c/\lambda^2 f_{\mathrm{rep}}|\tilde{A}(\omega)|^2$, where f_{rep} is the repetition rate. The spectrogram or time-frequency representation gives an excellent characterisation of the complex pulse dynamics, which is particularly useful for correlating temporal and spectral features. It is found by gating the field with a gate function $g(t-\tau)$ with variable delay τ, $S(\tau,\omega) = |\int A(t)g(t-\tau)\exp(-i\omega t)dt|^2$. Experimentally, the spectrogram can e.g. be measured using the frequency-resolved optical gating (FROG) technique [87, 88].

2.2.2 Self-phase and cross-phase modulation

The Kerr effect entails that the phase-velocity $v_p = c/n$ becomes intensity dependent, which leads to a self-phase modulation of a propagating pulse [89, 90] and a cross-phase modulation of co-propagating pulses [91–93].

The effects of SPM are easily observed from the NLSE (Eq. (2.12)) by neglecting GVD ($\beta_2 = 0$), which has the general solution [71]

$$A(z,\tau) = A(0,\tau)\exp(i\phi_{\mathrm{NL}}(z,\tau)); \quad \phi_{\mathrm{NL}}(z,\tau) = \gamma|A(0,\tau)|^2 z. \tag{2.13}$$

It is clearly seen that the temporal pulse shape $|A(z,\tau)|^2$ remains unchanged with propagation, while the pulse acquires a phase shift $\phi_{\mathrm{NL}}(z,\tau)$ that depends on the initial pulse shape and chirp. The time dependence of the phase shift leads to spectral changes: in general, for an unchirped Gaussian-like pulse, the leading edge will be downshifted in frequency and the trailing edge upshifted, respectively, which spectrally broadens the pulse [90].

The intensity dependence of the GV leads to self-steepening because the pulse peak moves at a lower speed than the edges. In combination with SPM this causes an asymmetric spectral broadening; for ultrashort pulses it shifts the pulse peak to the trailing edge with propagation, which ultimately creates an optical shock [71].

In addition to SPM, the Kerr effect implies that the refractive index can be modulated by the intensity of a co-propagating wave through XPM. The nonlinear phase shift experienced by a field A_1 in the presence of a co-propagating field A_2 at a different frequency can be approximated by [71]

$$\phi_{\mathrm{NL},1}(z,\tau) \approx \gamma(|A_1(0,\tau)|^2 + 2|A_2(0,\tau)|^2)z, \tag{2.14}$$

and similarly for the phase shift of A_2. The first term is due to SPM and the second term is from XPM, which is seen to be twice as effective. It is important to notice that two waves can interact through XPM without any transfer of energy. XPM depends strongly on the GVs of the involved waves to prevent temporal walk-off. This point is very important for SC generation, as we shall see.

2.2.3 Four-wave mixing and modulation instability

Four-wave mixing is a parametric $\chi^{(3)}$ process. As the name suggests, the process involves light at four (not necessarily distinct) frequencies that mix together in a way that satisfies energy and momentum conservation [71,94–96]. When light with frequencies ω_1 and ω_2 propagate in a $\chi^{(3)}$ medium, it can induce harmonics in the polarisation, which generates light at $\omega_3 = \omega_1 - (\omega_2 - \omega_1) = 2\omega_1 - \omega_2$ and $\omega_4 = \omega_2 + (\omega_2 - \omega_1) = 2\omega_2 - \omega_1$. The process can thus be used to parametrically amplify a pre-existing frequency at ω_3 or ω_4. And the FWM amplified frequencies can further interact with each other to generate a full comb of equidistantly spaced frequency components. This technique is utilised in Chapter 4.

Phase-matching is a prerequisite for FWM, and the process can be made very efficient in fibres by controlling the dispersion to ensure a vanishing phase-mismatch $\Delta k = \beta(\omega_3)+\beta(\omega_4)-\beta(\omega_1)-\beta(\omega_2)+2\gamma P_0 \approx 0$, where $2\gamma P_0$ is the nonlinear phase [71,95,96]. In a special case of FWM, two *degenerate* pump photons drive the generation of a Stokes/anti-Stokes photon pair at frequencies symmetrically positioned about the driving frequency. This automatically ensures phase-matching of the driving field.

Modulation instability is a nonlinear phenomenon in which amplitude and phase modulations of a wave experience growth. A weak perturbation of a continuous or quasi-continuous wave background can, if it falls within a certain frequency range, undergo an exponential amplification that breaks the wave into a pulse train. Although first observed in hydrodynamics [97], the MI process is recognised a universal process in nonlinear physics [13, 24–26]. In the specific context of fibre optics, MI is a consequence of the interplay between dispersive and nonlinear Kerr effects, resulting in an exponential amplification of a weak perturbation that is known to induce a break-up of quasi-continuous waves into trains of temporally short pulses [17, 22, 23, 26, 98]. The perturbation can be either quantum noise (spontaneous MI) or a signal with a frequency shift relative to the pump (induced MI). In the frequency domain, MI is a degenerate FWM process where two pump photons are converted to a Stokes/anti-Stokes photon pair and can be associated with a modulation frequency $\Delta\omega_{\mathrm{MI}} = (2\gamma P/|\beta_2|)^{1/2}$ [99].

2.2.4 Raman scattering

The electronic responses that give rise to Kerr nonlinearities are effectively instantaneous. In contrast, Raman scattering of light by molecular vibrations (phonons) is a non-instantaneous $\chi^{(3)}$ process. In *spontaneous* Raman scattering, a photon is downshifted in frequency by transferring some of its energy to a phonon [100] or upshifted by combining with a phonon. The downshifted and upshifted radiation are referred to as a Stokes and anti-Stokes wave, respectively. The latter process occurs less frequently as it requires a phonon of the right energy and momentum. It is similarly possible to utilise Raman scattering for *stimulated* amplification of a Stokes signal by a suitable pump. Spontaneous Raman scattering can act as a seed for further stimulated amplification [71].

The molecular vibrations of silica induced by an optical field can to a fair approximation be described by a simple damped oscillator model [71,83]

$$h_R(t) = \frac{\tau_1^2 + \tau_2^2}{\tau_1 \tau_2^2} \exp(-t/\tau_2) \sin(t/\tau_2) \Theta(t), \tag{2.15}$$

with $\tau_1 = 12.2$ fs and $\tau_2 = 32$ fs. $\Theta(t)$ is the unit step function. The Raman gain (i.e. the gain seen by a weak Stokes signal with a frequency offset relative to the pump) is given by the imaginary part of $h_R(t)$ in the frequency domain. The simple Raman gain is shown together with the full Raman response in Fig. 2.3. The simple model reproduces the overall shape of the full Raman gain and both show a clear maximum at $\sim$13.2 THz. Equation (2.15) has been used extensively for modelling pulse propagation with good results [1] and was used in this work. However, the model tends to underestimate the Raman-induced frequency shifts that will be discussed in the following [71].

2.3 Solitons and solitonic effects

In optical fibers with anomalous dispersion, the chirp from SPM can be exactly compensated by dispersion. This leads to one of the most intriguing phenomena in nonlinear physics: *the soliton*, a translational solitary wave that retains its shape with propagation. Solitons are known from a wide range of nonlinear systems and were first discovered in the early 1800s in the form of water waves [102]. The propagation of solitons in optical fibres was first considered in 1973 by Hasegawa and Tappert [103] and experimentally observed in 1980 by Mollenauer *et al.* [104], although optical solitons were in fact unknowingly generated in 1978 by Lin *et al.* [6].

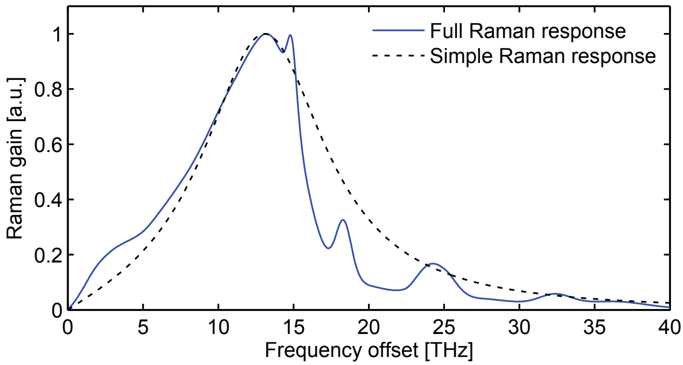

Figure 2.3: Normalised Raman gain spectrum of silica. The frequency offset is of the (weak) Stokes signal wave with respect to the pump. The full Raman response is based on [101].

Mathematically, solitons are exact solutions to the NLSE of the form [71]

$$A(z,\tau) = \sqrt{P_0}\mathrm{sech}\left(\frac{\tau}{\tau_0}\right)\exp\left(-i\frac{|\beta_2|}{2\tau_0^2}z\right), \tag{2.16}$$

where the width τ_0 and peak power P_0 are related through the *soliton number*

$$N^2 = \frac{\gamma P_0 \tau_0^2}{|\beta_2|}, \tag{2.17}$$

and the exponential function represents the nonlinear phase shift attained with propagation. *Fundamental solitons* have $N = 1$ and propagate without any change in temporal or spectral shape. Higher-order solitons have integer soliton numbers $N > 1$ and periodically return to their initial shape. However, the term soliton typically refers to a fundamental soliton, as we shall do here.

One of the most remarkable features of solitons is the stability: near-solitonic pulses automatically adjust their shape to that of a fundamental soliton, possibly by dispersing excess energy. Solitons are similarly known to be stable under small perturbations, such as losses and amplification [103,105–107] as well as changes in dispersion and nonlinearity [22,108]. The changes just need to be sufficiently slow for the soliton to *adiabatically* adjust its shape. Because of the stability solitons were quickly suggested as candidates for optical communication [105, 106, 109, 110]. In contrast, higher-order solitons are not stable under perturbations, rather they undergo *soliton fission* that breaks the higher-order soliton into its fundamental soliton constituents [35, 71, 111].

2.3.1 Soliton self-frequency shift

The spectrum of a temporally narrow soliton can be sufficiently broad for the short wavelength components of the soliton to act as a Raman amplifier for the long wavelength components [112]. This intra-pulse Raman scattering transfers energy from the blue to the red edge, which effectively shifts the soliton to gradually longer wavelengths, a phenomenon called the *soliton self-frequency shift* [113, 114]. The Raman gain is weak for small frequency offsets, as seen in Fig. 2.3. This causes a strong dependence of the redshift rate on the soliton duration that can be approximated by $\partial\omega_s/\partial z \propto -|\beta_2|/\tau_0^4$ for long pulses [114]. The self-shift rate (generally) slows down with propagation because energy is lost in the Raman process and the pulse broadens temporally.

The Raman self-frequency shift can be used to access spectral regions that are hard to reach with existing lasers. In Paper IX we investigated the possibility of coupling an ensemble of redshifting solitons between two different fibres, while ensuring that the solitons remain solitons without shedding energy. This can e.g. be utilised to extend the redshift of multiple co-propagating solitons into the mid-infrared by coupling them from a silica to a softglass fibre. However, this will not be discussed further in this thesis.

2.3.2 Dispersive wave generation

A soliton can, in the presence of higher-order dispersion, resonantly transfer energy into the normal dispersion regime to a so-called *dispersive wave* or *Cherenkov* radiation [115]. The amplification of DW radiation conditions resonant coupling, i.e. phase-matching from the soliton to the DW. This can occur for solitons in the vicinity of a ZDW with spectral components extending into the normal dispersion regime, so that the centre of the soliton can resonantly amplify its own spectral tail with propagation [116, 117]. A cancellation of the self-frequency shift has been demonstrated by a mechanism where a redshifting soliton slows down as it approaches a long-wavelength ZDW [34], which causes a recoil of the soliton due to phase-matched energy transfer across the ZDW.

Recently, Erkintalo *et al.* [118] identified phase-matched cascaded FWM as the driving mechanism in DW generation from soliton-like pulses perturbed by higher-order dispersion, where a bichromatic pump pair within the soliton spectrum generates frequencies in the opposite dispersion regime.

This directly explains the soliton recoil observed near a second ZDW and DW generation in the anomalous dispersion regime from pulses in the normal dispersion regime [119]. Also recently, it was demonstrated by Rubino *et al.* [120] that the soliton has an additional phase matched component in the negative frequency branch of the dispersion that can generate DWs at even shorter wavelengths. This can be understood by noting that an electromagnetic field is a real function, and can hence be described as a positive frequency envelope and its complex (negative frequency) conjugate, where the latter gives rise to additional phase-matching conditions [120, 121].

2.3.3 Trapping of dispersive waves

The dispersive radiation generated from a soliton typically propagates at a lower GV than the soliton, preventing any immediate interaction. However, as the soliton redshifts it decelerates, which eventually allows the soliton and DW to interact through a cascade of XPM collisional events. This leads to the fascinating phenomenon of *pulse trapping*, where the redshifting soliton traps the DW and forces it with to move with the GV of the soliton [35–37, 122–126]. This effect is principal for SC generation and its implications will be discussed in greater detail in Chapter 3. The manifestation of the trapping effect is demonstrated in Fig. 2.4, which shows the propagation of a 25 fs fundamental soliton and a GV matched DW package in a typical PCF with a ZDW at 1054 nm (the modelling in Chapter 4 is based on the same fibre). The spectral evolution in Fig. 2.4(a) shows how the soliton forces a continuous blueshift of the DW with propagation, so as to satisfy GV matching. This is detailed in the spectrograms in Fig. 2.4(b) for the soliton and DW, the soliton alone and the DW alone, respectively. When both pulses are present, the DW is trapped by the soliton, which forces it to propagate at the GV of the soliton and keeps the DW from dispersing. The soliton undergoes nearly the same redshift in the absence of the DW, although a small change in the final delay is observed. In contrast, when the DW propagates alone it is subject to significant dispersion, which clearly highlights the trapping effect.

The trapping effect has been explained as a consequence of XPM and the soliton deceleration: The soliton induces a modulation of the refractive index across the DW via XPM, which effectively creates a potential barrier that forces the DW to trail behind the soliton. In addition, the soliton deceleration imposes a gravity-like force on the DW, preventing it from dispersing behind the soliton. These two effects combined thus creates a gravity-like potential that effectively traps the DW and forces it to follow the GV of the soliton. This was first explained by Gorbach and Skryabin [37]

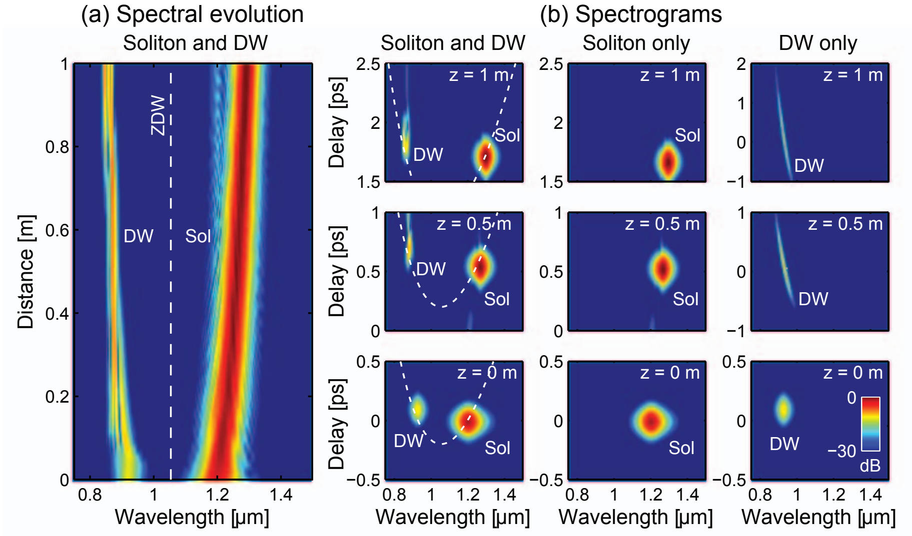

Figure 2.4: (a) Propagation of a fundamental soliton ($\lambda_s = 1200$ nm, $\tau_0 =$ 25 fs, $P_0 = 10.2$ kW) and GV matched DW (sech^2-shape, $\lambda_{DW} = 925$ nm, $\tau_0 =$ 25 fs, $P_0 = 1.02$ kW): as the soliton redshifts it traps and blueshifts the DW. (b) Spectrograms at 0, 0.5 and 1 m for the soliton and DW, the soliton alone and the DW alone, respectively. The dotted lines show the GV. The used PCF has hole-to-pitch ratio $d/\Lambda = 0.52$ and pitch $\Lambda = 3.6$ μm, which gives a ZDW of 1054 nm.

by investigating the process in the inertial frame of the soliton. The soliton deceleration is normally provided by the Raman redshift, but can likewise be achieved by tapering the fiber [127].

2.4 Supercontinuum generation

Supercontinuum generation occurs when short and intense pulses experience extremely large spectral broadening due to a range of interconnected linear and nonlinear effects. It is perhaps the most striking and dramatic effect in nonlinear fibre optics, and is particularly efficient in PCFs due to the excellent control of both nonlinear and dispersive properties. It was first observed in the 1970s in bulk by Alfano and Shapiro [3, 4] and later in optical fibres by Lin *et al.* [5, 6]. In these first experiments the pump fell in the normal dispersion regime and the spectral broadening was mainly caused by the Raman effect and SPM. However, in the 1980s SC generation was realised from a pump in the anomalous dispersion regime, where MI

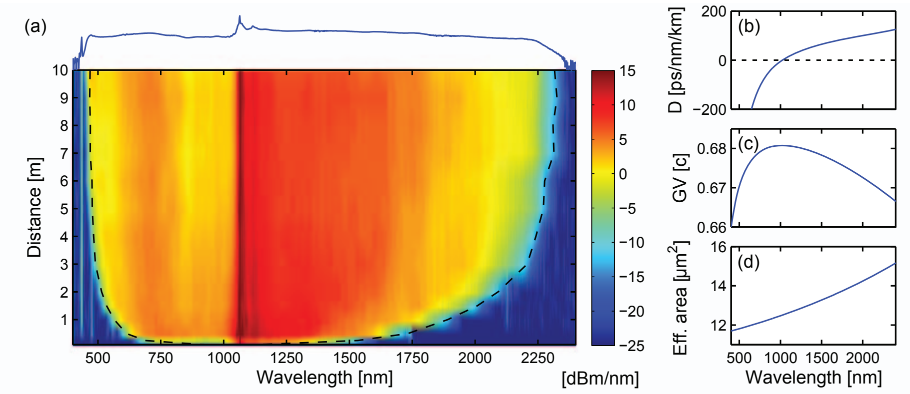

Figure 2.5: (a) Experimental cutback measurement of SC generation in a uniform PCF with hole-to-pitch ratio $d/\Lambda = 0.85$ and pitch $\Lambda = 4.4\ \mu$m. (b)–(d) Calculated dispersion, GV and effective area, respectively. The fibre was pumped at 1064 nm with 10 ps pulses at 15 W average power and 80 MHz repetition rate. The dotted lines in (a) show the measured long-wavelength edge and the theoretically calculated GV matched blue edge.

caused a break-up of the pump into a distributed spectrum of redshifting solitons [19, 35, 128]. The resulting broad spectra were attributed to the an ensemble average of the solitons that had redshifted by different amounts. The SC field really took off with the invention of the PCF, which greatly simplified the requirements needed for SC generation, as demonstrated in the 2000 experiment by Ranka *et al.* [12]. The first commercial SC source saw the light of day shortly after in 2003. Today the technology has matured and SC sources are available from several companies [129].

The commercially available SC sources are typically based on a picosecond high-power fibre laser and a length of PCF to broaden the spectrum. Here we shall focus on such sources. The spectral broadening as a function of length is shown in Fig. 2.5(a) for a laser and PCF typical of most high-power sources. The measurement was made by repeatedly shortening the fibre and measuring the spectrum. The spectrum broadens very rapidly over the first ∼2 m, but the broadening slows down in the remaining fibre length and effectively ceases after ∼8 m. The final SC spectrum is very smooth and extends over 2.5 optical octaves from 450–2300 nm. The calculated dispersion, GV and effective area are shown in Fig. 2.5(b)–(d). The SC broadening in this regime with a picosecond pump in the anomalous dispersion regime close the to ZDW can be described as follows:

(i) The broadening is initiated when MI breaks the picosecond pump into large a number of temporally short pulses that reshape into fundamental solitons [17–23].

(ii) The solitons generate DWs in the normal dispersion regime and start redshifting. As the solitons redshift they trap and blueshift DWs across the ZDW [35–37, 124, 125].

(iii) The broadening stops when the largest solitons reach the infrared material loss edge, which effectively prevents soliton propagation beyond $\sim$2.4 μm. This in turn defines the short-wavelength blue edge through GV matching, since this edge is comprised of the most blueshifted DWs that are linked to the most redshifted solitons at the long-wavelength red edge [35, 38].

The fundamental importance of the soliton-induced trapping can be seen in Fig. 2.5(a), where the dotted lines mark the experimentally determined red edge and theoretically calculated GV matched blue edge, respectively. The agreement is excellent and can be used to theoretically determine the blue edge [35, 38, 40], as we shall see. The broadening described above becomes much clearer when investigating the dynamics in spectrograms. To this end, simulated spectrograms of parameters similar to those of Fig. 2.5 are shown in Fig. 2.6 at select propagation distances. The initial stage of MI and the subsequent generation of ultrashort soliton-like pulses are clearly evident in Figs. 2.6(a)–(b), which is further supported by the close-up of the temporal dynamics near the pulse centre shown in Fig. 2.6(d). The final stage of soliton redshift and DW-trapping is apparent in Fig. 2.6(c), where a clear temporal overlap between the most redshifted solitons and the most blueshifted DWs is observed.

The break-up of a long pulse has later been linked to Akhmediev breather theory [13, 25]. Akhmediev breathers are exact analytical solutions to the NLSE that describe the evolution of a wave with a small time-periodic perturbation imposed on a constant background, resulting in the growth and return of a train of ultrashort pulses. It was suggested in [13] that the onset of long-pulse SC generation from spontaneous MI can be interpreted as the generation of large number of Akhmediev breathers that then reshape into solitons.

The distributed spectrum of MI-generated solitons will redshift at different velocities, which inevitable leads to temporal collisions. In fact, it turns out that inelastic soliton collisions are a key driver in the formation of the long-wavelength SC edge [128, 130, 131]. Left isolated, even the most powerful MI-generated soliton broadens and slows down before reaching the loss edge. During such collisions, inter-pulse Raman scattering transfers energy between the solitons; the energy transfer depends strongly on the relative

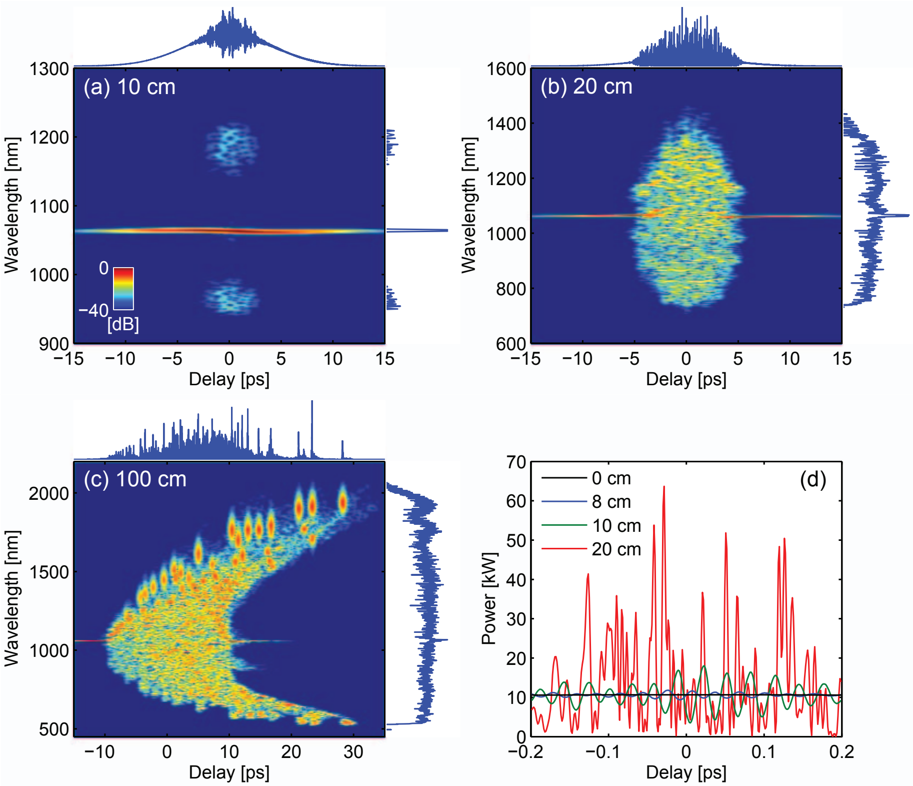

Figure 2.6: (a)–(c) Spectrograms at propagation distances of 10, 20 and 100 cm, respectively, calculated for parameters corresponding to those in Fig. 2.5. The spectra are downsampled to 1 nm resolution. (d) Close-up of the temporal evolution near the pulse centre at propagation distances of 0, 8, 10 and 20 cm, respectively.

phase and amplitude, but on average there is a preferential transfer of energy from the smaller to the larger soliton [128, 130, 131]. This energy transfer can lead to the formation of rare large amplitude solitons, also known as *rogue waves* [27], which we discuss in Chapter 4.

It is interesting to compare the *single-shot* spectra in Fig. 2.6 with the measured *averaged* spectra in Fig. 2.5: the MI process generates solitons with a spread in shape and power, which leads to a corresponding difference in the final spectra from shot to shot. This is characteristic of noise-seeded MI and explains why the experimental spectra measured over 1000s of shots are so remarkably smooth and flat. However, there is an intrinsic trade-off between the spectral flatness and noise.

Finally, it should be noted that the spectral broadening can be achieved through other mechanisms. The dominating broadening mechanisms depend on the dispersion, nonlinearity and pump duration and power. In particular, soliton fission generally takes precedence over MI for short (femtosecond) pulses and soliton-driven broadening is prohibited when pumping in the normal dispersion regime [1].

Chapter **3**

Blue-enhanced supercontinuum generation in tapered PCFs

Amongst the greatest advantages of SC generation in PCFs is the possibility to shape the SC spectrum through dispersion engineering. Indeed, by controlling the dispersion, and thereby the phase and GV landscape, the nonlinear processes that govern SC generation can be manipulated. In this chapter, tapered PCFs are utilised to extend the SC spectrum into the deep-blue. This is motivated by a great commercial interest in extending the bandwidth below 400 nm, in particular for biological applications in e.g. fluorescence microscopy due to the absorption bands of many fluorophores in this wavelength region [70]. The chapter summarises the results of Papers I-IV. Specifically, the importance of the taper shape on available power in the blue edge and the first single-mode high air-fill fraction PCF for deep-blue SC generation.

3.1 Tapered PCFs for blue-extended supercontinuum

In soliton-driven SC generation, dispersion engineering can be directly applied to yield a certain SC bandwidth, since the spectral edges are linked by GV matching [35, 38, 39]. The maximal attainable SC bandwidth in a given fibre is thus limited by the GV profile and where the soliton redshift ceases: the maximum extent of the soliton redshift defines the red edge, which in turn defines the blue edge by GV matching. Specifically, in Paper II we define the red edge λ_{red} for a high-power SC source as the wavelength where the spectral broadening is stopped by the increasing material loss

λ_{loss} (the loss "edge"), here set to 2300 nm, or a wavelength λ_2 close to the second ZDW, whichever is the lowest. Solitons always halt their redshift about 50-100 nm away from the second ZDW [34, 132] so λ_2 is chosen to $\lambda_{\text{ZDW},2} - 50$ nm, which means that $\lambda_{\text{red}} = \min\{\lambda_{\text{loss}}, \lambda_{\text{ZDW},2} - 50\text{nm}\}$. The blue edge is then simply determined through GV matching. This is demonstrated in Fig. 3.1 by showing the calculated dispersion, effective area and GV for PCFs with a hole-to-pitch ratio of 0.52 and values of the pitch in the range 4.0 to 2.0 μm. Reducing the pitch shifts the first ZDW to gradually shorter wavelengths and eventually also brings the second ZDW below the loss edge. The effective area reduces with the pitch due to the decreasing core size. But more importantly, the GV decreases with the pitch, which means that there is GV matching to gradually shorter wavelengths up to a certain point. This allows us to define an *optimum pitch* that yields the shortest possible blue edge (for a fixed hole-to-pitch ratio). Reducing the pitch below the optimum increases the GV near the loss edge due to the second ZDW, which increases the GV matched blue edge wavelength. However, simply starting out with a PCF with the optimum pitch is generally undesirable: a pulse break-up with an efficient transfer of energy into the normal dispersion regime requires a pump in the vicinity of the ZDW, and the optimum pitch generally shifts the ZDW far below the ytterbium pump wavelength of 1064 nm used in most commercial SC sources. It further gives a small core that complicates coupling. The trade-off between a short wavelength blue edge and an efficient conversion across the ZDW can be resolved by using tapered PCFs, in which an initial length of uniform fibre with a suitable ZDW ensures an efficient pulse break-up, and a subsequent tapered section with decreasing pitch (and fixed hole-to-pitch ratio) permits GV matching to gradually shorter wavelengths [39, 40, 66–68, 70, 133–137]. For the particular PCF in Fig. 3.1 (that we shall be using later) the blue edge is shifted from 496 nm at a pitch of 3.3 μm (ZDW at 1035 nm) to 476 nm at the optimum pitch of 2.5 μm (ZDW at 963 nm). We emphasise that the trends described here are applicable over a wide range of hole-to-pitch ratios.

Tapering has previously been demonstrated as an effective way of extending the SC bandwidth into the blue by changing the dispersion and increasing the nonlinearity [40, 66–68, 70, 133, 136, 138–143]. In particular, spectra extending down to wavelengths as short as 320 nm from a 1065 nm pump were reported in [67,68], which is at the limit of what can be achieved, as we shall see. An impressive 280 nm was reached in [69] by pumping an ultrashort taper with a femtosecond pump at 800 nm. However, in the latter case the light was generated directly in the UV region by a different mechanisms of soliton fission directly from the pump. Table 3.1 summarises

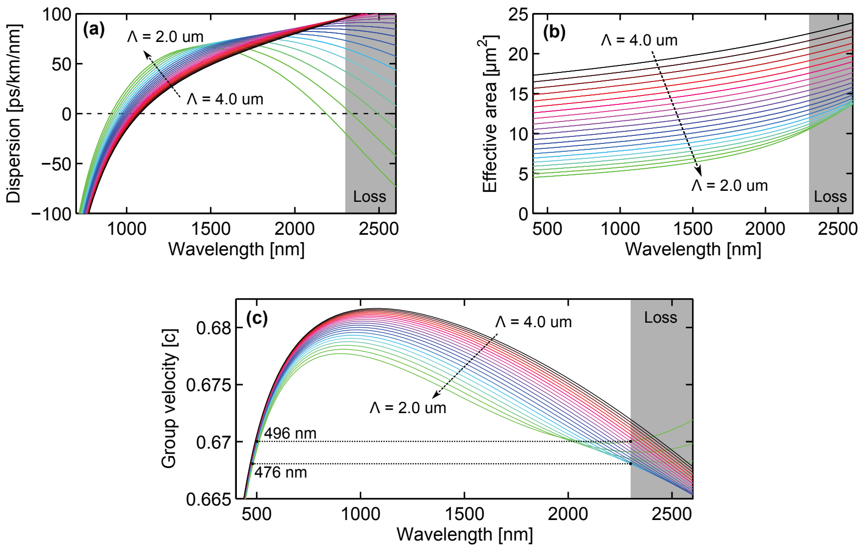

Figure 3.1: Calculated (a) dispersion, (b) effective area and (c) GV for PCFs with hole-to-pitch ratio 0.52 and values of the pitch from 4.0 to 2.0 μm. The shaded areas mark the loss region above 2300 nm, and the horizontal dotted lines in (c) show the GV matching from 2300 nm for a pitch of 3.3 and 2.5 μm, respectively.

a selective review of the literature on SC generation in tapered fibres, and a more general overview of blue-extended SC generation can be found in the 2010 review by Travers [40].

The use of tapered fibres was first suggested as a means of compensating temporal pulse broadening in lossy fibres [108, 153–156], where the propagation of a soliton can be made invariant by decreasing the dispersion along the fibre. Later the same method was used for pulse compression [157–162] and the generation of high repetition rate soliton trains [22, 23, 156]. Similarly, tapered PCFs have been used for more general soliton manipulation [163–166], including the observation of a soliton blue-shift [167]. And more straightforwardly, tapering has been used to increase the fibre nonlinearity [145, 168, 169]. Indeed, tapered single-mode fibres can be made to have dispersion and nonlinear properties similar to those of a PCF to facilitate SC generation [138, 144, 170]. This has further been utilised for mid-IR SC generation in soft glasses like chalcogenide and tellurite, where the taper increases the nonlinerity and hence expands the SC to longer wavelengths beyond the transmission window of silica [171–174].

PCFs can be tapered exactly like single-mode fibres either by post-

Reference	**Pump**[1]	**Fibre**	**SC width and power**
Birks, OL 2000 [138]	Ti:Saph, 850 nm, 70-100 fs, 76 MHz	SMF taper 1 m	370–1545 nm, 300 mW
Wadsworth, JOSA B 2002 [144]	Ti:Saph, mode-locked, 850 nm, <200 fs, 76 MHz	SMF-28 taper	400–1600 nm, 350 mW
Leon-Saval, OpEx 2004 [139]	Microchip, 532 nm, 0.6 ns, 6.33 kHz, 1 kW	Tapered PCF, 9 cm, 500 nm core	<400–850 nm, 1.7 mW
Foster, OpEx 2004 [145]	Ti:Saph, 25 fs, 80 MHz	PCF taper, sub-um core	400–1000 nm
Teipel, OpEx 2005 [146]	(a) Nd:YVO4, 1064 nm, 8 ps, 85 MHz, 350 nJ , 30 W (b) Nd:YVO4, 1064 nm, 9 ps, 120 MHz, 50 nJ, 6 W	SMF-28, multiple tapers	(a) 450–1600 nm, 4.2 W (b) 900–1600 nm, 1.4 W
Lu, OL 2005[2] [140]	Ti:Saph, 880-900 nm, 100 fs, 150 mW	PCF taper, short	∼380–1200+ nm
Travers, OL 2005 [147]	Yb, mode-locked, 1064nm, 3-4 ps, 51 MHz, 8 W (2.2 W)	Cascaded PCFs	350–1750+ nm, 0.95 W
Kudlinski, OpEx 2006[3] [66]	(a) Nd:YAG microchip, Q-switched, 1064 nm, 600 ps, 7.25 kHz, 15kW (60% coupling) (b) Yb, mode-locked, 1064 nm, 3-4 ps, 51 MHz, 60 kW peak, 8 W avg. (4-5 W)	PCF tapers, draw tower	(a) 370–1750+ nm (b) 375–1750+ nm, 3.5 W
Xiong, OpEx 2006 [148]	Nd:YAG, microchip, Q-switched, 1064 nm, 0.6 ns, 7.2 kHz, 15 kW	Inflated PCF: all normal ESM → taper (12 cm waist) → ESM	∼400–1700+ nm, 30 mW
Travers, CLEO 2007[4] [67]	Same as [66]	PCF tapers, draw tower	(a) 320–? nm (b) 330–2400 nm, 3.5 W
Kudlinski, OL 2008[5] [133]	Yb, CW, 1064 nm, 0.5 nm FWHM, 20 W (13.5 W)	PCF taper, 100 m. Germanium and flurine doped core	670–1350 nm, 9.55 W
Cascante-Vindas, OC 2008 [149]	Nd:YAG, 532 nm, 7 ns, 10 kHz, 282 W (70% coupling)	PCF cobweb taper, 10 cm	350–800 nm
Moselund, Thesis 2009[6] [136]	Yb, mode-locked, 1064 nm, 14.6 ps, 80 MHz, 14 W (70% coupling)	PCF tapers, cm length	∼380–1750+ nm
Kudlinski, JLT 2009 [39]; Mussot, EL 2009 [135]	Yb, CW, 1070 nm, 1 nm FWH , 50 W (35 W)	Tapered PCF, draw tower, 100 m	650–1380 nm, 19.5 W
Kudlinski, OL 2009 [52]	Same as [39], 45 W coupled	Tapered GeO_2-doped-core PCF, 130 m (135 to 85 μm OD)	470–1750+ nm, 9.3 W
Stark, JOSA B 2010 [150]	NOPA 490-700 nm, sub-50 fs, 250 kHz, 250 nJ	Short PCF taper, ZDWs at 509 and 640 nm	∼350–900 nm
Cascante-Vindas, OpEx 2010 [143]	Nd:YAG, 1064 nm, 0.6 ns, 20 kHz, 160 mW/13 kW	PCF taper, 35 cm, Ge doped	420–1850 nm
Kudlinski, OpEx 2010[7] [70, 137]	Nd:YAG, q-switched, 1064 nm, 0.6 ns, 7 kHz, 8 kW (5.8 kW, ∼43 mW avg.)	Tapered PCF, draw tower, 7 m	350–1750+ nm, 17 mW
Peiguang, OpEng 2011[8] [151]	$Nd:YVO_4$, 1064 nm, 7.76 ps, 76 MHz, 10 W	Tapered PCF, 145 m	430–2050 nm, 1.1 W
Stark[9], OL 2012 [69]	800 nm, 130 fs, 2 nJ	PCF tapers, 5-30 mm	280–1600 nm
Wadsworth, OPN 2012[10] [81]	Yb, pulsed, 1064 nm	PCF taper, draw tower	310–2500 nm
Stone, OFT 2012 [68]	1060 nm, 5 ps, 1 MHz	PCF taper, 5 m	330–2600 nm, 130 mW
Chen, COL 2012[11] [152]	Microchip, 1064 nm, 0.7 ns, 7 kHz, 8 kW/40 mW coupled	Multiple short PCF tapers	470–1670 nm

Comments: [1]Coupled power levels are specified in brackets. [2]Blue edge generated as a-Stokes radiation. [3](b) 3 dB flatness: 395-850 nm with 2 mW/nm. [4]Results similar to [66]. [5]A strong peak at 550 nm from a higher-order mode was observed. [6]Taper shape and noise properties investigated. [7] [70] High conversion to 350–600 nm region; [137] similar results, focus on noise reduction in blue edge. [8]Very large OH loss: 188 dB/km at 1380 nm. [9]UV light generated directly from the temporally compressed pump in ultra-steep taper. [10]Values estimated from spectrum in OPN News article. [11]Focus on spectral flatness.

Table 3.1: Selective literature overview on blue-extended supercontinuum generation in tapered fibres.

fabrication processes or during the fibre draw, and it has been demonstrated that even very short PCF tapers do not introduce coupling between modes [175]. In addition to decreasing the overall fibre diameter, PCFs allow for a longitudinal variation of the hole-size, which we utilise in Sec. 3.3. Post-processed tapers are fabricated by heating and stretching the fibre, thereby reducing the diameter. This can be done with high accuracy and hole-collapse can be avoided either by pressurising the air holes or tapering cold and fast [136, 149, 176–181]. Post-fabricated tapers are typically limited to 10s of cm, and although longer lengths have been fabricated, such fibres will be very fragile. This is circumvented by tapering directly at the draw-tower by varying the draw-speed during fabrication [40,66,70,133,151,160]. It has generally been the belief [179] that draw-tower tapers shorter than 10 m are difficult to fabricate. On the contrary, we find that tapering directly on the draw-tower offers high accuracy of the fibre parameters by pressure control of the air hole structure, and allows fabrication of accurate fibre tapers with lengths from less than a metre and up with high reproducibility, as shown in Paper III. This further makes it possible to use the draw-tower's coating system as an integrated part of the taper fabrication. A very short draw-tower taper of only 10 cm was recently reported in [182], showing the flexibility of draw-tower tapers.

Blue-extended SC generation has also been achieved by other kinds of dispersion engineering, such as immersing a post-processed tapered PCF in a liquid with a suitable refractive index [183] and by doping the silica glass with e.g. germanium [52, 184, 185]. Changing the material can have the additional advantage of enhancing the Kerr and Raman responses. Impressive results have been demonstrated by (mainly) SPM broadening in short lengths of fluoride fibres with an SC spanning 3 octaves from 350 nm to 3.85 μm [64]. And recently uniform PCFs with microstructured cores [186] were used to achieve GV matching to wavelengths below 400 nm, but at the expense of a very small effective area.

3.2 Optimum taper profiles for blue-enhanced supercontinuum

The idea of extending the SC into the deep-blue by changing the GV landscape has been described and demonstrated by several authors [39, 40, 66–68, 70, 133–137], but the importance of the taper shape remained largely unknown [40]. This section describes the importance of the taper profile on the available light in the blue edge. It should be emphasized that the approach pursued here is for long-pulsed MI-initiated SC generation, which is

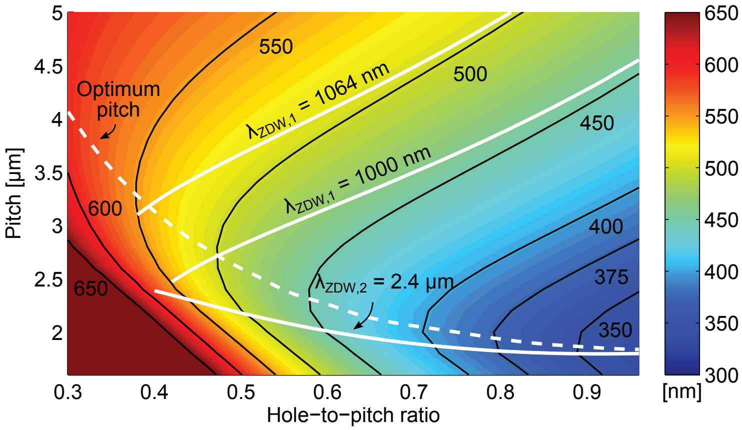

Figure 3.2: Calculated blue edge wavelength as a function of hole-to-pitch ratio d/Λ and pitch Λ, assuming GV match to a red edge at 2300 nm or 50 nm below the 2nd ZDW. The dashed line indicates the optimum pitch (shortest blue edge) for a given hole-to-pitch ratio. The full white lines mark where the first ZDW is at 1064 and 1000 nm, respectively, and where the second ZDW is at 2400 nm.

fundamentally different from e.g. [69, 150], where the blue edge is generated directly from a fs pump pulse in an ultrashort taper. The taper profile was optimised for this short-pulse SC regime in [142, 187], where the SC bandwidth and flatness were controlled by manipulating direct soliton fission of the pump in a short tapered fibre.

Analytical descriptions of soliton propagation in non-uniform fibres have been reported by several authors [163, 188, 189]. In particular, Judge *et al.* [163] theoretically calculated the condition for an increased soliton redshift by clever uptapering, where the long-wavelength ZDW is increased as the soliton redshifts so as to avoid DW generation and soliton recoil. However, the focus here is on the downtapering section where the solitons are decelerated and can trap DWs.

As a starting point, in Fig. 3.2 we extend the analysis of Fig. 3.1 by mapping out the calculated blue edge as a function of pitch and hole-to-pitch ratio, which suggests that ~330 nm can be achieved for $d/\Lambda > 0.95$, and that the optimum pitch is found near 2 μm for large hole-to-pitch ratios, in agreement with the similar analysis in [40]. This suggests that the results in [67, 68] are at the limit of what can be achieved in terms of achieving the shortest possible wavelength. The figure clearly shows the merits of tapered PCFs for blue extended SC generation: the full white lines mark

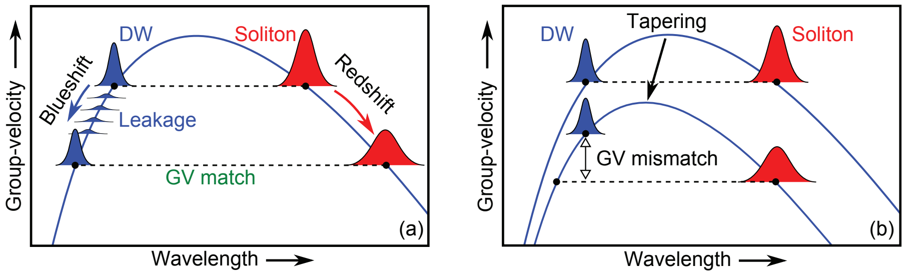

Figure 3.3: Radiation trapping and leakage in (a) uniform and (b) tapered fibres. In tapered fibres the asymmetric change in the GV of the soliton and DW gives rise to a group acceleration mismatch.

where the first ZDW is at 1064 nm and 1000 nm, respectively. PCFs with a ZDW of 1000 nm are seen to have GV matching to wavelengths above 450 nm, which demonstrates that achieving GV matching to wavelengths much below 450 nm in a uniform fibre is difficult without compromising the conversion efficiency to the visible due to the offset from the ZDW [38].

3.2.1 Group acceleration mismatch

In order to determine the optimum taper profile it is useful to first review the soliton-induced trapping of a DW package in a uniform fibre. It has generally been neglected that the soliton trapping process is in fact not complete, which means that a trapped DW may continuously loose energy. This is illustrated in Fig. 3.3(a): the soliton undergoes a continuous Raman redshift, which leads to a continuous change in GV with propagation length, i.e. a deceleration. The DW does, however, not move spectrally in its own right and is thus not subject to the same deceleration. This means that there is a small difference in GV, and thus potentially a small leakage of DW energy. The Raman effect therefore leads to a *group acceleration mismatch* (GAM); an asymmetric change in the GV of the solitons and DWs. The effect is not significant in uniform fibres, because the relatively weak Raman redshift leads only to small GV changes with propagation and hence a minor GAM. However, in a fibre taper the GV change can be orders of magnitude larger than the inherent Raman induced change. Moreover, the change in GV is generally highly asymmetric, i.e. the taper-induced GV change is much smaller for the DW than for the soliton, as illustrated in Fig. 3.3(b). Travers and Taylor [127] demonstrated that this taper-induced GV decrease enhances the trapping potential of the soliton and can in fact supply the needed soliton deceleration to trap a DW in the absence of the Raman effect.

In physical terms, the GAM lowers the XPM interaction length (the depth of the gravitational well), causing light to escape. To this end, Schreiber *et al.* demonstrated [190] that light can escape or pass unaffected through the XPM interaction region when the interaction length is sufficiently short, i.e. a large GV difference.

The GAM concept was introduced in Paper I, where we further demonstrated, for the first time, the impact of the taper gradient on the trapping of a DW by means of single soliton simulations. This directly translates to a dependence of the available light in the blue edge of an SC on the taper gradient. To investigate the full scale importance of GAM on SC generation comprised by hundreds of solitons and DWs, we fabricated an asymmetric draw-tower taper. The point of the asymmetry is to enforce a difference in the GAM depending on whether the fibre is pumped from the long or short downtapering side, while ensuring that the light passes through the same length of fibre. We based the taper on the commercial fibre SC-5.0-1040 from NKT Photonics A/S with a hole-to-pitch ratio of $d/\Lambda = 0.52$ and pitch 3.3 μm, which we analysed in Fig. 3.1. We chose this particular fibre, because it it is single-mode at the pump [191].

In all of the SC experiments in this work, we used a modelocked 1064 nm Yb fibre-laser typical for commercial SC sources. The laser emits 10 ps pulses with an average output power of 14 W at a repetition rate of 80 MHz. The PCFs were spliced directly to the laser using a filament splicer, resulting in typical coupling losses below 1 dB. The output was collimated and recorded with an optical spectrum analyser through an integrating sphere. The output power was measured with a power meter and the spectra normalised accordingly (see [192] for details). The IR part of the spectrum was measured with an additional spectrum analyser and the two spectra were stitched together.

The results of the asymmetric draw-tower taper are summarised in Fig. 3.4. We characterise the taper profile in Fig. 3.4(c), where the pitch as a function of length is determined from cross-sectional images. It is seen that the pitch is reduced from 3.3 to 2.5 μm in an asymmetric way that roughly can be described as a 1.5 m downtaper and a 0.5 m uptaper. The hole-to-pitch ratio of 0.52 was preserved throughout the taper. We used an additional 5 m of uniform fibre before and after the tapered section to generate an initial spectral broadening. The spectra recorded when pumping from the long (blue) and short (red) downtapering sides are shown in Fig. 3.4(a) together with a reference spectrum from a 10 m uniform fibre (black) with a constant pitch of 3.3 μm. A close up of the blue edge is shown in Fig. 3.4(b), where the theoretically calculated blue edges from Fig. 3.2 are marked; the discrepancy can be ascribed to deviations in the

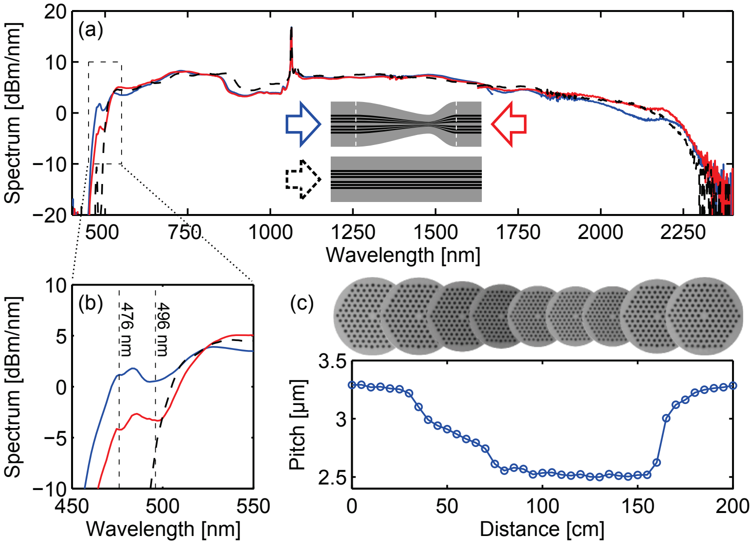

Figure 3.4: (a) Experimental output spectra of the asymmetric draw-tower taper. The spectra show the taper pumped from the long (blue) and short (red) downtapering sides. The spectrum of a 10 m uniform fibre (black dash) is shown for comparison. (b) Close-up of the blue edge marked in (a). The vertical lines denote the calculated spectral edges. (c) Measured profile of the taper. The pitch is calculated from the shown cross-sectional images recorded with an optical microscope at 100x magnification. The hole-to-pitch ratio $d/\Lambda = 0.52$ was constant through the taper.

hole-to-pitch ratio in the taper. Evidently, both spectra generated in the tapered fibre extend below the bandwidth achievable in the uniform fibre, as expected. But more importantly, pumping from the long downtapering side clearly yields a significantly higher power in the blue edge than pumping from the short, which confirms the importance of GAM: when the taper is too steep, the solitons at the red edge undergo a much larger deceleration than the DWs at the blue edge, and a fraction of the energy in the DWs therefore escapes the trapping potential and is consequently not blueshifted. In the present case, we see a threefold increase in the energy below 500 nm when the taper is pumped from the long downtapering side. These results form the basis of Paper II. The importance of GAM was complimented with additional experiments and simulations in Paper III.

3.2.2 Deep-blue supercontinuum generation

The GV matching landscape in Fig. 3.2 tells us, for a fixed hole-to-pitch ratio, what values of the pitch we should choose to (1) ensure an effective pulse break-up near the ZDW and (2) give the optimum short wavelength blue edge. The notion of GAM additionally says that the length of the downtapering section should be as long as possible to yield an efficient conversion of light to short wavelengths. However, in reality attenuation and soliton broadening will enforce an upper limit on the downtapering length. Specifically, the rapidly increasing loss at short wavelengths will eventually precede the amount of light that is continuously transferred to the edge, and for long tapers the solitons will temporally broaden and/or be stopped by the IR loss edge, and hence terminate the DW trapping and blueshift, before the optimum pitch is reached. For the tapers considered above and in Papers II-III, where the SC never extended below 450 nm, we saw a continual increase in power at the blue edge with increasing taper length. We later conducted additional experiments with downtaper lengths above 10 m, which further supported this conclusion. An SC extending down to 450 nm can, however, be realised in a uniform fibre, as suggested by Fig. 3.2. We therefore - among other things - turned to designing an SC extending below 400 nm. Although far from the 320 nm reported in the literature [67, 68] this is still a significant improvement over most commercially available high-power systems and an important intermediate step on the way to realising a system extending far into the deep-blue. To this end, we fabricated a number of tapers with a hole-to-pitch ratio of 0.7, all with a total length of 10 m. They consisted of $\sim$35 cm of uniform fibre with a pitch of 4.0 μm (ZDW at 1035 nm), followed by a downtapering section where the pitch is linearly reduced to either 2.2 or 1.85 μm over a varying length, and finally a length of uniform waist to fixate the total fibre length at 10 m. A pitch of 2.2 μm corresponds to the optimum tapering degree defined in Fig. 3.2. The lower pitch of 1.85 μm was chosen to investigate the influence and sensitivity of the spectrum on the final pitch and the accompanying increased attenuation due to the smaller core. The total length was fixed at 10 m to examine if a long downtapering section is preferable over a relatively shorter downtapering section and a correspondingly longer waist with a fixed pitch.

The results are shown in Fig. 3.5: all spectra show a peak with a high spectral power density around 395 nm and generally have spectral densities above 1 mW/nm across the entire visible spectrum. The exact position of the blue peak varies slightly, which again can be ascribed to slight variations in the actual fibre parameters. The position of the blue edge is particularly sensitive to variations in the hole-to-pitch ratio, and the spectrum of the

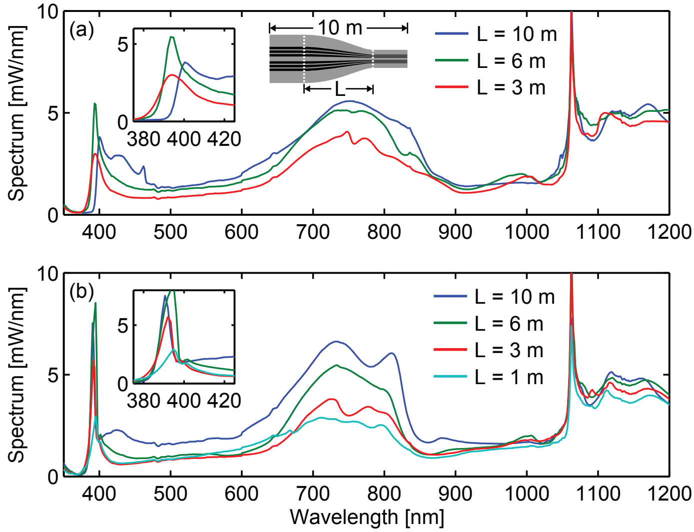

Figure 3.5: Experimental spectra of tapered fibres with a hole-to-pitch ratio of 0.7 and varying downtapering length. All fibres had a total length of approximately 10 m, and consisted of a ∼35 cm length of uniform fibre with a pitch of 4.0 μm, followed by a downtapering section of varying length L (see legend) and a length of waist with a constant pitch of (a) 2.2 μm (the optimum pitch) or (b) 1.85 μm.

Taper length [m]	10	6	3	1
Vis. power, 2.2 μm taper [W]	1.68	1.40	1.11	-
Vis. power, 1.85 μm taper [W]	1.67	1.41	1.02	1.00

Table 3.2: Visible spectral power below 900 nm of the tapers shown in Fig. 3.5. All spectra had a total power of 5.8 W.

10 m taper in Fig. 3.5(a) suggests that the optimum pitch and hole-to-pitch ratio was not entirely reached in this fibre. More importantly, there is a clear dependence on the downtaper length of the light in the blue edge. In fact, we observe a clear increase of the spectral density in the entire visible part of the spectrum with the length of the downtaper for both values of the final taper pitch. This is detailed in Table 3.2, which gives a list of the visible power below 900 nm measured through two $E0_2$ mirrors. Interestingly, the total power was 5.8 W in all cases, but the visible power has a clear dependence on the downtaper length independently on the final pitch. To understand this difference, we show in Fig. 3.6 the attenuation

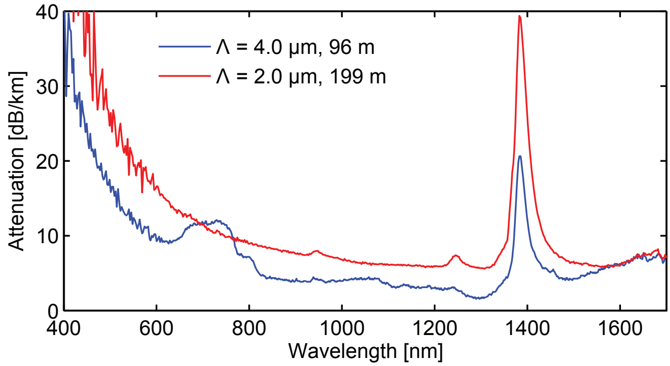

Figure 3.6: Attenuation for PCFs with hole-to-pitch ratio 0.7 and pitch 4.0 μm (blue) and 2.0 μm (red), respectively. Fibre lengths of 96 and 199 m were used to measure the loss. Courtesy of NKT Photonics A/S.

of two uniform fibres with hole-to-pitch ratio 0.7 and a pitch of 4.0 and 2.0 μm, respectively. The loss was measured with an incoherent broadband light source in a 96 and 199 m length of fibre, respectively. Because of the low loss and short fibre length the measurement of the 4.0 μm fibre must be considered relatively uncertain. Similarly, the uncertainty increases at low wavelengths due to a low spectral density of the used light source at these wavelengths. The trend is nonetheless clear: the attenuation increases at all wavelengths with decreasing fibre diameter, in line with [80, 82]. Even so, the loss is still very low at all wavelengths, which explains why we see a constant total power independent on the relative length of the downtaper and waist. The downtapering and waist hence redistribute the energy in the spectrum, but do not introduce any significant additional attenuation in this case. In [82] it was found that although the attenuation increases in small core PCFs, it is rather insignificant for core diameters above 2 μm, but rapidly increasing for smaller core diameters. The fibres considered here had core diameters in the taper waist of $\Lambda(2 - d/\Lambda) = 2.9$ μm and 2.4 μm, respectively, and are thus far from this high attenuation region.

These measurements suggest that a longer downtaper is beneficial in two ways: (1) it shifts more energy all the way to the blue edge due to a lower GAM, and (2) it allows an overall larger transfer of light into the visible. Finally, it is interesting to notice that tapering to 1.85 μm instead of 2.2 μm only has a minimal impact on the spectrum: the blue edge appears at the same wavelength, but is enhanced in the 1.85 μm taper. This could be because the final hole-to-pitch ratio is slightly higher than 0.7, in which case the optimum pitch is somewhere between 1.85 and 2.2 μm.

3.3 Single-mode air-fill fraction increasing PCFs

While PCF tapers have proven their worth for blue-extended SC generation, accessing the deep-blue spectral region requires a high air-fill fraction. This brings about the drawback that high air-fill fraction PCFs are inevitably (highly) multi-mode at the pump, which greatly complicates coupling and interfacing. To overcome this issue, we fabricated a PCF with longitudinally increasing air-fill fraction *and* decreasing pitch directly at the draw-tower. This uniquely ensures single-mode behaviour at the input and GV matching into the deep-blue at the output, because of the longitudinally increasing air-fill fraction. This can be appreciated from Fig. 3.2: where the previously considered tapers had a constant hole-to-pitch ratio and decreasing pitch, corresponding to moving vertically downwards in the figure, an increasing air-fill fraction and decreasing pitch corresponds to moving diagonally downwards. Specifically, we chose the same input parameters as the tapers in Fig. 3.4 with a 0.52 hole-to-pitch ratio and 3.3 μm pitch, which makes the PCF single-mode at 1064 nm [191]. However, this time we simultaneously increased the hole-to-pitch ratio to 0.85 and decreased the pitch to 2.0 μm, which gives a theoretical GV match to 360 nm, according to Fig. 3.2. Importantly, we show in Paper IV that the changes in dispersion and GV in this case follow exactly the same trends as in Fig. 3.1 for a taper with constant hole-to-pitch ratio. The conclusions from tapered fibres with constant hole-to-pitch ratio can therefore be immediately extrapolated to air-fill fraction increasing tapers.

The tapers considered so-far were fabricated by controlling the draw speed during fabrication. However, increasing the air-fill fraction necessitates an additional control of the pressure on the air holes during the draw. Left isolated, we found that increasing the air hole pressure leads to an undesirable increase in the pitch. It was thus necessary to control simultaneously the pressure and draw speed to achieve the desired structure with increasing hole-to-pitch ratio and decreasing pitch. The fibre structure realised after a number of iterative draws is shown in Fig. 3.7: the hole-to-pitch ratio increases from 0.52 to 0.85 over 7 m, while the pitch decreases from 3.3 to 2.15 μm. The hexagonal structure is well preserved during the air hole-expansion without introducing any structural defects. Although the final pitch is slightly larger than the optimum pitch of 2.0 μm, this highlights the amazing design freedom in PCFs and clearly verifies the feasibility of fabricating PCFs with longitudinally increasing air-fill fractions. A similar

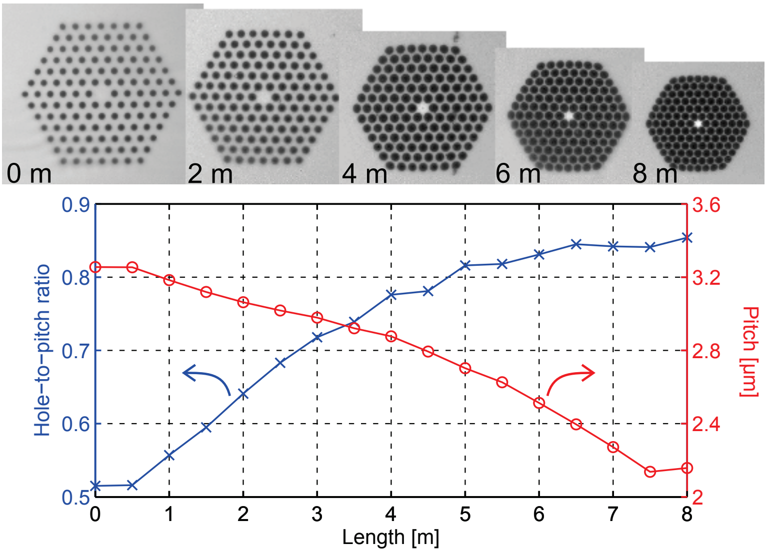

Figure 3.7: Characterisation of the fibre structure: the top row shows microscope images of the fibre end facet at selected distances from the input (on the same scale) and the plot shows the corresponding hole-to-pitch ratio and pitch calculated from 17 images equidistantly spaced along the 8 m fibre.

approach was pursued in [148, 193], where the air hole size was increased in a short section of an endlessly single-mode PCF using a post processing technique, but only to enhance the visible power.

Figure 3.8 shows the SC generated in the air-fill fraction increasing PCF, where an initial 40 cm length of uniform fibre was kept to initiate the spectral broadening. The spectrum generated in the fundamental mode had a total power of 5.8 W with 734 mW in the visible part of the spectrum, and extends down to 375 nm with a spectral density above 0.5 mW/nm in most of the visible bandwidth. The discrepancy between the measured spectral blue edge at 375 nm and the theoretical target at 360 nm is due to a perturbation of the innermost air holes, resulting in a reduction of the core size. This is detailed in Paper IV. Yet, these results clearly demonstrate the applicability of air-fill fraction increasing PCFs for single-mode pumped deep-blue SC generation.

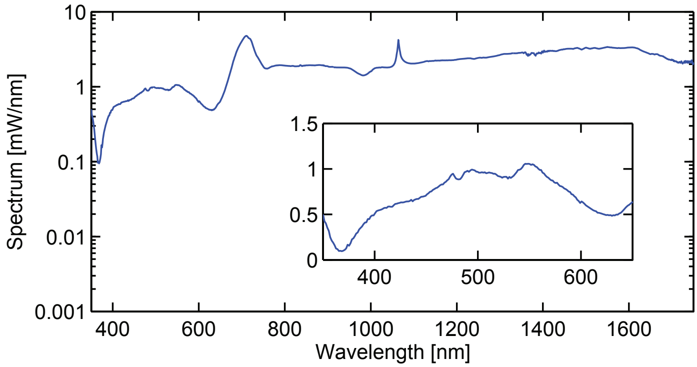

Figure 3.8: Measured SC spectrum. The inset shows a close up of the spectral blue edge on a linear scale. The total output power was 5.8 W with 734 mW in the visible part of the spectrum.

3.4 Conclusions, discussion and outlook

In this chapter we have investigated the applicability of PCF tapers for blue-extending SC generation into the commercially attractive deep-blue spectral region. Specifically, tapered fibres bring together two otherwise mutually exclusive features: an initial fibre section with a ZDW close to the pump and a subsequent fibre section with GV matching from the mid-infrared loss edge into the deep-blue. The former ensures an efficient break-up of the pump into solitons and DWs, while the latter allows the Raman solitons to trap and blueshift the DWs to short wavelengths.

By introducing the concept of a group acceleration mismatch, we explained that the amount of light transferred to the spectral blue edge is directly correlated with the gradient of the taper. This is because the taper-induced change in GV generally is much larger for the soliton than for its trapped DW package, which can cause light to escape from the soliton-induced trap. We verified this by pumping an asymmetric draw-tower taper from either end, where a longer downtaper significantly enhanced the blueshifted power. Subsequently, we fabricated a range of tapers with a 0.7 hole-to-pitch ratio and successfully demonstrated SC generation with spectral densities in excess of 1 mW/nm across the visible region down to 390 nm. We found that the spectral power in the entire visible region was enhanced by increasing the downtaper length, and that attenuation was not a limiting factor in these tapers. Finally, we fabricated the first single-mode high air-fill fraction PCF for deep-blue SC generation. For this, we exploited the full degrees of freedom to draw a PCF with longitudinally increasing air-fill fraction and decreasing pitch, which makes it single-mode at the input and resulted in an SC spectrum extending down to 375 nm.

Future directions would include further development of the air-fill increasing PCF to accurately realise the specified target, but also to vary the device length and increase the final air-fill fraction to shift the spectrum below 350 nm. A more thorough investigation of the attenuation must also be conducted to investigate when the increasing material attenuation at short wavelengths becomes a limiting factor for the spectral broadening. It would also be highly interesting to examine the effects of scaling the average and peak power.

It is also yet to be investigated if photodarkening is a limiting factor for SC sources based on tapered fibres. Photodarkening in pure silica has been attributed to the generation of structural defects in the silica network, where partially bound oxygen atoms with one free electron leads to strong absorption [194, 195]. This may become an increasing problem in tapers because of the increased intensity. In terms of reaching ultrashort wavelengths other methods have been pursued, including gas-filled hollow-core fibres [196–198], which resolves any degradation issues since the SC is generated in the injected gas rather than in silica. The combination of very short PCF tapers with sub-wavelength diameters and femtosecond pulses in [69, 150] yielded impressive results with a high energy transfer into the UV region. However, the merits of the method presented here lie in simple and robust all-fibre design that can be made completely compatible with existing technology, and the ability of these designs to work with simpler long-pulsed pump sources with high average powers.

Chapter **4**

Supercontinuum noise properties

The highly nonlinear nature that enables SC generation also makes the process very sensitive to noise; even small noise seeds and pump pulse variations can result in large amplitude variations in the resulting SC [199–203]. A considerable ongoing effort has been devoted to understand and control the SC noise properties, motivated both by application demands for low-noise broadband sources as well as in the fundamental context of clarifying links with instabilities in other systems. The primary sources of SC noise will be discussed in this chapter together with a review of the results of Papers V-VIII. Specifically, we introduce a higher-order moment description of the spectral noise and pursue two approaches to lower the noise: first numerically by actively seeding the pulse break-up with a minute seed and second experimentally by passively controlling the noise with tapered fibres.

4.1 Noise sources and rogue waves

There are two main sources of spectral SC noise [201]: the fundamental limit is set by quantum noise, i.e. input shot noise and spontaneous Raman scattering, leading to broadband SC noise. Additionally, the high sensitivity of SC generation to initial input pulse conditions makes the process sensitive to technical noise such as pump fluctuations. The relative importance of these sources depends on the dynamical regime. For most cases - and for long-pulsed SC generation in particular - input shot noise is the dominant noise seed, while Raman scattering plays a minor role [201]. Due to the high stability of modern pump lasers, it is well established that the main source

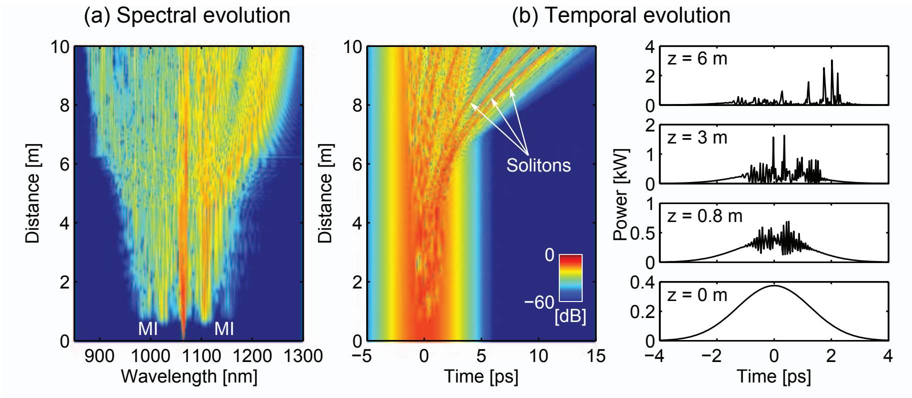

Figure 4.1: Spectral and temporal evolution of MI-driven SC generation, using a 3 ps (FWHM) Gaussian pump at 1064 nm with 262.5 W peak power (this odd peak power is chosen to match Fig. 4.3). The PCF has hole-to-pitch ratio 0.52 and pitch 3.6 μm and is used throughout the chapter.

of shot-to-shot noise in long-pulsed SC generation stems from the noise-driven MI process that breaks the pump into ultrashort pulses [55, 204]. This implies a shot-to-shot variation of the distributed soliton spectrum generated from the MI process, and consequently also of the subsequent soliton interaction and energy transfer. This adds to the noise, because soliton collisions depend strongly on the relative phase and amplitude [128, 130, 131, 205].

The noisy character of SC generation is illustrated in Fig. 4.1 by showing the spectral and temporal evolution of a typical (low-power) SC in the presence of noise. The hallmarks of the noise-initiated MI process are clearly seen in the form of spectral sidebands and a temporal modulation on the pulse envelope, which leads to a break up of the pulse into redshifting solitons. In what follows we shall quantify and discuss the spectral SC noise in more detail.

The long-wavelength edge of a high-power SC is thus constituted of a large number of solitons with a spread in shape and energy that varies from shot-to-shot. In typical experiments, where the SC is measured as an average over 1000s of individually generated spectra, this shot-to-shot information is completely washed-out. This also means that statistically rare rogue waves are not captured by averaged measurement techniques [128]. It was in fact exactly an investigation of spectrally filtered pulse trains of individually generated spectra that allowed Solli *et al.* [27] to observe optical rogue waves in the form of large amplitude solitons that experienced an enhanced Raman redshift, and hence appeared isolated at the red SC edge. Rogue solitons can either be generated directly as high-peak power solitons in the MI pulse break-up for certain initial noise conditions [27, 206] or through collisional events, where the convective nature of solitons generally transfers energy from the smaller to the larger soliton [29, 205, 207–209]. In that regard, it should be noted that collisional energy transfer between solitons is a necessity for rogue soliton formation in high-power SC generation; the individual MI-generated solitons do not have sufficient energy redshift to the spectral edge.

The rogue wave term is not clearly defined in optics. Following the hydrodynamic definition, rogue waves can be associated with solitons whose height (peak power) is more than twice the significant wave height, i.e. the mean peak power of the one-third largest amplitude solitons [210]. However, the term is commonly used to describe a single high-energy soliton that has experienced an enhanced redshift (relative to the statistical norm), and spectral regions with L-shaped wave energy (histogram) distributions are considered synonymous with rogue waves. In [210] it was further demonstrated that collisional events lead to higher peak powers than any single rogue soliton, suggesting that on-going collisions could in fact also be perceived as rogue events. It should further be noted that rogue waves - like all other waves - are quenched when they reach the loss edge. This has been demonstrated to transform the characteristic L-shaped statistics associated with rogue events into skewed Gaussian statistics [211].

Finally it should be stressed that although long-pulsed SC generation is not suitable for applications that require a high degree of spectral coherence, low pulse-to-pulse energy fluctuations are nonetheless of vital importance (also for incoherent sources) for several applications, such as fluorescence microscopy. In fact, relatively large shot-to-shot variation is not necessarily a disadvantage, since large variations lead to very smooth average spectra [200], which can be utilised for applications where the pulsed SC is treated as quasi-continuous. As an interesting example, the randomness of MI-driven SC generation was utilised to generate random numbers in [212].

4.2 Quantifying supercontinuum noise

SC noise is often quantified by the spectral coherence function calculated as an ensemble average over independently generated SC spectra $\tilde{A}_i(\omega)$

[204, 213, 214],

$$\left|g_{12}^{(1)}(\omega)\right| = \left|\frac{\left\langle \tilde{A}_i^*(\omega)\tilde{A}_j(\omega)\right\rangle_{i\neq j}}{\sqrt{\left\langle\left|\tilde{A}_i(\omega)\right|\right\rangle^2\left\langle\left|\tilde{A}_j(\omega)\right|\right\rangle^2}}\right|, \tag{4.1}$$

where angle brackets denote an ensemble average and the asterisk denotes complex conjugation. The spectral coherence function provides an inside into the stability of an SC and is primarily a measure of the shot-to-shot phase fluctuations, with $|g_{12}^{(1)}| = 1$ signifying perfect coherence. Experimentally, the spectral coherence is related to the fringe visibility of the spectral interference pattern generated by independently generated SC spectra. In contrast, intensity fluctuations are typically quantified in bandwidths of e.g. 10 nm across the SC spectrum, either from histograms of pulse heights (peak powers) [27,207,215] or the *relative intensity noise* (RIN) of the radio-frequency spectrum [201–203, 215]. Specifically, the latter is calculated as $\mathrm{RIN}(\omega) = \Delta\mathrm{P}(\omega)^2/\mathrm{P}_{\mathrm{avg}}(\omega)^2$, where ΔP and P_{avg} are the mean square intensity fluctuations and average optical power, respectively.

To demonstrate the limitations of the existing noise measures based on histograms, RIN and the spectral coherence, we use numerical simulations in the presence of noise to generate an ensemble of SC spectra under conditions where there are significant fluctuations between different realisations of the ensemble. Throughout this chapter and Papers V-VII, we shall consider a PCF typical for SC generation pumped at 1064 nm. The particular fibre has a pitch of 3.6 μm and a relative hole-size of 0.52, resulting in a ZDW of 1054 nm (for further details see Paper V or VI). These exact parameters are not special, but chosen because they are realistic and typical of many experiments.

The simulation results for a 3 ps Gaussian pulse with 250 W peak power are shown in Fig. 4.2: the spectral plot in Fig. 4.2(b) superposes results of the 500 individual simulations (grey) together with the calculated mean (solid line), with the top subplots showing the calculated degree of spectral coherence and RIN calculated in 10 nm bandwidths across the spectrum. Figure 4.2(c) shows histograms of the pulse energy fluctuations extracted over the 10 nm bandwidths marked in the spectral plot in Fig. 4.2(b) (Fig. 4.2(a) shows a re-analysis of the results described in the following section). The close-up of the long wavelength edge clearly shows the presence of a few rogue wave-like solitons that have redshifted significantly further than the statistical mean. This is also reflected in the histograms that show a transition from Gaussian near the pump to long-tailed (L-shaped) near the long wavelength edge. The spectral coherence and histograms clearly provide only limited and qualitative information. For example, whilst it is easy to calculate and display the coherence at all wavelengths across the spectrum, the fact we see that it is zero over most of the SC bandwidth indicates only the presence of severe noise over a wide wavelength range, without indicating anything specific about its nature. On the other hand, displaying histograms at specific wavelengths across the SC is useful to show how statistics can vary from Gaussian near the pump to long-tailed near the long wavelength edge, but the selection of which particular wavelengths to filter and analyse in this way is not a priori evident. The RIN gives a measure of the noise across the full SC bandwidth, and although it captures the increase in noise with detuning from the pump, it does not provide any information on the nature of the shot-to-shot fluctuations.

4.2.1 Higher-order moment description of spectral noise

To resolve the limitations of the noise measures discussed above, we introduced *higher-order moments* as SC noise and rogue wave descriptors in Paper V. The HOMs characterise the shape of a particular distribution and not only its location and spread. For a real-valued random variable X, the nth-order central moment around the mean is given by

$$\mu_n = \langle (X - \langle X \rangle)^n \rangle. \tag{4.2}$$

The zeroth and first central moments are $\mu_0 = 1$ and $\mu_1 = 0$, respectively. The second order central moment μ_2 is the well-known variance σ^2, which measures the distribution spread. Instead of σ^2 we shall be using the so-called *coefficient of variation*: $C_v = \sigma/\langle X \rangle$, which has the straightforward interpretation as being inversely proportional to the *signal-to-noise ratio* (SNR) that we shall also consider later. Of particular interest for analysing the asymmetric long-tailed distributions associated with SC generation are the third and fourth central moments, commonly expressed in normalised form relative to the variance. The third order central moment is referred to as the *skewness* $\gamma = \mu_3/\sigma^3$, which measures the asymmetry of the distribution, with $\gamma < 0$ for a left-skewed distribution, $\gamma > 0$ for a right-skewed distribution and $\gamma = 0$ for a symmetric distribution. The fourth-order central moment is referred to as *kurtosis* $\kappa = \mu_4/\sigma^4 - 3$, and measures whether the distribution is peaked or flat relative to a normal distribution of the same variance. A normal (Gaussian) distribution has $\kappa = 0$, and a high kurtosis arises from rare extreme deviations from the mean. The HOMs all relate to the pulse intensity, and should hence be considered complementary to the phase-sensitive spectral coherence, Eq. (4.1).

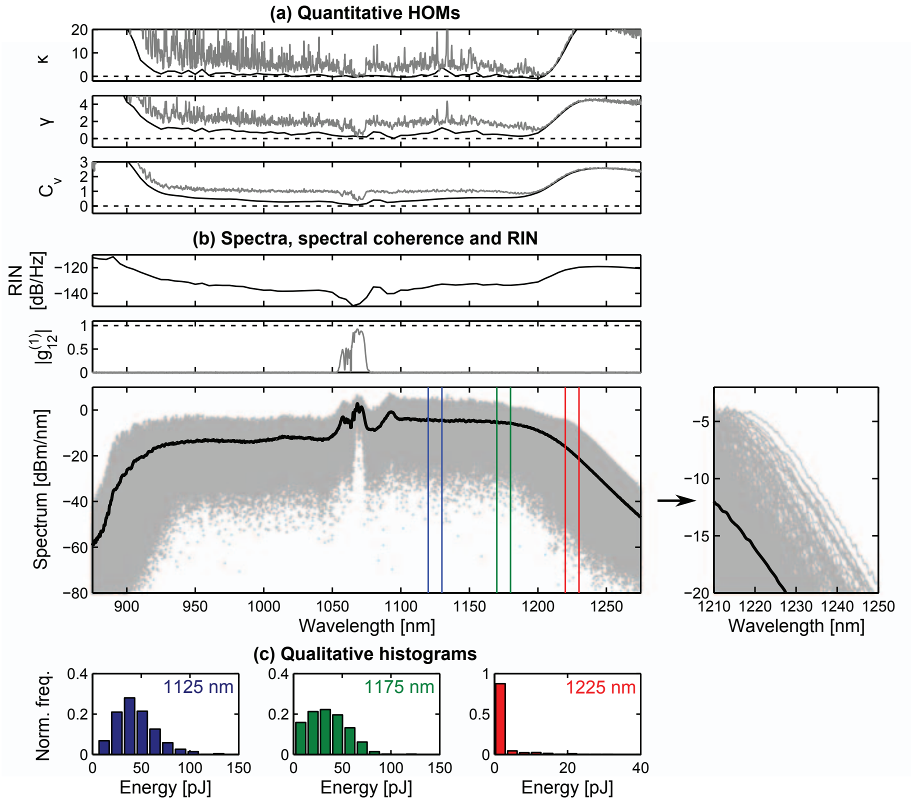

Figure 4.2: Numerical simulations in the presence of noise. (b) Spectra, calculated degree of spectral coherence ($|g_{12}^{(1)}|$) and RIN for a 3 ps Gaussian pulse with 250 W peak power after 10 m propagation. A close-up of the long wavelength edge is shown on the right. (a) Corresponding HOMs calculated both in 10 nm bandwidths (black lines) and using the numerical resolution (grey lines). The HOMs are kurtosis (κ), skewness (γ) and coefficient of variation (C_v), respectively. (c) Histograms calculated in the 10 nm spectral windows marked in spectrum in (b).

We re-analyse the simulation results presented above using HOMs in Fig. 4.2(a). The HOMs are calculated across the SC spectrum both in 10 nm bandwidths and using the numerical resolution (0.07 nm at 1064 nm). The moments clearly reflect the transition from low-noise near-Gaussian statistics to noisy highly skewed and peaked statistics when the window is moved into the spectral wing. A larger spectral window introduces a higher degree of averaging and hence results in lower values of the HOMs, but the particular choice of spectral windows does not affect the overall conclusions. The HOMs thus provide direct insight into the degree and nature of the noise across the SC bandwidth, and allows a direct quantitative comparison between modelling and experiment. In other words, the HOMs capture both the magnitude and character of the noise, which previously had only been analysed with a combination of qualitative histograms and a quantitative measure such as RIN.

In Paper V we detail how the HOMs can be used to gain insight into the nature of the intensity fluctuations in a few select cases. We further suggest, as a useful guideline, that rogue wave behaviour can be associated with the product of skew and kurtosis exceeding ten, $\gamma \cdot \kappa > 10$. This, however, should be taken as a rule of thumb and not a strict criteria. As a further example of the utility of the HOMs, Wetzel *et al.* [216] used a frequency-to-time mapping technique to measure single-shot SC spectra. The analysis of the noise properties based on HOMs showed an excellent agreement with simulation results across the full SC bandwidth.

4.3 Seeded supercontinnum generation

In the long-pulse MI-driven regime, it has been demonstrated that modifying the input conditions can stabilise the otherwise highly turbulent and noisy SC generation. Indeed, by inducing the MI with an externally applied modulation, a train of short soliton-like pulses can be generated with a desired repetition rate [17,18]. It was thus suggested by Islam *et al.* [128] that the distributed spectrum of solitons generated from the MI of a picosecond pulse could be generated deterministically with small shot-to-shot fluctuations by seeding at the MI frequency. Extensive investigations have used modulational control of the input pulse both to clarify the fundamental physics underlying instabilities and links to rogue wave phenomena [206,217–219], as well as in the application motivated context of lowering the SC noise [220–225].

To illustrate the basic principle of modulational control of the pump in SC generation, we revisit the results of Fig. 4.1 in Fig. 4.3, where the

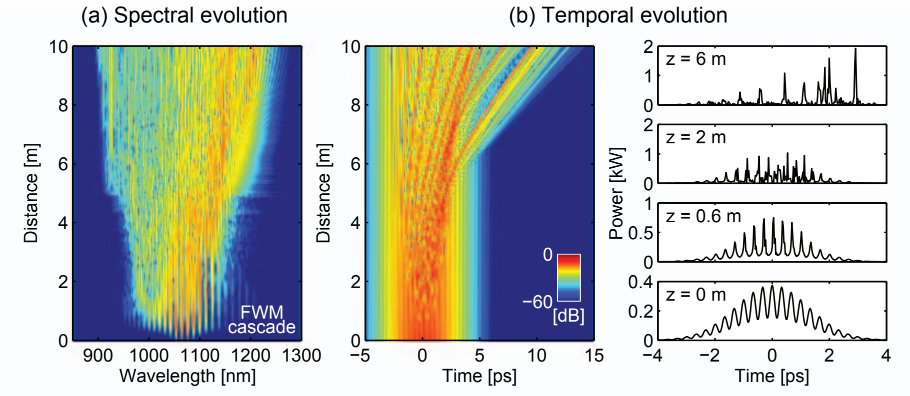

Figure 4.3: Spectral and temporal evolution of seeded SC generation, similar to Fig. 4.1, but with the pump power split between a 250 W pump and an identical seed with 5 % of the power and a 3 THz frequency offset relative to the pump.

pump is modulated with a weak seed pulse. This altogether changes the character of the pulse break up: whereas unseeded MI builds from noise that differs from shot to shot, the seed ensures the same beating of the temporal pulse envelope in every shot, and therefore leads to a *deterministic* rather than noise-driven pulse break-up. In the frequency domain the seed leads to the amplification of a FWM cascade rather than an amplification of MI sidebands from noise. The resulting noise reduction is quantified and discussed in the following.

Seeded SC generation was numerically investigated in [221, 222, 225]: Genty *et al.* [221] found that, for a pump with a low peak power of 75 W, an optimum SC broadening and stability was achieved for a seed pulse with a 5 THz offset relative to the pump. Similarly, [225] investigated the influence of a weak CW seed on low power SC generation in a dispersion-shifted fiber, and described how seeding leads to a pulse breakup caused by FWM. A high peak power of 10 kW was used in [222] to generate a coherent comb-like SC in a short PCF by introducing a seed. An optimal fibre length on the order of 5-10 cm was determined, for which the comb remains coherent, yet relatively narrow and highly structured. Experimentally, SC generation was induced by triggering a sub-threshold pump with a seed pulse or CW in [217,223,224]. This further led to improved spectral stability and coherence. This, however, is fundamentally different from the results of [221, 222, 225], where the pulse break-up is caused by the amplification of a FWM cascade. Rather than modulating the pump with a seed pulse, it has been attempted to feed back a fraction of generated SC from one pulse as a seed for the following pulse [220, 226–233]. Although very interesting, we shall not pursue this approach here.

While it has thus been shown that seeding can reduce the noise of an SC, this has been either at low pump power, often close to the MI threshold, or for very short fibres. The previous investigations are thus far from commercial SC sources with peak powers and fibre lengths on the order of 10 kW and 10 m, respectively. To this end, in Paper VI we investigated seeding under a variety of conditions, and explain what happens as we approach the parameters of a commercial SC source. In particular, we investigate the influence of the seed wavelength and MI gain spectrum on seeding at various power levels above the SC threshold, from which we highlight a number of distinct dynamical regimes. In Paper VII we further demonstrated that seeded SC generation is extremely sensitive to the degree of phase noise of the seed. The main results of Papers VI-VII are reviewed in the following.

4.3.1 Influence of seed wavelength and MI gain spectrum

As a starting point, we consider a 3 ps Gaussian pump with 250 W peak power and a seed with the same temporal width but 5% of the peak power, similar to Fig. 4.3. We use the same PCF as in Figs. 4.1–4.3 with a ZDW at 1054.2 nm. The results for pumping close to the ZDW at 1055 nm with varying seed frequency offset are shown in Fig. 4.4; pumping close to the ZDW shifts the MI gain peak far away from the pump and above the Raman gain peak, which yields the richest dynamics and is useful for highlighting the general dynamics. The MI and Raman gain spectra are shown in Fig. 4.4(f). For each set of parameters we carried out 200 simulations to quantify the noise properties with the spectral coherence and SNR.

Figure 4.4(a) shows the evolution of unseeded SC generation (overlapping pump and seed). Unseeded MI amplifies a single set of side-bands that evolves into solitons and DWs, as demonstrated in Fig. 4.1. This results in an incoherent spectrum with near-unity SNR over most of the bandwidth. The white lines mark the width of the MI gain spectrum, defined by where the gain is 5% of the maximum gain. By introducing a seed with a small 3 THz offset relative to the pump, the pulse breakup is initiated by a cascaded FWM process that causes a coherent broadening of the pump, as seen in Fig. 4.4(b) (and Fig. 4.3). The width of the frequency comb is limited by the width of the MI gain spectrum. With further propagation a soliton is generated from the FWM process with enough power to redshift outside the MI gain band. The output spectrum is coherent over most of the bandwidth, but the soliton at the long wavelength edge of the spectrum has a varying phase from shot to shot, which degrades the coherence at the spectral edges, but leads to a high intensity stability. When the seed is shifted further away to the peak of the Raman gain at 13 THz in Fig. 4.4(c), the spectral evolution is dominated by the amplification of a single set of coherent side-bands amplified through degenerate FWM. At ∼5 m a massive soliton is ejected from the long wavelength side-band, which is exactly what was referred to as 'harnessing and control of optical rogue waves' in [206], where the pump pulse was modulated with a well-defined frequency to eject a large amplitude soliton. The soliton is again not phase-stable from shot to shot, but it is highly intensity-stable. This is opposite to what was reported in [225], where the rogue soliton was coherently generated from a FWM side-band. By shifting the seed to the peak of the MI gain at 20 THz in Fig. 4.4(d), a single set of well-separated side-bands is amplified. The pump and side-bands broaden independently of each other, mainly by SPM. This leads to a spectrum with three clearly distinct bands of high coherence and SNR. Finally, in Fig. 4.4(e) the seed is shifted to the tail of the MI gain spectrum, and a single set of side-bands is slowly amplified. The pump is only slightly depleted and experiences noise-seeded MI unaffected by the seed at 1180 nm.

These general trends were confirmed over a larger parameter space in Paper VI. In particular, the best noise improvements were found for $0 < \nu_{\rm mod} \lesssim \frac{1}{4}\nu_{\rm MI}$, where $\nu_{\rm mod}$ and $\nu_{\rm MI}$ are the pump-seed frequency offset and MI gain bandwidth, respectively. In this regime, the amplification of a broad FWM cascade with many bands across the MI gain bandwidth leads to a spectrum with high coherence and SNR over most of the bandwidth, as in Fig. 4.4(b).

One of the main conclusions of Paper VI is that although it is possible to divide the results into regimes of high and low coherence and intensity stability, depending on the wavelength and power of the pump and seed, the seeding process is highly sensitive to the exact input parameters. Generally, we find that the shot-to-shot stability can be increased by pumping further away from the ZDW. This results in an increase of the MI gain at small frequency offsets, which gives a faster amplification of the FWM cascade that diminishes the influence of noise. This is illustrated in Fig. 4.5, where we show the temporal dynamics for pump wavelengths of 1055 and 1075 nm, respectively. The strong dependence of the MI gain spectrum on pump wavelength is clearly seen in the subfigures on the right. The seed causes a beating of the temporal profile, which, if chosen correctly, leads to a deterministic pulse break-up. When the pump is close to the ZDW as in Fig 4.5(a), the MI gain is relatively small at the seed wavelength (1070.1 nm) and slowly increasing with wavelength. The temporal profile is therefore only slowly broken up into solitons. The solitons are therefore

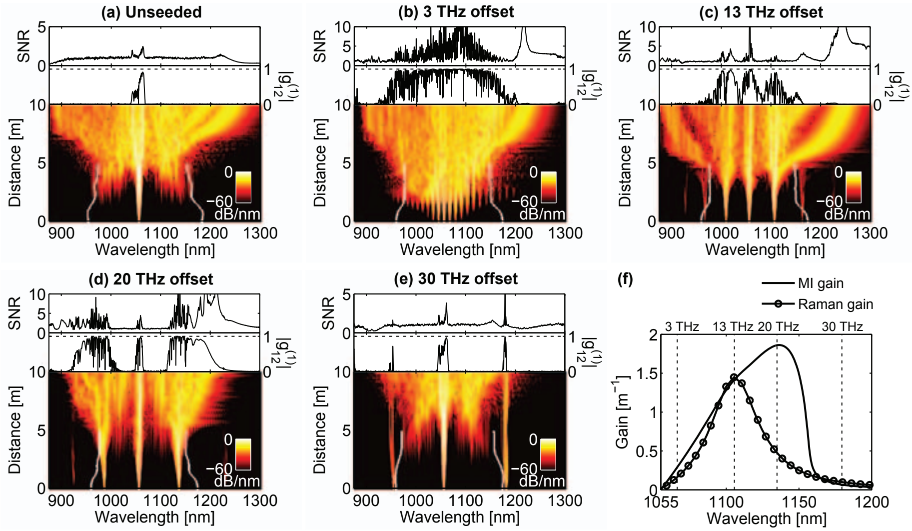

Figure 4.4: Single-shot simulations of pumping at 1055 nm with a 250 W pump and a 5% seed at frequency offsets of (a)-(e) 0, 3, 13, 20, and 30 THz, respectively. The white lines indicate the MI gain bandwidth. The top rows in (a)-(e) show the ensemble calculated signal-to-noise ratio (SNR) and spectral coherence ($|g_{12}^{(1)}|$). (f) MI and Raman gain curves, the vertical lines correspond to the frequency offsets used in (a)-(e). The frequency offset of 13 THz (c) is the Raman gain peak and 20 THz (d) is the MI gain peak.

mainly generated from the pulse centre where the peak power is highest. This gives the solitons time to redshift before the cascade is amplified and the dynamics is relatively turbulent. In contrast to this, pumping further from the ZDW gives a much larger gain at the seed wavelength (1090.6 nm) that increases more rapidly with wavelength. This causes a fast breakup of the temporal pulse, where the individual temporal fringes generate fundamental solitons in a controlled fashion that almost resembles soliton fission, as seen in Fig 4.5(b). The most powerful solitons are still generated near the centre of the pulse where the power is highest. The most powerful rogue-like soliton only collides with the smaller solitons generated from the trailing edge of the pulse. Interestingly, a closer inspection reveals that this rogue-like soliton is generated *incoherently* when pumping close to the ZDW, but *coherently* when the pump is shifted away from the ZDW.

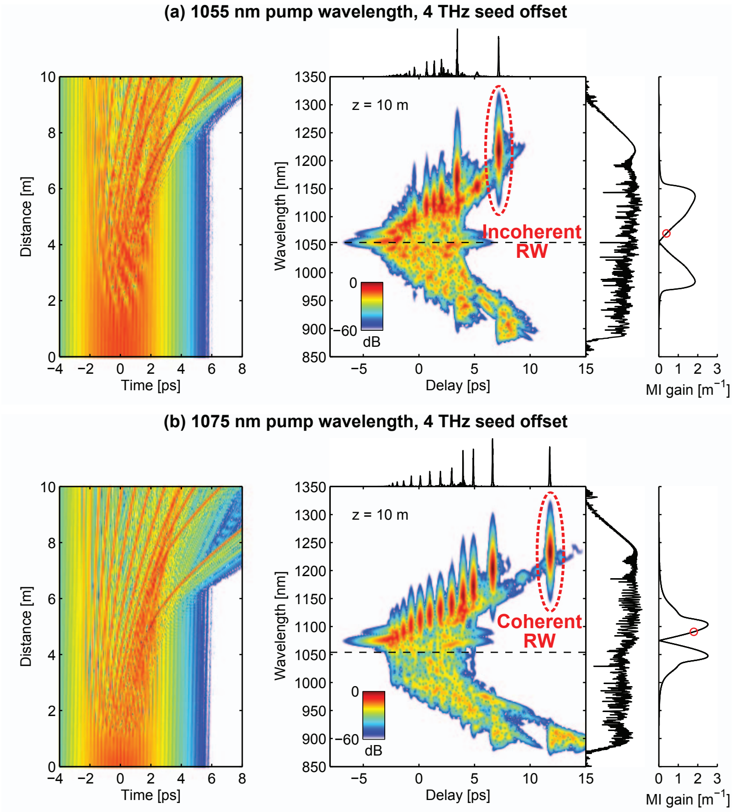

Figure 4.5: Temporal evolution, spectrogram at the fiber end (10 m) and MI gain spectrum for a 5% seed with a 4 THz offset for pump wavelengths of (a) 1055 nm and (b) 1075 nm. The black dashed lines in the spectrograms mark the ZDW at 1054 nm and the seed wavelength is marked with red circles in the MI gain spectra.

4.3.2 Seeding at high peak power

It thus seems safe to conclude that a suitably chosen seed can be used to effectively manipulate the pulse breakup and improve the noise characteristics. However, the situation changes drastically when we approach the power levels and fibre lengths of typical SC sources. To this end, we show in Fig. 4.6 the spectral evolution and noise statistics (calculated from an ensemble of 100 simulations) for a 1064 nm pump with peak powers of 500, 750, and 1500 W, respectively, and a seed at 3 THz offset. When the peak power of the pump is increased, the SC bandwidth increases and multiple distinct solitons and GV matched DWs become visible. However,

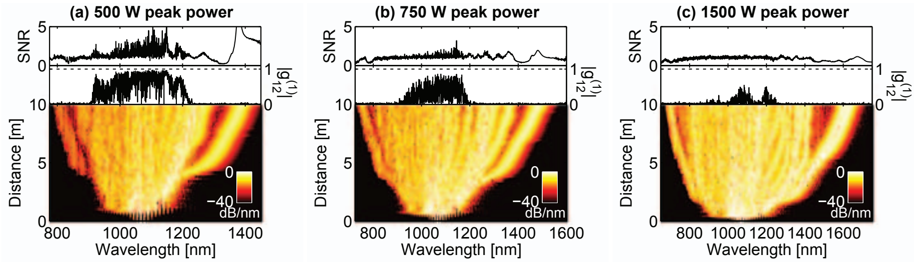

Figure 4.6: Single-shot simulations of pumping at 1064 nm with a 5% seed at a frequency offset of 3 THz for pump peak powers of (a)–(c) 500, 750, and 1500 W, respectively. The top rows show the signal-to-noise ratio (SNR) and spectral coherence ($|g_{12}^{(1)}|$).

the increasing pump power also severely degrades the noise properties and only the central part of the spectrum remains (partially) coherent. At the highest peak power of 1500 kW in Fig. 4.6(c), the initial FWM cascade is quickly washed out by the onset of phase-dependent soliton interactions and DW generation, and the output spectrum is incoherent over most of the bandwidth.

Although the pulse breakup can be completely deterministic also at high pump powers, the subsequent turbulent solitonic dynamics makes the resulting spectrum incoherent. In [220] it was experimentally demonstrated that the spectral noise increases with the pump power, although this was for a very different set-up where a fiber with two closely spaced ZDWs was back-seeded. It is interesting to notice that the typical broad and flat SC spectra reported in most high-power experiments come at a price of low coherence; the flatness is exactly a consequence of the averaging over solitons with large shot-to-shot variations in shape and energy. Similarly, the high power seeded SC generation in [222] resulted in highly structured spectra, but only with a sub-octave bandwidth due to the short fibre length.

4.3.3 Influence of phase coherence

The SC noise improvements afforded by seeding have all been obtained using a phase coherent seed. In particular, the numerical investigations in [206, 221, 222, 225] and Paper VI all used a perfectly coherent seed to modulate the pump. Experimentally, the seed was generated by filtering a fraction of the pump in [217] and in [223] the signal and idler from an optical parametric amplifier were used as pump and seed, respectively. A separate CW source was used as the seed in [224]. It thus seems fair to assume that in all these cases the seed was at least partially coherent with the pump. In Paper VII we therefore addressed the influence of the phase coherence of the seed with numerical simulations, to see which conditions this enforces on the mechanisms that can be used to generate the seed.

Figure 4.7 recaps the results of Paper VII of seeding with a partially (in)coherent seed. In addition to the broadband noise of the one-photon per-mode model, phase noise was added to the seed based on a physically justified phase-diffusion model. The model assumes fluctuations of the temporal phase with zero ensemble mean, resulting in a Lorentzian noise spectrum whose width is quantified by the linewidth $\Delta\nu_{\mathrm{FWHM}}$ (see Paper VII and Appendix A for details). The results in Figs. 4.7(a)–(c) show the spectral evolution and ensemble calculated statistics (from 500 simulations) for a 250 W pump at 1064 nm and a seed with 3 THz offset from the pump and varying phase noise linewidth. The phase coherent seed in Fig. 4.7(a) results in a highly coherent spectrum as described in the previous sections. When the linewidth of the seed is increased in Figs. 4.7(b)–(c), the broadening is still initiated by cascaded FWM, but the contrast of the FWM comb decreases, resulting in a significant degradation of the SNR and coherence. This is further detailed in Figs. 4.7(d)–(f) by the ensemble calculated spectra at a propagation distance 1 m for the same linewidths as Figs. 4.7(a)–(c). Although the comb structure is clearly seen in all cases, the fringe contrast is significantly decreased when the noise linewidth is increased, which results in a similar decrease in the spectral coherence and SNR. In Paper VII we confirm these results over a much larger parameter space. In particular, our results clearly show that the maximum tolerable phase noise of the seed is in fact quite small and that the specific phase-noise tolerance decreases with increasing pump power. This directly restricts the mechanisms that can be used to generate the seed.

Finally, it should be emphasized that quantitative validity of these results is limited by the numerical resolution: a numerical resolution of 19.1 GHz was used for Fig. 4.7. This is discussed in Paper VII, where we confirm that although we generally can not *quantitatively* determine the exact allowable phase noise linewidth, our results are *qualitatively* valid: The results clearly show that the SC becomes increasingly noisy when the seed noise linewidth is increased, and that the seed must be at least partially coherent with the pump to achieve a coherent SC.

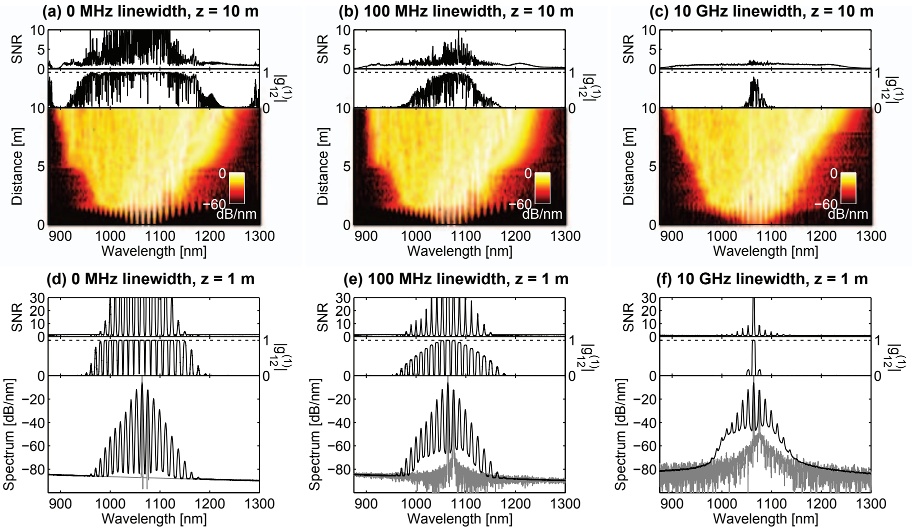

Figure 4.7: Single shot simulations of seeded SC generation with varying seed linewidth, $\Delta\nu_{\mathrm{FWHM}}$. (a)–(c) Spectral evolution and ensemble calculated spectral coherence ($|g_{12}^{(1)}|$) and signal-to-noise ratio (SNR) at the fiber output (10 m). (d)–(f) Ensemble calculated spectra and noise properties at a propagation distance of 1 m for the same linewidths as (a)–(c). The grey spectra show single shot input.

4.4 Noise properties of blue-extended supercontinuum

So far we considered active noise reduction by seeding the initial stages of the SC formation. In Paper VIII we experimentally investigated passive noise reduction by controlling the subsequent soliton-driven dynamics with tapered fibres. A discussion of this is also included in Paper III. This was first investigated by Moselund [136], who found a clear difference in the noise properties of the SC generated in a uniform and short ∼2 cm tapered PCF. However, the dynamics in such short tapers are very different from longer tapers, in that the taper length is very short compared to the soliton period and the conversion into the visible poor. The noise reduction in [136] can therefore not immediately be extrapolated to longer tapers. Longer tapers were investigated by Kudlinski *et al.* [137], who speculated that the taper increases the power density beyond 1750 nm (because of the increased nonlinearity and decreased dispersion), which translates into an increased number of solitons at these long wavelengths and hence a noise reduction. This, in turn, decreases the noise at the blue edge because of the GV matched link between the spectral edges. The shot-to-shot noise was quantified in filtered spectral regions across the SC as the variation of the smallest to the largest amplitudes in each recorded pulse train. The SC noise from a uniform and 7 m long tapered PCF were compared using this noise measure, and the tapered fibre was found to reduce the noise across the full SC bandwidth upto 1750 nm.

In Paper VIII we measured the RIN across the full SC bandwidth as a function of power in a uniform and tapered PCF. The RIN measured in filtered wavelength regions by an electric spectrum analyser are shown in Fig. 4.8(a) and the corresponding spectra in 4.8(b) (see Paper VIII for further details). The PCFs had a hole-to-pitch ratio of 0.52 and are thus similar to those in Fig. 3.4, but with a longer 4 m tapered section. The noise properties of the uniform and tapered fibres appear very similar; the RIN increases with the detuning from the pump and exceeds -75 dB/Hz on the blue side of the spectral edge for both the uniform and tapered fibre. The figure does, however, suggest that the noise around 600 nm is slightly lower in the SC generated in the tapered fibre. To investigate the noise on the edge further, Figs. 4.8(c)–(d) show measurements of the red and blue edges, respectively, where the pump power was adjusted to shift the spectral edge (at the -10 dBm/nm level) to a certain wavelength. The figure shows that the RIN follows the edge and is at the same level in both the uniform and tapered fibre. This result opposes the conclusions drawn in [137], although the interpretation is ambiguous: in as much as the noise follows the spectral SC edge, tapering can indeed lower the noise near the blue edge compared to an SC generated in the corresponding untapered fibre, simply because the blue edge is shifted to a shorter wavelength. The noise level near the edge will, however, remain the same according to our results based on RIN. One could therefore claim that tapering does indeed lower the noise in the visible part of the spectrum by moving the spectral blue edge. Notwithstanding, we do not observe a noise reduction across the full SC bandwidth as reported in [137]. These results are described in greater detail in Paper VII, where the RIN is mapped out as a function of peak power and wavelength. The results are complimented with numerical simulations in Paper III.

4.5 Conclusions, discussion and outlook

We investigated the noise properties of long-pulsed SC generation. This regime is characterised by large shot-to-shot fluctuations originating from the noise-driven MI process that breaks the pump into solitons and DWs.

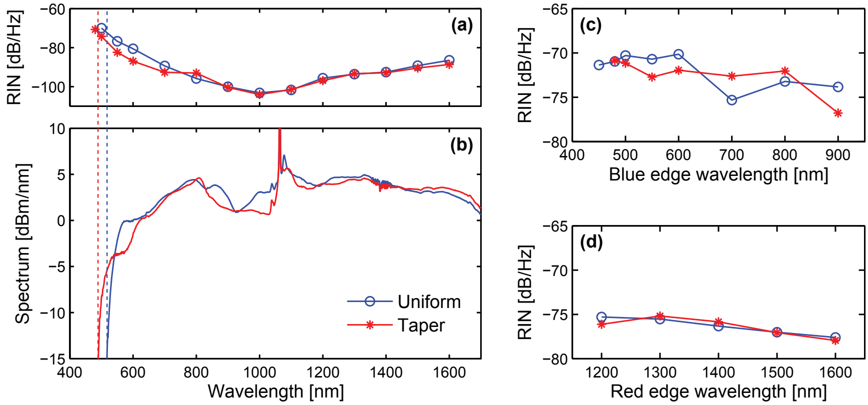

Figure 4.8: (a)–(b) Measured spectra and RIN for a uniform fibre (blue) and a taper (red) pumped with a peak power of 5 kW. The PCFs are similar to those of Fig. 3.4, but with a 4 m tapered section. (c)–(d) Noise at the spectral red and blue edge as a function of wavelength. The spectral edges were controlled by adjusting the pump power.

The subsequent turbulent solitonic dynamics adds to the noise and leads to the formation of statistically rare optical rogue waves. Previously, SC noise has been quantified by the phase-sensitive spectral coherence function and histograms of spectrally filtered pulse energies, which only gives limited and qualitative information about the noise without revealing anything about its nature. Here we introduced statistical higher-order moments that collectively give an accurate quantitative measure of the spectral noise across the full SC bandwidth, and provide a clear identification of regions of rogue wave behaviour.

Moreover, we attempted two approaches to lower the large spectral noise. First we numerically investigated noise reduction by seeding the pulse break-up, where a suitably chosen seed can deterministically break up the pump by the amplification of a FWM cascade rather than by noise-seeded MI. Although this method appears very promising at first glance, our results showed a high sensitivity to the exact parameters of the pump and seed. In particular, we found that turbulent soliton dynamics overpowers the deterministic pulse break-up for commercially relevant kW pump powers, thereby completely washing out the noise improvement of the seeded pulse break-up. Similarly, we found the process to be extremely sensitive to phase-noise on the seed, which limits the mechanisms that can be used to generate the seed. Rather than actively controlling the pulse break-up, we attempted to passively tame the subsequent soliton-driven spectral dynamics with tapered fibres. This had previously been demonstrated to reduce the spectral noise across the full SC bandwidth, but we observed no such clear noise reduction. On the contrary, we found that the spectral noise follows the spectral edge irrespectively of the fibre geometry.

These results thus clearly show that seeding has little or no impact on the noise properties of commercially relevant long-pulsed high-power SC sources. Future directions would include a thorough comparison of the noise properties of SC generation in various uniform and tapered fibres. In particular, the noise measure introduced in [137] must be compared to RIN and HOMs to shed some light on whether tapers can indeed reduce the noise.

The frequency-to-time mapping technique that was first used to reveal the existence of optical rogue waves in [27], was recently used to gain insight into the stochastic nature of MI [234–236] and correlations in the full SC spectrum [216]. It seems very likely that this approach will further aid the fundamental understanding of SC noise properties, and may prove especially useful in comparing experimental results with numerical simulations.

There has currently been renewed interested in generating fully coherent SC spectra in all-normal PCFs through SPM broadening [55–61]. This further means that the SC can be temporally compressed, but it comes at the price of a limited bandwidth and requires shorter pulses. This is in many ways a return to the roots of SC generation, where a single coherent broadening mechanism is used rather than a plethora of interconnected processes. Although such sources may find applications due to their noise properties, they can not compete with the available long-pulsed sources in terms of bandwidth and average power, and it is therefore still worthwhile to investigate noise-reduction of incoherent long-pulsed SC generation.

Chapter 5

Summary

In this thesis we have investigated various fundamental and application oriented aspects of SC generation in customised PCFs. We have focused on the commercially relevant long-pulsed high-power regime, where the spectral broadening is initiated by noise-seeded MI that breaks the pump into a distributed spectrum of redshifting solitons and DWs. Broadly speaking, we have manipulated both the initial pulse break-up by modulating the pump pulse and the subsequently soliton-driven dynamics with longitudinally invariant fibres, which permits a control of the spectral noise properties and bandwidth, respectively. This has been motivated by a large commercial potential in low-noise and spectrally blue-extended SC sources for e.g. biological applications.

The spectral bandwidth can be extended into the deep-blue region below 400 nm by shaping the dispersion and GV landscape. Specifically, PCFs with longitudinally varying dispersion and GV accommodate the ideal combination of an efficient pulse break-up near the ZDW and a subsequent spectral extension into the deep-blue by clever engineering of the GV profile. In Chapter 3 we utilised such tapered PCFs fabricated directly on the draw-tower to demonstrate SC generation with a spectral density in excess of 1 mW/nm across the entire visible region down to 390 nm. Importantly, we revisited the fundamental effect of soliton trapping in tapered fibres to introduce and verify the novel concept of a group acceleration mismatch. This allowed us to enhance the power in the spectral blue edge by optimising the taper shape. Finally, we pushed the PCF design freedom to the limit and fabricated the first PCF taper with longitudinally increasing air-fill fraction. This uniquely permits single-mode pumped SC generation down to 375 nm in one monolithic fibre device. Although more impressive results have been reported in the literature, our results provide a highly important step towards realising a commercial deep-blue SC source. In particular, our investigations of the importance of the taper shape and the concept of group acceleration matching collectively form an important milestone, which we expect to influence the further development. We similarly consider our single-mode high air-fill fraction PCF a very promising candidate for next generation SC sources with high spectral density below 400 nm. Importantly, we expect that the conclusions drawn here can be extrapolated to generate SC spectral extending below 350 nm, which would be the obvious next step.

The initial stages of long-pulsed SC generation are dominated by noise-initiated MI that tears the pump into a train of soliton-like pulses. Because the process is driven by noise, it is responsible for large shot-to-shot variations of the resulting SC and the generation of statistically rare optical rogue waves with abnormal peak powers. In Chapter 4 we quantified these spectral variations with statistical higher-order moments. Specifically, we demonstrated the utility of the moments of coefficient of variation, skew and kurtosis, which collectively provide improved quantitative and qualitative insight into the nature of the spectral fluctuations across the spectrum, and allows easy identification of regimes of rogue wave-like statistics. The large spectral shot-to-shot fluctuations pose a limiting factor for several applications. In Chapter 4 we investigated two approaches to bring down the spectral variations in commercial SC sources. Instead of allowing noise-driven MI to break the pump into a train of soliton-like pulses, the pump can be modulated with a weak seed pulse to achieve a coherent pulse break-up. While seeding works beautifully under a large variety of initial conditions for a low pump power, the situation changes drastically when we approach the parameters of a commercial system, where the subsequent chaotic solitonic dynamics completely overpowers the coherent pulse break-up. Similarly, we numerically demonstrated that the process is highly sensitive to phase-noise on the seed pulse, which restrains the mechanisms that can be used to generate the seed. Although these results are fundamentally highly interesting in the context of e.g. rogue phenomena, our results seem to unambiguously suggest that seeding is without effect for commercial high-power systems.

Whilst controlling the pulse break-up in a high-power SC source thus seems redundant for the noise properties of the resulting SC, we instead tried to control the subsequent soliton dominated dynamics. Specifically, it has been suggested that tapered fibres could be used to lower the spectral noise by taming the soliton propagation. However, we found no immediate noise reduction in tapered PCFs. Rather, we found that the spectral noise increases with the detuning from the pump, and is at a constant noise level at the spectral edge.

In summary, in this thesis we have investigated blue-extension and enhancement of SC generation into the deep-blue in axially non-uniform PCFs and various aspects of the spectral SC noise. The results presented in this work provide new insight into the broadening mechanisms and are expected to have a direct impact on the development of the next generation of high-power SC sources with deep-blue spectra. The results are further of a fundamental importance in the context of understanding the origin of the spectral SC noise and its links with other systems.

Appendix A

Implementing and solving the GNLSE

This appendix contains a collection of useful information on how to implement and solve the GNLSE with all the bells and whistles, such as fibre losses, noise sources, and frequency dependence of all fibre parameters. It is meant as a compilation of various bits and pieces of information that is not readily found elsewhere, and should be used to compliment the material in e.g. [1, 71]. Specifically, the particular implementation of the GNLSE used in this work is introduced, where the frequency dependence of the fibre parameters is included according to [85] and the GNLSE solved in the interaction picture. It is further discussed how to include noise and attenuation in the model.

A.1 Frequency dependence of material parameters

In the case of strong wavelength dependence of the effective area and refractive index, it has been argued by Lægsgaard [85] that the GNLSE in Eq. (2.9) does not accurately account for modal dispersion. This can be correctly included by introducing a new nonlinear coefficient

$$\gamma(\omega) = \frac{n_2 n_0 \omega_0}{c n_{\text{eff}}(\omega)\sqrt{A_{\text{eff}}(\omega) A_{\text{eff}}(\omega_0)}}, \tag{A.1}$$

where $n_0 = n_{\text{eff}}(\omega_0)$ is the effective refractive index at ω_0. The resulting modified GNLSE is then

$$\begin{aligned}\frac{\partial \tilde{C}}{\partial z} &= i\left[\beta(\omega) - \beta(\omega_0) - \beta_1(\omega_0)(\omega-\omega_0)\right]\tilde{C}(z,\omega) - \frac{\alpha(\omega)}{2}\tilde{C}(z,\omega) \qquad \text{(A.2)}\\ &+ i\gamma(\omega)\left(1+\frac{\omega-\omega_0}{\omega_0}\right)\mathcal{F}\left\{C(z,\tau)\int_{-\infty}^{+\infty} R(\tau')|C(z,\tau-\tau')|^2 d\tau'\right\},\end{aligned}$$

where $\mathcal{F}$ is the Fourier transform and frequency domain variables are denoted with a tilde. The modified envelope $\tilde{C}$ is related to the physical envelope $\tilde{A}$ by

$$\tilde{C}(z,\omega) = \left(\frac{A_{\text{eff}}(\omega)}{A_{\text{eff}}(\omega_0)}\right)^{-1/4}\tilde{A}(z,\omega). \qquad \text{(A.3)}$$

The above equations form the basis for all the numerical simulations in this work. It should be noted that working in the frequency domain is numerically faster than working in the time domain [237], and further allows the sum over dispersion terms (β_m coefficients) in Eq. (2.9) to be replaced with the approximation-free expression $\beta(\omega) - \beta(\omega_0) - \beta_1(\omega_0)(\omega-\omega_0)$ [71].

The modified GNLSE conserves a quantity proportional to the photon number,

$$\frac{\partial}{\partial z}\int n_{\text{eff}}(\omega)\sqrt{A_{\text{eff}}(\omega)}\frac{|\tilde{C}(z,\omega)|^2}{\omega}d\omega = 0, \qquad \text{(A.4)}$$

which can be used to check the numerical accuracy of the simulations.

For the sake of simplicity, we shall use the normal envelope A in what follows. It is, however, straightforward to substitute A with the modified envelope C.

A.1.1 Modelling tapered fibres

Modelling pulse propagation in tapered fibres corresponds to introducing a z dependence on all fibre parameters in the GNLSE. However, the interaction picture implementation discussed in the next section assumes that the fibre is invariant in each calculation step, and the taper is hence numerically modelled by updating the fibre parameters between the calculation steps. In practice, the modal properties (β, γ and A_{eff}) are calculated in COMSOL as a function of wavelength for a limited number of fixed fibre parameters (hole-to-pitch ratio d/Λ and pitch Λ), and these values are then interpolated and updated a sufficient number of times with propagation.

Vanvincq *et al.* [238] recently made a detailed derivation of a scalar propagation model and showed that an additional term is needed in Eq. (A.4) to conserve the photon number in tapered fibres. This, however, was resolved by Læsgaard [239] by adopting a different normalisation. In [239] it was further demonstrated that care must be taken when interpolating fibre parameters in a tapered fibre, but the exact interpolation scheme becomes less important for longer tapers like those investigated in this work. The difference in the results obtained with the normal GNLSE model and the corrected models are modest for long tapers, and all results presented here are based on the non-corrected model. It was, however, checked that the interpolation of fiber parameters was sufficiently fine.

A.2 The interaction picture implementation

The GNLSE has traditionally been solved using the so-called *split-step Fourier method*, where the pulse envelope $A(z,t)$ is propagated over a small distance h by alternately applying the dispersive and nonlinear effects, which yields $A(z+h,t)$. The nonlinear step is typically integrated with a second or fourth order Runge-Kutta solver. The local error of this scheme has a leading term that is third order in the step-size, $O(h^3)$ [71,86,237,240]. The work in this thesis is based on the closely related *four-order Runge-Kutta interaction picture* (RK4IP) method that is faster and firth-order locally accurate [86]. The RK4IP method works be expressing the GNLSE as

$$\frac{\partial A(z,\tau)}{\partial z} = \left(\hat{D} + \hat{N}\right) A(z,\tau), \tag{A.5}$$

where $\hat{D}$ and $\hat{N}$ are the dispersive and nonlinear operators, respectively,

$$\hat{D} = i \sum_{m\geq 2} \frac{i^m \beta_m}{m!} \frac{\partial^m}{\partial \tau^m}; \tag{A.6}$$

$$\hat{N}A(z,\tau) = i\gamma \left(1 + \frac{i}{\omega_0}\frac{\partial}{\partial \tau}\right) A(z,\tau) \int R(\tau')|A(z,\tau-\tau')|^2 d\tau'. \tag{A.7}$$

In the frequency-domain the operators read

$$\hat{D} = i\left(\beta(\omega) - \beta(\omega_0) - \beta_1(\omega_0)(\omega-\omega_0)\right); \tag{A.8}$$

$$\hat{N}A(z,\tau) = i\gamma \left(1 + \frac{\omega-\omega_0}{\omega_0}\right) \mathcal{F}\left\{A(z,\tau)\mathcal{F}^{-1}\left\{\tilde{R}(\omega-\omega_0)\mathcal{F}\left\{|A(z,\tau)|^2\right\}\right\}\right\}, \tag{A.9}$$

where $\mathcal{F}$ and $\mathcal{F}^{-1}$ are the Fourier and inverse Fourier transforms, respectively. The nonlinear operator is seen to involve several Fourier transforms. The RK4IP method explicitly gives the pulse envelope at $A(z+h,t)$ from

$A(z,t)$ calculated with a fourth-order Runge-Kutta solver. In the frequency domain the RK4IP scheme can be stated as follows [237]

$$\tilde{A}_I = \exp\left(\frac{h}{2}\tilde{D}\right)\tilde{A}(z,\omega) \tag{A.10}$$

$$k_1 = \exp\left(\frac{h}{2}\tilde{D}\right)\left[h\tilde{N}\left(\tilde{A}(z,\omega)\right)\right] \tag{A.11}$$

$$k_2 = h\tilde{N}\left(\tilde{A}(z,\omega) + k_1/2\right) \tag{A.12}$$

$$k_3 = h\tilde{N}\left(\tilde{A}(z,\omega) + k_2/2\right) \tag{A.13}$$

$$k_4 = h\tilde{N}\left(\exp\left(\frac{h}{2}\tilde{D}\right)\left(\tilde{A}(z,\omega) + k_3\right)\right) \tag{A.14}$$

$$\tilde{A}(z+h,\omega) = \exp\left(\frac{h}{2}\tilde{D}\right)\left[\tilde{A}_I + k_1/6 + k_2/3 + k_3/3\right] + k_4/6, \tag{A.15}$$

where $\hat{N}(\tilde{A})$ is the non-linear operator applied to $\tilde{A}$ and the k_i terms are slope increments.

A.3 Longitudinal step-size

The RK4IP can be straightforwardly implemented to calculate the evolution of the pulse envelope with propagation distance. However, treating the dispersive and nonlinear processes individually gives rise to a local error, which can be minimised with accurate numerical integration and intelligent control of longitudinal step-size.

The longitudinal step-size h is thus very important for the accuracy of a given simulation, and allowing it to adapt throughout a simulation can increase the accuracy while decreasing the computational effort. In general, when the nonlinearities are low h can be increased, as the error in splitting the dispersive and nonlinear processes is small. And visa-versa. An adaptive step-size can further mitigate issues with spurious FWM [86,241]. The most commonly applied method is the *local-error method* [242] that uses the step-doubling technique and local extrapolation. Each step is taken twice: once as a full step and once as two half steps, giving a coarse u_c and fine u_f solution. The difference between the two gives an estimate of the local error, $\delta = \|u_f - u_c\|/\|u_f\|$, and the step-size is adjusted by comparing with a predefined goal error δ_g, as described in [242]. The method further gives a higher accuracy, when a linear combination of the coarse and fine solution is used as input for the following step. It does however require 50% more

Fourier transforms than the constant step-size algorithm, and is therefore not necessarily more efficient that the constant step-size algorithm.

The extra calculations needed to find both the fine and coarse solution could be speeded up by using a Runge-Kutta-Fehlberg method, where the fine solution is found by including a fifth slope increment k_5 to the Runge-Kutta solver, which then can be compared to the solution found using the first four slope increments. This methods was however not tested here (if it ain't broke, don't fix it).

A.4 Numerical resolution

It is crucial to chose an appropriate numerical grid size and spacing to ensure that the involved dynamics can be correctly resolved. Thus, the width of the temporal grid should be sufficiently large to contain the pulse shape after propagating through the fibre, without any temporal wrapping arising from the large GV differences relative to the pump. The temporal grid resolution should be sufficiently fine to resolve all generated frequencies. According to the sampling theorem, the grid resolution should be at least twice the highest frequency [243].

A.4.1 Domain size

The frequency and time domains used in the simulations are dependent on the centre wavelength λ_0 and the spacing of points in the time domain Δt. Specifically, the maximum $\lambda_{\max}$ and minimum $\lambda_{\max}$ wavelengths are [244]

$$\lambda_{\min/\max} = \left(\frac{1}{2c\Delta t} \pm \frac{1}{\lambda_0} \right)^{-1}, \tag{A.16}$$

where λ_0 often is taken as the pulse centre frequency, which may limit $\lambda_{\min}$ at a too high value. This can be improved by choosing a centre frequency of the pulse ω_0 that is different from the centre frequency of the domain $\omega_{\exp}$, and in turn give the pulse an initial chirp, so that

$$A(z=0,\tau) = \sqrt{P_0}\mathrm{sech}\left(\frac{\tau}{\tau_0}\right)\exp\left(i\omega_{\exp}\tau\right), \tag{A.17}$$

which gives

$$\tilde{A}(z=0,\omega) = \sqrt{P_0}\pi\tau_0\mathrm{sech}\left(\frac{\pi}{2}\tau_0\left(\omega_{\exp}+\omega\right)\right). \tag{A.18}$$

That is, the chirp shifts the centre frequency by ω_{exp}, but does otherwise not change the pulse. The situation is similar for a Gaussian pulse

$$A(z=0,\tau) = \sqrt{P_0}\exp\left(\frac{-\tau^2}{2\tau_0^2}\right)\exp\left(i\omega_{\mathrm{exp}}\tau\right); \tag{A.19}$$

$$\tilde{A}(z=0,\omega) = \sqrt{P_0}\sqrt{2\pi}\tau_0\exp\left(-\frac{1}{2}\tau_0^2(\omega+\omega_{\mathrm{exp}})^2\right). \tag{A.20}$$

The GNLSE is derived in the retarded frame of reference moving with the GV of the carrier frequency of the pulse (ω_{exp}), and the dispersion operator must be changed to

$$\hat{D}(\omega) = \beta(\omega) - \beta_0(\omega_{\mathrm{exp}}) - \beta_1(\omega_0)(\omega - \omega_{\mathrm{exp}}) \tag{A.21}$$

in order to compensate for this. Here $\beta_0(\omega_{\mathrm{exp}})$ is the zeroth β-coefficient expanded at ω_{exp}, and $\beta_1(\omega_0)$ the first β-coefficient expanded at ω_0. It should also be noticed that Eq. (A.16) dictates $\Delta t > \lambda_0/(2c)$ in order to avoid negative frequency components.

Fibre parameters

When using $\omega_{\mathrm{exp}} \neq \omega_0$ one must take care in the definitions of the fibre parameters. That is, the nonlinear coefficient is given by (using the standard definition)

$$\gamma(\omega) = \frac{n_2\omega_{\mathrm{exp}}}{cA_{\mathrm{eff}}(\omega)}, \tag{A.22}$$

but when calculating e.g. the peak power of a soliton $P_0 = |\beta_2|/(\tau_0^2\gamma)$ the correct expression reads

$$\gamma(\omega) = \frac{n_2\omega_0}{cA_{\mathrm{eff}}(\omega)}. \tag{A.23}$$

The first definition is used when defining the vector used in the simulation, as this must be the same independently on the input pulse. That latter definition, on the other hand, is directly related to the pulse, and must be independent on the chosen expansion frequency.

A.5 Noise sources

Nonlinear pulse propagation in optical fibres is highly influenced by noise, and noise sources must be included in simulations to obtain meaningful results. This section describes two such numerical noise sources: the *one photon per mode* background noise model and the *phase-diffusion* laser linewidth model.

A.5.1 One photon per mode model

Noise on the input field is commonly included as a fictitious field consisting of one photon with a random phase in each spectral discretisational bin. Smith [245] showed that the Raman amplification of spontaneous emission in a fibre is equivalent to injecting this one photon per mode field. Inclusion of background noise is highly important for MI-initiated SC generation.

It is straightforward to include this model: the envelope at frequency bin ν_n of a field consisting of one photon per mode with random phase is

$$\tilde{A}(\nu_n) = (T_{\max} h\nu)^{1/2} \exp\left\{i\phi(\nu_n)\right\}, \tag{A.24}$$

where $\phi(\nu_n)$ is a random spectral phase in the interval $[0; 2\pi]$ and $T_{\max}$ the width of the temporal window. The Fourier transform of $\tilde{A}(\nu_n)$ can then be added to the input field.

A.5.2 Phase-diffusion model

In addition to the background noise from the one photon per mode model, it is often necessary to include the spectral noise linewidth of the laser. The phase-diffusion model naturally includes a spectral linewidth and leads to a Lorentzian spectrum of the laser. The Lorentzian spectrum can, however, be reshaped into a Gaussian spectrum [246]. The underlying physics is well-founded [247, 248].

The starting point is the input envelope of the quasi-CW field with power $P(\tau)$

$$A(0,\tau) = \sqrt{P(\tau)} \exp\left(i\delta\phi(\tau)\right), \tag{A.25}$$

where $\delta\phi(\tau)$ is a small fluctuation with $\langle\delta\phi(\tau)\rangle = 0$. The fluctuations correspond to random phase fluctuations ν_R of the (CW) frequency ν_0, resulting in an instantaneous frequency

$$\nu_i = \nu_0 + \frac{1}{2\pi}\frac{d\delta\phi}{d\tau} = \nu_0 + \nu_R(\tau). \tag{A.26}$$

The phase fluctuation is hence

$$\delta\phi(\tau) = 2\pi \int_{-\infty}^{\tau} \nu_R(\eta) d\eta, \tag{A.27}$$

where $\nu_R(\tau)$ is modelled as white noise with zero mean and variance, $\sigma^2_{\nu_R}$. The variance is related to the FWHM spectral linewidth of the spectrum $\Delta\nu_{\text{FWHM}}$

$$\sigma^2_{\nu_R} = \frac{\Delta\nu_{\text{FWHM}} B}{2\pi}, \tag{A.28}$$

where $B = 1/\Delta t$ is the bandwidth of the spectral window. These equations form the basis for the phase-diffusion model, and provide an input field envelope $A(0,\tau)$ with the Lorentzian power spectrum

$$|\tilde{A}_L(\omega)|^2 = P_{avg}\frac{\Delta\nu_{\mathrm{FWHM}}}{2\pi}\frac{1}{(\nu-\nu_0)^2 + (\Delta\nu_{\mathrm{FWHM}}/2)^2}. \tag{A.29}$$

Note that $\int_0^\infty |\tilde{A}_L(\omega)|^2 d\omega = P_{avg}$. This can be reshaped into Gaussian spectrum with same average power [246].

A.6 Attenuation in optical fibres

The attenuation, or power loss, of an optical signal with propagation distance is an important parameter in optical fibres. Generally, if a signal with power P_0 propagates though a fiber, the transmitted power P_T can be described as

$$P_T = P_0 \exp(-\alpha L), \tag{A.30}$$

where the constant α contains all attenuations sources and L is the progation distance. The attenuation is often expressed in units of dB/km [71]

$$\alpha_{\mathrm{dB}} = -\frac{1}{L}10\log_{10}\left(\frac{P_T}{P_0}\right) = -\frac{1}{L}10\log_{10}(\exp(-\alpha L)) \approx 4.343\alpha. \tag{A.31}$$

The attenuation originates from several physical processes. Pure silica glass has a very low loss over the full range 500-2000 nm, but shows increasing absorption above and below this region due to electronic resonances in the ultraviolet and vibrational resonances in the mid/far-infrared, respectively. These losses are intrinsic material properties of silica, and are known to depend exponentially on the photon energy [78, 136]

$$\alpha_{\mathrm{UV}} = a_{\mathrm{UV}} \exp\left(\lambda_{\mathrm{UV}}/\lambda\right) \tag{A.32}$$

$$\alpha_{\mathrm{IR}} = a_{\mathrm{IR}} \exp\left(-\lambda_{\mathrm{IR}}/\lambda\right), \tag{A.33}$$

where $a_{\mathrm{UV}} = 0.001$ dB/km, $\lambda_{\mathrm{UV}} = 4.67$ μm, and $a_{\mathrm{IR}} = 6 \cdot 10^{11}$ dB/km, $\lambda_{\mathrm{UV}} = 47.8$ μm. The values for the UV loss are from [249] and the IR from [136, 184]. According to these values, the loss at 350 nm is 1.6 dB/m.

Local fluctuations in the refractive index due to density fluctuations in silica from the fabrication causes scattering in all direction, also known as *Raleigh scattering*. This scattering depends strongly on the wavelength. Raleigh scattering is accompanied by wavelength independent imperfection scattering due to inhomogeneities of the fiber [136]

$$\alpha_{\mathrm{sc}} = a_{\mathrm{Ray}}/\lambda^4 + c_{\mathrm{sc}}, \tag{A.34}$$

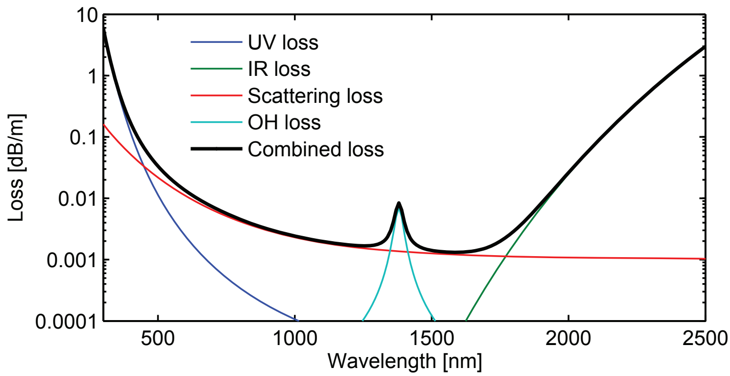

Figure A.1: Plot of the individual and combined losses mentioned in this section.

where $a_{\mathrm{Ray}} = 1.3$ dB/(km μm^4), $c_{\mathrm{sc}} = 1.0$ dB/km was measured for a commercial PCF in [136].

Impurities will add to the attenuation, and most important is the characteristic absorption peak near 1.4 μm, which stems from the presence of water. The OH ion has a fundamental vibrational resonance at 2.73 μm, and the overtones of this resonance causes the strong absorption peak in the near infrared. In [136] the OH absorption was found to be well described by a Lorentzian profile

$$\alpha_{\mathrm{OH}} = a_{\mathrm{OH}}/(1 + ((\lambda - \lambda_{\mathrm{OH}})/c_{\mathrm{OH}})^2) \tag{A.35}$$

with parameters $a_{\mathrm{OH}} = 7$ dB/km, $c_{\mathrm{OH}} = 16$ nm, $\lambda_{\mathrm{OH}} = 1,380$ nm found for a typical commercial PCF. The parameter a_{OH} reflects the OH content.

The individual and combined losses are shown in Fig. A.1. In simulations with long pulses and fibre lengths below 10 m, only the UV and IR losses are high enough to have any significant effects on the SC generation. However, many PCFs have significantly higher OH losses, which can be detrimental for SC generation. Additionally, PCFs have confinement losses due to light leakage from the core to the microstructured cladding. These losses are thus strongly dependent on the fibre structure and can generally be limited by increasing the number of air-hole rings. The confinement losses can be calculated from the imaginary part of the refractive index, although the values obtained from finite element solvers like COMSOL tend to be rather unreliable.

A.7 Pulse parameters

Gaussian pulse

Envelope (time domain):	$A(\tau) = \sqrt{P_0} \exp\left(-\tau^2/(2\tau_0^2)\right)$
Envelope (freq. domain):	$\tilde{A}(\omega) = \sqrt{2\pi}\sqrt{P_0}\tau_0 \exp\left(-\frac{1}{2}\tau_0^2\omega^2\right)$
Intensity FWHM:	$\tau_{\text{FWHM}} = 2\sqrt{\ln(2)}\tau_0 \approx 1.6651\tau_0$
	$\omega_{\text{FWHM}} = 4\ln(2)/\tau_{\text{FWHM}}$
	$\approx 2.77/\tau_{\text{FWHM}}$
	$\lambda_{\text{FWHM}} \approx \lambda_0^2/(2\pi c)\omega_{\text{FWHM}}$
	$\approx 0.441\lambda_0^2/(c\tau_{\text{FWHM}})$
Energy:	$E = \int_{-\infty}^{\infty} \lvert A(t)\rvert^2 dt = \sqrt{\pi} P_0 \tau_0$
Avg. power:	$P_{avg} = E f_{rep} = \sqrt{\pi} P_0 \tau_0 f_{rep}$

Sech pulse

Envelope (time domain):	$A(\tau) = \sqrt{P_0}\operatorname{sech}(\tau/\tau_0)$
Envelope (freq. domain):	$\tilde{A}(\omega) = \pi\sqrt{P_0}\tau_0 \operatorname{sech}\left(\frac{\pi}{2}\tau_0\omega\right)$
Intensity FWHM:	$\tau_{\text{FWHM}} = 2\ln(1+\sqrt{2})\tau_0 \approx 1.7627\tau_0$
	$\omega_{\text{FWHM}} = (2\sqrt{\ln(2)}\ln(1+\sqrt{2}))/(\pi\tau_{\text{FWHM}})$
	$\approx 0.4671/\tau_{\text{FWHM}}$
	$\lambda_{\text{FWHM}} \approx \lambda_0^2/(2\pi c)\omega_{\text{FWHM}}$
	$\approx 0.07435\lambda_0^2/(c\tau_{\text{FWHM}})$
Energy:	$E = \int_{-\infty}^{\infty} \lvert A(t)\rvert^2 dt = 2P_0\tau_0$
Avg. power:	$P_{avg} = E f_{rep} = 2P_0\tau_0 f_{rep}$

Paper I

Optimum fiber tapers for increasing the power in the blue edge of a supercontinuum — group-acceleration matching

S. T. Sørensen, A. Judge, C. L. Thomsen, and O. Bang
Opt. Lett. **36**, 816–818 (2011).

Abstract: We demonstrate how the gradient of the tapering in a tapered fiber can significantly affect the trapping and blueshift of dispersive waves (DWs) by a soliton. By modeling the propagation of a fundamental 10 fs soliton through tapered fibers with varying gradients, it is shown that the soliton traps and blueshifts an increased fraction of the energy in its DW when the gradient is decreased. This is quantified by the group-acceleration mismatch between the soliton and DW at the entrance of the taper. These findings have direct implications for the achievable power in the blue edge of a supercontinuum generated in a tapered fiber and explain observations of a lack of power in the blue edge.

http://dx.doi.org/10.1364/OL.36.000816

Optimum fiber tapers for increasing the power in the blue edge of a supercontinuum—group-acceleration matching

Simon Toft Sørensen,[1,*] Alex Judge,[2] Carsten L. Thomsen,[3] and Ole Bang[1,3]

[1]*DTU Fotonik, Department of Photonics Engineering, Technical University of Denmark, 2800 Kongens Lyngby, Denmark*

[2]*Centre for Ultrahigh-Bandwidth Devices for Optical Systems, Institute of Photonics and Optical Sciences, School of Physics, University of Sydney, Sydney, New South Wales 2006, Australia*

[3]*NKT Photonics A/S, Blokken 84, DK-3460, Birkerød, Denmark*

**Corresponding author: stso@fotonik.dtu.dk*

Received January 7, 2011; revised February 8, 2011; accepted February 8, 2011; posted February 11, 2011 (Doc. ID 140588); published March 8, 2011

We demonstrate how the gradient of the tapering in a tapered fiber can significantly affect the trapping and blueshift of dispersive waves (DWs) by a soliton. By modeling the propagation of a fundamental 10 fs soliton through tapered fibers with varying gradients, it is shown that the soliton traps and blueshifts an increased fraction of the energy in its DW when the gradient is decreased. This is quantified by the group-acceleration mismatch between the soliton and DW at the entrance of the taper. These findings have direct implications for the achievable power in the blue edge of a supercontinuum generated in a tapered fiber and explain observations of a lack of power in the blue edge.

OCIS codes: 060.4370, 060.5530.

Most of the physics underlying the generation of a supercontinuum (SC) has been described in both the long and short pulse regimes [1]. In particular, it is now understood that the spectrum of an SC is comprised of a soliton red edge linked to a dispersive wave (DW) blue edge through group-velocity matching (GVM) [2]. The edges are formed when a redshifting soliton catches up with a DW, allowing them to interact through cross-phase modulation (XPM) [3]. An elegant approach described the process in the inertial frame of the soliton, which explains the existence of a trapping potential set up by the decelerating soliton [4]. The trapping process requires a *decelerating* soliton. This deceleration normally comes from intrapulse Raman scattering, but it can likewise be achieved by tapering the fiber. In the latter case, a change in the group velocity (GV) causes a deceleration, which enables the trapping process [5]. The trapping process has been described as a combination of two effects that set up a potential around the trapped pulse: on one side, the potential is caused by a refractive index change induced by the soliton via XPM. The other side is provided by the inertial force arising from the soliton deceleration [4].

Recently, much interest has been devoted to moving the short wavelength edge further into the blue below 370 nm. This is motivated by the commercial potential in areas such as fluorescence microscopy [6]. As an example, Leica replaced the need for several sources with a single SC source (NKT Photonics A/S) in their new generation TCS SP5 X confocal microscope. Tapered fibers have been used for SC generation, because it allows one to move the zero-dispersion wavelength (ZDW) and obtain a small core with a high nonlinearity [7–10]. Recently, tapering has been used to move the blue edge further into the blue, due to what was first believed to be a varying phase-matching point to Cherenkov radiation or four-wave mixing [11,12]. Later it was shown to be due to a change in the GV profile, allowing GVM to shorter wavelengths [5,13,14]. Alternative approaches include doping the fiber [15] and concatenating multiple fibers [16]. The soliton redshift was optimized in [17], and in [18] a theory was developed for the interaction between the soliton and DW in a nonuniform fiber, which describes the spectral position of the DW, but not the energy. While all previous work has focused on shifting the spectral edges (see, e.g., [19]), little attention has been devoted to maximizing the power of the blueshifted light. Here we show by single soliton simulations that the gradient of the taper has a high impact on the power actually available in the blue edge, and that the key parameter quantifying the impact is the *group-acceleration mismatch* (GAM).

The pulse envelope $\tilde{A} = \tilde{A}(z, \omega)$ at position z and angular frequency ω is calculated by the generalized nonlinear Schrödinger equation (GNLSE), as described in [20]. The GNLSE is solved using a fourth-order Runge–Kutta in the interaction picture [21]. The mode profile and effective area are calculated with a finite element mode solver. The profile of the tapered fiber is taken into account by interpolating a number of calculated mode profiles and effective areas found at fixed points along the fiber. From the simulations, the evolution of the dominant spectral components are found by calculating the center of mass wavelength, $\lambda_c(z) = \int \lambda |\tilde{A}|^2 d\lambda / \int |\tilde{A}|^2 d\lambda$.

A sech pulse centered at 1064 nm was used in all simulations, $A(z = 0, t) = \sqrt{P_0}\mathrm{sech}(t/T_0)$, where $P_0 = 20.3$ kW and $T_{\mathrm{FWHM}} \approx 1.763 T_0 = 10$ fs. We first consider a fiber taper, in which the pitch is linearly decreased from 3.7 μm to 1.85 μm and back again, while keeping the hole-to-pitch ratio constant. The associated change in dispersion and effective area are shown in Fig. 1.

The taper has an initial 2 m of uniform fiber to make sure that the soliton has fully caught up and established GVM with the DW before entering the taper. The 2 m uniform fiber is followed by 0.5 m of downtapering and 3.5 m of uptapering, and a final 1 m of uniform fiber.

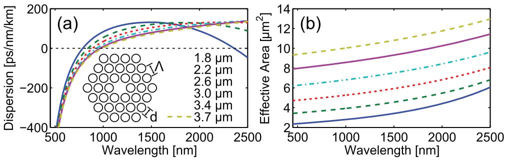

Fig. 1. (Color online) (a) Dispersion and (b) effective area for fibers with hole-to-pitch ratio $d/\Lambda = 0.79$ and varying pitch Λ. The inset in (a) shows the cross section.

The hole-to-pitch ratio is constant over the tapered section, and the gradient of the downtapering section is $\Delta\Lambda/\Delta z = 3.7\,\mu\text{m/m}$. The evolution of the dominant spectral components through this fiber taper is shown in Fig. 2(a). It can be roughly divided into five steps: (1) The soliton (red cross) generates a DW (purple diamond) around 820 nm. (2) The soliton redshifts, is temporally delayed, catches up with the DW, and traps a fraction of it (green square). (3) As the soliton is further redshifted, it blueshifts the trapped DW to satisfy GVM. In a uniform fiber, this process would continue as long as the soliton is redshifting. (4) However, as the downtapering starts, the soliton instantaneously accelerates and leaves behind part of the DW at 767 nm due to the difference in GV induced by the taper. (5) The trapped DW (blue circle) blueshifts with the soliton to 511 nm at the taper waist, where the GVM is broken by the discontinuous change of the dispersion. The four spectral components, the soliton and DWs 1–3, are clearly visible in the spectrum and spectrogram in Fig. 2(b).

Even for a uniform fiber, the soliton is only able to trap and blueshift a part of the DW. This is a result of a too short XPM interaction length, caused by the difference in the GV of the two pulses when they collide. It is only after several collisions that GVM is achieved between the soliton and DW. It was demonstrated in [22] that light can escape the interaction region of the XPM with the soliton, or even pass unaffected through the soliton.

Because of our initial length of 2 m fiber, the soliton and DW will have identical GV at the entrance of the taper. In the taper, the GVs of the soliton and DW change at different rates, which again means that the soliton can only trap and blueshift a fraction of the DW. The GV difference of the soliton and DW in a taper are illustrated in Fig. 3 for the extreme case of a transition directly from

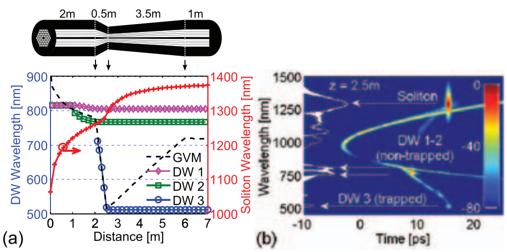

Fig. 2. (Color online) (a) Spectral evolution of the soliton and DWs through the illustrated taper; the pitch is reduced from 3.7 to 1.85 μm. The dotted line shows the DW wavelength with GVM to the soliton. (b) Spectrogram and spectrum at the taper waist (2.5 m). The spectral components in (a) are visible in (b).

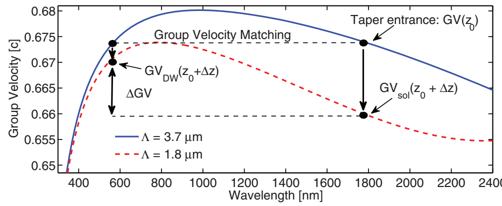

Fig. 3. (Color online) Group-velocity curves for fibers with pitch $\Lambda = 3.7$ and $1.8\,\mu$m. The GVs of the soliton and DW change at different rates in a taper.

the uniform fiber ($\Lambda = 3.7\,\mu$m) to $\Lambda = 1.8\,\mu$m. From this we define the *group acceleration* (GA) as the derivative of the GV with respect to z, i.e., for the soliton,

$$\mathrm{GA}_{\mathrm{sol}} = \frac{\partial \mathrm{GV}_{\mathrm{sol}}}{\partial z}\Big|_{\lambda=\lambda_{\mathrm{sol}}}, \tag{1}$$

and similarly for the DW. In Eq. (1), the wavelength is assumed to be constant, which is only true over short distances. An interesting measure is the GAM of the DW and soliton, which can be calculated as shown in Fig. 3:

$$\mathrm{GAM} \approx \{\mathrm{GV}_{\mathrm{DW}}(z_0 + \Delta z) - \mathrm{GV}_{\mathrm{sol}}(z_0 + \Delta z)\}/\Delta z. \tag{2}$$

Clearly, the GAM depends on the soliton wavelength, pitch, and taper gradient. The DW wavelength at the taper entrance is fixed by GVM. Figures 4(a) and 4(b) show how the GAM increases with gradient and soliton wavelength for $\Delta z = 10$ mm. For long wavelengths and very steep tapers, the proximity of the long-wavelength ZDW decreases the GAM.

The interaction between the soliton and DW depends on the taper profile. We therefore simulated tapers with the same total length as above but varying gradients; the profiles are shown in Fig. 5(c). The soliton has a wavelength of 1260 nm as it enters the taper. Based on Fig. 4(b) (solid blue line), we therefore expect the efficiency of the trapping to increase when the gradient is decreased.

The simulations all showed the same basic dynamics as in Fig. 2. The spectral position of the soliton and DW 3 are presented in Fig. 5 together with the energy of DW 3. The energy is determined in a 40 nm region around λ_c and normalized to that of DW 3 at the waist in the taper with the smallest gradient of 3.7 μm/m. The values are calculated at both the waist and fiber end. In Figs. 5(a) and 5(b) we show that the redshift at the taper waist increases as the length of the downtapering section is increased, i.e.,

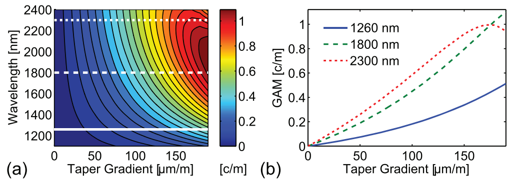

Fig. 4. (Color online) (a) GAM as a function of taper gradient and soliton wavelength for step size $\Delta z = 10$ mm and pitch $\Lambda = 3.7\,\mu$m, (b) GAM for the three fixed wavelengths indicated in (a).

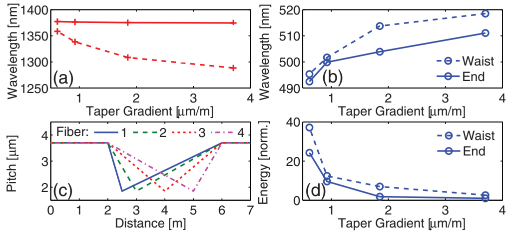

Fig. 5. (Color online) Wavelength of (a) the soliton and (b) DW 3 as a function of the gradient. (c) The investigated taper profiles. (d) Energy of DW 3 normalized to the energy at the waist in the taper with the smallest gradient. The dashed and full lines show the values at the taper waist and fiber end, respectively.

the gradient is decreased. The redshift at the fiber end is similar for all tapers, as the taper length is constant. The position of DW 3 in the waist directly reflects the position of the soliton, and it is therefore blueshifted more when the length of the downtapering section is increased, i.e., when the gradient is decreased. In the very beginning of the uptapering, the tail of the soliton gives DW 3 a small blueshift before the GVM is broken entirely. The energy in the most blueshifted DW 3 is shown in Fig. 5(d), which confirms that the energy decreases with increasing gradient. In the present case, the blueshifted energy is increased by a factor of almost 15 when the gradient is reduced by a factor of 6.

Our results show that for maximizing the blue power in SC generation, the optimum profile for a taper of a given length is the one that minimizes the GAM, i.e., the gradient of the taper. This conclusion relies on two assumptions: (1) the soliton and DW are GV matched when entering the taper, and (2) the soliton does not get near the long-wavelength ZDW or loss edge of the fiber material. The second assumption effectively enforces an upper limit on the taper length, which we are currently investigating. These observations explain the previously observed lack of power in the blue edge in, for example, [23].

In conclusion, numerical simulations were carried out for tapers with varying gradients, and it was shown that the soliton is able to keep more of the energy of its DW trapped when the gradient of the taper is decreased. This was explained as a GAM of the soliton and DW induced by the taper.

We acknowledge the Danish Agency for Science, Technology and Innovation for support of the project no. 09-070566.

References

1. J. M. Dudley, G. Genty, and S. Coen, Rev. Mod. Phys. **78**, 1135 (2006).
2. J. M. Stone and J. C. Knight, Opt. Express **16**, 2670 (2008).
3. G. Genty, M. Lehtonen, and H. Ludvigsen, Opt. Express **12**, 4614 (2004).
4. A. V. Gorbach and D. V. Skryabin, Phys. Rev. A **76**, 053803 (2007).
5. J. C. Travers and J. R. Taylor, Opt. Lett. **34**, 115 (2009).
6. A. Kudlinski, M. Lelek, B. Barviau, L. Audry, and A. Mussot, Opt. Express **18**, 16640 (2010).
7. T. A. Birks, W. J. Wadsworth, and P. St. J. Russell, Opt. Lett. **25**, 1415 (2000).
8. P. Falk, M. Frosz, and O. Bang, Opt. Express **13**, 7535 (2005).
9. S. Leon-Saval, T. Birks, W. Wadsworth, P. St. J. Russell, and M. Mason, Opt. Express **12**, 2864 (2004).
10. S. P. Stark, A. Podlipensky, N. Y. Joly, and P. St. J. Russell, J. Opt. Soc. Am. B **27**, 592 (2010).
11. F. Lu, Y. Deng, and W. H. Knox, Opt. Lett. **30**, 1566 (2005).
12. A. Kudlinski, A. K. George, J. C. Knight, J. C. Travers, A. B. Rulkov, S. V. Popov, and J. R. Taylor, Opt. Express **14**, 5715 (2006).
13. S. Pricking and H. Giessen, Opt. Express **18**, 20151 (2010).
14. J. C. Travers, J. Opt. **12**, 113001 (2010).
15. M. H. Frosz, P. M. Moselund, P. D. Rasmussen, C. L. Thomsen, and O. Bang, Opt. Express **16**, 21076 (2008).
16. J. C. Travers, S. V. Popov, and J. R. Taylor, Opt. Lett. **30**, 3132 (2005).
17. A. C. Judge, O. Bang, B. J. Eggleton, B. T. Kuhlmey, E. C. Mägi, R. Pant, and C. M. de Sterke, J. Opt. Soc. Am. B **26**, 2064 (2009).
18. A. C. Judge, O. Bang, and C. M. de Sterke, J. Opt. Soc. Am. B **27**, 2195 (2010).
19. Z. Chen, A. J. Taylor, and A. Efimov, J. Opt. Soc. Am. B **27**, 1022 (2010).
20. J. C. Travers, M. H. Frosz, and J. M. Dudley, in *Supercontinuum Generation in Optical Fibers*, J. M. Dudley and J. R. Taylor, eds. (Cambridge University Press, 2010), pp. 32–51.
21. J. Hult, J. Lightwave Technol. **25**, 3770 (2007).
22. T. Schreiber, T. Andersen, D. Schimpf, J. Limpert, and A. Tünnermann, Opt. Express **13**, 9556 (2005).
23. P. M. Moselund, "Long-pulse supercontinuum light sources," Ph.D. thesis (Technical University of Denmark, 2009).

Paper II

Deep-blue supercontinnum sources with optimum taper profiles – verification of GAM

S. T. Sørensen, U. Møller, C. Larsen, P. M. Moselund, C. Jakobsen, J. Johansen, T. V. Andersen, C. L. Thomsen, and O. Bang
Opt. Express **20**, 10635-10645 (2012).

Abstract: We use an asymmetric 2 m draw-tower photonic crystal fiber taper to demonstrate that the taper profile needs careful optimisation if you want to develop a supercontinuum light source with as much power as possible in the blue edge of the spectrum. In particular we show, that for a given taper length, the downtapering should be as long as possible. We argue how this may be explained by the concept of group-acceleration mismatch (GAM) and we confirm the results using conventional symmetrical short tapers made on a taper station, which have varying downtapering lengths.

http://dx.doi.org/10.1364/OE.20.01063

Deep-blue supercontinnum sources with optimum taper profiles – verification of GAM

S. T. Sørensen,[1,*] U. Møller,[1] C. Larsen,[1] P. M. Moselund,[2] C. Jakobsen,[2] J. Johansen,[2] T. V. Andersen,[2] C. L. Thomsen,[2] and O. Bang[1,2]

[1] *DTU Fotonik, Department of Photonics Engineering, Technical University of Denmark, 2800 Kgs. Lyngby, Denmark*

[2] *NKT Photonics A/S, Blokken 84, DK-3460, Birkerød, Denmark*

[*] *stso@fotonik.dtu.dk*

Abstract: We use an asymmetric 2 m draw-tower photonic crystal fiber taper to demonstrate that the taper profile needs careful optimisation if you want to develop a supercontinuum light source with as much power as possible in the blue edge of the spectrum. In particular we show, that for a given taper length, the downtapering should be as long as possible. We argue how this may be explained by the concept of group-acceleration mismatch (GAM) and we confirm the results using conventional symmetrical short tapers made on a taper station, which have varying downtapering lengths.

OCIS codes: (060.4370) Nonlinear optics, fibers; (060.5295) Photonic crystal fibers; (320.6629) Supercontinuum generation.

References and links

1. J. M. Dudley and J. R. Taylor, "Ten years of nonlinear optics in photonic crystal fibre," Nat. Photonics **3**, 85–90 (2009).
2. J. C. Knight, T. A. Birks, P. S. J. Russell, and D. M. Atkin, "All-silica single-mode optical fiber with photonic crystal cladding," Opt. Lett. **21**, 1547–1549 (1996).
3. P. Russel, "Photonic crystal fiber," Science **299**, 358–362 (2003).
4. J. Herrmann, U. Griebner, N. Zhavoronkov, A. Husakou, D. Nickel, J. C. Knight, W. J. Wadsworth, P. S. J. Russell, and G. Korn, "Experimental evidence for supercontinuum generation by fission of higher-order solitons in photonic fibers," Phys. Rev. Lett. **88**, 173901 (2002).
5. T. A. Birks, J. C. Knight, and P. S. Russell, "Endlessly single-mode photonic crystal fiber," Opt. Lett. **22**, 961–963 (1997).
6. J. C. Knight, "Photonic crystal fibres," Nature **424**, 847–851 (2003).
7. A. V. Husakou and J. Herrmann, "Supercontinuum generation of higher-order solitons by fission in photonic crystal fibers," Phys. Rev. Lett. **87**, 203901 (2001).
8. D. V. Skryabin, F. Luan, J. C. Knight, and P. S. J. Russell, "Soliton self-frequency shift cancellation in photonic crystal fibers," Science **301**, 1705–1708 (2003).
9. A. V. Gorbach and D. V. Skryabin, "Theory of radiation trapping by the accelerating solitons in optical fibers," Phys. Rev. A **76**, 053803 (2007).
10. A. V. Gorbach and D. V. Skryabin, "Light trapping in gravity-like potentials and expansion of supercontinuum spectra in photonic-crystal fibres," Nat. Photonics **1**, 653–657 (2007).
11. M. N. Islam, G. Sucha, I. Bar-Joseph, M. Wegener, J. P. Gordon, and D. S. Chemla, "Femtosecond distributed soliton spectrum in fibers," J. Opt. Soc. Am. B **6**, 1149–1158 (1989).
12. M. H. Frosz, O. Bang, and A. Bjarklev, "Soliton collision and raman gain regimes in continuous-wave pumped supercontinuum generation," Opt. Express **14**, 9391–9407 (2006).
13. D. R. Solli, C. Ropers, P. Koonath, and B. Jalali, "Optical rogue waves," Nature **450**, 1054–1057 (2007).

14. J. M. Dudley, G. Genty, and B. J. Eggleton, "Harnessing and control of optical rogue waves in supercontinuum generation," Opt. Express **16**, 3644–3651 (2008).
15. D. R. Solli, C. Ropers, and B. Jalali, "Active control of rogue waves for stimulated supercontinuum generation," Phys. Rev. Lett. **101**, 233902 (2008).
16. O. Bang and M. Peyrard, "Generation of high-energy localized vibrational modes in nonlinear klein-gordon lattices," Phys. Rev. E **53**, 4143–4152 (1996).
17. N. Akhmediev, J. M. Soto-Crespo, and A. Ankiewicz, "Could rogue waves be used as efficient weapons against enemy ships?" Eur. Phys. J. Special Topics **185**, 259–266 (2010).
18. P. Beaud, W. Hodel, B. Zysset, and H. P. Weber, "Ultrashort pulse propagation, pulse breakup, and fundamental soliton formation in a single-mode optical fiber," IEEE J. Quantum Elect. **23**, 1938–1946 (1987).
19. J. M. Stone and J. C. Knight, "Visibly "white" light generation in uniformphotonic crystal fiber using a microchip laser," Opt. Express **16**, 2670–2675 (2008).
20. A. V. Gorbach, D. V. Skryabin, J. M. Stone, and J. C. Knight, "Four-wave mixing of solitons with radiation and quasi-nondispersive wave packets at the short-wavelength edge of a supercontinuum," Opt. Express **14**, 9854–9863 (2006).
21. S. T. Sørensen, A. Judge, C. L. Thomsen, and O. Bang, "Optimum fiber tapers for increasing the power in the blue edge of a supercontinuum—group-acceleration matching," Opt. Lett. **36**, 816–818 (2011).
22. J. C. Travers and J. R. Taylor, "Soliton trapping of dispersive waves in tapered optical fibers," Opt. Lett. **34**, 115–117 (2009).
23. T. Schreiber, T. Andersen, D. Schimpf, J. Limpert, and A. Tünnermann, "Supercontinuum generation by femtosecond single and dual wavelength pumping in photonic crystal fibers with two zero dispersion wavelengths," Opt. Express **13**, 9556–9569 (2005).
24. S. Pricking and H. Giessen, "Tailoring the soliton and supercontinuum dynamics by engineering the profile of tapered fibers," Opt. Express **18**, 20151–20163 (2010).
25. J. C. Travers, "Blue extension of optical fibre supercontinuum generation," J. Opt. **12**, 113001 (2010).
26. J. M. Dudley, G. Genty, and S. Coen, "Supercontinuum generation in photonic crystal fiber," Rev. Mod. Phys. **78**, 1135–1184 (2006).
27. C. Agger, C. Petersen, S. Dupont, H. Steffensen, J. K. Lyngsø, C. L. Thomsen, J. Thøgersen, S. R. Keiding, and O. Bang, "Supercontinuum generation in zblan fibers—detailed comparison between measurement and simulation," J. Opt. Soc. Am. B **29**, 635–645 (2012).
28. T. A. Birks, W. J. Wadsworth, and P. S. J. Russell, "Supercontinuum generation in tapered fibers," Opt. Lett. **25**, 1415–1417 (2000).
29. S. Leon-Saval, T. Birks, W. Wadsworth, P. S. J. Russell, and M. Mason, "Supercontinuum generation in submicron fibre waveguides," Opt. Express **12**, 2864–2869 (2004).
30. F. Lu, Y. Deng, and W. H. Knox, "Generation of broadband femtosecond visible pulses in dispersion-micromanaged holey fibers," Opt. Lett. **30**, 1566–1568 (2005).
31. P. Falk, M. Frosz, and O. Bang, "Supercontinuum generation in a photonic crystal fiber with two zero-dispersion wavelengths tapered to normal dispersion at all wavelengths," Opt. Express **13**, 7535–7540 (2005).
32. A. Kudlinski, A. K. George, J. C. Knight, J. C. Travers, A. B. Rulkov, S. V. Popov, and J. R. Taylor, "Zero-dispersion wavelength decreasing photonic crystal fibers for ultraviolet-extended supercontinuum generation," Opt. Express **14**, 5715–5722 (2006).
33. J. C. Travers, J. M. Stone, A. B. Rulkov, B. A. Cumberland, A. K. George, S. V. Popov, J. C. Knight, and J. R. Taylor, "Optical pulse compression in dispersion decreasing photonic crystal fiber," Opt. Express **15**, 13203–13211 (2007).
34. A. Kudlinski and A. Mussot, "Visible cw-pumped supercontinuum," Opt. Lett. **33**, 2407–2409 (2008).
35. A. Kudlinski, M. Lelek, B. Barviau, L. Audry, and A. Mussot, "Efficient blue conversion from a 1064 nm microchip laser in long photonic crystal fiber tapers for fluorescence microscopy," Opt. Express **18**, 16640–16645 (2010).
36. J. Cascante-Vindas, A. Díez, J. L. Cruz, and M. Andrés, "White light supercontinuum generation in a y-shaped microstructured tapered fiber pumped at 1064 nm," Opt. Express **18**, 14535–14540 (2010).
37. M. Liao, W. Gao, Z. Duan, X. Yan, T. Suzuki, and Y. Ohishi, "Directly draw highly nonlinear tellurite microstructured fiber with diameter varying sharply in a short fiber length," Opt. Express **20**, 1141–1150 (2012).
38. S. P. Stark, J. C. Travers, and P. S. J. Russell, "Extreme supercontinuum generation to the deep uv," Opt. Lett. **37**, 770–772 (2012).
39. N. Vukovic, N. Broderick, M. Petrovich, and G. Brambilla, "Novel method for the fabrication of long optical fiber tapers," IEEE Photon. Technol. Lett. **20**, 1264–1266 (2008).
40. P. Falk, M. H. Frosz, O. Bang, L. Thrane, P. E. Andersen, A. O. Bjarklev, K. P. Hansen, and J. Broeng, "Broadband light generation at 1300 nm through spectrally recoiled solitons and dispersive waves," Opt. Lett. **33**, 621–623 (2008).
41. M. Koshiba and K. Saitoh, "Applicability of classical optical fiber theories to holey fibers," Opt. Lett. **29**, 1739–1741 (2004).

#161502 - $15.00 USD Received 13 Jan 2012; revised 26 Mar 2012; accepted 18 Apr 2012; published 24 Apr 2012

1. Introduction

Supercontinuum (SC) generation is a striking phenomenon of extreme spectral broadening involving a wealth of beautiful nonlinear physics [1]. Although being first observed in bulk glass and later studied in telecom optical fibers, the study of SC generation and the development of today's commercial SC sources first really took off with the invention of the photonic crystal fiber (PCF) [2], in which light can be manipulated by air-hole structuring [3]. The study of SC generation is inherently linked to the fundamental field of soliton physics and due to the striking efficiency of SC generation in PCFs, researchers have been able to reveal numerous new and important fundamental effects and surprising links with other physical systems. The advent of the PCF therefore spawned a re-birth of not only SC generation, but nonlinear fiber optics in general [1], due to the tremendous degree of design freedom that has enabled engineers to push the properties of PCFs to limits that could never have been achieved with standard optical fibers or in bulk materials [3]. For example, one can move their zero-dispersion wavelength (ZDW) down in the visible [4], make them endlessly single-moded [5], and even make them guide light in air [6]. The PCF further enabled the discovery of several fundamental nonlinear phenomena, such as soliton fission [7], Raman redshift cancellation by the presence of a second ZDW [8], soliton trapping of dispersive waves (DWs) in gravitational wells [9, 10], generation of large-amplitude optical rogue waves [11–13] and the control of rogue waves by minute seeds [14,15]. Rogue waves are in fact a fundamental nonlinear phenomenon generated by soliton collision in nonlinear physical models [16]. Thus they appear in such diverse systems as ocean waves, where they appear out of nowhere and cause serious damage on ships [17], and in biology, where they are known as ”highly localized modes” that break the bonds in DNA and initiate DNA denaturation [16].

SC generation involves the full scale of soliton physics and thus all the above mentioned effects; even rogue waves appear in the form of mega solitons that are subject to large Raman redshifts and thus define the long-wavelength ”red” spectral edge of the SC. This in turn defines the short-wavelength ”blue” edge through a complex trapping mechanism that manifests itself as a lock between the two edges; when the solitons at the red edge are redshifted by the Raman effect, they push the DWs at the blue edge to shorter wavelengths in a way that satisfies group-velocity (GV) matching [18,19]. The blueshift of a DW package has been explained as a cascade of cross-phase modulation (XPM) collision events that continuously blueshifts the DW package in discrete steps [20]. Alternatively, the trapping can be elegantly explained as an effect imposed by the accelerating soliton that sets up a gravitational well around the DW package and prevents it from dispersing [9,10]. The trapping effect is of fundamental importance for the SC generation dynamics, and GV matching is hence of equal importance to ensure a continued interaction between the spectral components in the normal and anomalous dispersion regime, and thereby allowing generation of SC spectra with a blue edge reaching into the ultraviolet below 400 nm.

A topic that has so far remained largely uninvestigated is the consequences of the fact that the trapping is not complete: the DWs continuously loose energy. The solitons undergo a continuous Raman redshift, which leads to a continuous change in GV with propagation length, i.e. a *group-acceleration*, but the DWs do not in their own right move spectrally and are thus not subject to the same acceleration. This means that there is continuously a small difference in GV, and thus a constant small leakage of DW energy, as illustrated in Fig. 1(a). The Raman effect thus leads to a *group-acceleration mismatch* (GAM), an asymmetric change in the group-acceleration of the solitons and DWs [21]. The effect is not significant in uniform fibers, because the weak redshift leads only to a minor GAM. However, in a fiber taper the group-acceleration can be orders of magnitude larger than the inherent Raman induced change and it is generally highly asymmetric, in the sense that the taper-induced shift in GV at the DW wave-

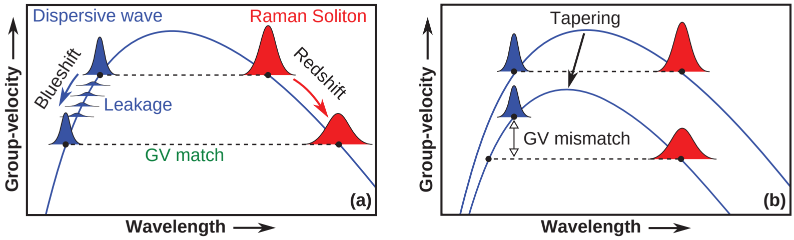

Fig. 1. Radiation trapping and leakage. (a) In a uniform fiber a soliton can trap and blueshift a GV matched DW, while it is slowly redshifting and thus decelerating. The trapping is incomplete, i.e. part of the DW continuously leaks out of the trap, as illustrated. (b) In a taper, there is an asymmetric change in GV of the soliton and trapped DW. That is, there is a mismatch in the group-acceleration, the rate with which the GV changes, which increases the amount of light that leaks out of the trap (not illustrated). In the figure it is assumed that the dispersion increases for the soliton both when it is redshifted and when the fiber is tapered.

length is much smaller than at the longer soliton wavelength, as illustrated in Fig. 1(b) and for the real fiber tapers used in this work. In [22] it was demonstrated that the group-acceleration in a taper can in fact supply the needed soliton deceleration to trap a DW even in the absence of the Raman effect. In physical terms, the GAM lowers the XPM interaction length, whereas in the trapping picture GAM lowers the depth of the gravitational well, causing light to escape. It has been demonstrated in [23] that light can escape or pass unaffected through the XPM interaction region in the extreme case when the interaction length is very short, i.e., when the GV difference is very large.

In this work, we investigate the influence of the enforced asymmetry in the group-acceleration of the solitons and trapped DWs in tapered PCFs. The influence of the taper shape on the spectrum was investigated in [24], where short femtosecond pulses were launched directly into ultra-short tapers to push the pulse break-up into the tapered part of the fiber. Although interesting, the results in [24] describe a dynamical regime different from that typical of long-pulsed commercial SC systems investigated this work, where long tapers are used and where MI breaks up the long pulse into a large number of fundamental solitons and not higher-order solitons. First we illustrate the fundamental physics behind GAM with numerical simulations of the propagation of a single soliton and GV matched DW in a taper. We then present experimental results of high-power SC generation in tapered PCFs of varying lengths and shapes. In particular, we experimentally demonstrate for the first time that the length of the downtapering section has a major impact on the available power in the blue edge of the spectrum, which provide the first clear evidence of the importance of GAM. The results provide the first step towards determining the optimum shape of a fiber taper for deep-blue supercontinuum sources, which has so-far remained largely unknown [25].

2. Numerical results

In [19, 25] it was shown how the position of the blue edge can be accurately predicted from the dispersion characteristics of any given fiber. The red edge is ultimately limited by the silica loss edge starting at 2200-2400 nm, and the position of the blue edge is then determined by GV matching with the red edge. Although useful for tailoring the spectral width, this does not give any information on the available spectral density in the blue edge of the SC.

#161502 - $15.00 USD Received 13 Jan 2012; revised 26 Mar 2012; accepted 18 Apr 2012; published 24 Apr 2012

At a first glance, the SC dynamics may seem overwhelmingly complicated. However, due to the solitonic nature of SC generation, one can gain a lot of insight into the basic dynamics on the basis of single soliton simulations. It is particularly illustrative to neglect the central part of the SC and treat only the edges. To get a basic understanding of the SC generation in a tapered fiber, it will hence suffice to analyse the propagation of a soliton and appropriately delayed and GV matched DW package. Here we do this by numerical modelling of the generalised nonlinear Schrödinger equation, which is often utilised to aid the understanding of the dynamics, and has successfully been demonstrated to accurately reproduce experimental results in both silica [26] and soft-glass fibers [27].

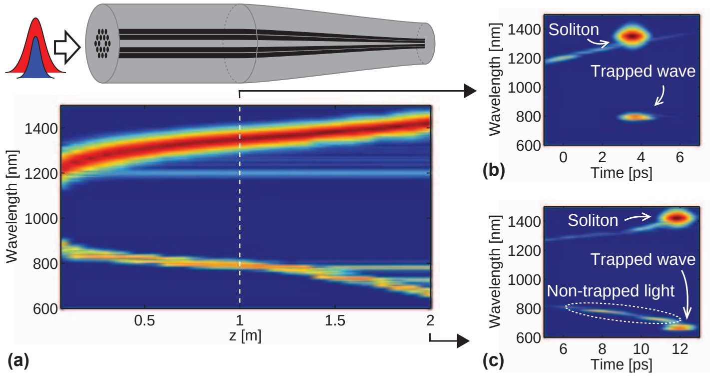

Fig. 2. (a) Spectral evolution of a 20 fs fundamental soliton and trapped wave through a fiber taper with an initial 1 m uniform fiber. (b)-(c) Spectrograms at the entrance (1 m) of the taper and at the taper waist (2 m). The wave is fully trapped at the taper entrance, but the taper increases the soliton redshift and deceleration, which causes light to leak from the soliton induced trapping region.

The propagation of a 20 fs fundamental soliton and GV matched DW in Fig. 2(a) illustrates the basic dynamics in a tapered fiber: the soliton redshifts throughout the length of the fiber, and while doing so, it causes a blueshift of the trapped wave. In the first meter of uniform fiber, the two co-propagate without the DW shedding much energy. As the downtapering starts at 1 m, both the redshift rate of the soliton and the blueshift rate of the trapped wave increase due to the increase in nonlinearity and change in GV. However, due to the taper induced GAM, a significant fraction of the trapped DW escapes the trap. The spectrograms in Fig. 2(b)-2(c) show the pulses in the spectral and time-domain simultaneously; at the taper entrance (Fig. 2(b)), the two waves are temporally overlapping and the decelerating soliton has fully trapped the DW. At the taper end (Fig. 2(c)) only a fraction of the originally trapped DW is still trapped and has a temporal overlap with the soliton. The remaining light has escaped the trap and not been decelerated and blueshifted by the soliton. This clearly illustrates the need for matching not only the GVs but also the rate with which they change, i.e. the need for minimising the GAM as predicted numerically in [21].

3. Experimental results

To investigate the full scale importance of GAM on SC generation comprised by hundreds of solitons and DWs, we fabricated an asymmetric draw-tower taper. The asymmetry enforces a

#161502 - $15.00 USD Received 13 Jan 2012; revised 26 Mar 2012; accepted 18 Apr 2012; published 24 Apr 2012

difference in the GAM depending on whether the fiber is pumped from the long or short down-tapering side, while ensuring that the light passes through the same length of fiber. Tapering has previously been demonstrated as an effective way of manipulating the pulse propagation by changing the dispersion and increasing the effective nonlinearity, and thereby move the short-wavelength edge of an SC further into the blue [24, 25, 28–37]. Spectra extending down to 330 nm from a 1065 nm pump have been reported [25], and an impressive 280 nm was reached in [38] by pumping an ultrashort taper with a femtosecond pump at 800 nm. In the latter case the light was generated directly in the UV region by a completely different mechanism.

Unlike the draw-tower tapers presented in, e.g. [25,32–35,37], our taper is tapered back to its original diameter, which makes splicing and interfacing easier and allows for an investigation of the impact of the asymmetry. It has generally been the belief [39] that such tapers shorter than 10 m are difficult to fabricate on a draw-tower. On the contrary, we find that tapering directly on the draw-tower offers high accuracy of the fiber parameters by pressure control, and allows fabrication of accurate fiber tapers with lengths from a few meters and up. This further makes it possible to use the draw-tower's coating system as an integrated part of the taper fabrication. A very short draw-tower taper of only 10 cm was recently fabricated in [37] showing the flexibility of draw-tower tapering.

As an additional investigation of the influence of the taper shape on the spectrum, we fabricated three ultra-short tapers using a well-known post-processing technique on a tapering station (Vytran LDS-1250). This technique limits the length of the tapered section to around 15 cm.

The draw-tower taper was based on the commercial fiber SC-5.0-1040 from NKT Photonics A/S with a hole-to-pitch ratio of $d/\Lambda = 0.52$. In the tapered section its pitch was reduced from 3.3 to 2.5 μm. The ultra-short Vytran tapers were based on a standard fiber with a hole-to-pitch ratio of $d/\Lambda = 0.79$ and a pitch of $\Lambda = 3.7$ μm that was reduced by 50% in the tapered section. The dispersion and GV profiles are shown in Fig. 3 along with an illustration of how the optimum degree of tapering was determined: We define the red edge $\lambda_{\rm red}$ as the loss edge $\lambda_{\rm loss}$ (here set to 2300 nm), or a wavelength λ_2 close to the second ZDW, whichever is the lowest. Solitons always halt their redshift about 50-100 nm away from the 2nd ZDW [8, 40] so λ_2 is chosen to $\lambda_{\rm ZDW,2} - 50$ nm, which means that

$$\lambda_{\rm red} = \min\{\lambda_{\rm loss},\ \lambda_{\rm ZDW,2} - 50\ {\rm nm}\}. \tag{1}$$

The red edge in turn defines the blue edge through GV matching, and the optimum degree of tapering is determined by finding the pitch at which GV matching is achieved to the shortest possible wavelength. In Fig. 3(c) and 3(f) we show the so defined red and blue edges together with both ZDWs. The optimum blue edge, i.e. shortest wavelength, is found at the turning point, which is for a pitch of 2.6 and 1.8 μm for the draw-tower and Vytran tapers, respectively, giving a blue edge of 476 and 378 nm, respectively. The realized pitch at the taper waist is very close to the optimum. In Fig. 4 we have plotted the optimum pitch and blue edge versus the relative hole size. We see that the optimum pitch approaches ~ 1.8 μm for increasing relative hole sizes, which corresponds to the point where the second ZDW crosses the loss edge, as can be seen from Fig. 3(f). For smaller relative hole sizes, where the optimum pitch is larger than 2 μm, the optimum is obtained before the second ZDW has crossed the loss edge. We emphasize that the fibers used in this work are not the optimum in terms of generating light at the shortest possible wavelength. The focus in this work is on how to maximise the amount of light in the blue edge, and we therefore chose a fiber with $d/\Lambda = 0.52$ because it is single-moded at the pump [41].

The blue edge versus pitch between 1.4-2.4 and relative hole sizes larger than 0.6 was mapped out by Travers in [25], who defined the blue edge as the shortest GV matched wavelength, without relating it to the inherent material loss edge. Travers found that the optimum pitch was

#161502 - $15.00 USD Received 13 Jan 2012; revised 26 Mar 2012; accepted 18 Apr 2012; published 24 Apr 2012

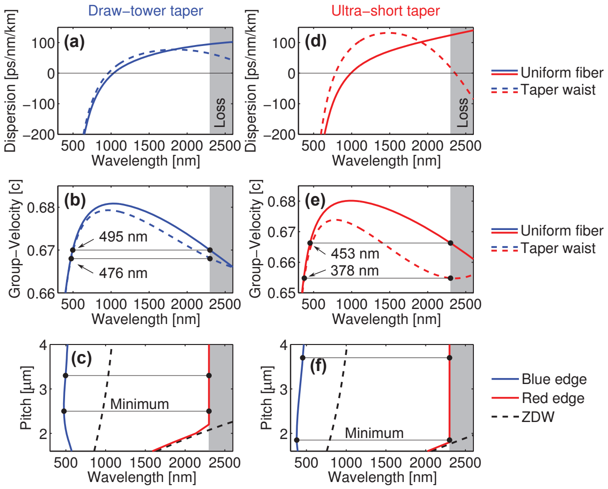

Fig. 3. (a) Dispersion and (b) GV for the draw-tower taper for the uniform fiber (solid line) and at the taper waist (dashed line). The shaded areas mark the loss region above 2300 nm where the soliton redshift halts, and the horizontal lines in (b) show the GV matching of the expected red edge to the blue edge for the uniform fiber and taper. (c) Blue edge (blue line), red edge (red line) and ZDWs (dashed lines) as a function of wavelength and pitch defined as described in the text. The horizontal lines are as in (b) and confirm that the shortest possible wavelength is reached in the taper. (d)-(f) show the same for the ultra-short tapers.

2 μm almost independently of the relative hole size and provided a qualitative explanation [25]. Introducing the loss edge has here allowed us to give a quantitative measure of the blue edge and an explanation of why the optimum pitch saturates close to 1.8 μm for large relative hole sizes.

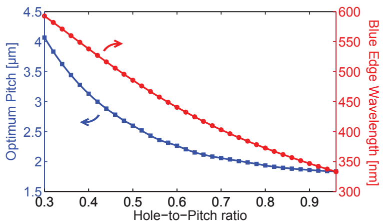

Fig. 4. Optimum pitch and corresponding minimum wavelength of the blue edge as a function of the fiber's hole-to-pitch ratio, calculated as described in the text by GV matching to the loss edge at 2300 nm or 50 nm below the second ZDW. For higher hole-to-pitch ratios the minimum wavelength is generally found for a pitch around 1.8 μm.

#161502 - $15.00 USD Received 13 Jan 2012; revised 26 Mar 2012; accepted 18 Apr 2012; published 24 Apr 2012

The fibers were pumped with a 1064 nm Yb fiber-laser typical for commercial SC sources. The laser emits 10 ps pulses with an average output power of 14 W at a repetition rate of 80 MHz. For the draw-tower taper, the fiber was spliced directly to the laser for maximum coupling efficiency and stability. For the ultra-short Vytran tapers the laser output was free-space coupled with an efficiency of approximately 70 %. In both cases the output was collimated and recorded with an optical spectrum analyser (OSA) through an integrating sphere. The output power was measured with a power meter and the spectra normalised accordingly. For the draw-tower taper the infrared edge was measured with an additional OSA and the two spectra were stitched together.

3.1. Draw-tower taper

First we analyse the draw-tower taper. The taper profile was monitored during the fabrication by measuring the coating diameter. Figure 5(a) shows a final cutback measurement of the cross-section, which was carried out after the experiments had been performed. The images captured with an optical microscope confirm that the fiber's hole structure was maintained and a hole-collapse avoided. The measured coating diameter and pitch calculated from cross-sectional images are shown in Fig. 5(b). They are nicely correlated and show how the pitch is reduced from 3.3 to 2.5 μm in an asymmetric way that roughly can be described as a 1.5 m downtapering section and a 0.5 m uptapering section. The coating diameter can thus be used to get a good estimate of the taper profile. The hole-to-pitch ratio of 0.52 was preserved throughout the taper. In the experiment there was 5 m of uniform fiber before and after the tapered section to allow for an initial spectral broadening.

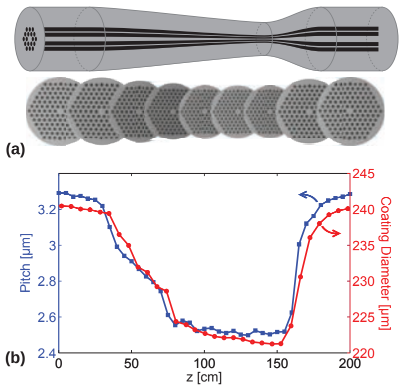

Fig. 5. Measured profile of the asymmetric draw-tower taper. (a) Schematic with cross-section images captured with an optical microscope at 100x magnification. The structure was maintained throughout the length of the taper. (b) Coating diameter and fiber pitch (hole spacing) calculated from cross-section images through the tapered section. The hole-to-pitch ratio of 0.52 was constant though the taper.

Figure 6(a) shows the spectra recorded when pumping from the long (blue) and short (red) downtapering sides. A reference spectrum from a 10 m uniform fiber (black) is included to show the maximum bandwidth achievable in a uniform fiber. Figures 6(b)-6(c) show a close up of the blue edge and the integrated power. It is clearly evident that pumping from the long downtapering side yields a higher power in the blue edge than pumping from the short. Both

#161502 - $15.00 USD Received 13 Jan 2012; revised 26 Mar 2012; accepted 18 Apr 2012; published 24 Apr 2012

spectra from the tapered fiber extend below the bandwidth achievable in the uniform fiber, as expected. These results confirm the importance of GAM: when the taper is too steep, the solitons at the red edge are decelerated too fast relative to the DWs at the blue edge. A fraction of the energy in the DWs hence escapes the trapping potentials from the solitons and is consequently not blueshifted. In the present taper, pumping from even the optimum long downtapering side gives only a small addition to the energy below 500 nm compared to the uniform fiber. However, the energy below the spectral edge of the uniform fiber is increased threefold from 12.8 to 37.7 mW when the taper is pumped from the long downtapering side.

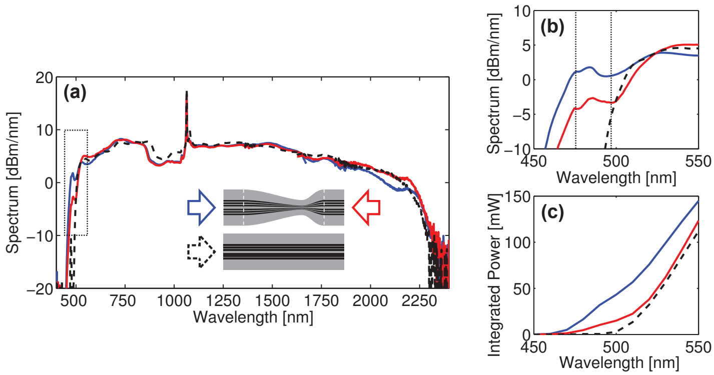

Fig. 6. Experimental output spectra of the asymmetric draw-tower taper. (a) Output spectra when pumping the taper from the long (blue) and short (red) downtapering sides. The spectrum of a 10 m uniform fiber (black dash) is shown for comparison. The insets show the pump directions. (b) Close up of the blue edge marked in (a), the vertical dotted lines mark the spectral edges calculated in Fig. 3(b). (c) Integrated power in the blue edge. Pumping from the long downtapering side clearly gives a higher power in the blue edge.

The prediction of the blue edge from Fig. 3(b)-3(c) is marked by vertical lines in Fig. 6(b). The agreement is best for the uniform fiber, which may be due to small changes in the hole-to-pitch ratio in the taper. Furthermore, determining the exact red edge is ambiguous in terms of the specific wavelength of the loss edge.

3.2. Ultra-short tapers

For the ultra-short Vytran taperes the total fiber length was fixed to 50 cm with a 6 cm symmetrically tapered section in the middle. The tapers differed from each other in the length of the up and downtapering sections that was set to 30, 20 and 5 mm, respectively. This corresponds to waists of 0, 20 and 50 mm, respectively. The results shown in Fig. 7 again clearly confirm the importance of GAM: increasing the length of the downtapering section with just a few millimetres gives a dramatic increase in the power in the blue edge.

In Fig. 3(e)-3(f) we found that the blue edge should be at 453 and 378 nm for the uniform and tapered fiber, respectively. This, however, was found by assuming a red edge at 2300 nm, which can only be achieved by increasing the fiber length to allow the solitons to redshift all the way to the loss edge. The results for the ultra-short tapers nonetheless demonstrate that the blue edge can be easily shifted to much shorter wavelengths than what was demonstrated for the draw-tower taper by increasing the fiber's relative hole-size to alter the dispersion and GV

#161502 - $15.00 USD Received 13 Jan 2012; revised 26 Mar 2012; accepted 18 Apr 2012; published 24 Apr 2012

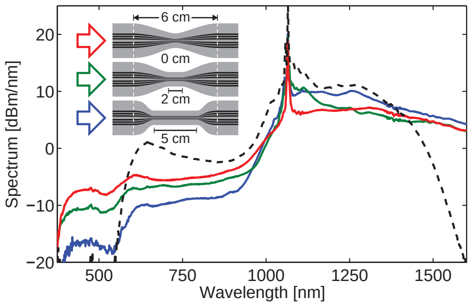

Fig. 7. Experimental spectra from ultra-short symmetrical tapers with increasing transition lengths: The blue, green and red lines show the spectra from tapers with increasing lengths of the downtapering section. The black dashed line shows the spectrum at the entrance of the tapers. A longer downtapering section again clearly increases the power in the blue edge.

profile as shown in Fig. 4 and predicted in [25]. Here our goal was to maximize the energy in the blue-edge and verify the importance of GAM. The conclusions can be straightforwardly applied to fibers with higher relative hole-sizes and thus make an important step in optimising the taper profile for SC sources with high power in the deep-blue.

4. Discussion

So far, we have ascribed the energy leakage of the DWs to GAM alone. However, we would like to point out that a taper can be viewed as a continuous perturbation of the solitons that causes them to oscillate and shed energy in order to remain fundamental solitons. This oscillatory behaviour and energy shedding is also seen in Fig. 2 although the effect is minor here. A decrease in the peak-power of a soliton will decrease the potential well around the DW and could therefore also explain why the soliton can not blueshift all the energy of a DW package thought a taper. The importance of this effect will strongly depend on the size of the perturbation, e.g., a very short taper will cause a large perturbation of the soliton and make it harder to remain a fundamental soltion.

For the fibers investigated here, the soliton period for the most redshifted solitons at the entrance of the taper is in the order of a few millimetres assuming a realistic soliton width of 10 fs. This length is very small compared to the length of the draw-tower taper, and the solitons should therefore propagate adiabatically without oscillating and shedding more energy than they would in a uniform fiber due to the Raman effect alone. However, for the ultra-short Vytran tapers the soliton period is comparable to the length of the taper, which will lead to a non-adiabatic propagation of the solitons. We thus expect that the dynamics observed in the draw-tower tapers is dominated by GAM, whereas the dynamics in the ultra-short tapers will be affected both by GAM and the non-adiabatic propagation of the solitons. We emphasize that both explanations give the same results, i.e., for a fixed taper length, the available power in the blue edge will increase with the length of the downtapering section.

#161502 - $15.00 USD Received 13 Jan 2012; revised 26 Mar 2012; accepted 18 Apr 2012; published 24 Apr 2012

5. Conclusion

In conclusion, we fabricated an asymmetric short draw-tower taper and verified experimentally the importance of the novel concept of *group-acceleration mismatch*, or GAM, on solitonic dynamics and the efficiency of SC generation. In particular, it was demonstrated that, for a fixed taper length, a longer downtapering section yields a higher power in the blue edge of the spectrum due to a correspondingly lower GAM. In the present case, the energy in the blue edge was tripled when the length of the downtapering section was increased from 0.5 to 1.5 m. The same tendencies were observed in three ultra-short symmetric tapers fabricated on a tapering station, but for these very short tapers other effects may also play a role. These results are highly important in the design of deep-blue SC sources with high power in the blue edge based on tapered fibers.

Acknowledgments

We thank the Danish Agency for Science, Technology and Innovation for support of the project no. 09-070566.

Paper III

Optimum PCF tapers for blue-enhanced supercontinuum sources [Invited]

U. Møller, S. T. Sørensen, C. Larsen, P. M. Moselund, C. Jakobsen, J. Johansen, C. L. Thomsen, O. Bang
Opt. Fiber Technol. **18**, 304-314 (2012).

Abstract: Tapering of photonic crystal fibers has proven to be an effective way of blueshifting the dispersive wavelength edge of a supercontinuum spectrum down in the deep-blue. In this article we will review the state-of-the-art in fiber tapers, and discuss the underlying mechanisms of supercontinuum generation in tapers. We show, by introducing the concept of a group-acceleration mismatch, that for a given taper length, the downtapering section should be as long as possible to enhance the amount of blueshifted light. We also discuss the noise properties of supercontinuum generation in uniform and tapered fibers, and we demonstrate that the intensity noise at the spectral edges of the generated supercontinuum is at a constant level independent on the pump power in both tapered and uniform fibers.

`http://dx.doi.org/10.1016/j.yofte.2012.07.010`

Optical Fiber Technology 18 (2012) 304–314

Contents lists available at SciVerse ScienceDirect

Optical Fiber Technology

www.elsevier.com/locate/yofte

Invited Papers

Optimum PCF tapers for blue-enhanced supercontinuum sources

Uffe Møller [a,*], Simon T. Sørensen [a], Casper Larsen [a], Peter M. Moselund [b], Christian Jakobsen [b], Jeppe Johansen [b], Carsten L. Thomsen [b], Ole Bang [a,b]

[a] DTU Fotonik, Department of Photonics Engineering, Technical University of Denmark, Ørsteds Plads, DK-2800 Kgs. Lyngby, Denmark
[b] NKT Photonics A/S, Blokken 84, DK-3400 Birkerød, Denmark

ARTICLE INFO

Article history:
Available online 22 August 2012

Keywords:
Supercontinuum generation
Photonic crystal fibers
Nonlinear fiber optics
Relative intensity noise
Tapered fibers
Group-acceleration mismatch

ABSTRACT

Tapering of photonic crystal fibers has proven to be an effective way of blueshifting the dispersive wavelength edge of a supercontinuum spectrum down in the deep-blue. In this article we will review the state-of-the-art in fiber tapers, and discuss the underlying mechanisms of supercontinuum generation in tapers. We show, by introducing the concept of a group-acceleration mismatch, that for a given taper length, the downtapering section should be as long as possible to enhance the amount of blueshifted light. We also discuss the noise properties of supercontinuum generation in uniform and tapered fibers, and we demonstrate that the intensity noise at the spectral edges of the generated supercontinuum is at a constant level independent on the pump power in both tapered and uniform fibers.

1. Introduction

Since the discovery of supercontinuum generation in bulk glasses more than 40 years ago by Alfano and Shapiro [1], a revival of the supercontinuum field with the advert of optical fibers in general [2], and photonic crystal fibers (PCFs) in particular [3,4], has paved the way for the development of high-power commercial SC light sources and the technology has found its way into many applications [5].

In a simplified physical picture high-power long-pulsed supercontinuum generation in the anomalous dispersion regime can be understood by looking at the dynamics of single solitons. Modulation instability (MI) will lead to temporal break-up of the high-power pump pulse into a distribution of soliton-like pulses and dispersive waves [6,7]. Each of these solitons may furthermore resonantly transfer energy to the normal group velocity dispersion (GVD) regime if they have sufficient spectral overlap across the zero dispersion wavelength (ZDW) [8]. For efficient visible supercontinuum generation it is thus of great importance that the pump wavelength is close to the ZDW. Intra-pulse stimulated Raman scattering leads to a continuous redshift of the soliton, also known as soliton self-frequency shift [9–12]. While the soliton is being redshifted due to the soliton self-frequency shift it keeps a packet of dispersive waves trapped in a group-velocity matched bound state, so that the dispersive waves are blueshifted to maintain group-velocity matching [13,14]. As the soliton is redshifted it slows down due to temporal broadening when the dispersion is increasing as in typical used PCFs, such as our fiber (see Fig. 2b, solid line). The dispersive waves then catch up with the soliton and interact with it. The process of pulse break-up and the formation of dispersive waves and solitons is illustrated in Fig. 1. The redshift of the solitons can be limited by the material loss edge, a 2nd ZDW, or temporal broadening due to increasing dispersion. Silica has an increasing absorption above 2200 nm, which effectively prohibits the solitons from propagating beyond the region of 2300–2400 nm. Interaction through collisions of solitons will lead to high-energy solitons capable of reaching the silica material loss edge [15]. In some cases these collisions can even lead to ultra-high-energy solitons, also known as rogue waves [16–21].

The fundamental physical interpretation of supercontinuum generation was well established in the early 1990s. However, the first commercial supercontinuum light source was still more than 10 years away. The main reason for this gap was that the step-index telecom fiber at the time had a relatively fixed ZDW of 1300–1550 nm, which meant that the available high-power, commercial laser sources, e.g. ytterbium (∼1064 nm) and Ti:Sapphire (∼800 nm) solid state lasers, were in the normal GVD regime and thus could not be used for efficient supercontinuum generation. Although lasers were available above 1300 nm with sufficient power, they were still bulky and expensive Q-switched solid state lasers requiring free-space coupling to the nonlinear fiber. What was missing for commercial supercontinuum sources was therefore reliable high-power fiber lasers to allow efficient coupling to the nonlinear fiber *and* a suitable nonlinear fiber that allowed moving the ZDW down to the wavelength of the laser source. During the telecom boom in the 1990s reliable fiber lasers were readily developed, and with the advent of the photonic crystal fiber

* Corresponding author.
E-mail address: ufmo@fotonik.dtu.dk (U. Møller).

1068-5200/$ - see front matter © 2012 Elsevier Inc. All rights reserved.
http://dx.doi.org/10.1016/j.yofte.2012.07.010

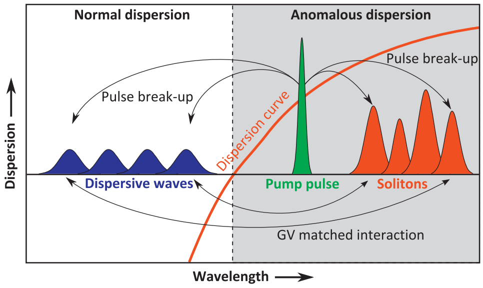

Fig. 1. Schematic of supercontinuum generation. By pumping close to the ZDW in the anomalous dispersion regime solitons will be generated and trap dispersive waves. Group-velocity matching will force the dispersive waves to blueshift while the solitons are redshifting due to soliton self-frequency shift.

(PCF) in 1996 the solution to the fiber challenge was also given [3]. The air-hole structuring in the PCF manipulates the properties of light and gives a tremendous degree of design freedom, which has enabled pushing the properties of PCFs to limits that can never be achieved with standard step index fibers. For example, one can move the ZDW into the visible [4], guide light in air [22], and make them endlessly single moded, even for large mode area (LMA) PCFs [23].

The visible part of the electromagnetic spectrum (350–800 nm) is very important for biological applications, e.g. optical coherence tomography [24,25], confocal microscopy [26], Förster resonance energy transfer (FRET) [27,28], and fluorescence lifetime imaging microscopy (FLIM) [29]. For these applications it is thus beneficial that as much light as possible is available in the whole visible part of the spectrum.

A highly nonlinear fiber is desirable for efficient supercontinuum generation. This can be designed by modifying the core diameter and the hole-to-pitch ratio of the fiber. There will, however, be a practical lower limit to how small the fiber core can be since a too small fiber core (diameter < 2–3 μm) makes it hard to couple light into the fiber. This problem can be overcome by longitudinally altering the fiber diameter, i.e. by tapering. In the recent years, much research has been devoted to tailoring the fibers for optimizing the desired supercontinuum spectrum [30–33]. Tapering of fibers have been shown to be an effective way to blueshift the short wavelength edge of the supercontinuum by means of changing the fiber dispersion and increasing the nonlinearity [34–36]. Previously, supercontinuum generation in draw-tower tapers has been examined experimentally by Kudlinski et al. [34,37] and Travers [35] where they generated light down to 340 nm. Travers and Taylor have numerically investigated soliton and dispersive wave propagation in tapers of a few meters [38] and Sørensen et al. have studied the effect of the taper gradient [36,39]. Recently, Stark et al. have demonstrated supercontinuum generation down to 280 nm by pumping short, sharply tapered solid-core PCFs with femtosecond pulses. They used a steep taper gradient to trigger pulse breakup inside the taper to form an intense and broadband spike of electromagnetic radiation [40]. Note that the UV-light generation is in this case not an effect of blueshifted group-velocity matched dispersive waves.

In this article we will focus on supercontinuum generation in PCFs pumped in the anomalous dispersion regime with intense picosecond pulses. We specifically outline how high-energy solitons reaching the infrared loss edge through trapped and group-velocity matched dispersive waves is an effective way of blueshifting the blue edge. The power in the blue edge can furthermore be enhanced by considering the taper shape. Continuous wave (CW) supercontinuum generation [41], gain-switched pumping [42] or pumping with long pulses offers high average power as well as broadband spectra. However, since this type of supercontinuum generation is initiated by noise induced MI, the generated supercontinuum will have low coherence and high intensity fluctuations across the whole bandwidth and in particular at the edges [43,44]. Femtosecond supercontinuum generation is initiated by soliton fission and is as such less noisy and has better coherence properties, but it suffers from a low average power [43].

Several methods have been proposed to modify the supercontinuum spectrum and reduce the noise, including seeding by modulation of the input pulse [16,45], seeding with minute pulsed and CW light [18,46,47], seeding with the 2nd harmonic [48], and back seeding [49]. Here we will discuss the intensity noise properties in tapered fibers, and we show that the intensity noise at the spectral edges of the generated supercontinuum is at a constant level independent on the pump power in both tapered and uniform fibers.

The article is organized as follows. In Section 2 we describe the numerical method and experimental setup used throughout the article, and the reproducibility of tower-drawn tapers is discussed. In Section 3 we go through the underlying dynamics of supercontinuum generation in tapered PCFs. In Section 4 we introduce the concept of group-acceleration mismatch (GAM) and we present results on supercontinuum generation in tapered PCFs with varying taper length in order to investigate the possible optimum taper profile capable of generating a fully developed blue-enhanced edge. Finally, Section 5 goes through the power dependence of the intensity noise in uniform and tapered PCFs.

2. Material and methods

For the experiments we used an ytterbium fiber laser, which delivers 10 ps pulses at 1064 nm at a repetition rate of 80 MHz. The laser delivery fiber was spliced to the PCFs to minimize coupling losses and instabilities. The average input power was 10 W, corresponding to a pulse energy of 125 nJ and a peak power of 11.7 kW when assuming Gaussian shaped pulses. The generated supercontinuum output was collimated and the spectra were measured with two optical spectrum analyzers and stitched together. For the relative intensity noise (RIN) measurements, the collimated supercontinuum output was guided through narrow band-pass filters of 10–30 nm full width at half maximum (450–1600 nm filters from Thorlabs and 1810–2310 nm from Multi-IR Optoelectronics Co., Ltd.) and onto a photoreceiver (Newfocus 125 MHz Si and InGaAs photoreceivers for measurements in the 450–1000 and 1000–1600 nm range, respectively, and a Redwave Labs 100 MHz extended InGaAs photoreceiver for measurements in the 1600–2400 nm range). The photoreceiver was connected to an electrical spectrum analyzer (sweeping for 30 s with a bandwidth of 10 kHz) and a voltmeter to characterize the DC and AC voltage, respectively [44].

The simulations use a generalized nonlinear Schrödinger equation (GNLSE) model, which is often utilized to aid the understanding of the supercontinuum dynamics, and has demonstrated good agreement with experimental results [43,50–52]. We use the particular implementation described in [53,54], with input noise included in the frequency domain through a noise seed of one photon per mode with random phase added to each discretization bin. Loss is neglegted and care is taken to conserve the photon number. The numerical RIN is calculated from an ensemble of 1000 simulations that only differed in the input noise. Time series of pulse powers, $P(t)$, were calculated in 10 nm bandwidths across the spectrum and assumed to be spaced by $(80\ \mathrm{MHz})^{-1}$; the same bandwidth and temporal spacing that was used in the experiment. The RIN is then given as the square of the Fourier transform of the time series normalized to the average power, P_{avg} [55].

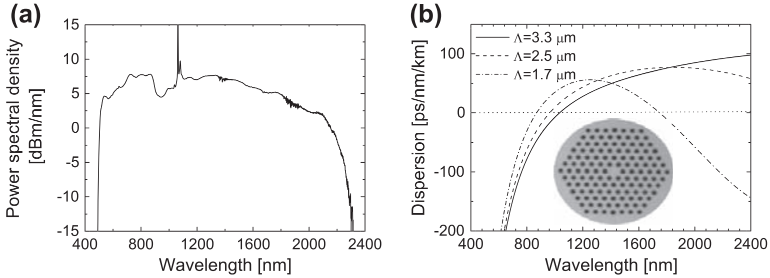

Fig. 2. (a) Measured spectrum from a 10 m PCF. (b) Calculated dispersion of fibers with constant hole-to-pitch ratio $d/\Lambda = 0.52$ and 3 different pitches Λ. Inset in (b): microscope image of the fiber cross-section.

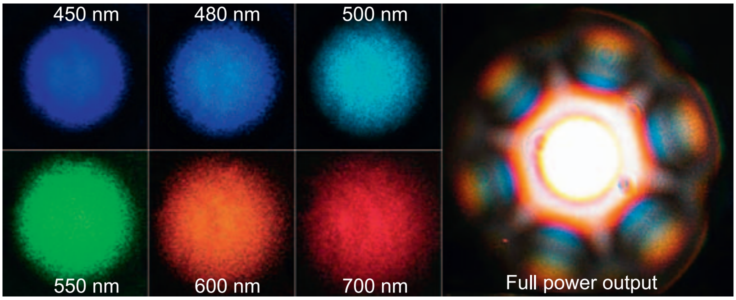

Fig. 3. Far-field images of the fiber output at different filtered wavelengths as well as the total output field at maximum output power.

We have focussed on one particular PCF geometry throughout this article to illustrate our points. The fiber has a hole-to-pitch ratio (d/Λ) of 0.52 and is a commercially available fiber (SC-5.0-1040, NKT Photonics A/S), which has been shown to be single moded near the pump wavelength [56]. The supercontinuum spectrum from a uniform fiber ($\Lambda = 3.3$ μm) when pumping with the above mentioned conditions is shown in Fig. 2a, and the calculated dispersion profiles for various pitches are depicted in Fig. 2b.

The far-field output of a tapered fiber (shown in Fig. 9) at different filtered wavelengths (10 nm bandpass filters used) as well as the total output field are imaged in Fig. 3. Note that the outputs of the filtered wavelengths only show the core region to avoid overexposure of the camera. Leakage to the inner cladding structure is visible in the image of the full power output. The images clearly illustrate that the output is predominately single moded.

The PCF tapers discussed in this article are fabricated directly on the draw-tower by modifying the drawing conditions, and unlike earlier published work on tapers, e.g. [32,34,35,37,57], these tapers are tapered back to their original fiber diameter, thereby allowing easier handling, splicing, and termination of the fibers. Contrary to earlier reports [58] we find that relatively short tapers with lengths of 2–7 m can be made directly on the draw-tower with excellent reproducibility and accurate control of the fiber diameter as demonstrated in Fig. 4.

A standard deviation of 0.5 μm on the cladding diameter corresponds to a deviation of 0.4% relative to the cladding diameter, which in this case will correspond to a standard deviation of less than 7 nm of the hole diameter. The increased standard deviation at the uptapering edge is due to the measurement discretization of 15 cm. The laser gauge measuring the cladding diameter has an accuracy of 0.25 μm, which means that the measured standard deviation is close to, and in some cases limited by, the instrumental

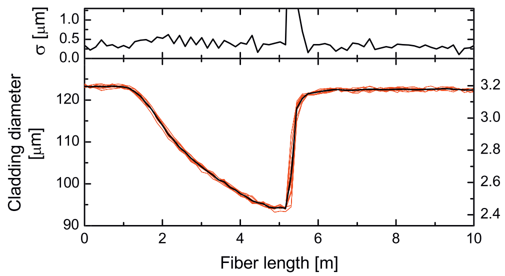

Fig. 4. Demonstration of taper drawing reproducibility. Bottom: the red lines show the cladding diameter as a function of length for 10 different taper drawings while the black line shows the mean. Top: standard deviation σ of the cladding diameter for the 10 fiber drawings. (For interpretation of the references to colour in this figure legend, the reader is referred to the web version of this article.)

resolution. Such excellent reproducibility is highly important for commercial applications.

3. Tapered photonic crystal fibers

Tapering is an effective way to manipulate the fiber properties. Not only does it increase the nonlinearity but it also alters the dispersion of the fiber. The spectral edges of the supercontinuum are comprised by solitons and group-velocity matched dispersive waves [13,59]. The position of the blue edge for a given fiber can hence be estimated from numerically calculated group-velocity curves if the position of the solitonic red edge is known. The calculated spectral blue edge for the fiber under investigation is shown

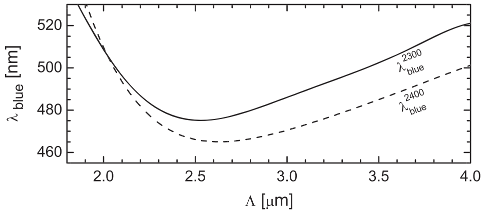

Fig. 5. Blue edge wavelength λ_{blue} as a function of pitch Λ assuming group-velocity matching to a loss edge of 2300 nm or 2400 nm.

Table 1
Blue edge wavelength for different pitches and red edges.

Λ (µm)	$\lambda_{\text{blue}}^{2300}$ (nm)	$\lambda_{\text{blue}}^{2400}$ (nm)
3.3	495	479
2.8	480	467
2.5	477	465

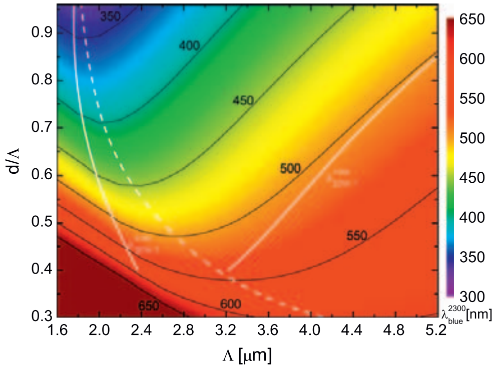

Fig. 6. Blue edge wavelength $\lambda_{\text{blue}}^{2300}$ as a function of hole-to-pitch ratio d/Λ and pitch Λ assuming group velocity matching to a loss edge of 2300 nm or 50 nm below the 2nd ZDW. The dashed white line indicates the optimum Λ for a given d/Λ. The two solid white lines show the 1st ZDW at 1064 nm and the 2nd ZDW at 2350 nm, respectively.

in Fig. 5 as a function of pitch Λ. The material loss region is not a well-defined and asymptotic loss edge but it is a region where the soliton as it redshifts more and more will experience an increased loss, i.e. more energetic solitons will be capable of redshifting more before they have lost their energy. The difference in the maximum blueshift of dispersive waves from a soliton reaching 2400 nm and a soliton reaching 2300 nm is illustrated in Fig. 5 for a fixed hole-to-pitch ratio of 0.52. Clearly, the less energetic soliton reaching 2300 nm will not blueshift its trapped and group velocity matched dispersive waves as much as the more energetic soliton reaching 2400 nm. In Table 1 the blue edge wavelengths for defined red edges at 2300 nm and 2400 nm, respectively, are listed for different pitches.

Calculations of the blue edge for an arbitrary pitch and hole-to-pitch ratio (d/Λ) can also be performed. This has previously been done by Travers [35], who defined the blue edge as the shortest group-velocity matched wavelength and calculated the blue edge wavelengths for $d/\Lambda > 0.6$. Travers found that the optimum pitch for large hole-to-pitch ratios was around 2 µm almost independent of the hole-to-pitch ratio. Introducing the loss edge in the calculations, the spectral blue edge is shown in Fig. 6 as a function of hole-to-pitch ratio and pitch. We define the red edge as the loss edge (set to 2300 nm in Fig. 6), or a wavelength λ_2 close to the 2nd ZDW, whichever is the lowest [39]. Solitons always halt their redshift about 50–100 nm away from the 2nd ZDW [60,61], so λ_2 is chosen to $\lambda_{\text{ZDW},2}$ − 50 nm, thus assuming group-velocity matching to a loss edge of 2300 nm or 50 nm below the 2nd ZDW.

The dashed line in Fig. 6 shows the optimum pitch giving the lowest blue edge for a given hole-to-pitch ratio. By tapering, the pitch will be altered whereas the hole-to-pitch ratio can be constant, i.e. tapering will cause a horizontal move to the left in Fig. 6. Tapering further down than the optimum pitch will for larger hole-to-pitch ratios let the 2nd ZDW come into play as it is shifted below 2300 nm, i.e. below the silica material loss edge. When this happens the redshifting solitons will be limited by the 2nd ZDW, which then again limits the blueshift of the group-velocity matched dispersive waves. For smaller hole-to-pitch ratios the optimum pitch is reached before the 2nd ZDW has crossed the loss edge and is thus solely determined by the loss edge. The blue edge of a fiber with parameters to the right of the dashed line in Fig. 6 will therefore be limited by the material loss edge and not by the 2nd ZDW of the fiber. In this case, the blue edge can be blueshifted by tapering. In the opposite case, where the blue edge is limited by the 2nd ZDW of the fiber for larger hole-to-pitch ratios, tapering will not increase the blueshift of the blue edge.

According to Fig. 6, one should have a fiber with a hole-to-pitch ratio as high as possible and a pitch around 1.84 µm to generate the most blueshifted light. A fiber with a pitch of 1.84 µm and a hole-to-pitch ratio of 0.96 will yield a blue edge at 333 nm when assuming a loss edge at 2300 nm. Previously, Kudlinski et al. [34,37] and Travers [35] have generated light down to 340 nm in a fiber with a hole-to-pitch ratio between $d/\Lambda = 0.87$ and 0.89, where the fiber was tapered from a pitch of ~6 µm to ~2 µm over a length of 3 meters.

As mentioned in Section 1 there has been some previous work on tapered fibers with the purpose of modifying the supercontinuum generation process. Generally, there are two main techniques for taper fabrication: post-processing of fibers or during fiber manufacturing. Post-processing is typically used to produce short tapers (<20 cm) by subsequent heating and stretching the fiber. This technique has previously been used to demonstrate enhanced self-phase modulation [62], soliton self-frequency shift [63], and to shift the ZDW and increasing the nonlinearity in standard telecommunication fibers [30] and solid-core microstructured fibers [31,33,64–67] for efficient supercontinuum generation.

Taper fabrication during fiber manufacturing is typically used to produce tapers in the order of meters to kilometers. Tapers as short as 10 cm [57], a few meters [39], and several kilometers [68] have previously been made directly on the draw tower. Importantly, longer tapers allows the fiber characteristics to change slowly while the long-pulsed supercontinuum evolves.

4. Tapers for optimum blue-enhanced supercontinuum generation

Now that we have theoretically predicted how the blue edge can be shifted by high-energy solitons, one of the remaining challenges is to shift as much light as possible to the edge. It is clear from Fig. 6 that the optimum tapering degree, i.e. the depth of the taper, can be found from group-velocity matching of solitons and their corresponding dispersive waves. But what about other tapering parameters, such as down- and up tapering length and taper waist length? This has so far been an open question as stated by Travers [35].

To clarify this one has to recall the trapping effect, which is of fundamental importance for the supercontinuum generation dynamics. As previously described, the MI process causes the input pulse to break up and solitons and dispersive waves will be generated. As a soliton redshifts it is temporally delayed in typical PCFs as ours, which allows the dispersive wave to catch up with the soliton and be trapped in a potential created by the soliton. When the soliton is further redshifted, the trapped dispersive wave is blueshifted to satisfy group-velocity matching. For a uniform fiber this process would continue as long as the soliton redshifts [14,69]. However, as the soliton enters the downtapering section it is accelerated and leaves some of the dispersive wave behind. The rest of the trapped dispersive wave blueshifts with the soliton through the taper waist and to the uptapering section where the group-velocity match is broken due to the acceleration of the soliton relative to the dispersive wave. The uptapering section should therefore have limited influence on the blueshifted part of the spectrum. Left is therefore to determine the ratio between the downtapering length and the length of the taper waist. Alternatively, the blueshift of dispersive waves can be explained as a cascade of cross-phase modulation (XPM) collision events that continuously blueshifts the dispersive waves in discrete steps [70].

In a fiber, the soliton undergoes a continuous Raman redshift, which leads to a continuous change of its group-velocity as a function of the propagation length, i.e. a *group-acceleration*. However, the dispersive waves do not on their own move spectrally and are thereby not subject to the same acceleration. This means that the dispersive waves will continuously loose energy because of the difference in group-velocity, which diminishes the interaction length and hence the trapping effect, as illustrated in Fig. 7a. The Raman effect thus leads to a *group-acceleration mismatch* (GAM), an asymmetric change of the group-acceleration of the solitons and dispersive waves [36,39]. This effect is not dramatic in a uniform fiber because of the relatively weak Raman redshift and thereby correspondingly low GAM. In a taper, however, the group-acceleration can be orders of magnitude higher than the inherent Raman induced change [38]. Furthermore, it is asymmetric in the sense that the group-velocity change induced by the taper is different for the blue edge compared to the red edge as illustrated in Fig. 7b. In order to minimize GAM and thereby maximizing the power transferred to the blue edge due to high-energy solitons reaching the loss edge, the taper gradient should be as small as possible.

4.1. GAM illustrated with simulations

Due to the solitonic nature of supercontinuum generation, a lot of insight into the supercontinuum generation process can be gained by single soliton simulations. To get a basic understanding of supercontinuum generation and edge formation in a tapered

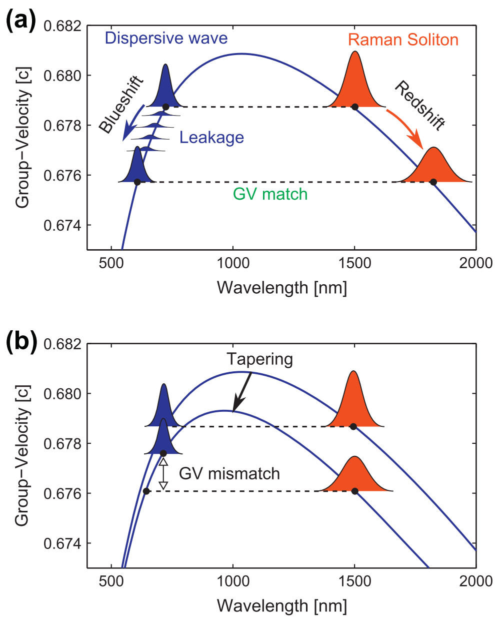

Fig. 7. Radiation trapping and leakage. (a) In a uniform fiber a soliton can trap and blueshift a group-velocity matched dispersive wave, while it is slowly redshifting and thus decelerating. The trapping is incomplete, i.e. part of the dispersive wave continuously leaks out of the trap, as illustrated. (b) In a taper, there is a mismatch in the group-acceleration, the rate with which the group-velocity changes, which increases the amount of light that leaks out of the trap (not illustrated). The group-velocity curves are calculated for a fiber with a $(d/\Lambda) = 0.52$ μm, $\Lambda = 3.3$ μm and $\Lambda = 2.5$ μm. (For interpretation of the references to colour in this figure legend, the reader is referred to the web version of this article.)

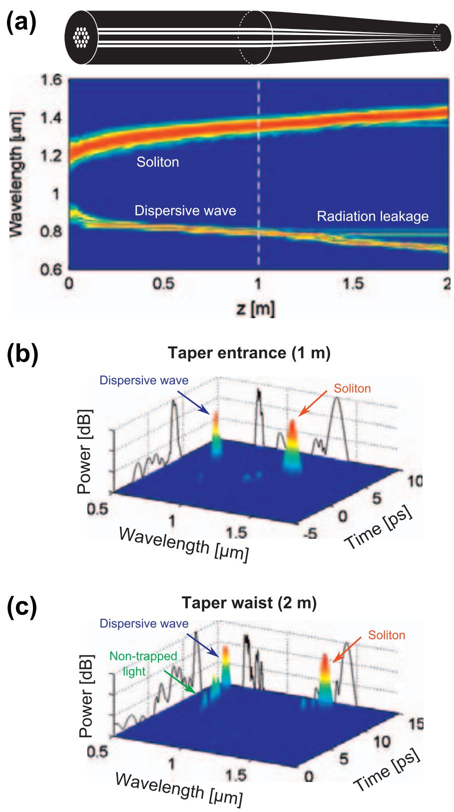

Fig. 8. (a) Spectral evolution of a 20 fs fundamental soliton and trapped dispersive wave through a fiber taper with an initial 1 m uniform fiber. (b) and (c) Spectrograms at the entrance (1 m) of the taper and at the taper waist (2 m). The wave is fully trapped at the taper entrance, but the taper increases the soliton redshift and deceleration, which causes part of the dispersive wave package to leak from the soliton induced trapping region.

fiber it is hence instructive to analyze the propagation of a soliton and an appropriately delayed and group-velocity matched dispersive wave package [36,38,39].

The propagation of a 20 fs fundamental soliton and a group-velocity matched dispersive wave is illustrated in Fig. 8. The soliton redshifts throughout the length of the fiber, and while doing so, it causes a blueshift of the trapped wave as seen in Fig. 8a. In the first meter of uniform fiber, the two co-propagate without the dispersive wave shedding much energy. As the downtapering starts at 1 m, both the redshift rate of the soliton and the blueshift rate of the trapped dispersive wave increase due to the increase in nonlinearity and change in group velocity. However, due to the taper induced GAM, a significant fraction of the trapped dispersive wave now escapes the trap. The spectrograms in Fig. 8b and c show the pulses in the spectral and time-domain simultaneously; at the taper entrance (Fig. 8b), the two waves are temporally overlapping and the decelerating soliton has fully trapped the dispersive wave. At the taper end (Fig. 8c) only a fraction of the originally trapped dispersive wave is still trapped and has a temporal overlap with the soliton. The remaining light has escaped the trap and not been decelerated and blueshifted by the soliton. This clearly illustrates the need for matching not only the group velocities but also the rate of which they change, i.e. minimizing the GAM as predicted numerically in [36] and verified experimentally in [39].

4.2. GAM demonstrated with experiments

Experimentally it is straightforward to demonstrate the concept of GAM. Fig. 9 shows the spectra from an asymmetrically tapered fiber pumped from each end. The asymmetry will yield a difference of the GAM in the two cases even though the light passes through the same length of fiber. The dashed line shows the spectrum from 10 m of uniform fiber. It is noticed that the red edge is at 2300 nm while the blue edge is at 492 nm. This fits well with the predicted blue edge of 495 nm (Figs. 5 and 6). For this particular fiber the blue edge is blueshifted the most by tapering it from a pitch of 3.3 μm to the optimum pitch of 2.5 μm. The tapered fiber consists of a 3 m uniform section before and after the 4 m asymmetrically tapered section, which is illustrated in the inset of Fig. 9. As expected the tapering causes a blueshift of the blue edge relative to the uniform fiber. Pumping the tapered fiber from the steep downtapering end (blue line in Fig. 9) gives a red edge at 2380 nm and a blue edge of 462 nm at a level of −15 dBm/nm while pumping from the other end of the tapered fiber (red line in Fig. 9) gives a red and blue edge at 2435 nm and 454 nm, respectively. Again, this fits reasonably well with the predicted blue edge of 465 nm when assuming the red edge at 2400 nm.

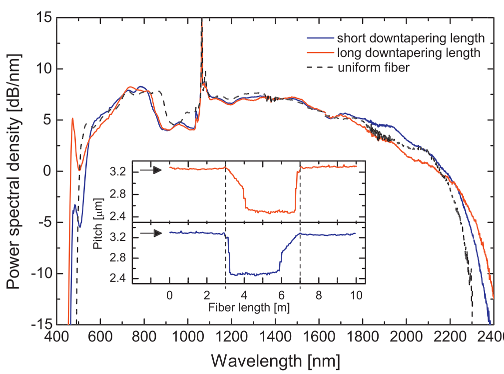

Fig. 9. Effect of downtapering length. Experimental output spectra when pumping the asymmetric taper from the short (blue) and long (red) downtapering ends. The spectrum of a 10 m uniform fiber (black dash) is shown for comparison. The inset shows the tapering profile and the arrows indicate the pump direction. (For interpretation of the references to colour in this figure legend, the reader is referred to the web version of this article.)

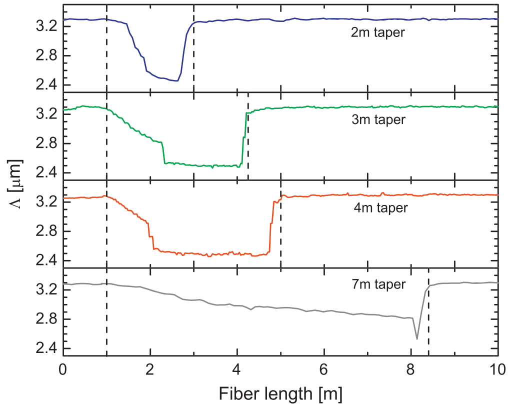

Fig. 10. Pitch Λ as a function of fiber length for the four different tapers. The dashed lines indicate the beginning and end of each taper.

In the case of pumping from the long downtapering side it is however not evident if the blue edge is influenced by the abrupt steepness change of the downtaper after ~1 m. The steepness change happens at a pitch of Λ = 2.8 μm for which the group velocity matched blue edge is 2 nm higher than for the optimum pitch of Λ = 2.5 μm (see Table 1).

The main difference between the two spectra is the amount of light generated at the blue edge. Pumping from the long downtapering side clearly yields a higher power in the blue edge than pumping from the short downtapering side. These results confirm the importance of GAM: The steeper the downtapering section is, the faster the solitons at the red edge are decelerated relative to the dispersive waves at the blue edge. A larger fraction of the energy in the dispersive waves hence escapes the trapping potentials from the solitons and is accordingly not blueshifted [36,39].

To further illustrate the concept of GAM, different tapers were fabricated. The pitch as a function of fiber length for 4 different tapers, where the total fiber length is 10 m and the initial fiber length before the taper is 1 m, is shown in Fig. 10. When no hole collapse occurs during the tapering process the variation of the fiber pitch is correlated to the variation of the fiber cladding diameter. For this particular fiber it was previously shown that no hole collapse occurs during fiber tapering [39] and the fiber pitch can thus be found from measuring the cladding diameter of the fiber. The tapered sections of the fibers are approximately 2.0 m, 3.2 m,

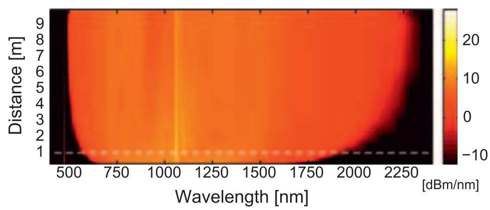

Fig. 11. Cutback measurement of the uniform fiber. The dashed white line show the spectrum after propagation in 1 m fiber.

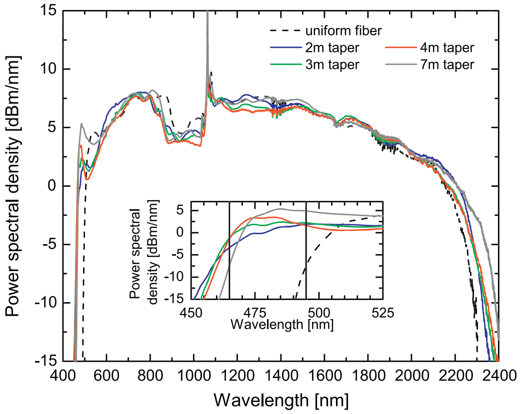

Fig. 12. (a) Output spectra of a 10 m uniform fiber (dashed black), the 2 m taper (blue), the 3 m taper (green), the 4 m taper (red), and the 7 m taper (gray). Inset: Close-up of the blue edge. The vertical lines indicate the predicted edges. (For interpretation of the references to colour in this figure legend, the reader is referred to the web version of this article.)

4.0 m, and 7.5 m and will in the following be referred to as the 2 m, 3 m, 4 m, and 7 m tapers, respectively. We note that these tapers are some of our earliest tower-drawn fiber tapers before the tapering process had been improved to produce tapers of the quality shown in Fig. 4.

In order to have a well-documented reference we conducted a cutback measurement on a 10 m uniform fiber. Fig. 11 shows how the spectrum widens in the first few meters of the fiber and after 5 m the spectral width barely increases. The dashed white line in Fig. 11 indicates the spectrum after propagation in 1 m uniform fiber, which is the fiber length before each taper. This fiber length is much longer than the characteristic length, $16/(\gamma P_0)$, where a supercontinuum will be developed [43]. This characteristic length is in this case ~8 cm. Thus, a distribution of solitons has been formed and a supercontinuum has been partially developed at the taper entrance.

A comparison of the spectra obtained from the uniform and tapered fibers is shown in Fig. 12. In all cases the tapered fibers exhibit broader spectra compared to the output spectrum of a 10 m uniform fiber. The spectral red edge is limited by the material loss edge in silica at approximately 2400 nm, which also will limit the blue edge.

As also shown in the previous example (Fig. 9), the blue edge of the 10 m uniform fiber at a level of −15 dBm/nm is measured to be at 492 nm, which is in good agreement with the predicted 495 nm when matching to the red edge at 2300 nm. As expected, the blue edges of the tapered fibers are shifted below that of the uniform fiber as seen in the inset of Fig. 12. In the case of a pitch of 2.5 μm the edge is expected to be at 465 nm when matching to the red edge at 2400 nm. This also fits well with the experimental blue edges, which are measured to be in the region of 452–455 nm for the 2 m, 3 m, and 4 m tapers, corresponding to a blueshift of 37–40 nm. The measured blue edge of the 7 m taper is slightly higher at 462 nm. This is attributed to the form of the taper; the diameter of the 7 m taper is gradually decreased as seen in Fig. 10, but right before the uptapering section the fiber diameter is rapidly decreased to its minimum. This will lead to an increased GAM, which means that the taper is only efficient down to a fiber pitch of 2.8 μm. As a result, the dispersive waves will experience a reduced blueshift, which can be seen in Fig. 5. However, since the variation of the blue edge wavelength is small near the optimum fiber pitch, it is not crucial to have an exact match between the optimum and actual tapered fiber pitch. For this fiber the blue edge wavelength will only shift additionally 2 nm when tapering from a pitch of 2.8 μm to a pitch of 2.5 μm, as seen in Fig. 5 and Table 1.

The amount of blueshifted light is however not identical for the tapers. The spectral shoulder in the blue edge caused by the taper is increasing for increasing taper length as clearly seen in the inset of Fig. 12. This is further quantified in Fig. 13 where the integrated power in the blue edge of the different fibers are shown. Comparing the tapered fibers it is seen that the power density in the blue edge is increased for increasing tapering length. All light below 495 nm is created in the tapered section of the fiber. The amount of shifted light below 495 nm is 38.6 mW, 51.3 mW, 60.2 mW, and 78.8 mW for the 2 m, 3 m, 4 m, and 7 m taper, respectively. It is noticeable that the 3 m and 4 m tapers have comparable downtapering lengths, which should blueshift the same amount of dispersive waves and thus give rise to similar power densities in the blue edge. The increased power in the spectral region below 495 nm can however be ascribed to the difference in taper waist length. The group-velocity match will not be broken until the uptapering starts. The dispersive waves are hence blueshifted both in the downtapering section and in the taper waist. The longest of the investigated tapers, the 7 m taper, clearly blueshifts the most light which is attributed to lowest GAM of all the investigated tapers [36,39].

To clarify the impact of the length of uniform fiber after the taper we cut off approximately 1.5 m of the 7 m tapered fiber and measured the output spectrum directly after the taper. This output spectrum (not shown) was identical to the output spectrum of the original 7 m tapered fiber. The uniform fiber after the taper has, in this case, no impact on the resulting output spectrum but leads to temporal broadening, pulse walk-off, and loss. This suggests that

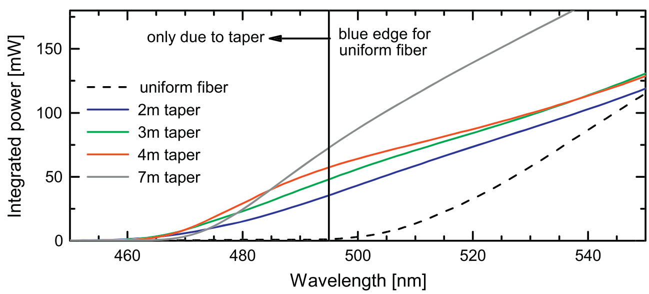

Fig. 13. Integrated power in the blue edge for the fibers shown in Fig. 12. The vertical line indicates the blue edge of the uniform fiber (495 nm), all power shifted below this wavelength is generated in the taper. (For interpretation of the references to color in this figure legend, the reader is referred to the web version of this article.)

the optimum taper for a fully developed blue edge should be as long as possible and the length of the uniform fiber after the taper as short as possible.

5. Intensity noise in tapered supercontinuum sources

A lot of attention has been drawn to the phenomenon of large amplitude rogue wave generation [6,17,21,51,71] and ways to control these extreme and rare events [16,18]. This attention has been understandable because of the fundamental nature of rogue waves and because they appear in diverse systems such as optics [17,19,21], ocean waves [20,72], breaking of DNA bonds [73], superfluid helium [74], the atmosphere [75], and even finance [76]. The hydrodynamic definition of the events that constitute rogue phenomena is defined as a soliton, whose height (peak power) is more than twice the significant wave height, i.e. the mean peak power of the one-third largest amplitude solitons [21]. Seen from a commercial point of view on supercontinuum light sources, these statistically rare optical rogue waves are of less importance, because of their minimal contribution to the overall intensity fluctuations of the supercontinuum spectrum. Instead, the stability of the supercontinuum source can be quantified in terms of shot-to-shot fluctuation. This has previously been done in different ways, including calculating higher order moments of intensity fluctuations [77], looking at minima and maxima of the pulse trains [78], and in terms of the relative intensity noise (RIN) [55].

Recently, Kudlinski et al. have measured the shot-to-shot fluctuations from a uniform and a tapered fiber for one fixed power level. They defined a noise measure given by the ratio $\sigma = 100 \cdot (V_{\max} - V_{\min})/(V_{\max} + V_{\min})$, where $V_{\max}$ and $V_{\min}$ are the maximum and minimum photodiode signal amplitudes, respectively, measured for at least 10 out of 10,000 recorded pulses, and showed that the noise was reduced in the tapered fiber when observing a fixed wavelength near the blue edge [78]. They observed that the noise was reduced at the blue wavelength edge when the fiber was tapered and attributed it to a presumed increase of the spectral power density beyond 1750 nm. This increase will lead to an increased probability to encounter solitons at the long wavelength side of the supercontinuum. Since the dispersive waves at the blue edge are group-velocity matched to these solitons, the intensity noise will also decrease in the blue edge of the supercontinuum. Vanvincq et al. described a significant reduction of power fluctuations at the long-wavelength edge of a SC generated in solid-core photonic bandgap (PBG) fibers [79]. However, PBG fibers are less attractive from an application point of view, since the spectral bandwidth of SC generated in PBGs will be limited and thus not utilize the full potential of silica. One should also keep in mind that there is a fundamental difference between the guiding mechanisms and the soliton dynamics in PBG fibers compared to solid-core PCFs. When a soliton is approaching the bandgap edge in a PBG fiber it will experience a very strong change of the GVD. This change will cause the soliton to broaden in time and decrease in peak power adiabatically. It will never cross the bandgap edge due to the temporal broadening (and thereby reduction in redshift) arising from the abruptly increasing dispersion. Near the loss edge in a PCF the soliton will experience much less variation in the GVD when redshifting, and the soliton energy will drop because of the *gradually* increasing material loss. However, it is still possible for the solitons to propagate into the loss region, with high-power solitons penetrating furthest. Since the soliton dynamics is different it is not obvious that the noise properties are the same for the two fibers. We have recently shown that the noise at the spectral edges of the generated supercontinuum is at a constant level independent on the pump power in both tapered and uniform fibers. At high input power the spectral bandwidth is limited by the infrared loss edge, this however has no effect on the noise properties [44].

RIN is a standard way of measuring noise in laser systems and is quantified by the noise power in an electrical frequency bandwidth of 1 Hz normalized to the DC signal power,

$$RIN(\omega) = \frac{(\Delta P(\omega))^2}{(P_{\rm avg}(\omega))^2}, \tag{1}$$

where $(\Delta P)^2$ is the mean square intensity fluctuation and $P_{\rm avg}$ is the average optical power. The shot-to-shot fluctuations σ can then be found by integrating the RIN up to the Nyquist frequency (1/2 repetition rate frequency) and taking the square root to obtain the amplitude of the fluctuations:

$$\sigma = \left(\int_0^{\omega rep/2} RIN(\omega) d\omega \right)^{1/2}. \tag{2}$$

We have numerically investigated the RIN in different taper structures, which is illustrated in Fig. 14. Three tapers with a total length of 4 m, but with different up- and downtapering lengths are compared to a uniform fiber. The relatively low input power and short pulse length (FWHM of 3 ps with peak-power of 500 W) compared to the experimental measurements have been used to decrease the computational time. Although this parameter choice disables a direct quantitative comparison between simulations and measurements, the simulations still contribute with valuable information about the intensity noise in MI-initiated supercontinuum, which gives a qualitative agreement with the measurements. Fig. 14 clearly illustrates the effect of tapers and the importance of GAM. As expected, the tapered fibers all have blue edges at shorter wavelengths than the uniform fiber. It is furthermore noticed that both the position and amount of energy in the blue edge depends on the downtapering gradient: decreasing the gradient of the downtaper shifts the blue edge to a shorter wavelength *and* increases the amount of energy in the edge. The trapping process and blueshift of dispersive waves cease at the taper waist, where the group-velocity match to the solitons at the red edge is broken. A longer downtaper allows the solitons to redshift more and hence to blueshift the dispersive waves more. If the most redshifted solitons were limited by the infrared loss edge, the blue edge would be equally blueshifted in all tapers. The amount of blueshifted light

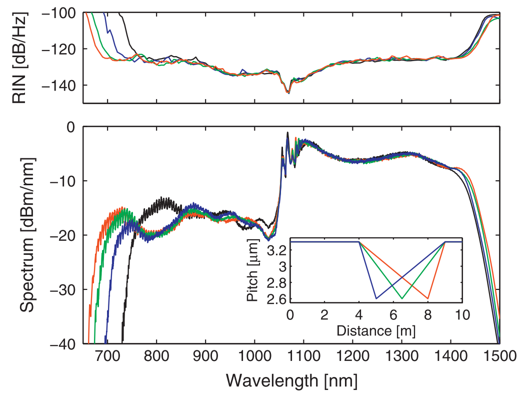

Fig. 14. Simulated output spectra (bottom) and corresponding relative intensity noise (top) for a 10 m uniform fiber (black), and 3 different tapers (blue, green, red) with the profiles shown in the inset. The fibers are pumped with 3 ps (FWHM) pulses with a peak power of 500 W at 1064 nm at a repetition rate of 80 MHz. The spectra are the mean of 1000 simulations. (For interpretation of the references to colour in this figure legend, the reader is referred to the web version of this article.)

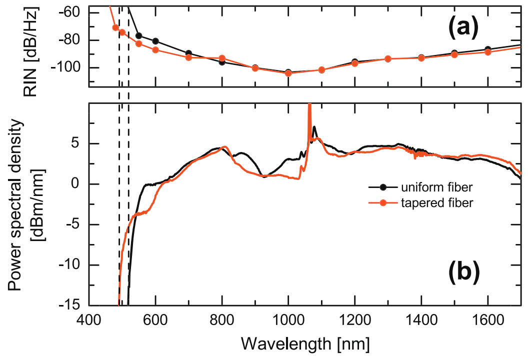

Fig. 15. Measured output spectra (b) and corresponding relative intensity noise (a) for a 10 m uniform fiber (black) and a taper (red) with the profiles shown in Fig. 10. The circles in (a) show the actual measurement points. The fibers are pumped with a peak power of 5 kW. (For interpretation of the references to colour in this figure legend, the reader is referred to the web version of this article.)

can be explained by GAM. In a high-gradient downtaper a larger pool of the dispersive waves will be leaked from the potential trap and left behind compared to a low-gradient downtaper. Thus, fewer dispersive waves will be shifted all the way to the edge.

The RIN illustrated in Fig. 14 is in all cases lowest at the pump wavelength with a value below −140 dB/Hz and it then slightly increases when moving away from the pump wavelength. When not considering the spectral edge regions the RIN is similar for the tapers and the uniform fiber. The RIN is strongly increased at the spectral edges to a level exceeding −100 dB/Hz. This means that for at fixed near-edge wavelength, e.g. at 700 nm, there will be a difference in RIN where a less noisy spectral region can be obtained by choosing the taper with the smallest downtaper gradient. In the case of tapering down to achieve the maximum blueshift of the spectral edge, the noise improvement is however primarily due to the spectral improvement [44].

Fig. 15 shows measurements of a 10 m uniform fiber and a 10 m fiber with a 4 m tapered section (shown in Fig. 10) when pumping with a peak-power of 5 kW. The blue edge from the tapered fiber is blueshifted compared to that of the uniform fiber as expected. Again, the RIN is lowest near the pump wavelength, it increases when moving towards the edge, and it exceeds −75 dB/Hz on the blue side of the spectral edge for both the uniform and the tapered fiber. It is again seen that due to the spectral improvement caused by the taper, the RIN is lower for the tapered fiber compared to the uniform fiber for a fixed near-edge wavelength.

Generally, the measured intensity noise shown in Fig. 15 is higher than the numerical results shown in Fig. 14. However, the pump power is different and the general trend is in the two cases the same: lowest intensity noise at the pump wavelength and a difference in the intensity noise between uniform and tapered fibers at near-edge wavelengths due to the broader spectra from tapered fibers.

To further quantify the dynamics of RIN in tapered fibers we have measured the RIN in the whole parameter space of input power and wavelength, including the region of the silica material loss edge above 2 μm [44]. The RIN as a function of input peak power and wavelength is illustrated in Fig. 16 for both a 10 m uniform fiber and a 10 m fiber containing 4 m tapered fiber (shown in Fig. 10). The thick black line indicates the spectral edges of the generated supercontinuum, defined at the −10 dBm/nm level, and the black dots indicate the actual measurement points The noise properties of the supercontinuum generated in the uniform and tapered

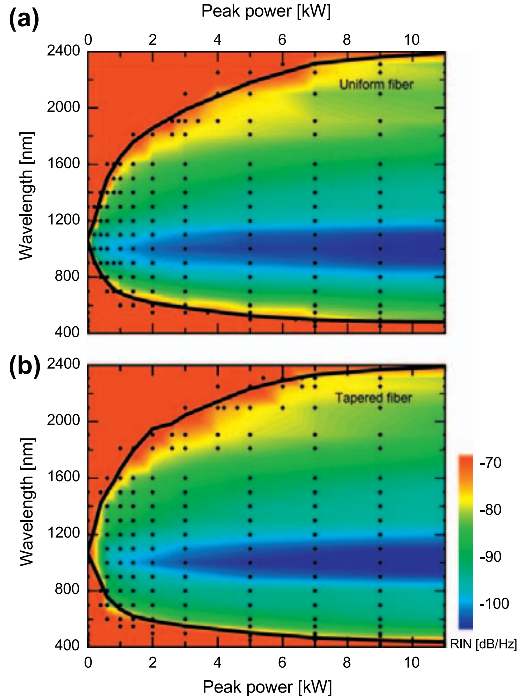

Fig. 16. RIN as a function of input peak-power and wavelength in (a) the uniform fiber and (b) the tapered fiber. The black lines show the spectral edges and the dots show the measurement points.

fibers are similar. At the spectral edge of the supercontinuum the RIN is about −75 dB/Hz corresponding to shot-to-shot fluctuations of ∼112%. Generally, it decreases when the input power is increased (moving horizontally in Fig. 16) or the wavelength is chosen closer to the pump wavelength (moving vertically in Fig. 16). Thus, the minimum noise level of about −105 dB/Hz, corresponding to shot-to-shot fluctuations of ∼3.5%, is observed close to the pump at a wavelength between 1000–1100 nm at the maximum input power level. On the outer sides of the spectral edges the noise increases rapidly.

Both our numerical and experimental results show that the noise will decrease when the fiber is tapered for a *fixed* near-edge wavelength. This is, however, only due to spectral broadening. Thus, looking at a near-edge wavelength *relative* to the spectral edge, e.g. 20 nm from the edge at the −10 dBm/nm level, of a supercontinuum generated in a uniform and a tapered fiber, respectively, will yield the same noise level.

To illustrate the intensity noise *on* the spectral edges we have measured the RIN by adjusting the input power so that the spectral edge at a level of −10 dBm/nm is equivalent to the central wavelength of the narrow band filters. The RIN in the 1600–2400 nm range was not measured due to less well-defined filters and a noisier photoreceiver. Fig. 17 clearly shows that the level of the RIN on the spectral edge at the −10 dBm/nm level is fixed at around −75 dB/Hz. The lower red edge noise level can be explained by the shape of the spectra. At the blue edge the spectrum is steep while it is more flat at the red edge, as seen in Fig. 9. Since we have defined the edge to be at a fixed power level the presence of a finite power spectral density on the outer side of the red edge will lead to

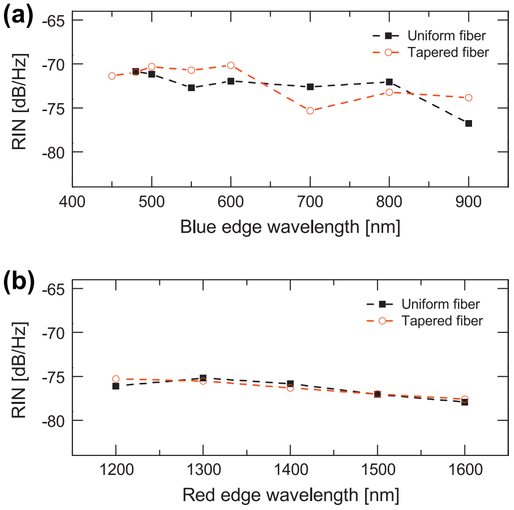

Fig. 17. RIN at the spectral (a) blue and (b) red edge of the uniform and tapered fiber, respectively, as a function of wavelength. (For interpretation of the references to colour in this figure legend, the reader is referred to the web version of this article.)

a reduction of the measured noise compared to the blue edge, where there is no power spectral density on the outer side of the blue edge because of the steep edge. Vanvincq et al. observed a significant reduction of power fluctuations at the long-wavelength edge of a supercontinuum generated in solid-core photonic bandgap fibers due to suppression of soliton self-frequency shift near the bandgap edge [79]. The dispersive waves below 550 nm in Fig. 17a will be matched to solitons above 2000 nm, i.e. solitons in the material loss region. Since we observe a nearly constant RIN in the blue edge, the materiel loss edge is thus not affecting the RIN of the dispersive waves GVD matched to solitons in the loss region.

6. Conclusion

High-power fiber lasers combined with tailored photonic crystal fibers provide efficient and compact supercontinuum sources spanning from the deep-blue to the near infrared, and tapering of these photonic crystal fibers is an effective way to blueshift the visible part of the spectrum. The degree of blueshift depends on the tapering degree, which can be optimized by calculating the blue wavelength edge based on the group-velocity of solitons and their group-velocity matched dispersive waves. The mechanism of trapped and group-velocity matched dispersive waves responsible for the formation of the blue edge is now well understood and has been demonstrated to be accurately predicted. Thus, group-velocity matching is an efficient fiber design tool. To optimize the power in the blue edge the downtapering length of the taper should be as long as possible to minimize the group-acceleration mismatch between the solitons and their group-velocity matched dispersive waves.

For the investigated PCF structure, which allows single-mode operation at 1064 nm, the blue edge of the output spectrum was blueshifted by 35 nm by tapering the fiber down to 75% of its original diameter. The highest amount of blueshifted light is achieved for tapers with the longest down tapering length. For the longest investigated taper 78.8 mW was shifted below the blue edge of the uniform fiber. A blue edge below 350 nm can be achieved in PCFs with a large d/Λ, and the maximum blueshift is obtained by tapering to a pitch of 1.8–2 μm. To achieve this pitch, a tapering degree of more that 50% will typically be required, but these fibers will however be multi-moded at a pump wavelength of 1064 nm.

A higher power in the blue edge is achieved with long tapers. However, fiber lengths of more than 10–15 m will cause temporal walk-off, which in practice limits the total fiber length to about 10 m for commercial applications. Excellent reproducibility of tower-drawn tapers can now be achieved, also for tapering degrees exceeding 50%.

Since tapering influences the spectral width of the supercontinuum it also has an influence on the noise properties. When observing a fixed wavelength near the spectral edge in a 10 nm bandwidth the noise is reduced in a tapered fiber due to the spectral broadening. The noise at the spectral edge of a supercontinuum is however constant independent of input power for both tapered and uniform fibers. An increase of power will generally lead to a decrease of noise for a fixed wavelength and the noise for a fixed power level will be lowest at the pump wavelength and highest at the spectral edges.

Acknowledgment

The authors acknowledge the Danish Agency for Science, Technology and Innovation for the financial support of Project No. 09-070566.

References

[1] R. Alfano, S. Shapiro, Observation of self-phase modulation and small-scale filaments in crystals and glasses, Phys. Rev. Lett. 24 (1970) 592–594.
[2] C. Lin, R.H. Stolen, New nanosecond continuum for excited-state spectroscopy, Appl. Phys. Lett. 28 (1976) 216–218.
[3] J.C. Knight, T.A. Birks, P.S.J. Russell, D.M. Atkin, All-silica single-mode optical fiber with photonic crystal cladding, Opt. Lett. 21 (1996) 1547–1549.
[4] J.K. Ranka, R.S. Windeler, A.J. Stentz, Visible continuum generation in air-silica microstructure optical fibers with anomalous dispersion at 800 nm, Opt. Lett. 25 (2000) 25–27.
[5] N. Savage, Supercontinuum sources, Nat. Photonics 3 (2009) 114–115.
[6] M.N. Islam, G. Sucha, I. Bar-Joseph, M. Wegener, J.P. Gordon, D.S. Chemla, Femtosecond distributed soliton spectrum in fibers, J. Opt. Soc. Am. B 6 (1989) 1149–1158.
[7] J.M. Dudley, G. Genty, F. Dias, B. Kibler, N. Akhmediev, Modulation instability, Akhmediev breathers and continuous wave supercontinuum generation, Opt. Express 17 (2009) 21497–21508.
[8] P.K.A. Wai, H.H. Chen, Y.C. Lee, Radiations by solitons at the zero group-dispersion wavelength of single-mode optical fibers, Phys. Rev. A 41 (1990) 426–439.
[9] F.M. Mitschke, L.F. Mollenauer, Discovery of the soliton self-frequency shift, Opt. Lett. 11 (1986) 659–661.
[10] J.P. Gordon, Theory of the soliton self-frequency shift, Opt. Lett. 11 (1986) 662–664.
[11] A. Judge, O. Bang, B. Eggleton, B. Kuhlmey, E. Mägi, R. Pant, C. de Sterke, Optimization of the soliton self-frequency shift in a tapered photonic crystal fiber, J. Opt. Soc. Am. B 26 (2009) 2064–2071.
[12] A.C. Judge, O. Bang, C. Martijn de Sterke, Theory of dispersive wave frequency shift via trapping by a soliton in an axially nonuniform optical fiber, J. Opt. Soc. Am. B 27 (2010) 2195–2202.
[13] P. Beaud, W. Hodel, B. Zysset, H. Weber, Ultrashort pulse propagation, pulse breakup, and fundamental soliton formation in a single-mode optical fiber, IEEE J. Quantum Elect. 23 (1987) 1938–1946.
[14] A.V. Gorbach, D.V. Skryabin, Light trapping in gravity-like potentials and expansion of supercontinuum spectra in photonic-crystal fibres, Nat. Photonics 1 (2007) 653–657.
[15] M.H. Frosz, O. Bang, A. Bjarklev, Soliton collision and Raman gain regimes in continuous-wave pumped supercontinuum generation, Opt. Express 14 (2006) 9391–9407.
[16] J.M. Dudley, G. Genty, B.J. Eggleton, Harnessing and control of optical rogue waves in supercontinuum generation, Opt. Express 16 (2008) 3644–3651.
[17] D.R. Solli, C. Ropers, P. Koonath, B. Jalali, Optical rogue waves, Nature 450 (2007) 1054–1057.
[18] D.R. Solli, C. Ropers, B. Jalali, Active control of rogue waves for stimulated supercontinuum generation, Phys. Rev. Lett. 101 (2008) 18–21.
[19] N. Akhmediev, J.M. Soto-Crespo, A. Ankiewicz, Extreme waves that appear from nowhere: on the nature of rogue waves, Phys. Lett. A 373 (2009) 2137–2145.

[20] N. Akhmediev, A. Ankiewicz, M. Taki, Waves that appear from nowhere and disappear without a trace, Phys. Lett. A 373 (2009) 675–678.
[21] M. Erkintalo, G. Genty, J.M. Dudley, On the statistical interpretation of optical rogue waves, Eur. Phys. J. – Spec. Top. 185 (2010) 135–144.
[22] R.F. Cregan, B.J. Mangan, J.C. Knight, T.A. Birks, P.S.J. Russell, P.J. Roberts, D.C. Allan, Single-mode photonic band gap guidance of light in air, Science 285 (1999) 1537–1539.
[23] T.A. Birks, J.C. Knight, P.S.J. Russell, Endlessly single-mode photonic crystal fiber, Opt. Lett. 22 (1997) 961–963.
[24] I. Hartl, X.D. Li, C. Chudoba, R.K. Ghanta, T.H. Ko, J.G. Fujimoto, J.K. Ranka, R.S. Windeler, Ultrahigh-resolution optical coherence tomography using continuum generation in an air-silica microstructure optical fiber, Opt. Lett. 26 (2001) 608–610.
[25] P. Cimalla, J. Walther, M. Mehner, M. Cuevas, E. Koch, Simultaneous dual-band optical coherence tomography in the spectral domain for high resolution in vivo imaging, Opt. Express 17 (2009) 19486–19500.
[26] A. Diaspro, Confocal and two-photon microscopy: foundations, applications, and advances, Wiley-Liss, 2002.
[27] J.R. Silvius, I.R. Nabi, Fluorescence-quenching and resonance energy transfer studies of lipid microdomains in model and biological membranes (review), Mol. Membr. Biol. 23 (2006) 5–16.
[28] Y. Sun, C.F. Booker, S. Kumari, R.N. Day, M. Davidson, A. Periasamy, Characterization of an orange acceptor fluorescent protein for sensitized spectral fluorescence resonance energy transfer microscopy using a white-light laser, J. Biomed. Opt. 14 (2009) 054009.
[29] C.-W. Chang, D. Sud, M.-A. Mycek, Fluorescence lifetime imaging microscopy, in: G. Sluder, D.E. Wolf (Eds.), Digital Microscopy, Methods in Cell Biology, third ed., vol. 81, Academic Press, 2007, pp. 495–524.
[30] T.A. Birks, W.J. Wadsworth, P.S.J. Russell, Supercontinuum generation in tapered fibers, Opt. Lett. 25 (2000) 1415–1417.
[31] S. Leon-Saval, T.A. Birks, W.J. Wadsworth, P.S.J. Russell, M. Mason, Supercontinuum generation in submicron fibre waveguides, Opt. Express 12 (2004) 2864–2869.
[32] F. Lu, Y. Deng, W.H. Knox, Generation of broadband femtosecond visible pulses in dispersion-micromanaged holey fibers, Opt. Lett. 30 (2005) 1566–1568.
[33] S. Pricking, H. Giessen, Tailoring the soliton and supercontinuum dynamics by engineering the profile of tapered fibers, Opt. Express 18 (2010) 20151–20163.
[34] A. Kudlinski, A.K. George, J.C. Knight, J.C. Travers, A.B. Rulkov, S.V. Popov, J.R. Taylor, Zero-dispersion wavelength decreasing photonic crystal fibers for ultraviolet-extended supercontinuum generation, Opt. Express 14 (2006) 5715–5722.
[35] J.C. Travers, Blue extension of optical fibre supercontinuum generation, J. Opt. 12 (2010) 113001.
[36] S.T. Sørensen, A.C. Judge, C.L. Thomsen, O. Bang, Optimum fiber tapers for increasing the power in the blue edge of a supercontinuum-group-acceleration matching, Opt. Lett. 36 (2011) 816–818.
[37] A. Kudlinski, M. Lelek, B. Barviau, L. Audry, A. Mussot, Efficient blue conversion from a 1064 nm microchip laser in long photonic crystal fiber tapers for fluorescence microscopy, Opt. Express 18 (2010) 16640–16645.
[38] J.C. Travers, J.R. Taylor, Soliton trapping of dispersive waves in tapered optical fibers, Opt. Lett. 34 (2009) 115–117.
[39] S.T. Sørensen, U. Møller, C. Larsen, P.M. Moselund, C. Jacobsen, J. Johansen, T.V. Andersen, C.L. Thomsen, O. Bang, Deep-blue supercontinuum sources with optimum taper profiles – verification of GAM, Opt. Express 20 (2012) 10635–10645.
[40] S.P. Stark, J.C. Travers, P.S.J. Russell, Extreme supercontinuum generation to the deep UV, Opt. Lett. 37 (2012) 770–772.
[41] A. Avdokhin, S. Popov, J. Taylor, Continuous-wave, high-power, Raman continuum generation in holey fibers, Opt. Lett. 28 (2003) 1353–1355.
[42] C. Larsen, D. Noordegraaf, P.M.W. Skovgaard, K.P. Hansen, K.E. Mattsson, O. Bang, Gain-switched CW fiber laser for improved supercontinuum generation in a PCF, Opt. Express 19 (2011) 14883–14891.
[43] J.M. Dudley, G. Genty, S. Coen, Supercontinuum generation in photonic crystal fiber, Rev. Mod. Phys. 78 (2006) 1135–1184.
[44] U. Møller, S.T. Sørensen, C. Jakobsen, J. Johansen, P.M. Moselund, C. Thomsen, O. Bang, Power dependence of supercontinuum noise in uniform and tapered PCFs, Opt. Express 20 (2012) 2851–2858. Please notice that the RIN measurements presented here are 26 dB higher than those in [44], where an error was made when calculating the RIN. The DC transimpedance gain of the New Focus photodetectors was mistakenly specified by the manufacturer to be $G_{DC} = 1$ V/mA. The correct DC transimpedance gain is $G_{DC} = 10$ V/mA for an input impedance of 50Ω and $G_{DC} = 20$ V/mA for an infinite input impedance. The AC transimpedance gain is as specified $G_{DC} = 40$ V/mA. These values have been measured and confirmed by the manufacturer. Since the relative intensity noise (RIN) is proportional to $[G_{DC}/G_{AC}]^2$ the RIN is increased by a factor of 400 corresponding to 26 dB.
[45] G. Genty, J.M. Dudley, B.J. Eggleton, Modulation control and spectral shaping of optical fiber supercontinuum generation in the picosecond regime, Appl. Phy. B – Lasers O. 94 (2008) 187–194.
[46] K.K.Y. Cheung, C. Zhang, Y. Zhou, K.K.Y. Wong, K.K. Tsia, Manipulating supercontinuum generation by minute continuous wave, Opt. Lett. 36 (2011) 160–162.
[47] Q. Li, F. Li, K.K.Y. Wong, A. Pak, T. Lau, K.K. Tsia, Investigating the influence of a weak continuous-wave-trigger on picosecond supercontinuum generation, Opt. Express 19 (2011) 377–381.
[48] V. Tombelaine, P. Leproux, V. Couderc, A. Barthlmy, Visible supercontinuum generation in holey fibers by dual-wavelength subnanosecond pumping, IEEE Photon. Technol. Lett. 18 (2006) 2466–2468.
[49] P.M. Moselund, M.H. Frosz, C.L. Thomsen, O. Bang, Back-seeding of higher order gain processes in picosecond supercontinuum generation, Opt. Express 16 (2008) 11954–11968.
[50] X. Gu, M. Kimmel, A. Shreenath, R. Trebino, J.M. Dudley, S. Coen, R. Windeler, Experimental studies of the coherence of microstructure-fiber supercontinuum, Opt. Express 11 (2003) 2697–2703.
[51] M.H. Frosz, Validation of input-noise model for simulations of supercontinuum generation and rogue waves, Opt. Express 18 (2010) 14778–14787.
[52] C. Agger, C. Petersen, S. Dupont, H. Steffensen, J.K. Lyngsø, C.L. Thomsen, J. Thøgersen, S.R. Keiding, O. Bang, Supercontinuum generation in ZBLAN fibers – detailed comparison between measurement and simulation, J. Opt. Soc. Am. B 29 (2012) 635–645.
[53] J. Lægsgaard, Mode profile dispersion in the generalised nonlinear Schrödinger equation, Opt. Express 15 (2007) 16110–16123.
[54] J. Hult, A fourth-order Runge–Kutta in the interaction picture method for simulating supercontinuum generation in optical fibers, J. Lightwave Technol. 25 (2007) 3770–3775.
[55] K.L. Corwin, N.R. Newbury, J.M. Dudley, S. Coen, S.a. Diddams, K. Weber, R.S. Windeler, Fundamental noise limitations to supercontinuum generation in microstructure fiber, Phys. Rev. Lett. 90 (2003) 113904.
[56] M. Koshiba, K. Saitoh, Applicability of classical optical fiber theories to holey fibers, Opt. Lett. 29 (2004) 1739–1741.
[57] M. Liao, W. Gao, Z. Duan, X. Yan, T. Suzuki, Y. Ohishi, Directly draw highly nonlinear tellurite microstructured fiber with diameter varying sharply in a short fiber length, Opt. Express 20 (2012) 1141–1150.
[58] N. Vukovic, N.G.R. Broderick, M. Petrovich, G. Brambilla, Novel method for the fabrication of long optical fiber tapers, IEEE Photonic. Technol. Lett. 20 (2008) 1264–1266.
[59] J.M. Stone, J.C. Knight, Visibly white light generation in uniform photonic crystal fiber using a microchip laser, Opt. Express 16 (2008) 2670–2675.
[60] D.V. Skryabin, F. Luan, J.C. Knight, P.S.J. Russell, Soliton self-frequency shift cancellation in photonic crystal fibers, Science 301 (2003) 1705–1708.
[61] P. Falk, M.H. Frosz, O. Bang, L. Thrane, P.E. Andersen, A.O. Bjarklev, K.P. Hansen, J. Broeng, Broadband light generation at approximately 1300 nm through spectrally recoiled solitons and dispersive waves, Opt. Lett. 33 (2008) 621–623.
[62] P. Dumais, F. Gonthier, S. Lacroix, J. Bures, A. Villeneuve, P. Wigley, G. Stegeman, Enhanced self-phase modulation in tapered fibers, Opt. Lett. 18 (1993) 1996–1998.
[63] X. Liu, C. Xu, W.H. Knox, J.K. Chandalia, B.J. Eggleton, S.G. Kosinski, R.S. Windeler, Soliton self-frequency shift in a short tapered air-silica microstructure fiber, Opt. Lett. 26 (2001) 358–360.
[64] W.J. Wadsworth, A. Ortigosa-Blanch, J.C. Knight, T.a. Birks, T.-P.M. Man, P.S.J. Russell, Supercontinuum generation in photonic crystal fibers and optical fiber tapers: a novel light source, J. Opt. Soc. Am. B 19 (2002) 2148–2155.
[65] M. Foster, A. Gaeta, Ultra-low threshold supercontinuum generation in sub-wavelength waveguides, Opt. Express 12 (2004) 3137–3143.
[66] P. Falk, M.H. Frosz, O. Bang, Supercontinuum generation in a photonic crystal fiber with two zero-dispersion wavelengths tapered to normal dispersion at all wavelengths, Opt. Express 13 (2005) 7535–7540.
[67] P.M. Moselund, Long-pulse Supercontinuum Light Sources, Ph.D. thesis, Technical University of Denmark, Denmark, 2009.
[68] D. Richardson, R. Chamberlin, L. Dong, High quality soliton loss-compensation in 38 km dispersion-decreasing fibre, Electron. Lett. 31 (1995) 1681–1682.
[69] A.V. Gorbach, D.V. Skryabin, Theory of radiation trapping by the accelerating solitons in optical fibers, Phys. Rev. A 76 (2007) 053803.
[70] A.V. Gorbach, D.V. Skryabin, J.M. Stone, J.C. Knight, Four-wave mixing of solitons with radiation and quasi-nondispersive wave packets at the short-wavelength edge of a supercontinuum, Opt. Express 14 (2006) 9854–9863.
[71] D. Buccoliero, H. Steffensen, H. Ebendorff-Heidepriem, T.M. Monro, O. Bang, Midinfrared optical rogue waves in soft glass photonic crystal fiber, Opt. Express 19 (2011) 17973–17978.
[72] S. Perkins, Dashing rogues, Sci. News 170 (2006) 328–329.
[73] O. Bang, M. Peyrard, Generation of high-energy localized vibrational modes in nonlinear Klein-Gordon lattices, Phys. Rev. E 53 (1996) 4143–4152.
[74] A.N. Ganshin, V.B. Efimov, G.V. Kolmakov, L.P. Mezhov-Deglin, P.V.E. McClintock, Energy cascades and rogue waves in superfluid 4 He, J. Phys. Conf. Ser. 150 (2009) 032056.
[75] L. Stenflo, M. Marklund, Rogue waves in the atmosphere, J. Plasma Phys. 76 (2010) 293–295.
[76] Z. Yan, Vector financial rogue waves, Phys. Lett. A 375 (2011) 4274–4279.
[77] S.T. Sørensen, O. Bang, B. Wetzel, J.M. Dudley, Describing supercontinuum noise and rogue wave statistics using higher-order moments, Opt. Commun. 285 (2012) 2451–2455.
[78] A. Kudlinski, B. Barviau, A. Leray, C. Spriet, L. Héliot, A. Mussot, Control of pulse-to-pulse fluctuations in visible supercontinuum, Opt. Express 18 (2010) 27445–27454.
[79] O. Vanvincq, B. Barviau, A. Mussot, G. Bouwmans, Y. Quiquempois, A. Kudlinski, Significant reduction of power fluctuations at the long-wavelength edge of a supercontinuum generated in solid-core photonic bandgap fibers, Opt. Express 18 (2010) 24352–24360.

Paper IV

Single-mode high air-fill fraction photonic crystal fiber for high-power deep-blue supercontinuum sources

S. T. Sørensen, C. Larsen, C. Jakobsen, C. L. Thomsen, and O. Bang
Submitted to Opt. Lett. 29 April 2013

Abstract: Dispersion control with axially nonuniform photonic crystal fibers (PCFs) permits supercontinuum (SC) generation into the deep-blue from an ytterbium pump laser. In this letter, we exploit the full degrees of freedom afforded by PCFs to fabricate a fiber with longitudinally increasing air-fill fraction and decreasing diameter directly at the draw-tower. We demonstrate SC generation extending down to 375 nm in one such monolithic fiber device that is single-mode at 1064 nm at the input end.

Single-mode high air-fill fraction photonic crystal fiber for high-power deep-blue supercontinuum sources

Simon T. Sørensen[1], **Casper Larsen**[1,2], **Christian Jakobsen**[2], **Carsten L. Thomsen**[2] **and Ole Bang**[1,2,*]

[1]*DTU Fotonik, Department of Photonics Engineering, Technical University of Denmark, 2800 Kgs. Lyngby, Denmark*

[2]*NKT Photonics A/S, Blokken 84, DK-3460, Birkerød, Denmark*

[*]*Corresponding author: oban@fotonik.dtu.dk*

Compiled April 29, 2013

Dispersion control with axially nonuniform photonic crystal fibers (PCFs) permits supercontinuum (SC) generation into the deep-blue from an ytterbium pump laser. In this letter, we exploit the full degrees of freedom afforded by PCFs to fabricate a fiber with longitudinally increasing air-fill fraction and decreasing diameter directly at the draw-tower. We demonstrate SC generation extending down to 375 nm in one such monolithic fiber device that is single-mode at 1064 nm at the input end.

OCIS codes: 060.4370, 060.5295, 320.6629.

The formation of extremely broad SC spectra in highly nonlinear optical fibers has been extensively studied, driven both by an interest in understanding the underlying physics and due to a large commercial potential [1]. A considerable ongoing effort has been devoted to extend the SC into the infrared in non-silica glasses [2–5] and into the deep-blue in tapered silica PCFs [6–11]. Specifically, the deep-blue spectral region below 400 nm is highly desirable for biological applications such as fluorescent microscopy [6], but not immediately accessible with typical commercial SC sources based on long-pulsed ytterbium fiber-lasers with 10s of kW of peak power. In such sources, the spectral broadening is initiated by noise-driven modulation instability (MI) that breaks the pump pulse into a distributed spectrum of solitons and dispersive waves (DWs) [12]. The SC spectrum is subsequently shaped by a complex process in which the Raman redshifting solitons trap the cohort of DWs, thereby forcing them to blueshift so as to propagate with the group velocity (GV) of the redshifting solitons [13, 14]. Ultimately, the spectral width is determined, on the long wavelength "red" side, by the maximum extent of the soliton redshift and, on the short wavelength "blue" side, by the GV matching to the solitons. The soliton redshift typically is limited by the increasing material loss at ∼2.3 μm and the blue SC edge can then be predicted by the GV match from this wavelength [7, 9].

Tapering of PCFs with high air-fill fractions has proven an effective way of extending the spectra into the deep-blue by shaping the GV landscape [6–11]. This facilitates the ideal combination of (1) an initial fiber section to initiate the spectral broadening by MI in the vicinity of the zero-dispersion wavelength (ZDW) with an efficient energy transfer into the visible, and (2) a subsequent fiber section with GV matching to gradually shorter wavelengths. Previous reports on blue-extended SC generation typically relied on tapered PCFs where the air hole structure is preserved [6–11], i.e. with constant hole-to-pitch ratio (d/Λ) and decreasing hole-to-hole pitch (Λ). However, high air-fill fraction PCFs are inevitably (highly) multi-mode at the pump, which can greatly complicate coupling and interfacing. In [15, 16] this was overcome by increasing the air hole size in a short section of an endlessly single-mode PCF using a post processing technique, but only to enhance the visible power. In this letter, we present the first high-power SC generation into the deep-blue in a single-mode PCF with longitudinally increasing air-fill fraction *and* decreasing pitch fabricated directly at the draw-tower. This uniquely ensures single-mode behavior at the input and GV matching into the deep-blue at the output.

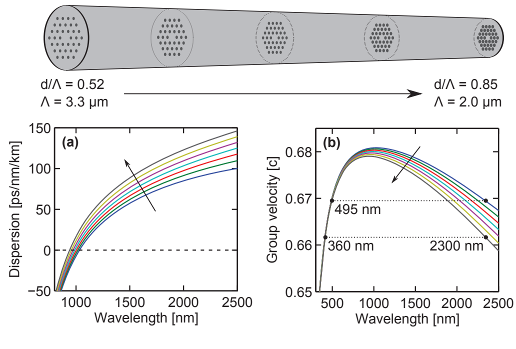

Fig. 1. (Color online) Calculated (a) dispersion and (b) GV for the illustrated hole-size increasing PCF taper. The hole-to-pitch ratio d/Λ and pitch Λ are assumed to vary linearly with length, and the dispersion and GV are calculated at equidistant points.

To motivate our fiber design, we show in Fig. 1 the calculated dispersion and GV at equidistant points along the length of a PCF, in which the hole-to-pitch ratio is linearly increased from 0.52 to 0.85 while the pitch is linearly decreased from 3.3 to 2.0 μm. The final structure with a hole-to-pitch ratio of 0.85 and a pitch of 2.0 μm is our target design, for which GV matching to the loss edge of 2.3 μm gives a theoretical blue edge of 360 nm [7, 9]. Figure 1 shows that the ZDW shifts from 1033 nm at the input to gradually shorter wavelengths. The GV decreases at long wavelengths where waveguide dispersion dominates over material dispersion, which gives GV matching to gradually shorter wavelengths from these long wavelengths. It should be noted that a continually decreasing GV is essential for the trapping process, although a too rapid decrease can be detrimental due to group-acceleration mismatch (GAM) [8,9,14,17]. Importantly, the trends in Fig. 1 are exactly as for tapered PCFs with a constant hole-to-pitch ratio and the conclusions from e.g. [7–9, 17] are therefore directly applicable here. We chose the particular fiber parameters in Fig. 1 to give the optimum conditions in both ends of the fiber: at the input end, the low air-fill fraction and large core makes the PCF single-mode at 1064 nm [18] and gives a ZDW near the pump, while at the output end, the high air-fill fraction and small pitch ensures GV matching from the loss edge at 2.3 μm into the deep-blue at 360 nm. This is more than a 100 nm shorter than what can be achieved in a PCF with the hole-to-pitch ratio and pitch of the input end, as illustrated in Fig. 1.

PCFs can be tapered with high accuracy during the fiber draw by controlling the draw speed [9–11]. However, increasing the air-fill fraction necessitates an additional control of the pressure on the air holes during fabrication. Left isolated, we found that increasing the air hole pressure leads to an undesirable increase in the pitch. It was thus necessary to control simultaneously the pressure and draw speed to achieve the desired structure with increasing hole-to-pitch ratio and decreasing pitch. The fiber structure realized after a number of iterative fiber drawings is shown in Fig. 2: the hole-to-pitch ratio increases from 0.52 to 0.85 over 7 m, while the pitch decreases from 3.3 to 2.15 μm. This is very close to the targeted hole-to-pitch ratio of 0.85 and pitch of 2.0 μm, albeit a slightly too large pitch. Indeed, the hexagonal structure is well preserved during the air hole expansion without introducing any structural defects. This highlights the amazing design freedom in PCFs and clearly verifies the feasibility of our design.

To investigate the PCF's applicability for SC generation, we pumped the fiber with a 1064 nm Yb fiber-laser typical of many SC experiments emitting 10 ps pulses at 15 W average power and 80 MHz repetition rate. The PCF was spliced directly to the fiber-laser using a filament splicer, resulting in a coupling loss of approximately 1.2 dB. We kept an initial 40 cm length of uniform fiber to initiate the spectral broadening. The generated spectrum recorded with an optical spectrum analyzer and an integrating sphere is shown in Fig. 3: The SC spectrum indeed extends into the deep-blue with a spectral density above 0.5 mW/nm in most of the visible bandwidth. The spectrum had a total power of 5.8 W with 734 mW in the visible part below 900 nm and extends down to 375 nm; the spectral intensity measured below this wavelength is due to stray light.

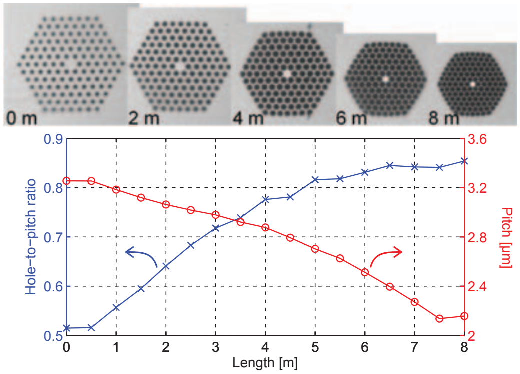

Fig. 2. (Color online) Characterization of the fiber structure: the top row shows microscope images of the fiber end facet at selected distances from the input (on the same scale) and the plot shows the corresponding hole-to-pitch ratio and pitch calculated from 17 images equidistantly spaced along the 8 m fiber.

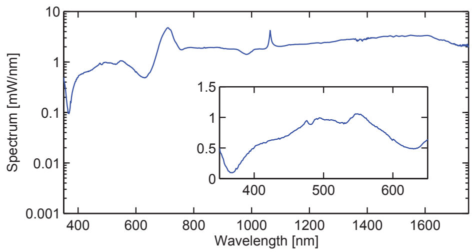

Fig. 3. (Color online) Measured SC spectrum. The inset shows a close up of the spectral blue edge on a linear scale. The total output power was 5.8 W with 734 mW in the visible part of the spectrum below 900 nm.

The discrepancy between the measured spectral blue edge at 375 nm and the theoretical target at 360 nm can be understood by investigating the fiber structure in more detail: a closer inspection of the fiber structure reveals that the innermost air holes are elongated due to the air hole expansion (see insets in Fig. 4). An ideal hexagonal PCF with a 0.85 hole-to-pitch ratio and 2.0 μm pitch has a core diameter of approximately $\Lambda(2 - d/\Lambda) \approx 2.3$ μm, whereas the core diameter of our PCF is approximately 1.8 μm measured from the microscope images. This core size corresponds to an effective pitch of 1.6 μm. To verify this approximation, we show in Fig. 4 the measured dispersion (thick lines) at the input and output end of the fiber together with the calculated dispersion (thin lines) for the input ($d/\Lambda = 0.52$, $\Lambda = 3.3$ μm) and the ideal ($d/\Lambda = 0.85$, $\Lambda = 2.0$ μm) and effective ($d/\Lambda = 0.85$, $\Lambda = 1.6$ μm) output parameters. The dispersion was measured in 8 cm lengths of fiber with a low coherence Mach-Zender interferometer in the frequency domain, and is shown in individually measured 100 nm bandwidths. The results in Fig. 4 show an excellent agreement between experiment and theory at the input and output, which verifies that the output end is well described by an effective pitch of 1.6 μm. Moreover, this effective pitch gives a theoretical GV matched blue edge of 370 nm in fair agreement with the measured spectrum.

We emphasize that the fiber parameters in Fig. 1 are calculated over the entire PCF structure. The structure only deviates from an ideal hexagonal structure in the innermost air holes for high air-fill fractions, where the extreme air hole expansion causes perturbations to the air-silica matrix. We believe this can be mitigated with a slower air hole expansion by e.g. decreasing the draw speed or by using a cane designed for a higher air-fill fraction. Nonetheless, our results clearly demonstrate the applicability of air-fill fraction increasing PCFs for single-mode pumped deep-blue SC generation.

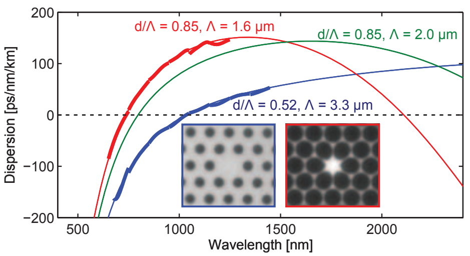

Fig. 4. (Color online) Measured dispersion (thick lines) at the input and output of the PCF in Fig. 2, and corresponding calculated dispersion (thin lines) for PCFs with the values of the hole-to-pitch ratio d/Λ and pitch Λ stated in the plot. The insets show a close up of the fiber structure around the core at the input (left) and output (right) end.

To conclude, we fabricated the first single-mode high air-fill fraction PCF directly on the draw-tower and demonstrated SC generation extending down to 375 nm from a 1064 nm pump. The PCF was designed with increasing hole-to-pitch ratio and decreasing pitch, which permits single-mode operation at the pump wavelength at the input and a GV match into the deep-blue at the output. This unique combination makes our air-fill fraction increasing PCF a very promising candidate for high-power deep-blue SC sources.

We would like to thank J. K. Lyngsø for help with the dispersion measurements and the Danish Agency for Science, Technology and Innovation for support of the project no. 09-070566.

References

1. J. M. Dudley, G. Genty, and S. Coen, Rev. Mod. Phys. **78**, 1135 (2006).
2. C. Xia, M. Kumar, O. P. Kulkarni, M. N. Islam, F. L. Terry, M. J. Freeman, M. Poulain, and G. Mazé, Opt. Lett. **31**, 2553 (2006).
3. G. Qin, X. Yan, C. Kito, M. Liao, C. Chaudhari, T. Suzuki, and Y. Ohishi, Appl. Phys. Lett. **95**, 161103 (2009).
4. C. Agger, C. Petersen, S. Dupont, H. Steffensen, J. K. Lyngsø, C. L. Thomsen, J. Thøgersen, S. R. Keiding, and O. Bang, J. Opt. Soc. Am. B **29**, 635 (2012).
5. C. L. Thomsen, F. D. Nielsen, J. Johansen, P. M. Moselund, U. Møller, S. T. Sørensen, C. Larsen, and O. Bang, Proc. SPIE **8637**, 86370T (2013).
6. A. Kudlinski, M. Lelek, B. Barviau, L. Audry, and A. Mussot, Opt. Express **18**, 16640 (2010).
7. J. C. Travers, J. Opt. **12**, 113001 (2010).
8. S. T. Sørensen, A. Judge, C. L. Thomsen, and O. Bang, Opt. Lett. **36**, 816 (2011).
9. S. T. Sørensen, U. Møller, C. Larsen, P. M. Moselund, C. Jakobsen, J. Johansen, T. V. Andersen, C. L. Thomsen, and O. Bang, Opt. Express **20**, 10635 (2012).
10. U. Møller, S. T. Sørensen, C. Larsen, P. M. Moselund, C. Jakobsen, J. Johansen, C. L. Thomsen, and O. Bang, Opt. Fiber Technol. **18**, 304174 (2012).
11. J. Stone and J. Knight, Opt. Fiber Technol. **18**, 315 (2012).
12. M. Islam, G. Sucha, and I. Bar-Joseph, J. Opt. Soc. Am. B **6**, 1149 (1989).
13. P. Beaud, W. Hodel, B. Zysset, and H. P. Weber, IEEE J. Quantum Electron. **QE-23**, 1938 (1987).
14. A. V. Gorbach and D. V. Skryabin, Nat. Photon. **1**, 653 (2007).
15. W. Wadsworth, A. Witkowska, S. Leon-Saval, and T. Birks, Opt. Express **13**, 6541 (2005).
16. C. Xiong, A. Witkowska, S. G. Leon-Saval, T. A. Birks, and W. J. Wadsworth, Opt. Express **14**, 6188 (2006).
17. J. C. Travers and J. R. Taylor, Opt. Lett. **34**, 115 (2009).
18. M. Koshiba and K. Saitoh, Opt. Lett. **29**, 1739 (2004).

Paper V

Describing supercontinuum noise and rogue wave statistics using higher-order moments

S. T. Sørensen, O. Bang, B. Wetzel, J. M. Dudley
Opt. Comm. **285**, 2451-2455 (2012).

Abstract: We show that the noise properties of fiber supercontinuum generation and the appearance of long-tailed rogue wave statistics can be accurately quantified using statistical higher-order central moments. Statistical measures of skew and kurtosis, as well as the coefficient of variation provide improved insight into the nature of spectral fluctuations across the supercontinuum and allow regions of long-tailed statistics to be clearly identified. These moments that depend only on analyzing intensity fluctuations provide a complementary tool to phase-dependent coherence measures to interpret supercontinuum noise.

`http://dx.doi.org/10.1016/j.optcom.2012.01.030`

Optics Communications 285 (2012) 2451–2455

Contents lists available at SciVerse ScienceDirect

Optics Communications

journal homepage: www.elsevier.com/locate/optcom

Describing supercontinuum noise and rogue wave statistics using higher-order moments

Simon Toft Sørensen [a,*], Ole Bang [a], Benjamin Wetzel [b], John M. Dudley [b]

[a] DTU Fotonik, Department of Photonics Engineering, Technical University of Denmark, 2800 Kgs. Lyngby, Denmark
[b] Institut FEMTO-ST, UMR 6174 CNRS-Université de Franche-Comté, 25030 Besançon, France

ARTICLE INFO

Article history:
Received 13 December 2011
Received in revised form 14 January 2012
Accepted 16 January 2012
Available online 30 January 2012

Keywords:
Supercontinuum generation
Higher-order central moments
Rogue waves
Extreme events
Spectral coherence

ABSTRACT

We show that the noise properties of fiber supercontinuum generation and the appearance of long-tailed "rogue wave" statistics can be accurately quantified using statistical higher-order central moments. Statistical measures of skew and kurtosis, as well as the coefficient of variation provide improved insight into the nature of spectral fluctuations across the supercontinuum and allow regions of long-tailed statistics to be clearly identified. These moments – that depend only on analyzing intensity fluctuations – provide a complementary tool to phase-dependent coherence measures to interpret supercontinuum noise.

1. Introduction

There is currently intense research into the noise properties of fiber supercontinuum (SC) generation, motivated both by application demands for low noise broadband sources as well as in the fundamental context of clarifying links with instabilities in other systems [1]. The fluctuation properties of SC generation were initially studied using radio-frequency and coherence based techniques [2,3], but a new technique was introduced in 2007 by Solli et al., who showed that the direct measurement of pulse height histograms at particular wavelengths in the SC spectrum was a powerful technique to reveal long-tailed statistics on the SC long wavelength edge [4]. This allowed a statistical verification of the early observation of Islam et al. [5], that high-intensity solitons in the red SC edge appeared as rare events, not present in each pulse. Such a high-intensity strongly redshifted soliton was also observed numerically as a result of soliton-collision in continuous wave SC generation [6]. The measurement of Solli et al. of long-tailed histograms in this way has opened a new field of research studying analogies between optical fiber and the formation of extreme "rogue wave" events in other systems ranging from ocean waves [7,8] to biology [9]. The associated statistical analysis has been widely used to determine conditions under which such optical rogue waves can be generated or suppressed [10–12] and has found application in assessing novel fiber designs to generate reduced noise SC spectra for imaging [13–15].

Existing use of histogram-based analysis of SC noise, however, is qualitative. Although this is certainly useful to sample and identify regimes where rogue wave-like statistics might be observed [16], such an approach is difficult to use for quantitative comparisons between modeling and experiment when large amounts of data is involved. In this work, we show how histogram analysis of rogue wave like fluctuations can be quantified using the statistical shape descriptors of *higher-order central moments* that quantify not only the mean and variance of a distribution, but also the asymmetry and the presence of long tails. We show how this approach provides a clear and quantitative means of identifying variations at the spectral edges associated with rogue wave events. These central moments – that depend only on analyzing intensity fluctuations – provide a complementary tool to phase-dependent coherence measures to interpret supercontinuum noise and stability. Significantly, these measures are readily accessible in experiments, since they can be derived from simple photodiode measurements [17], whereas measuring the coherence is experimentally very demanding. We suggest that this approach is adopted widely in numerical and experimental characterization of SC noise properties, particularly those focusing on the link with long-tailed statistics.

The analysis is based on the statistical framework of central moments used in the study of probability distributions, where we wish to characterize the shape of a particular distribution and not only its location and spread [18]. For a real-valued random variable X, the nth-order central moment around the mean is given by

$$\mu_n = \left\langle (X - \langle X \rangle)^n \right\rangle \tag{1}$$

* Corresponding author. Tel.: +45 45256387.
E-mail address: stso@fotonik.dtu.dk (S.T. Sørensen).

0030-4018/$ – see front matter © 2012 Elsevier B.V. All rights reserved.
doi:10.1016/j.optcom.2012.01.030

where angle brackets denote an ensemble average. The zeroth and first central moments are $\mu_0 = 1$ and $\mu_1 = 0$, respectively. The second order central moment μ_2 is the well-known variance σ^2, which measures the distribution spread. Instead of σ^2 we shall be using the so-called *coefficient of variation*: $C_v = \sigma/\langle X\rangle$, which has the straightforward interpretation as being inversely proportional to the signal-to-noise ratio.

Of particular interest for analyzing the asymmetric long-tailed distributions associated with SC generation are the third and fourth central moments, commonly expressed in normalized form relative to the variance. The third order central moment is referred to as the *skewness* $\gamma = \mu_3/\sigma^3$, which measures the asymmetry of the distribution, with $\gamma < 0$ for a left-skewed distribution, $\gamma > 0$ for a right-skewed distribution and $\gamma = 0$ for a symmetric distribution. The fourth-order central moment is referred to as *kurtosis* (sometimes also called the "coefficient of excess") $\kappa = \mu_4/\sigma^4 - 3$, and measures whether the distribution is peaked or flat relative to a normal distribution of the same variance. A normal (Gaussian) distribution has $\kappa = 0$, and a high kurtosis arises from rare extreme deviations from the mean.

The skew and kurtosis are particularly important in revealing the presence of long tails in a distribution and, as we shall see, are key parameters in allowing the general statistical properties of noisy SC spectra to be conveniently described. The higher-order moments all relate to the pulse intensity, and should hence be considered complementary to the phase-sensitive spectral coherence [19],

$$\left|g_{12}^{(1)}(\omega)\right| = \left|\frac{\left\langle \tilde{A}_i^*(\omega)\tilde{A}_j(\omega)\right\rangle_{i\neq j}}{\sqrt{\left\langle \left|A_i(\omega)\right|^2\right\rangle\left\langle \left|A_j(\omega)\right|^2\right\rangle}}\right| \tag{2}$$

calculated as an ensemble average of independent SC spectra, $\tilde{A}_i(\omega)$, in the frequency domain, where the asterisk denotes complex conjugation.

Although our focus here is on the use of these higher-order moments for the study of histogram measures of rogue wave regimes in SC generation, it is appropriate to comment briefly on other possible methods of SC noise characterization. An additional way in which the histogram measures could be quantified would be via appropriate distribution fitting (e.g. Weibull) at all wavelengths across the spectrum. Whilst the distribution parameters obtained would certainly provide an alternative measure of distribution asymmetry, a meaningful comparison between different wavelengths would be difficult since the goodness of fit would very likely vary with wavelength. The advantage of the higher-order moments in this context is that they are both easy to calculate and they do not depend on any a priori particular choice of distribution. In what follows, we therefore focus on the use of higher-order moments, choosing to compare the results obtained using this approach with the widely used spectral coherence function. We note that future work could consider comparison with the recently-introduced measure of two-time two-frequency second-order coherence function, which provides additional information about the physical nature of contributing noise sources [20,21].

2. Results

To demonstrate the utility of the statistical descriptors (C_v, γ, κ) to characterize SC generation, we use numerical simulations in the presence of noise to generate an ensemble of SC spectra under conditions where there are significant fluctuations between different realizations of the ensemble. The simulations use a noise-seeded generalized nonlinear Schrödinger equation (GNLSE) model, which has been shown to produce average spectra, radio frequency noise and coherence properties in agreement with experiment [3,13,22,23]. We use the particular implementation described in [24,25], with input noise included in the frequency domain through a noise seed of one photon per mode with random phase added to each discretization bin. However, we note that the particular model used to introduce noise into the simulations is not significant, and qualitatively-similar results to those below can be obtained using other approaches to noise inclusion [23].

We considered a silica photonic crystal fiber (PCF) with parameters typical for SC generation pumped at 1064 nm. The particular fiber that we model has a hexagonal hole structure with a pitch of 3.6 μm and a relative hole-size of 0.52, resulting in a zero-dispersion wavelength (ZDW) of 1054 nm. At the pump wavelength, the group velocity dispersion $\beta_2 = -1.1434$ ps^2/km, and nonlinearity $\gamma_{NL} = 10$ W^{-1}km^{-1}, but our simulations included higher-order dispersion and nonlinearity via the frequency-dependence of all parameters calculated from the mode profile of the fiber. We considered hyperbolic sechant input pulses of FWHM 300 fs, with pump wavelength and peak-power set to 1064 nm and 20 kW, respectively, and a fiber length of 50 cm in all simulations. With these parameters the pulse break-up is dominated by modulational instability (MI). We stress that the parameters are realistic and typical of many experiments.

We carried out simulations to generate an ensemble of 1000 SC spectra under identical conditions apart from different noise seeds. Under the conditions presented in this paper and for those in a variety of similar supercontinuum parameter regimes, we found that the choice of 1000 simulations was satisfactory to obtain consistent values of calculated higher-order moments. It should be noted that if explicit identification of very rare events (e.g. at the 10^{-5} probability level) is desired, a greater number of simulations would be required.

We first present results using basic coherence and histogram characterization as is typical of current approaches used to characterize SC fluctuations. For these results, the spectral plot in Fig. 1(a) superposes results of the individual simulations (gray) together with the calculated mean smoothed by a 3 nm FWHM Gaussian (solid line), with the top subplot in the figure also showing the calculated degree of spectral coherence. Fig. 1(b) shows histograms of the pulse energy fluctuations extracted over a 10 nm bandwidth around 1.35, 1.4 and 1.55 μm. These wavelength ranges are also indicated in the spectral plot in Fig. 1(a).

The spectral coherence and histograms seen as in Fig. 1, clearly provide only limited and qualitative information. For example, whilst it is easy to calculate and display the coherence at all wavelengths across the spectrum, the fact we see that it is zero over most of the SC bandwidth indicates only the presence of severe noise over a wide wavelength range, without indicating anything specific about its nature. On the other hand, displaying histograms at specific wavelengths across the SC is useful to show how statistics can vary from Gaussian near the pump to long-tailed near the long wavelength (Raman soliton dominated) edge, but the selection of which particular wavelengths to filter and analyze in this way is not a priori evident.

It is here that the higher-order central moments provide a convenient and clear solution that show – at each wavelength across the SC spectra – the detailed characteristics of the probability distribution of the spectral fluctuations. We first show this in Table 1, where we calculate γ, κ and C_v of the histograms of Fig. 1. The moments clearly reflect the transition from low-noise near-Gaussian statistics to noisy highly skewed and peaked statistics when the window is moved into the spectral wing. In Fig. 2, we re-analyze the simulations of Fig. 1 to show ensemble averaged results as a function of propagation distance, but also showing for each case the higher-order central moments and spectral coherence function $|g_{12}^{(1)}|$ for the entire bandwidth. These are readily calculated from the numerical histograms for each wavelength in the SC over a 10 nm bandwidth as above. This bandwidth was chosen to be typical for the band-pass filters used in

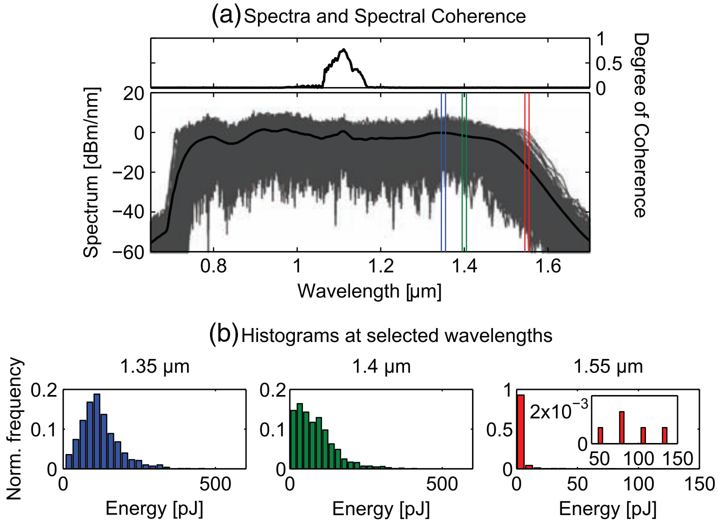

Fig. 1. (a) Spectra and calculated degree of coherence for a 300 fs pulse after 50 cm propagation. (b) Corresponding histograms calculated in the 10 nm spectral windows marked in (a). The inset in the 1.55 μm histogram shows a close-up of infrequent high-energy counts. Note the change of scale in the histograms.

most experiments, but we have checked that the choice of spectral window width does not alter our conclusions.

We can now see how these measures aid in the interpretation of the results. For example, at 5 cm (Fig. 2(a)), the pulse has not yet broken up into solitons and the spectrum is still relatively narrow. At this stage the central part of the pulse is still fully coherent and the noise characteristics are dominated by low amplitude sidebands generated through spontaneous MI. The coefficient of variation, skew and kurtosis are zero around the pump region that has undergone essentially only self-phase modulation, indicating that the fluctuations in this regime are small and quasi-symmetric, i.e. largely Gaussian. The near constant-nature of these measures across the sidebands indicates that the nature of the fluctuations is the same; the fact that the coefficient of variation C_v is much greater across the sidebands than around the pump reflects how the sidebands develop from an incoherent noise background. This is reflected in the phase-sensitive coherence plot that shows complete incoherence in the sidebands.

Following the evolution of these parameters with distance provides further illustration of how they add significant additional insight into the propagation dynamics. At distances exceeding 15 cm (Fig. 2(b)–(d)) the noise level has increased almost uniformly across the spectrum, with the intensity noise level and distribution symmetry in the vicinity of the pump comparable to that at the wavelengths of the broader SC. Note that the high intensity noise in the vicinity of the pump is not inconsistent with the residual pump coherence, which depends more strongly on phase fluctuations. Conversely, a high spectral coherence implies low phase noise but in general in SC generation, low phase fluctuations are also associated with low intensity fluctuations, leading to low values of the higher-order moments. This is particularly visible in Fig. 2(d) where the coherent part of the spectrum shows low values of all the moments. It is worth noticing that this coherent region is generated by self-phase modulation of the pump, and that only the wavelength region above the pump stays coherent with propagation distance; the coherence of the region below the pump degrades when it crosses the ZDW. The difference in coherence properties above and below the pump arises because of the different signs of dispersion, and has been previously seen in simulations (e.g. Fig. 20(b) of Ref. [22]). We interpret this in terms of the different nature of the dynamics in the anomalous and normal dispersion regimes. In the anomalous dispersion regime (above the pump) even in the presence of noise, residual localized structures can form which we expect will preserve coherence over a limited bandwidth [26]. On the other hand in the normal dispersion regime (below the pump) no such nonlinear localization occurs; the dispersive nature of propagation in this wavelength range favors decoherence.

Table 1
Coefficient of variation (C_v), skewness (γ) and kurtosis (κ) calculated from the histograms in Fig. 1(a)–(c). The null values of γ and κ for a normal distribution are shown for comparison. The value of C_v for a normal distribution depends on the particular case considered and is thus not shown.

Wavelength [μm]	C_v	γ	κ
1.35	0.517	1.16	2.25
1.40	0.754	1.35	2.55
1.55	3.49	10.4	142
Normal distribution	–	0	0

As the propagation distance increases, the figure also shows how the *nature* of the intensity fluctuations changes near the spectral edges, as the dynamics become dominated by extreme sensitivity to variations in the peak-power of the most redshifted solitons ejected from the pump pulse and their subsequent collisions. The larger coefficient of variation, skew and kurtosis in the spectral wings clearly show the presence of the noisy, peaked long-tailed rogue wave statistics in this wavelength regime. This is in sharp contrast to the coherence that only contains information about the central part of the SC, and thus cannot be used to analyze the extreme rogue events near the spectral edges.

As an additional illustration of the convenient insight afforded by the calculation of these statistical moments, Fig. 3 shows simulation ensembles for 20 kW peak power but with pulse durations of 50, 150 and 300 fs. We see the transition from coherent to incoherent SC with increasing pulse duration, but it is particularly significant that even though 150 fs and 300 fs both show significant intensity fluctuations across the spectrum, it is only for the 300 fs case that we see long-tailed statistics with elevated skew and kurtosis near

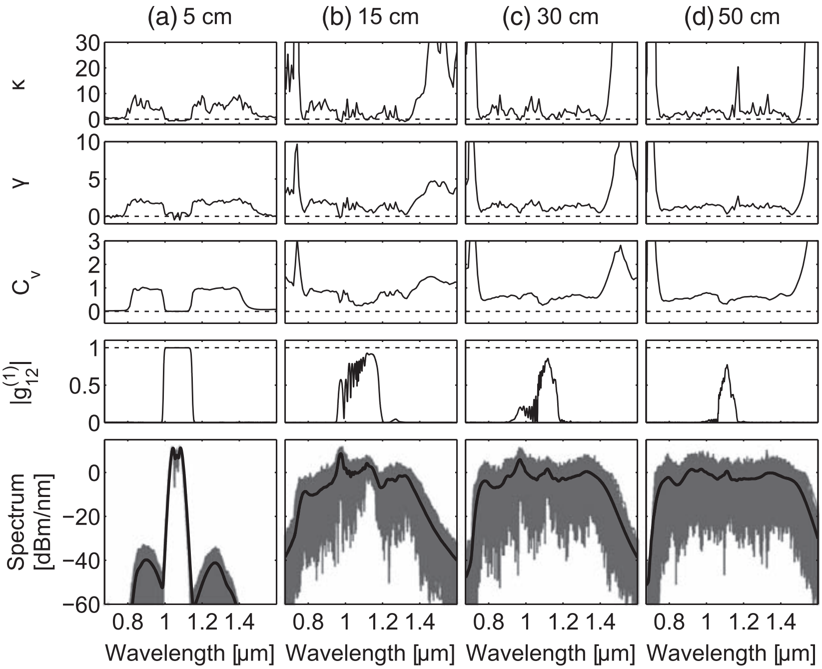

Fig. 2. Noise and spectral characteristics of a 300 fs pulse for propagation distances of (a)–(d): 5, 15, 30 and 50 cm. The four top rows show the kurtosis (κ), skewness (γ), coefficient of variation (C_v) and spectral coherence ($|g_{12}^{(1)}|$), respectively. The corresponding spectra are shown in the bottom row.

the spectral edges. This highlights the transition to the SC being more and more generated by noise-driven MI and the presence of extreme rogue wave type fluctuations.

In the specific case of MI-driven SC generation, we have found that for the extreme degree of long-tailedness generally linked with rogue waves as seen in experiments and numerical studies in the literature,

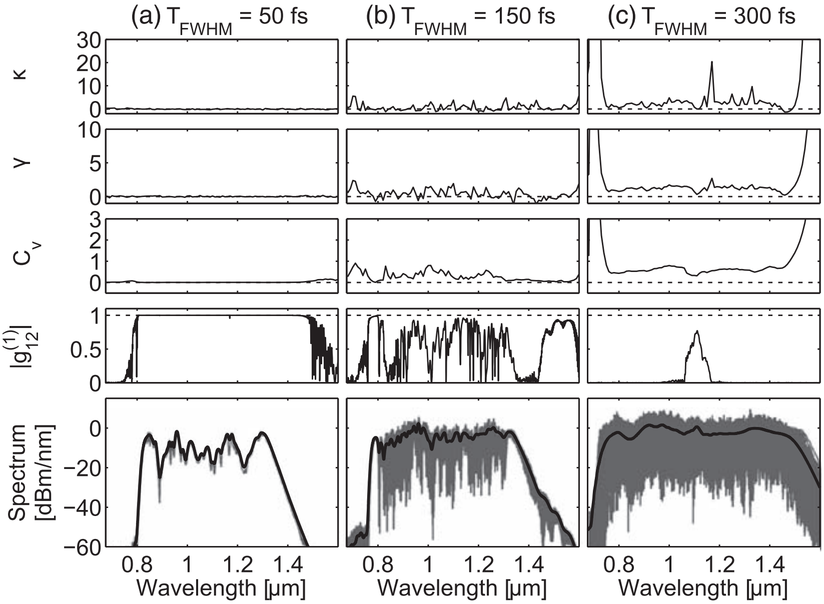

Fig. 3. Noise and spectral characteristics at a propagation distance of 50 cm for pulse durations of (a)–(c): 50, 150 and 300 fs. The four top rows show the kurtosis (κ), skewness (γ), coefficient of variation (C_v) and spectral coherence ($|g_{12}^{(1)}|$), respectively. The corresponding spectra are shown in the bottom row.

a useful guideline is that rogue wave behavior can be associated with the product of skew and kurtosis exceeding ten, $\gamma \cdot \kappa > 10$. We stress that although this particular value is well supported by the results presented here, it should be taken as a rule of thumb and not a strict criteria for identifying rogue wave behavior under all conditions. But we suggest that the use of higher-order moments and the skew-kurtosis product appropriately calculated for different SC scenarios may prove a useful and quantitative guideline allowing regimes of rogue wave behavior to be identified in future work studying SC noise properties.

3. Conclusion

In this paper, we have shown the utility and advantages in using higher-order statistical moments to provide complementary and important information about the degree and the nature of noise across the bandwidth of the optical SC. The coherence function that has been previously used widely in studies of SC noise is strongly phase dependent and, in the presence of large phase fluctuations is effectively zero across the bandwidth for MI driven SC generation. This means that it is incapable of identifying regimes of long-tailed distributions and the presence of rogue waves in the intensity fluctuations. To address this limitation, we have introduced the central moments, which together with the coherence function provide a complete tool for analyzing large amounts of data to identify rogue wave signatures. We suggest that the use of higher-order moments and the complementary coherence measure is adopted as the norm for analyzing SC noise properties. To this end, we propose as a useful guideline to associate extreme event rogue wave statistics in MI-driven SC generation in terms of a skew-kurtosis product. For the regime considered in this paper, a skew-kurtosis product of $\gamma \cdot \kappa > 10$ was found as a useful guideline where rogue wave like behavior could be identified.

Acknowledgment

We thank the Danish Agency for Science, Technology and Innovation for support of the project no. 09-070566, and the French Agence Nationale de la Recherche projects MANUREVA (ANR-08-SYSC-019) and IMFINI (ANR-09-BLAN-0065).

References

[1] J.M. Dudley, J.R. Taylor (Eds.), Supercontinuum Generation in Optical Fiber, Cambridge University Press, 2010.
[2] K.L. Corwin, N.R. Newbury, J.M. Dudley, S. Coen, S.A. Diddams, K. Weber, R.S. Windeler, Physical Review Letters 90 (2003) 113904.
[3] X. Gu, M. Kimmel, A.P. Shreenath, R. Trebino, J.M. Dudley, S. Coen, R.S. Windeler, Optics Express 11 (2003) 2697.
[4] D.R. Solli, Nature 450 (2007) 1054.
[5] M.N. Islam, G. Sucha, I. Bar-Joseph, M. Wegener, J.P. Gordon, D.S. Chemla, Journal of the Optical Society of America B 6 (1989) 1149.
[6] M.H. Frosz, O. Bang, A. Bjarklev, Optics Express 14 (2006) 9391.
[7] D.I. Yeom, B.J. Eggleton, Nature 430 (2007) 953.
[8] N. Akhmediev, E. Pelinovsky, The European Physical Journal Special Topics 185 (2010).
[9] O. Bang, M. Peyrard, Physical Review E 53 (1996) 4143.
[10] J.M. Dudley, G. Genty, B.J. Eggleton, Optics Express 16 (2008) 3644.
[11] G. Genty, J.M. Dudley, B.J. Eggleton, Applied Physics B: Lasers and Optics 94 (2009) 187.
[12] D. Buccoliero, H. Steffensen, H. Ebendorff-Heidepriem, T.M. Monro, O. Bang, Optics Express 19 (2011) 17973.
[13] O. Vanvincq, B. Barviau, A. Mussot, G. Bouwmans, Y. Quiquempois, A. Kudlinski, Optics Express 18 (2010) 24352.
[14] A. Kudlinski, B. Barviau, A. Leray, C. Spriet, L. Héliot, A. Mussot, Optics Express 18 (2010) 27445.
[15] U. Møller, S.T. Sørensen, C. Jakobsen, J. Johansen, P.M. Moselund, C.L. Thomsen, O. Bang, Optics Express 20 (2012) 2851.
[16] M. Erkintalo, G. Genty, J.M. Dudley, The European Physical Journal Special Topics 185 (2010) 135.
[17] C. Lafargue, J. Bolger, G. Genty, F. Dias, J.M. Dudley, B. Eggelton, Electronics Letters 45 (2009) 217.
[18] H. Cramér, Mathematical Methods of Statistics, Princeton University Press, 1999.
[19] J.M. Dudley, S. Coen, Optics Letters 27 (2002) 1180.
[20] G. Genty, M. Surakka, J. Turunen, A.T. Friberg, Optics Letters 35 (2010) 3057.
[21] G. Genty, M. Surakka, J. Turunen, A.T. Friberg, Journal of the Optical Society of America B 28 (2011) 2301.
[22] J.M. Dudley, G. Genty, S. Coen, Reviews of Modern Physics 78 (2006) 1135.
[23] M.H. Frosz, Optics Express 18 (2010) 14778.
[24] J. Laegsgaard, Optics Express 15 (2007) 16110.
[25] J. Hult, Journal of Lightwave Technology 25 (2007) 3770.
[26] J.M. Dudley, G. Genty, F. Dias, B. Kibler, N. Akhmediev, Optics Express 17 (2009) 21497.

Paper VI

Influence of pump power and modulation instability gain spectrum on seeded supercontinuum and rogue wave generation

S. T. Sørensen, C. Larsen, U. Møller, P. M. Moselund, C. L. Thomsen, and O. Bang
J. Opt. Soc. Am. B **29**, 2875-2885 (2012).

Abstract: The noise properties of a supercontiuum can be significantly improved both in terms of coherence and intensity stability by modulating the input pulse with a seed. In this paper, we numerically investigate the influence of the seed wavelength, the pump power, and the modulation instability gain spectrum on the seeding process. The results can be clearly divided into a number of distinct dynamical regimes depending on the initial four-wave mixing process. We further demonstrate that seeding can be used to generate coherent and incoherent rogue waves, depending on the modulation instability gain spectrum. Finally, we show that the coherent pulse breakup afforded by seeding is washed out by turbulent solitonic dynamics when the pump power is increased to the kilowatt level. Thus our results show that seeding cannot improve the noise performance of a high power supercontinuum source.

`http://dx.doi.org/10.1364/JOSAB.29.002875`

Influence of pump power and modulation instability gain spectrum on seeded supercontinuum and rogue wave generation

Simon Toft Sørensen,[1,*] Casper Larsen,[1] Uffe Møller,[1] Peter M. Moselund,[2] Carsten L. Thomsen,[2] and Ole Bang[1,2]

[1]*DTU Fotonik, Department of Photonics Engineering, Technical University of Denmark, 2800 Kgs. Lyngby, Denmark*
[2]*NKT Photonics A/S, Blokken 84, DK-3460, Birkerød, Denmark*
**Corresponding author: stso@fotonik.dtu.dk*

Received April 5, 2012; revised August 23, 2012; accepted August 28, 2012; posted August 28, 2012 (Doc. ID 166112); published September 21, 2012

The noise properties of a supercontiuum can be significantly improved both in terms of coherence and intensity stability by modulating the input pulse with a seed. In this paper, we numerically investigate the influence of the seed wavelength, the pump power, and the modulation instability gain spectrum on the seeding process. The results can be clearly divided into a number of distinct dynamical regimes depending on the initial four-wave mixing process. We further demonstrate that seeding can be used to generate coherent and incoherent rogue waves, depending on the modulation instability gain spectrum. Finally, we show that the coherent pulse breakup afforded by seeding is washed out by turbulent solitonic dynamics when the pump power is increased to the kilowatt level. Thus our results show that seeding cannot improve the noise performance of a high power supercontinuum source. © 2012 Optical Society of America

OCIS codes: 030.1640, 190.4370, 190.4380, 320.6629.

1. INTRODUCTION

Supercontinuum (SC) sources have by now been established as a new type of light source well suited for many characterization and imaging applications [1]. Many of these applications require spectra with high power density in the visible part of the spectrum, which can be achieved in nonlinear fibers with a group-velocity (GV) profile that allows GV matching between long wavelength solitons and dispersive waves at visible wavelengths [2]. The concept of GV matching has been used to show how the spectra can be extended into the deep-blue by optimizing the fiber structure [3], by tapering the fiber [4–6], or by doping the fiber [7]. Other ways of pushing the spectrum toward the blue include seeding with the second harmonic [8], using concatenated fibers [9], or back-seeding part of the SC [10–12].

Today's commercial SC sources are using high-power picosecond (ps) or nanosecond (ns) pump lasers, where the SC generation is initiated by unseeded modulational instability (MI). Because of the high stability of the pump laser the main source of shot-to-shot noise stems from the fact that unseeded MI grows from noise. Subsequently, MI leads to a pulse breakup, which generates a distributed spectrum of solitons that interact and transfer energy between each other during collisions [13]. The interaction will add to the noise, because it depends strongly on the relative phase and amplitude of the solitons, but on average there is a preferential transfer of energy from the smaller to the larger solitons [14–17]. This energy transfer can lead to the formation of rare large amplitude solitons, also known as rogue waves in optics [18] or highly localized modes in biophysics [14].

To reduce the noise it has been proposed to provide a seed, i.e., a weak pulse with a frequency offset relative to the pump, within the MI gain spectrum in order to ensure a deterministic rather than noise-seeded pulse breakup [13,19–24]. In particular, Genty *et al.* [20] numerically investigated seeding with different seed frequencies in a silica fiber with an MI gain peak at 8 THz and showed that a seed at 5 THz from the pump, i.e., at approximately two-thirds of the MI gain peak, gave an optimum improvement of the broadening and stability of the SC. In all cases a low pump peak power of 75 W (pulse energy 0.4 nJ) was used, which was then split between the pump and seed. In [21], a coherent comb-like SC was generated by seeding a high peak power (10 kW) ps pulse, and an optimal fiber length was determined, for which the comb remains coherent. The optimum length was found to be 5–10 cm for typical commercial SC sources; broad spectra without comb structure requires longer fiber lengths and was hence not investigated. Li *et al.* [24] investigated the influence of a weak CW seed on low power SC generation in a dispersion-shifted fiber, and described how seeding leads to a pulse breakup caused by four-wave mixing (FWM).

Experimentally, seeded SC generation was investigated in [10,12,19,22,23]. In [19,22,23] the SC generation was induced by triggering a sub-threshold pump with a seed pulse or continuous wave. Improved spectral stability and coherence was demonstrated in [19], and in [22,23] an optimum spectral broadening was found when seeding near the MI gain peak. An enhancement of the spectral bandwidth with increasing pump or seed power was further demonstrated in [22], but only for low power near the SC threshold where the spectral broadening is caused by a single soliton generated from the seeding process. The results presented in [19,22,23] are different from the optimum conditions found in [20,24] and here, where the pulse break-up is caused by the amplification of a FWM cascade. A different approach was pursued in [10,12], where a fraction of the generated SC from one pulse was used as a seed for the following pump pulse. This, however, is fundamentally different from modulating the pump pulse with a seed as in this work and [19–24].

While it has thus been shown that seeding can reduce the noise of an SC, this has been either at low pump power, often close to the MI threshold, or for very short fibers. The previous investigations are thus far from commercial SC sources with spectra extending down in the visible, which are typically pumped using ns or ps pump pulses at 1064 nm with high peak powers in the order of ~10 kW and fiber lengths of ~10 m. Here we investigate the effect of seeding under a variety of conditions, and explain what happens as we approach the parameters of a commercial SC source. In particular, we investigate the influence of the seed wavelength and MI gain spectrum on seeding at various power levels above the SC threshold, from which we highlight a number of distinct dynamical regimes. We further demonstrate for the first time how seeding leads to the generation of coherent or incoherent rogue solitons depending on the MI spectrum. Finally, we explain how the coherent pulse breakup caused by the seeding is eventually washed out by turbulent solitonic dynamics when the peak power is increased to the kilowatt (kW) level.

This paper is structured as follows. In Sections 2 and 3, we explain how the MI gain spectrum can be calculated and altered, and how the statistical properties of an SC can be analyzed both in terms of coherence and intensity stability. In Section 4 we proceed to analyze the effects of seeding at a relatively low peak power of 250 W to illustrate the general improvements in coherence and intensity stability, and explain the influence of the MI gain spectrum on seeding. We further describe how this can be used to generate a coherent or incoherent rogue soliton. Finally, in Section 5 we investigate the effects of seeding at higher peak powers.

2. MODULATIONAL INSTABILITY GAIN AND SEEDING

The MI gain spectrum $g(\Omega)$, taking into account the Raman response function, is given by (see, e.g., [25])

$$g(\Omega) = \mathrm{Im}\left\{\Delta k_o \pm \sqrt{(\Delta k_e + 2\gamma P_0 \tilde{R}(\Omega))\Delta k_e}\right\}, \tag{1}$$

where Ω is the angular frequency offset relative to the pump. Δk_o and Δk_e are sums over odd and even order derivatives of the propagation constant β,

$$\Delta k_o = \sum_{m=1}^{\infty} \frac{\bar{\beta}_{2m+1}}{(2m+1)!}\Omega^{2m+1}, \qquad \Delta k_e = \sum_{m=1}^{\infty} \frac{\bar{\beta}_{2m}}{2m!}\Omega^{2m}, \tag{2}$$

where $\bar{\beta}_m = \partial^m \beta / \partial \Omega^m |_{\Omega=0}$. γ is the nonlinear parameter, P_0 is the peak power, and $\tilde{R}(\Omega)$ is the Raman response for silica, which can be approximated by [26]

$$\tilde{R}(\Omega) = (1 - f_R) + f_R \frac{\tau_1^2 + \tau_2^2}{\tau_2^2 - \tau_1^2 (i + \tau_2 \Omega)^2}, \tag{3}$$

where $f_R = 0.18$ is the fractional contribution of the Raman response, $\tau_1 = 12.2$ fs and $\tau_2 = 32$ fs.

The MI gain is strongly influenced by the Raman effect, and in order to make a detailed investigation of the influence of the MI gain spectrum on seeding under a variety of conditions, we wanted the possibility of tuning the peak of the MI gain spectrum from significantly below to significantly above the peak of the Raman gain spectrum at 13.2 THz (in silica). For a given fiber this can be achieved by changing either the pump wavelength or peak power. In this work we use a solid core silica photonic crystal fiber (PCF) with pitch (hole spacing) $\Lambda = 3.6$ μm and hole-to-pitch ratio $d/\Lambda = 0.52$, resulting in a zero-dispersion wavelength (ZDW) at 1054.2 nm. Pump pulses with a temporal width (FWHM) of 3 ps ($T_0 \approx 3$ ps/1.665 for a Gaussian pulse) and a fiber length of 10 m were used in all simulations presented in this paper. The dispersion and effective area are shown in Fig. 1(a), whereas Figs. 1(b)–1(c) show how the MI gain spectrum changes with wavelength and peak power, respectively. For this particular fiber the peak of the MI spectrum can thus easily be swept over the desired range by simply changing the wavelength or peak power of the pump over a range that is experimentally realisable. The frequency of the MI gain maximum increases, i.e., moves away from the pump, when the pump wavelength is decreased or the peak power is increased. We stress that although the pump powers in Figs. 1(b)–1(c) are all significantly lower than the ~10 kW used in high-power commercial SC sources, it is well above the threshold for SC generation and the power levels previously reported in the literature on seeding in, e.g., [19,20,22–24]. As mentioned earlier, seeding at high-power was investigated in [21] but only for very short fiber lengths.

Figure 1(d) shows the walk-off length of the pump and seed and MI gain length, respectively. The walk-off length is the propagation distance over which the two pulses are separated by less than the pulse width, i.e., $T_0/|v_{g,\mathrm{pump}}^{-1} - v_{g,\mathrm{seed}}^{-1}|$, where $v_{g,i}$ is the group-velocity. When the walk-off length is shorter than the MI gain length, the seed cannot have an effect. In other words, a seed placed in the tail of the gain spectrum cannot be expected to have any significant effect because of a too short interaction length with the pump.

The work in this paper is based on solutions to the generalized nonlinear Schrödinger equation (GNLSE), which has become the standard for simulating nonlinear pulse propagation in optical fibers due to its ability to reproduce spectra and noise properties in agreement with experiments [1,27]. The GNLSE takes into account the effects of nonlinearities, the delayed Raman response, and higher-order dispersion. We used the implementation of [28] with the GNLSE solved in the interaction-picture [29], and included a noise background of one photon with a random phase in each discretization bin. This allows ensemble statistics to be calculated by carrying out simulations under identical conditions, but with different initial noise. In the simulations we used a Gaussian pump and seed of identical temporal width T_0. The two pulses were temporally overlapping, and the seed given a frequency offset ν_{mod}, where $\nu_{\mathrm{mod}} > 0$ corresponds to seeding at a wavelength longer than that of the pump, i.e., in the Stokes band. The temporal pulse envelope $A(t)$ was hence,

$$A(t) = \left(\sqrt{P_p} + \sqrt{P_s} e^{i2\pi\nu_{\mathrm{mod}} t}\right) \exp\left(\frac{-t^2}{2T_0^2}\right), \tag{4}$$

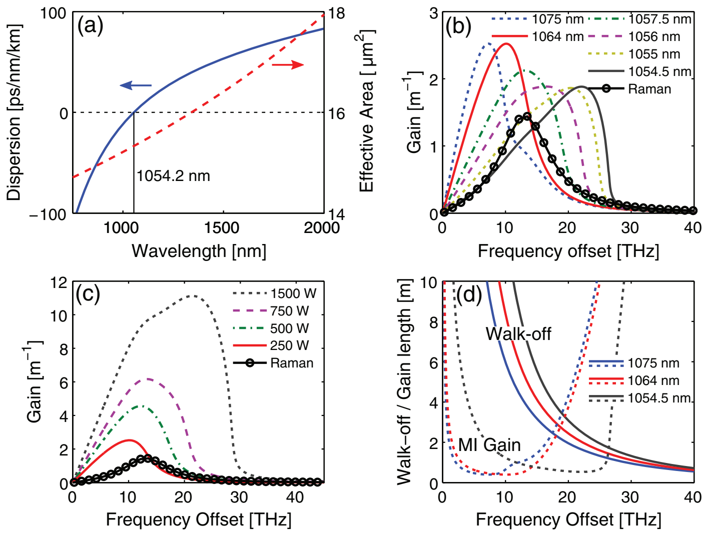

Fig. 1. (Color online) (a) Dispersion and effective area for the used PCF with $\Lambda = 3.6$ μm and $d/\Lambda = 0.52$. (b)–(c) MI gain spectra as a function of seed frequency offset relative to the pump for varying pump wavelength (b) and peak power (c). The peak power in (b) is 250 W and the pump wavelength in (c) is 1064 nm. The Raman gain is shown for comparison. (d) Walk-off length (solid lines) and MI gain length (dotted lines) as a function of frequency offset, calculated for $T_0 = 3$ ps/1.665 and a peak power of 250 W.

where P_p and P_s are the peak powers of the pump and seed, respectively. This is similar to what was used in [20], although in [20] the peak power was shared between the pump and seed as would be the case if the seed is generated from the pump by some frequency shifting technique. This however means that changing the power of the seed also causes a change of the MI gain spectrum. Here we consider a seed that is independent of the pump in order to have the same MI gain spectrum irrespectively of the seed peak power. Using Eq. (4) it is thus straightforward to sweep the pump-seed frequency offset and peak power of the seed for a fixed MI gain spectrum. We emphasize that the narrow-banded pulses used here have a FWHM spectral width of only 0.15 THz. The seed therefore only has a substantial spectral overlap with the pump for very small offsets, i.e. $\nu_{\mathrm{mod}} \approx 0$ THz, which results in an effective increase of the peak power and hence the MI gain spectrum.

3. QUANTIFYING SUPERCONTINUUM NOISE

Typically, the noise is quantified by the widely used spectral coherence function calculated as an ensemble average over independent SC spectra, $\tilde{A}_i(\omega)$ [30],

$$|g_{12}^{(1)}(\omega)| = \left| \frac{\langle \tilde{A}_i^*(\omega)\tilde{A}_j(\omega)\rangle_{i\neq j}}{\sqrt{\langle|\tilde{A}_i(\omega)|^2\rangle\langle|\tilde{A}_j(\omega)|^2\rangle}} \right|, \tag{5}$$

where the angle brackets denote ensemble averages and the asterisk denotes complex conjugation. The spectral coherence function provides insight into the stability of an SC and is sensitive to shot-to-shot phase fluctuations. However, high-power and long-pulsed MI-driven SC generation is predominantly incoherent, as we shall see in the following, and we will therefore also consider the intensity stability quantified here by the signal-to-noise ratio (SNR) defined as the ratio of the mean μ to the standard deviation σ,

$$\mathrm{SNR}(\omega) = \frac{\mu(\omega)}{\sigma(\omega)}. \tag{6}$$

The SNR is inversely proportional to the coefficient of variation introduced as an SC noise measure in [31]. The SNR is better suited for highlighting regions of high intensity stability, whereas the coefficient of variation is a good indicator of noisy regions dominated by statistically rare events.

It is illustrative to integrate the spectral coherence to get the spectrally averaged or so-called overall spectral coherence of an SC ensemble [1],

$$\langle|g_{12}^{(1)}|\rangle = \frac{\int_0^\infty |g_{12}^{(1)}(\omega)|\langle|\tilde{A}(\omega)|^2\rangle \mathrm{d}\omega}{\int_0^\infty \langle|\tilde{A}(\omega)|^2\rangle \mathrm{d}\omega}. \tag{7}$$

The overall coherence is, like the spectral coherence function itself, bounded by the interval $0 \leq \langle|g_{12}^{(1)}|\rangle \leq 1$, and gives a single value measure of the overall coherence of an SC. Similarly, we introduce the overall SNR to quantify the overall intensity stability of an SC,

$$\langle\mathrm{SNR}\rangle = \frac{\int_0^\infty \mathrm{SNR}(\omega)\langle|\tilde{A}(\omega)|^2\rangle \mathrm{d}\omega}{\int_0^\infty \langle|\tilde{A}(\omega)|^2\rangle \mathrm{d}\omega}. \tag{8}$$

It should be noted that the overall SNR has no upper boundary.

The statistical properties of the SC are calculated in each numerical discretization bin across the spectrum. For each set of parameters we carried out 200 simulations to calculate the statistics of the generated SC. However, for the higher peak powers in Section 5 only 100 simulations were carried out for each set of parameters. This was in all cases found to be sufficient to get consistent results under the conditions considered here, which was checked by using 1000 simulations in selected cases.

4. SEEDING AT LOW PEAK POWER

A. Single Shot Dynamics

We start our analysis by a detailed discussion of seeding a low peak power pump. The reason for this is both to demonstrate the utility of the noise measures introduced in the previous section, but also to highlight a number of general regimes as a reference for the further analysis. To this end, we show in Figs. 2(a)–2(e) the spectral evolution of single simulations for selected pump-seed frequency offsets for a 1055 nm pump with $P_p = 250$ W and a seed with $P_s = 5\% P_p$. In all cases we also show the coherence and SNR calculated over the ensemble of 200 simulations. The white lines mark the width of the MI gain spectrum calculated for the local pump peak power. We define the MI gain width as the region where the gain is larger than 5% of the maximum MI gain, but show only the upper gain limit and not the one for the low gain region close to the pump. We start the analysis with a pump wavelength of 1055 nm because pumping close to the ZDW shifts the MI gain peak far away from the pump and above the Raman gain peak, which, as we shall see, yields the richest dynamics. Figure 2(f) shows the MI gain spectrum of the undepleted pump.

Figure 2(a) shows the evolution for zero frequency offset, i.e., overlapping pump and seed, and the results are as expected for unseeded SC generation: The spectral broadening is initiated by noise-seeded MI, which manifests itself as a single set of sidebands positioned at the peaks of the calculated MI gain spectrum. This is followed by the onset of soliton and DW generation from around 5 m. The resulting statistics show only coherence near the residual pump and a flat near-unity

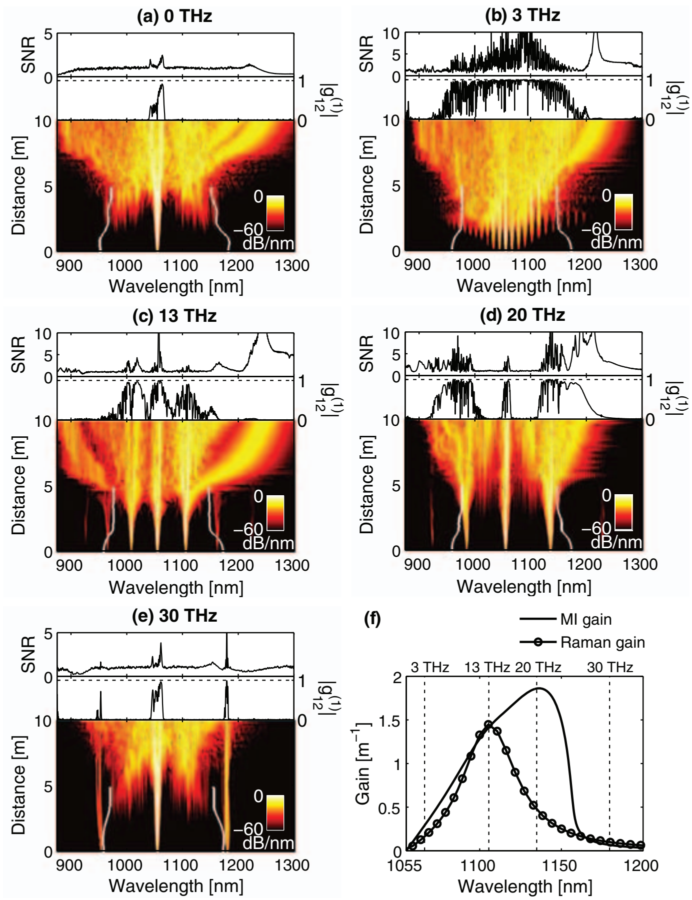

Fig. 2. (Color online) Single-shot simulations of pumping at 1055 nm with a 250 W pump and a 5% seed at frequency offsets of (a)–(e) 0, 3, 13, 20, and 30 THz, respectively. The white lines indicate the MI gain bandwidth. The top rows in (a)–(e) show the ensemble calculated signal-to-noise ratio (SNR) and spectral coherence ($|g_{12}^{(12)}|$). (f) MI and Raman gain curves, the vertical lines correspond to the frequency offsets used in (a)–(e). The frequency offset of 13 THz (c) is the Raman gain peak and 20 THz (d) is the MI gain peak.

SNR over the entire spectral bandwidth, except near the pump and the soliton at ~1225 nm. We emphasize that the MI gain spectrum in (f) is calculated for the peak power of the pump alone. The extra peak power added by the overlapping seed in (a) causes a slight shift of the spectrum towards a longer wavelength.

For a small frequency offset of 3 THz in Fig. 2(b), the pulse breakup is initiated by a cascaded FWM process that causes a coherent broadening of the pump. The FWM cascade generates a frequency comb of sidebands with a 3 THz frequency separation. The width of the frequency comb is limited by the width of the MI gain spectrum. It should be noted that the MI gain spectrum is the degenerate FWM gain spectrum of the pump, which amplifies the FWM cascade of the pump and seed. With further propagation a soliton is generated from the FWM process with enough power to redshift outside the MI gain band, with the redshift being enhanced by preferential energy transfer during collisions [14–17]. The output spectrum is coherent over most of the bandwidth, but the soliton at the long wavelength edge of the spectrum has a varying phase from shot to shot, which degrades the coherence at the spectral edges, but leads to a high intensity stability.

In Fig. 2(c) the seed is placed 13 THz from the pump, which is near the peak of the Raman gain. In this case the spectral evolution is dominated by the amplification of a single set of coherent sidebands amplified through degenerate FWM. The second set of sidebands are shifted 26 THz from the pump, which is just on the edge of the initial MI gain spectrum and therefore quickly becomes outside the gain spectrum when the pump depletes. At ~5 m a massive soliton is ejected from the long wavelength sideband, which is exactly what was referred to as "harnessing and control of optical rogue waves" in [32], where the pump pulse was modulated with a well-defined frequency to eject a large amplitude soliton. The soliton is again not phase-stable from shot to shot, but it is highly intensity-stable. This is opposite to what was reported in [24], where the rogue soliton was coherently generated from a FWM sideband. We will elaborate further on this later in the paper.

In Fig. 2(d) the seed is shifted to the peak of the MI gain at 20 THz, which leads to the amplification of a set of well-separated sidebands through FWM. The second FWM lines effectively lie outside the MI gain band. The residual pump and sidebands all undergo SPM and broaden independently of each other. This leads to an output spectrum with three clearly distinct bands with high coherence and SNR. Finally, in Fig. 2(e) the seed is shifted to the tail of the MI gain spectrum, and a single set of sidebands is slowly amplified. The short wavelength nonseeded sideband is entirely generated by FWM and is therefore very weak. The pump is only slightly depleted and experiences noise-seeded MI unaffected by the seed at 1180 nm.

To clarify the influence of the Raman effect on seeding, we show in Fig. 3 the spectral evolution with and without the Raman effect for a seed near the Raman gain peak at 13 THz. All other parameters are as in Fig. 2(c). The initial dynamics is similar irrespectively of the Raman effect, but the MI gain bandwidth is reduced much faster without the Raman effect, Eq. (1). When the Raman effect is included, a large soliton is generated from the FWM sideband at ~5 m. The soliton also appears when the Raman effect is turned off, but it is much weaker and does not give rise to any significant intensity stability. This is in good agreement with [17]. In both cases the output spectrum is coherent only near the residual pump and FWM sidebands, resulting in a comparable overall coherence of 0.45 and 0.39 with and without the Raman effect, respectively.

From the above discussion, it is possible to divide the seeding results in Fig. 2 into four distinct regimes depending on the pump-seed frequency offset, ν_{mod}, and the MI gain bandwidth, ν_{MI}.

(i) $0 < \nu_{\mathrm{mod}} \lesssim \frac{1}{4}\nu_{\mathrm{MI}}$: A broad FWM cascade gives many bands across the MI gain bandwidth, which leads to a coherent broadening and a spectrum with high coherence and SNR over most of the bandwidth.

(ii) $\frac{1}{4}\nu_{\mathrm{MI}} \lesssim \nu_{\mathrm{mod}} \lesssim \frac{1}{2}\nu_{\mathrm{MI}}$: A decreasing number of FWM sidebands are amplified, which diminishes the coherence and SNR improvement.

(iii) $\frac{1}{2}\nu_{\mathrm{MI}} \lesssim \nu_{\mathrm{mod}} \lesssim \nu_{\mathrm{MI}}$: Amplification of effectively only one set of FWM sidebands, subsequent generation of incoherent large amplitude soliton. Spectrum only coherent near pump and FWM sidebands.

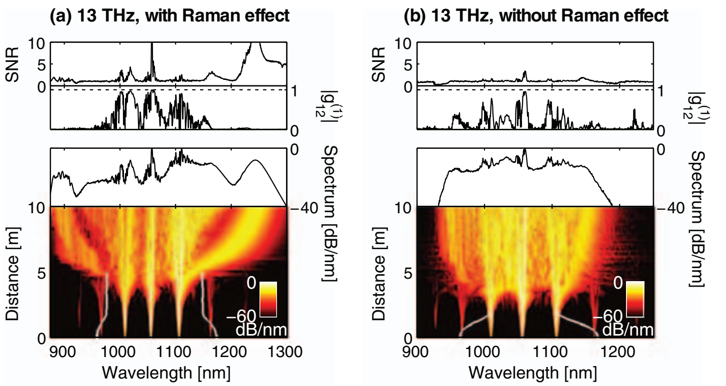

Fig. 3. (Color online) Single-shot simulation (a) with and (b) without the Raman effect. Parameters like in Fig. 2(c): 1055 nm pump with 250 W peak power and a 5% seed at 13 THz. The white lines indicate the MI gain bandwidth. The top rows show the ensemble calculated signal-to-noise ratio (SNR), spectral coherence ($|g_{12}^{(12)}|$), and averaged output spectrum.

(iv) $\nu_{\mathrm{MI}} < \nu_{\mathrm{mod}}$: FWM sidebands outside MI gain, no improvement of seeding.

These conclusions will be further specified in the next section in terms of overall coherence and SNR.

B. Overall Statistics

The ensemble averaged results for both the spectrum, coherence and SNR from Fig. 2 are shown in Fig. 4 for pump-seed frequency offsets spanning well beyond the entire MI gain spectrum. The results in Fig. 4 show an almost perfect symmetry around zero frequency offset, which indicates that seeding the Stokes and anti-Stokes bands yield near identical results. We found that this was a general trend in agreement with the results reported in [24], and we will therefore limit the further analysis to seeding in the Stokes band.

The regimes highlighted in connection with Fig. 2 are easily identified in Fig. 4: For small frequency offsets ($\lesssim$5 THz), cascaded FWM with many peaks leads to a coherent pulse breakup and a spectrum with high coherence and SNR. When the frequency offset is increased, the number of amplified peaks decreases and the coherence of the central part of the spectrum degrades. For frequency offsets of ~10–20 THz only a single set of sidebands are amplified via FWM and a large amplitude soliton is generated. The spectrum is only coherent near the residual pump and FWM sidebands, but the soliton is intensity stable. In a frequency range around ~20 THz no large amplitude soliton is ejected, but the FWM sidebands undergo SPM and broaden coherently with a high intensity stability. In this regime, the coherence improves when the frequency offset approaches the MI gain peak. This growth has not been clearly observed before. When the seed is shifted outside the MI gain spectrum, the spectrum is largely incoherent except near the weak FWM sidebands. The coherence plot further shows a high degree of coherence near the higher-order sidebands, but they are too low in amplitude to be visible in the output spectra and will hence only have a minimal effect on the overall coherence.

These general trends are all nicely captured by the overall coherence and SNR. As a rule of thumb for the parameters considered here, regimes of improved coherence can be associated with $\langle|g_{12}^{(1)}|\rangle > 0.5$. From this criteria the two regimes of improved coherence are easily identified in the overall coherence. The second regime of high coherence is found around 3/4th of the peak of the MI gain of the undepleted pump, which is roughly where the set of FWM sidebands see the highest gain when pump depletion is taken into account.

The spectral coherence is almost mirror symmetric around the pump wavelength, whereas the SNR is asymmetric and generally higher for wavelengths above the pump. This reflects the FWM nature of the seeding that leads to a deterministic and symmetric pulse breakup with high coherence near the FWM bands. The subsequent soliton generation is phase-dependent and incoherent, but tends to give a high intensity stability in the wavelength region above the pump. As we shall see, it is actually possible for some seeding conditions to generate the soliton coherently.

C. Effect of MI Gain Spectrum and Seed Power

With the general mechanisms dominating seeding at varying pump-seed frequency offsets established, we now turn to investigating the influence of the MI gain spectrum and seed power. Figure 5 shows the overall coherence and SNR as a function of frequency offset for pump wavelengths ranging from 1054.5 to 1075 nm, which gradually decreases the MI gain bandwidth. For all pump wavelengths we show the results for an extensive range of seed peak powers from 0.01% to 20% of the pump, and for 5% we also show the results without the Raman effect [see legend in (f)].

The best coherence improvement is observed for a seed power above 1% of the pump, which gives sufficient power to initiate the FWM cascade. The intensity improvement is more sensitive to the exact seed power and frequency offset, but is again best for seed powers above 1% of the pump. The coherence and SNR are generally improved in the long wavelength end of the MI gain spectrum when the power of the seed is increased, because the seed acts like a separate pump that remains (partly) coherent like the pump. The effects of seeding the pulse break-up will be diminished in this regime because of temporal walk-off (see Fig. 1).

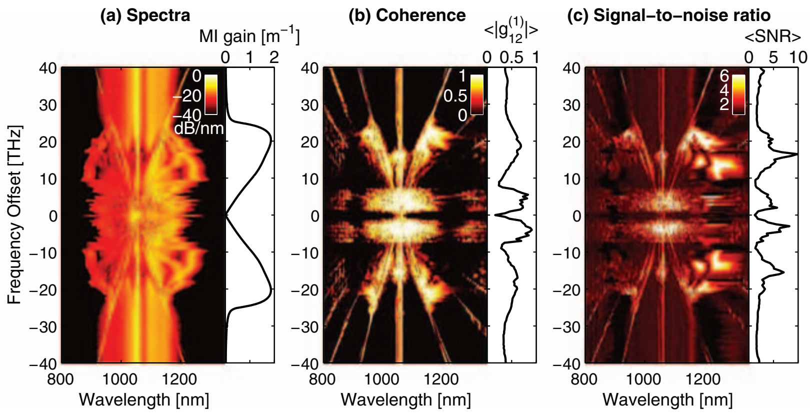

Fig. 4. (Color online) Results of pumping at 1055 nm with a 5% seed. Density plots of the (a) output spectral density, (b) coherence, and (c) SNR as a function of wavelength and pump-seed frequency offset. The figures to the right of the density plots show the (a) MI gain, (b) overall coherence, and (c) overall SNR as a function of pump-seed frequency offset.

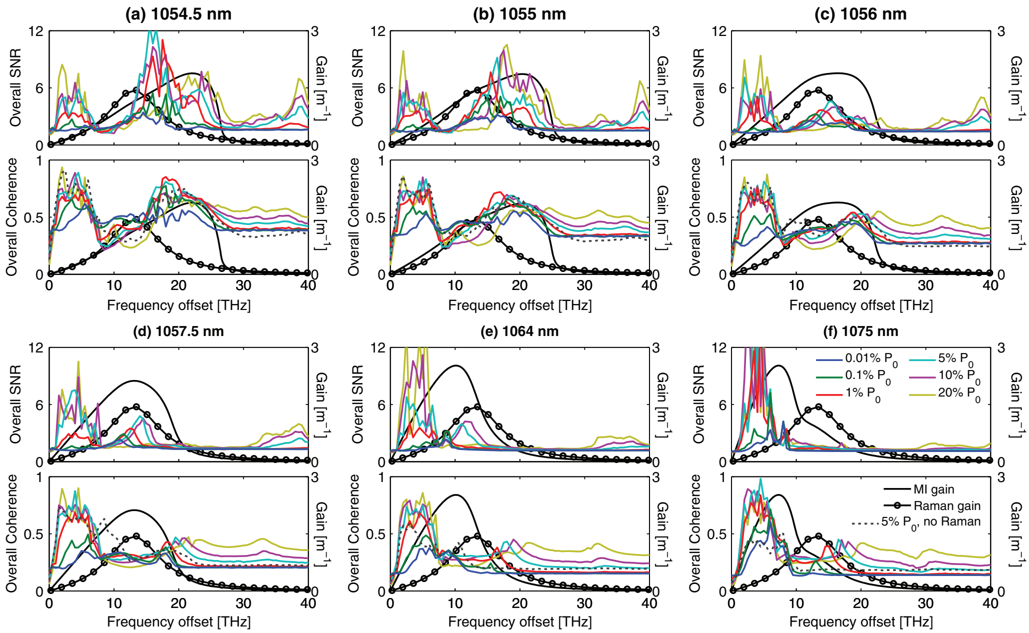

Fig. 5. (Color online) Overall SNR and coherence as a function of pump-seed frequency offset for seed peak powers ranging from 0.01% to 20% of the pump peak power, $P_P = 250$ W [see legend in (f)]. The pump wavelength is (a)–(f) 1054.5, 1055, 1056, 1057.5, 1064, and 1075 nm, respectively, which gradually narrows the MI gain spectrum (full black line). The black circled line shows the Raman spectrum.

Pumping at 1054.5 and 1055 nm [Figs. 5(a)–5(b)] gives very similar results, and the general trends can be clearly divided into regimes of high and low coherence, as discussed earlier. Interestingly, the overall coherence is almost unaffected when the Raman effect is turned off and the dip from ~8–12 THz remains. This can be explained by the wide MI gain spectrum that is almost uninfluenced by the Raman effect, which gives a smooth gain curve with a sharp cut-off. When the pump is moved further away from the ZDW the MI gain bandwidth decreases and becomes increasingly influenced by the Raman effect, in particular the tail of the Raman gain. In Figs. 5(e)–5(f) the MI gain bandwidth is very narrow, and it is only possible to amplify FWM sidebands that are relatively close to the pump. An overall coherence and stability improvement is therefore only observed for small frequency offsets, i.e., for cascaded FWM with several closely spaced sidebands.

In Figs. 5(a)–5(c), the MI gain peak is above the Raman gain peak, and the gain spectrum therefore has a very sharp cut-off due to a minimal contribution from the long-tailed Raman gain. The coherence improvement is consequently nearly the same irrespectively of the Raman effect. In Figs. 5(c)–5(f) the Raman gain has a much stronger effect on the MI gain spectrum that adds a shoulder to the tail of the spectrum, and the coherence improvement is hence decreased without the Raman effect.

The MI gain for small frequency offsets increases significantly when the pump wavelength is increased, which results in higher overall SNR. To further illustrate the difference for small frequency offsets, we show in Fig. 6 the spectral evolution for single simulations for the same pump wavelengths as in Fig. 5 but for a fixed frequency offset of 4 THz. In Figs. 6(a)–6(d) the pump is very close to the ZDW (black dashed line) and the FWM cascade is slowly amplified and broadened. When the pump is moved further away from the ZDW in Figs. 6(e)–6(f), the MI gain is higher and the FWM cascaded is amplified faster. A higher gain and faster amplification of the FWM cascade diminish the influence of noise.

These results can be divided into two broad regimes depending on the bandwidth of the MI gain, ν_{MI}, and the peak of the Raman gain, ν_{Raman}.

(i) $\nu_{\mathrm{MI}} \gg \nu_{\mathrm{Raman}}$: The MI gain spectrum has a sharp cut-off and the coherence will be improved both for small frequency offsets and in a band near ν_{MI}.

(ii) $\nu_{\mathrm{MI}} \ll \nu_{\mathrm{Raman}}$: The MI gain is high for small frequency offsets and has a slowly decreasing tail from the Raman effect. This gives a single region with improved coherence and SNR for small frequency offsets.

The results in [24] correspond to the first case while [20] corresponds to the second.

The overall coherence and SNR in all cases show a strong dependence on the exact frequency offset of the seed. We emphasize that this is not a numerical artefact but reflects that the seeding process is very sensitive to the exact input parameters.

D. Coherent and Incoherent Rogue Waves

There is a striking difference in the statistical properties of the large rogue-like solitons generated in Fig. 6: In (b) a powerful soliton is generated completely incoherently, but

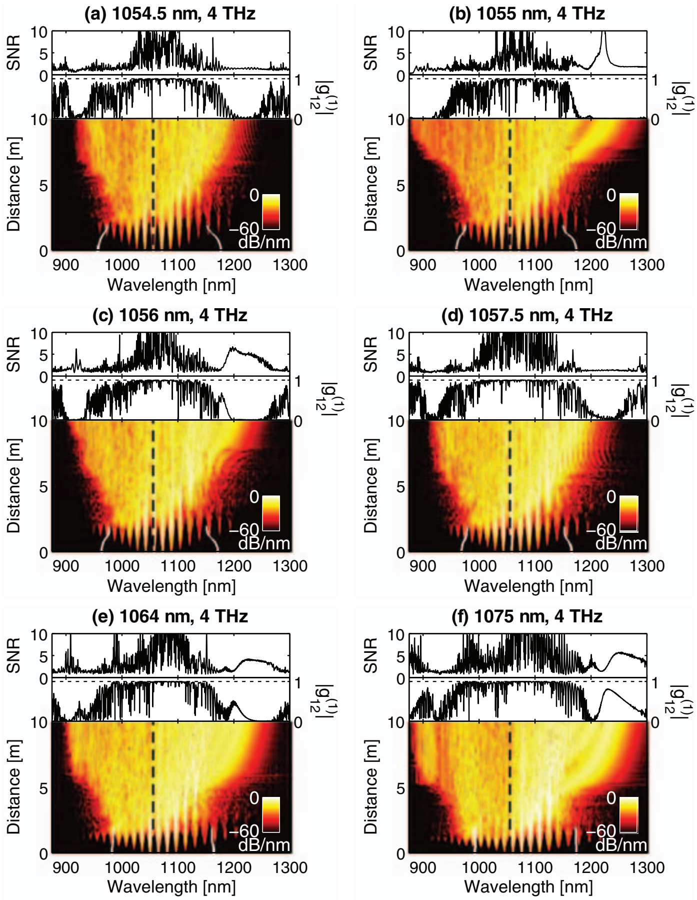

Fig. 6. (Color online) Single-shot simulations of a 5% seed with a 4 THz offset for the pump wavelengths in Fig. 5. The white lines indicate the MI gain bandwidth and the black dashed line the ZDW. The top rows show the ensemble calculated SNR and spectral coherence ($|g_{12}^{(12)}|$).

with high SNR, whereas in (f) the rogue soliton is generated with both high coherence and SNR. The existence of such two distinct different types of rogue waves has, to the best of our knowledge, not been demonstrated before.

To understand the difference between a coherent and incoherent rogue wave, we show in Fig. 7 the temporal evolution and spectrogram at the fiber output corresponding to the results in Figs. 6(b) and 6(f). The seed causes a beating of the temporal profile, which leads to a deterministic pulse breakup. When the pump is close to the ZDW [Fig. 7(a)], the MI gain is small and slowly increasing with frequency. The temporal profile is therefore only slowly broken up into solitons. This means that the solitons are mainly generated from the pulse center where the peak power is highest. The solitons have time to redshift before the cascade is amplified and the dynamics is relatively turbulent. In contrast to this, pumping further from the ZDW [Fig. 7(b)] gives a much larger and more rapidly increasing gain. This causes a fast breakup of the temporal pulse, where the individual temporal fringes generate fundamental solitons in a controlled fashion that almost resembles soliton fission. The most powerful solitons are still generated near the center of the pulse where the power is highest. These powerful solitons only collide with the smaller solitons generated from the trailing edge of the pulse. To summarize,

(i) Coherent rogue wave (high coherence and SNR): A large and rapidly increasing MI gain gives a fast breakup of the pulse into solitons. The solitons are generated deterministically with high coherence and are not very affected by collisions.

(ii) Incoherent rogue wave (low coherence, high SNR): A small and slowly increasing gain allows the solitons to start redshifting before the FWM cascade is fully amplified. The coherence is degraded due to collisions.

We emphasize that the generation of both coherent and incoherent rogue solitons was observed for several of the frequency offsets and pump wavelengths considered here.

5. SEEDING AT HIGH PEAK POWER

The results presented in the previous sections and in the literature [19,20,22–24,32] all indicate that a cleverly chosen

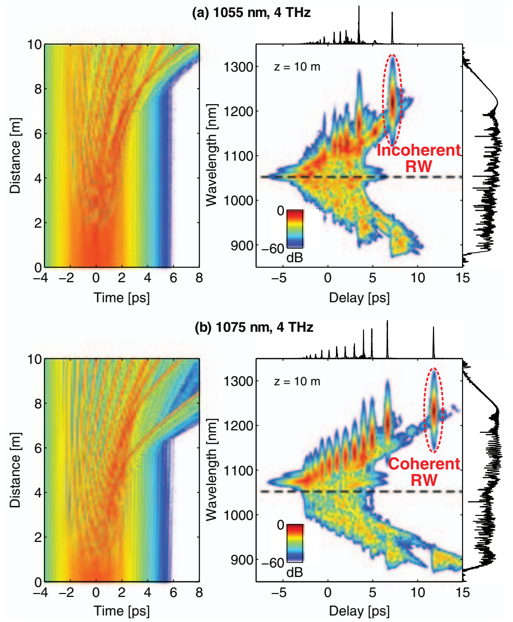

Fig. 7. (Color online) Temporal evolution and spectrogram at the fiber end (10 m) for a 5% seed with a 4 THz offset for pump wavelengths of (a) 1055 nm and (b) 1075 nm, corresponding to Figs. 6(b) and 6(f). The black dashed lines in the spectrograms mark the ZDW.

seed can be used to effectively manipulate the pulse breakup and improve the noise characteristics or even trigger the SC generation. While it has thus been demonstrated that seeding a low peak power pump offers several improvements, the situation is very different when the peak power of the pump is increased, as we shall now demonstrate. The coherence properties at high power were discussed in [21], but only over very short propagation distances where the spectrum remains narrow.

Figure 8 shows the spectral evolution of single shot simulations when pumping at the Ytterbium wavelength of 1064 nm with a 5% seed at 3 THz offset for pump peak powers of 500, 750, and 1500 W, respectively. For a 250 W pump the 3 THz frequency offset gave the best coherence improvement [see Fig. 5(e)], due to the controlled breakup of the pump by cascaded FWM, resulting in an overall coherence of 0.66. In Fig. 8(a) the peak power is doubled to 500 W. The increased pump power results in a wider spectrum, but the overall coherence is reduced to 0.33 and the coherence improvement is limited to the central part of the spectrum that was directly generated by the initial cascaded FWM. The peak power is increased to 750 W in Fig. 8(b), which leads to the generation of several distinct solitons and GV matched DWs. The spectrum is not nearly as coherent as Fig. 8(a): The overall coherence is 0.16 and the coherence improvement is again limited to the central part of the spectrum. When the peak power is increased to 1500 W in Fig. 8(c), the initial FWM cascade is quickly washed out by the onset of highly phase-dependent soliton interaction and DW generation, and the output spectrum is incoherent over nearly the entire bandwidth with

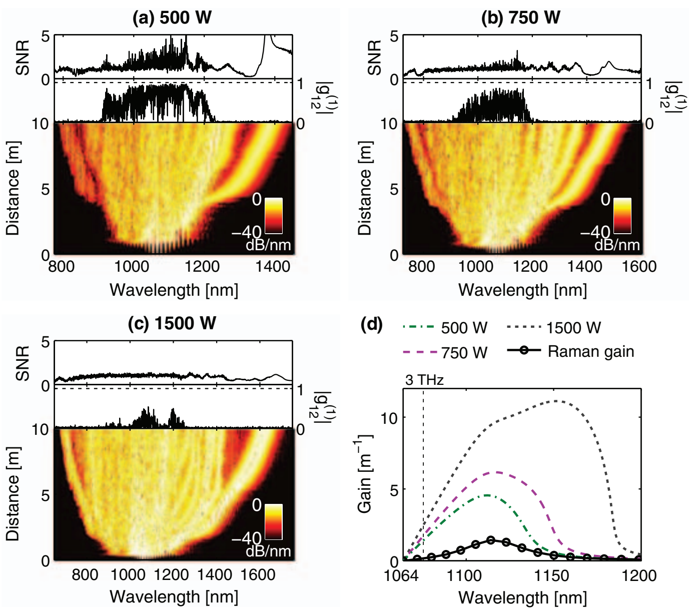

Fig. 8. (Color online) Single-shot simulations of pumping at 1064 nm with a 5% seed at a frequency offset of 3 THz for pump peak powers of (a)–(c) 500, 750, and 1500 W, respectively. The top rows show the signal-to-noise ratio (SNR) and spectral coherence ($|g_{12}^{(12)}|$). (d) MI and Raman gain spectra. The vertical line marks 3 THz offset.

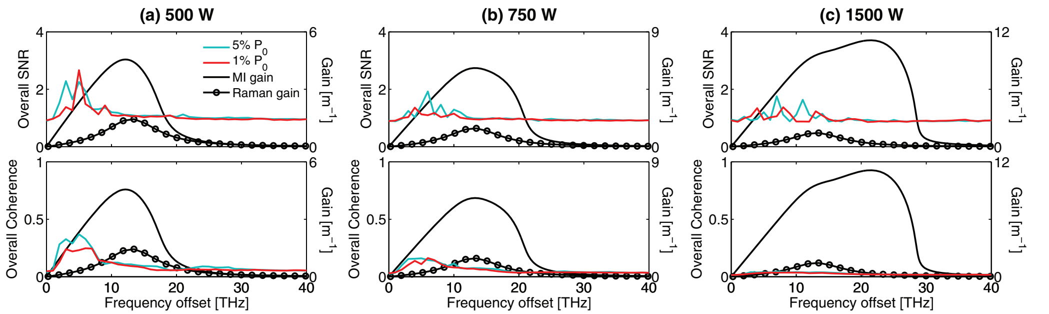

Fig. 9. (Color online) Overall SNR and coherence as a function of pump-seed frequency offset, shown for seed peak powers of 1% and 5% of the pump peak power [see legend in (a)]. The pump wavelength was 1064 nm and the peak power (a)–(c) 500, 700, and 1500 W. The MI and Raman spectra are shown with the full and circled black lines, respectively.

an overall coherence of just 0.040. In all cases, the formation of rouge-like solitons leads to small improvements in the intensity stability around the soliton, but this too seems to be gradually washed out by the turbulent dynamics that govern the evolution and interaction of many solitons and DWs when the peak power is increased.

In Fig. 9 is shown the overall coherence and SNR corresponding to peak powers of 500, 750, and 1500 W, which are the same peak powers that were used in Fig. 8. The results for the lowest peak power in Fig. 9(a) show a minor improvement for seeding close to the pump, but nothing like what was observed in Fig. 5(e) at 250 W. When the peak power is increased further in Figs. 9(b)–9(c), there is basically no overall improvement in coherence and intensity stability irrespectively of the pump-seed frequency offset.

When the pump power is increased the improvements afforded by seeding are thus quickly washed out by turbulent solitonic dynamics. In [10] it was experimentally demonstrated that the spectral noise increases with the pump power, although this was for a very different set-up where a fiber with two closely spaced ZDWs was back-seeded. As discussed in [21], the pulse breakup can be completely deterministic and coherent also at high pump powers, but as soon as the initial comb structure is broken into solitons the coherence is degraded by the subsequent highly phase-dependent interactions. In other words, the typical broadband and flat SC spectrum in most high-power experiments comes at a price of a low coherence as it is intrinsically dominated by solitonic dynamics.

6. DISCUSSION AND CONCLUSIONS

It seems doubtful that seeding can improve the noise properties at power levels like those in commercial SC sources. Although a coherent pulse breakup can be achieved at these power levels, the coherence will only be preserved over a very short propagation distance for which the spectrum remains relatively narrow. Seeding nonetheless remains an interesting approach for optical switching [19], where the presence of a seed pulse triggers the SC broadening that would otherwise be below threshold.

Seeding is very sensitive to the exact input parameters, such as the wavelength and power of both the pump and seed, and ultimately has to be studied case-by-case. It is however possible to identify some broad regimes dominated by certain mechanisms, as demonstrated in this work. Controlling the generation of rogue waves by modulating the pump pulse therefore also seems limited to relatively low power levels. In particular, it is difficult to imagine that extremely large solitonic rogue waves can be deterministically generated by seeding a high power pump, as these waves can only be generated through energy transfer from many collisions, which cannot be controlled by seeding.

In conclusion, we have investigated the influence of the pump power and MI gain spectrum on seeding. We analyzed the results both in terms of spectral coherence and intensity stability. For a low pump power we found that seeding can give a deterministic pulse breakup due to FWM between the seed and pump. The overall stability of the spectrum can be improved by seeding close to the pump, which gives a broad FWM cascade with many sidebands. However, for a broad MI spectrum, an overall stability improvement is also observed when seeding close to the peak of the MI spectrum, which allows a single set of FWM sidebands to be coherently amplified. It was demonstrated that rogue waves can be excited both coherently and incoherently from the FWM cascade, depending on the MI gain. Finally, it was found that seeding has no or little influence on the noise properties when the pump power is increased to the kW level. At these power levels turbulent solitonic dynamics quickly washes out the coherent pulse breakup.

ACKNLOWLEDGMENT

The authors thank the Danish Agency of Science, Technology and Innovation for support of the project no. 09-070566.

REFERENCES

1. J. M. Dudley, G. Genty, and S. Coen, "Supercontinuum generation in photonic crystal fiber," Rev. Mod. Phys. **78**, 1135–1184 (2006).
2. P. Beaud, W. Hodel, B. Zysset, and H. Weber, "Ultrashort pulse propagation, pulse breakup, and fundamental soliton formation in a single-mode optical fiber," IEEE J. Quantum Electron. **23**, 1938–1946 (1987).
3. J. M. Stone and J. C. Knight, "Visibly 'white' light generation in uniformphotonic crystal fiber using a microchip laser," Opt. Express **16**, 2670–2675 (2008).
4. J. C. Travers and J. R. Taylor, "Soliton trapping of dispersive waves in tapered optical fibers," Opt. Lett. **34**, 115–117 (2009).
5. J. C. Travers, "Blue extension of optical fibre supercontinuum generation," J. Opt. **12**, 113001 (2010).

6. S. T. Sørensen, A. Judge, C. L. Thomsen, and O. Bang, "Optimum fiber tapers for increasing the power in the blue edge of a supercontinuum—group-acceleration matching," Opt. Lett. **36**, 816–818 (2011).
7. M. H. Frosz, P. M. Moselund, P. D. Rasmussen, C. L. Thomsen, and O. Bang, "Increasing the blue-shift of a supercontinuum by modifying the fiber glass composition," Opt. Express **16**, 21076–21086 (2008).
8. V. Tombelaine, C. Lesvigne, P. Leproux, L. Grossard, V. Couderc, J.-L. Auguste, J.-M. Blondy, G. Huss, and P.-H. Pioger, "Ultra wide band supercontinuum generation in air-silica holey fibers by SHG-induced modulation instabilities," Opt. Express **13**, 7399–7404 (2005).
9. J. C. Travers, S. V. Popov, and J. R. Taylor, "Extended blue supercontinuum generation in cascaded holey fibers," Opt. Lett. **30**, 3132–3134 (2005).
10. P. M. Moselund, M. H. Frosz, C. L. Thomsen, and O. Bang, "Back-seeding of higher order gain processes in picosecond supercontinuum generation," Opt. Express **16**, 11954–11968 (2008).
11. P. M. Moselund, "Long-pulsed supercontinuum sources," Ph.D. dissertation, DTU Fotonik, Dept. of Photonics Engineering, Technical Univ. of Denmark (2009).
12. N. Brauckmann, M. Kues, T. Walbaum, P. Groß, and C. Fallnich, "Experimental investigations on nonlinear dynamics in supercontinuum generation with feedback," Opt. Express **18**, 7190–7202 (2010).
13. M. N. Islam, G. Sucha, I. Bar-Joseph, M. Wegener, J. P. Gordon, and D. S. Chemla, "Femtosecond distributed soliton spectrum in fibers," J. Opt. Soc. Am. B **6**, 1149–1158 (1989).
14. O. Bang and M. Peyrard, "Generation of high-energy localized vibrational modes in nonlinear Klein-Gordon lattices," Phys. Rev. E **53**, 4143–4152 (1996).
15. O. Bang and P. D. Miller, "Exploiting discreteness for switching in waveguide arrays," Opt. Lett. **21**, 1105–1107 (1996).
16. F. Luan, D. V. Skryabin, A. V. Yulin, and J. C. Knight, "Energy exchange between colliding solitons in photonic crystal fibers," Opt. Express **14**, 9844–9853 (2006).
17. G. Genty, C. M. de Sterke, O. Bang, F. Dias, N. Akhmediev, and J. M. Dudley, "Collisions and turbulence in optical rogue wave formation," Phys. Lett. A **374**, 989–996 (2010).
18. D. R. Solli, C. Ropers, P. Koonath, and B. Jalali, "Optical rogue waves," Nature **450**, 1054–1057 (2007).
19. D. R. Solli, C. Ropers, and B. Jalali, "Active control of rogue waves for stimulated supercontinuum generation," Phys. Rev. Lett. **101**, 233902 (2008).
20. G. Genty, J. Dudley, and B. Eggleton, "Modulation control and spectral shaping of optical fiber supercontinuum generation in the picosecond regime," Appl. Phys. B **94**, 187–194 (2009).
21. G. Genty and J. Dudley, "Route to coherent supercontinuum generation in the long pulse regime," IEEE J. Quantum Electron. **45**, 1331–1335 (2009).
22. D. R. Solli, B. Jalali, and C. Ropers, "Seeded supercontinuum generation with optical parametric down-conversion," Phys. Rev. Lett. **105**, 233902 (2010).
23. K. K. Y. Cheung, C. Zhang, Y. Zhou, K. K. Y. Wong, and K. K. Tsia, "Manipulating supercontinuum generation by minute continuous wave," Opt. Lett. **36**, 160–162 (2011).
24. Q. Li, F. Li, K. K. Y. Wong, A. P. T. Lau, K. K. Tsia, and P. K. A. Wai, "Investigating the influence of a weak continuous-wave-trigger on picosecond supercontinuum generation," Opt. Express **19**, 13757–13769 (2011).
25. M. H. Frosz, T. Sørensen, and O. Bang, "Nanoengineering of photonic crystal fibers for supercontinuum spectral shaping," J. Opt. Soc. Am. B **23**, 1692–1699 (2006).
26. G. Agrawal, *Nonlinear Fiber Optics*, 4th ed. (Academic, 2007).
27. C. Agger, C. Petersen, S. Dupont, H. Steffensen, J. K. Lyngsø, C. L. Thomsen, J. Thøgersen, S. R. Keiding, and O. Bang, "Supercontinuum generation in ZBLAN fibers—detailed comparison between measurement and simulation," J. Opt. Soc. Am. B **29**, 635–645 (2012).
28. J. Laegsgaard, "Mode profile dispersion in the generalised nonlinear Schrödinger equation," Opt. Express **15**, 16110–16123 (2007).
29. J. Hult, "A fourth-order Runge–Kutta in the interaction picture method for simulating supercontinuum generation in optical fibers," J. Lightwave Technol. **25**, 3770–3775 (2007).
30. J. M. Dudley and S. Coen, "Coherence properties of supercontinuum spectra generated in photonic crystal and tapered optical fibers," Opt. Lett. **27**, 1180–1182 (2002).
31. S. T. Sørensen, O. Bang, B. Wetzel, and J. M. Dudley, "Describing supercontinuum noise and rogue wave statistics using higher-order moments," Opt. Commun. **285**, 2451–2455 (2012).
32. J. M. Dudley, G. Genty, and B. J. Eggleton, "Harnessing and control of optical rogue waves in supercontinuum generation," Opt. Express **16**, 3644–3651 (2008).

Paper VII

The role of phase coherence in seeded supercontinuum generation

S. T. Sørensen, C. Larsen, U. Møller, P. M. Moselund, C. L. Thomsen, and O. Bang
Opt. Express **20**, 22886-22894 (2012).

Abstract: The noise properties of a supercontinuum can be controlled by modulating the pump with a seed pulse. In this paper, we numerically investigate the influence of seeding with a partially phase coherent weak pulse or continuous wave. We demonstrate that the noise properties of the generated supercontinuum are highly sensitive to the degree of phase noise of the seed and that a nearly coherent seed pulse is needed to achieve a coherent pulse break-up and low noise supercontinuum. The specific maximum allowable linewidth of the seed laser is found to decrease with increasing pump power.

http://dx.doi.org/10.1364/OE.20.022886

The role of phase coherence in seeded supercontinuum generation

Simon Toft Sørensen,[1,*] **Casper Larsen,**[1] **Uffe Møller,**[1]
Peter M. Moselund,[2] **Carsten L. Thomsen,**[2] **and Ole Bang**[1,2]

[1] *DTU Fotonik, Department of Photonics Engineering, Technical University of Denmark, 2800 Kgs. Lyngby, Denmark*
[2] *NKT Photonics A/S, Blokken 84, DK-3460, Birkerød, Denmark*
[*] *stso@fotonik.dtu.dk*

Abstract: The noise properties of a supercontinuum can be controlled by modulating the pump with a seed pulse. In this paper, we numerically investigate the influence of seeding with a partially phase coherent weak pulse or continuous wave. We demonstrate that the noise properties of the generated supercontinuum are highly sensitive to the degree of phase noise of the seed and that a nearly coherent seed pulse is needed to achieve a coherent pulse break-up and low noise supercontinuum. The specific maximum allowable linewidth of the seed laser is found to decrease with increasing pump power.

OCIS codes: (030.1640) Coherence; (190.4370) Nonlinear Optics, fibers; (190.4380) Nonlinear optics, four-wave mixing; (320.6629) Supercontinuum generation.

References and links

1. J. M. Dudley, G. Genty, and S. Coen, "Supercontinuum generation in photonic crystal fiber," Rev. Mod. Phys. **78**, 1135–1184 (2006).
2. U. Møller, S. T. Sørensen, C. Jakobsen, J. Johansen, P. M. Moselund, C. L. Thomsen, and O. Bang, "Power dependence of supercontinuum noise in uniform and tapered PCFs," Opt. Express **20**, 2851–2857 (2012).
3. D. R. Solli, C. Ropers, and B. Jalali, "Active control of rogue waves for stimulated supercontinuum generation," Phys. Rev. Lett. **101**, 233902 (2008).
4. P. M. Moselund, M. H. Frosz, C. L. Thomsen, and O. Bang, "Back-seeding of higher order gain processes in picosecond supercontinuum generation," Opt. Express **16**, 11954–11968 (2008).
5. G. Genty, J. Dudley, and B. Eggleton, "Modulation control and spectral shaping of optical fiber supercontinuum generation in the picosecond regime," Appl. Phys. B **94**, 187–194 (2009).
6. G. Genty and J. Dudley, "Route to coherent supercontinuum generation in the long pulse regime," IEEE J. Quantum Electron. **45**, 1331 –1335 (2009).
7. N. Brauckmann, M. Kues, T. Walbaum, P. Groß, and C. Fallnich, "Experimental investigations on nonlinear dynamics in supercontinuum generation with feedback," Opt. Express **18**, 7190–7202 (2010).
8. D. R. Solli, B. Jalali, and C. Ropers, "Seeded supercontinuum generation with optical parametric down-conversion," Phys. Rev. Lett. **105**, 233902 (2010).
9. K. K. Y. Cheung, C. Zhang, Y. Zhou, K. K. Y. Wong, and K. K. Tsia, "Manipulating supercontinuum generation by minute continuous wave," Opt. Lett. **36**, 160–162 (2011).
10. Q. Li, F. Li, K. K. Y. Wong, A. P. T. Lau, K. K. Tsia, and P. K. A. Wai, "Investigating the influence of a weak continuous-wave-trigger on picosecond supercontinuum generation," Opt. Express **19**, 13757–13769 (2011).
11. S. T. Sørensen, C. Larsen, U. Møller, P. M. Moselund, C. L. Thomsen, and O. Bang, "Influence of pump power and modulation instability gain spectrum on seeded supercontinuum and rogue wave generation," J. Opt. Soc. Am. B. **29**, 2875–2885 (2012).
12. J. Laegsgaard, "Mode profile dispersion in the generalised nonlinear Schrödinger equation," Opt. Express **15**, 16110–16123 (2007).
13. S. B. Cavalcanti, G. P. Agrawal, and M. Yu, "Noise amplification in dispersive nonlinear media," Phys. Rev. A **51**, 4086–4092 (1995).

#172872 - $15.00 USD Received 18 Jul 2012; revised 5 Sep 2012; accepted 16 Sep 2012; published 21 Sep 2012

14. M. H. Frosz, "Validation of input-noise model for simulations of supercontinuum generation and rogue waves," Opt. Express **18**, 14778–14787 (2010).
15. J. M. Dudley and S. Coen, "Coherence properties of supercontinuum spectra generated in photonic crystal and tapered optical fibers," Opt. Lett. **27**, 1180–1182 (2002).
16. S. T. Sørensen, O. Bang, B. Wetzel, and J. M. Dudley, "Describing supercontinuum noise and rogue wave statistics using higher-order moments," Opt. Commun. **285**, 2451 – 2455 (2012).
17. G. Genty, M. Surakka, J. Turunen, and A. T. Friberg, "Complete characterization of supercontinuum coherence," J. Opt. Soc. Am. B **28**, 2301–2309 (2011).
18. P. M. Moselund, "Long-pulse supercontinuum light sources," Ph.D. thesis (Technical University of Denmark, 2009).

1. Introduction

The noise properties of supercontinuum (SC) generation have attracted a lot of attention due to a large application demand for low noise SC sources [1,2]. Commercial SC sources are typically based on high-power picosecond or nanosecond pump lasers. For such lasers the pulse break-up is initiated by noise-driven modulational instability (MI), which causes large shot-to-shot fluctuations. It has been demonstrated that the noise can be significantly reduced by modulating the pump pulse in order to ensure a deterministic rather than noise-driven pulse breakup [3–11]. Seeding was numerically investigated in [5, 6, 10, 11]. In all cases a phase coherent seed was used to achieve a coherent pulse break-up through the amplification of a cascade of four-wave mixing (FWM) side-bands. Experimentally, seeding was investigated in [3, 4, 7–9]. In [3, 8, 9] the seed was used to trigger sub-threshold SC generation. The seed was generated by stretching and filtering a fraction of the pump in [3], while [8] used the signal and idler from an optical parametric amplifier as pump and seed. In [9] a separate continuous wave (CW) source was used as seed. It is thus fair to assume that the seeds in [3, 8, 9] were at least partially coherent with the pump. In [4, 7] the generated SC from one pulse was used as a broadband seed for the following pulse either by back-seeding or using a ring cavity. SC generation with feedback is however dynamically different from the approach used in this work, where the pump pulse is modulated with a seed as in [3, 5, 6, 8–11].

While it has thus been shown that seeding can reduce the SC noise, this has been for coherent seeds. In this paper, we numerically investigate the influence of pump power and the phase coherence of the seed on the seeding process, and demonstrate the need for seeding nearly coherently to get a deterministic pulse break-up and thus an improvement in noise. This has, to the best of our knowledge, not been shown before. The results are important in designing seeded low noise SC sources.

2. Numerical model and statistical analysis

We base the numerical work on solutions to the generalised nonlinear Schrödinger equation (GNLSE), which is known to produce spectra and noise properties in excellent agreement with experiments [1]. The GNLSE includes the effects of nonlinearties, the delayed Raman effect, self-steepening and higher-order dispersion necessary to accurately simulate pulse propagation in nonlinear fibers. We used the particular implementation described in [12] with the GNLSE solved in the interaction picture by an adaptive step-size fourth order Runge-Kutta solver. Noise was included as a background of one photon with a random phase in each discretisation bin. Additionally, noise was added to the seed pulse obtained from a physically justified phase-diffusion model [13, 14]. This model assumes fluctuations of the temporal phase, $\delta\phi(t)$, with zero ensemble mean, which results in a Lorentzian spectrum of linewidth $\Delta\nu_{\mathrm{FWHM}}$. The noise linewidth, $\Delta\nu_{\mathrm{FWHM}}$, is the only free parameter of the phase-diffusion model. Experimentally the noise linewidth will typically by fixed for a given laser source.

For the sake of simplicity, we assume a perfectly phase coherent pump and add phase noise

#172872 - $15.00 USD Received 18 Jul 2012; revised 5 Sep 2012; accepted 16 Sep 2012; published 21 Sep 2012

to the seed only. For a Gaussian pump and seed with the same temporal width, T_0, and peak powers P_p and P_s, respectively, the input field can thus be written as,

$$A(t) = \sqrt{P_p}\exp\left[\frac{-t^2}{2T_0^2}\right] + \sqrt{P_s}\exp\left[\frac{-t^2}{2T_0^2}\right] e^{i\Omega_{\mathrm{mod}}t}\exp\left[i\delta\phi(t)\right] + A_{\mathrm{OPPM}} \tag{1}$$

where Ω_{mod} is the modulation frequency of the seed relative to the pump and A_{OPPM} is the one photon per mode background noise. Both the background noise and the phase noise of the seed were varied from simulation to simulation. It should be noted that in Eq. (1) the Lorentzian power spectrum of the phase-diffusion model is convolved with the Gaussian power spectrum of the seed.

Ensemble statistics were calculated by carrying out simulations under identical conditions apart from the initial noise. The noise of the generated SC is quantified with the phase-sensitive spectral coherence function calculated from independent spectra, $\tilde{A}_i(\omega)$, [15],

$$\left|g_{12}^{(1)}(\omega)\right| = \left|\frac{\left\langle \tilde{A}_i^*(\omega)\tilde{A}_j(\omega)\right\rangle_{i\neq j}}{\sqrt{\left\langle|\tilde{A}_i(\omega)|^2\right\rangle\left\langle|\tilde{A}_j(\omega)|^2\right\rangle}}\right|, \tag{2}$$

where the angle brackets denote ensemble averages and the asterisk denotes complex conjugation. We will further use the overall coherence, $\int_0^\infty |g_{12}^{(1)}(\omega)|\langle|\tilde{A}(\omega)|^2\rangle d\omega / \int_0^\infty \langle|\tilde{A}(\omega)|^2\rangle d\omega$, to get a single value for the degree of coherence of an SC ensemble. The intensity noise is quantified by the signal-to-noise ratio (SNR) defined as the ratio of the mean, $\mu(\omega) = \langle|\tilde{A}_i(\omega)|^2\rangle$, to the standard deviation, $\sigma(\omega) = \langle(|\tilde{A}_i(\omega)|^2 - \mu(\omega))^2\rangle^{1/2}$,

$$\mathrm{SNR}(\omega) = \frac{\mu(\omega)}{\sigma(\omega)}. \tag{3}$$

The SNR is inversely proportional to the coefficient of variation introduced as an SC noise measure in [16], and is related to the relative intensity noise (RIN) used in most experiments on laser noise.

In the simulations we used a photonic crystal fiber (PCF) with pitch $\Lambda = 3.6$ μm and hole-to-pitch ratio $d/\Lambda = 0.52$, which gives a zero-dispersion wavelength of 1054 nm. The dispersion, effective area and MI gain spectrum are shown in Fig. 1. We used a Gaussian pump at 1064 nm with a peak power of $P_p = 250$ W and temporal width $T_{\mathrm{FWHM}} = 3$ ps. The seed had the same temporal width but only 5% of the peak power, and was given a frequency offset of 3 THz relative to the pump, i.e. a wavelength of 1075.5 nm. These parameters were found to give an optimum coherent pulse break-up into a FWM cascade for a fully coherent seed [11]. For each set of parameters 500 simulations were carried out, except for cases with a higher peak power or numerical resolution where only 250 simulations were used, which was found to be sufficient to get consistent statistical results. Loss was neglected and care was taken to avoid time-wrapping and conserve the photon number.

The coherence of the seed relative to the pump is quantified by the two-frequency cross-spectral density (CSD) function [17],

$$\left|\mathrm{CSD}(\omega_i,\omega_j)\right| = \left|\frac{\left\langle \tilde{A}^*(\omega_i)\tilde{A}(\omega_j)\right\rangle}{\sqrt{\left\langle|\tilde{A}(\omega_i)|^2\right\rangle\left\langle|\tilde{A}(\omega_j)|^2\right\rangle}}\right|, \tag{4}$$

which characterises the correlation between frequencies of the SC spectrum. In contrast, the spectral coherence function measures the correlation between an ensemble of SC spectra at

#172872 - $15.00 USD Received 18 Jul 2012; revised 5 Sep 2012; accepted 16 Sep 2012; published 21 Sep 2012

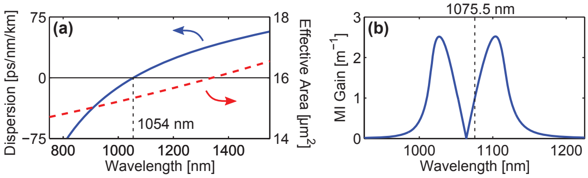

Fig. 1. (a) Dispersion and effective area for the used PCF with pitch $\Lambda = 3.6\ \mu$m and hole-to-pitch ratio $d/\Lambda = 0.52$. (b) MI gain as a function of wavelength for the 1064 nm pump with a peak power of 250 W. The dashed line marks the seed wavelength.

a single frequency. Figure 2 shows the ensemble averaged input spectra and CSD function for varying seed linewidth; the CSD function is calculated relative to the pump (1064 nm) and shows how the seed becomes increasingly incoherent with the pump when the linewidth is increased. The seed is partially coherent with the pump for linewidths larger than 1 GHz. The Lorentzian shape of the phase-diffusion model applied to the seed is clearly visible in the spectra, and it is seen that the seed linewidth is a simple way of changing the coherence of the seed relative to the pump.

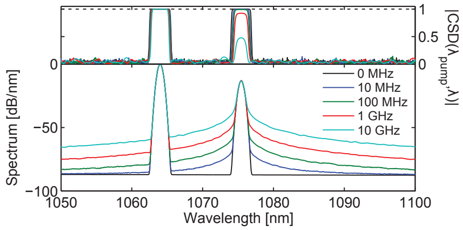

Fig. 2. Ensemble averaged input spectra (bottom) and cross-spectral density (CSD) function relative to the pump (top) for varying seed linewidth, $\Delta\nu_{\mathrm{FWHM}}$.

In [14] it was suggested to reshape the Lorentzian power spectrum into a Gaussian, which falls off much more rapidly. A Gaussian noise spectrum was demonstrated to give good agreement between simulations and experiments. This approach can, however, not be used for the seed linewidths considered in this work, as we shall elaborate on in more detail in the next section.

3. Results

The results of seeding with varying seed linewidth is shown in Fig. 3 for a select number of linewidths. In the absence of a seed the spectral broadening is initiated by noise-induced MI, as seen in Fig. 3(a). Unseeded MI amplifies a single set of side-bands that eventually evolves into solitons and dispersive waves. This results in an incoherent spectrum with unity SNR, except near the residual pump. By introducing a coherent seed near the pump, the spectral broadening is initiated by the coherent amplification of a cascaded FWM comb, as seen in Fig. 3(b). Subsequently, the comb leads to soliton formation. The resulting spectrum is coherent and with high SNR over most of the spectral bandwidth, where there is MI gain to allow a coherent broadening. When the linewidth of the seed is increased, as seen in Figs. 3(c)-(f), the broadening is still initiated by a FWM cascade, but the contrast of the comb is gradually washed out. This leads to a significant reduction of the coherence and SNR of the generated spectrum. In fact, for a seed linewidth in the GHz range, the noise properties are only marginally better than for an unseeded SC.

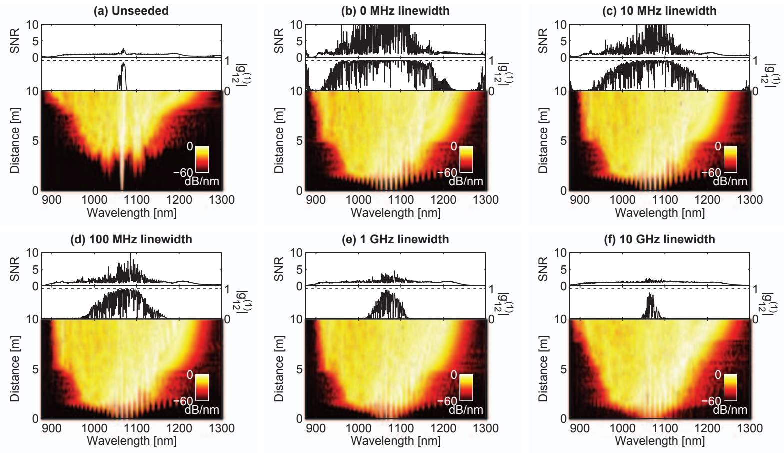

Fig. 3. Single shot simulations of (a) unseeded and (b)-(f) seeded SC generation with varying seed linewidth, $\Delta\nu_{\mathrm{FWHM}}$. The top rows show the ensemble calculated spectral coherence function and SNR at the fiber output (10 m).

To further illustrate the effect of seeding with a noisy seed, we show in Fig. 4 the ensemble calculated spectrum, spectral coherence function and SNR at a propagation distance of 1 m for the same seed linewidths used in Fig. 3. The input spectrum from a single shot is shown by a grey line. The comb structure is clearly visible in all cases, except the unseeded where only a single set of side-bands is incoherently amplified. In Fig. 4(c) the comb structure and noise properties are similar to those of the fully coherent seed in Fig. 4(b). However, when the seed linewidth is increased in Figs. 4(d)-(f) the fringe contrast of the comb is decreased and the coherence and SNR significantly diminished.

Figures 2 and 4 show how the Lorentzian noise spectrum raises the noise floor above that of the one photon per mode background noise. To confirm that the noise properties of the generated SC are indeed controlled by the phase noise of the seed and not the higher background noise imposed by the Lorentzian spectrum, we performed additional simulations with a background of multiple photons per mode and a fully coherent seed. To this end, we show in Fig. 5(a) a comparison of the ensemble calculated spectra, coherence and SNR for a coherent seed with normal (black line) and raised (blue line) background noise for which the noise floor at the pump is at approximately -90 and -70 dB/nm, respectively. The noise floor of -70 dB/nm corresponds to the average noise level at the pump from a partially coherent seed with a 1 GHz noise linewidth (see Fig. 2). It is seen that the outermost fringes of the comb are not generated when they are below the noise background. More importantly, we find that the comb is always generated with high fringe contrast, SNR and coherence irrespectively of the background noise level when the seed is fully coherent. In contrast, Fig. 5(b) shows a comparison of the results obtained for seed linewidths of 0 MHz and 1 GHz (average noise at the pump equal to -70 dB/nm) with a normal

#172872 - $15.00 USD Received 18 Jul 2012; revised 5 Sep 2012; accepted 16 Sep 2012; published 21 Sep 2012

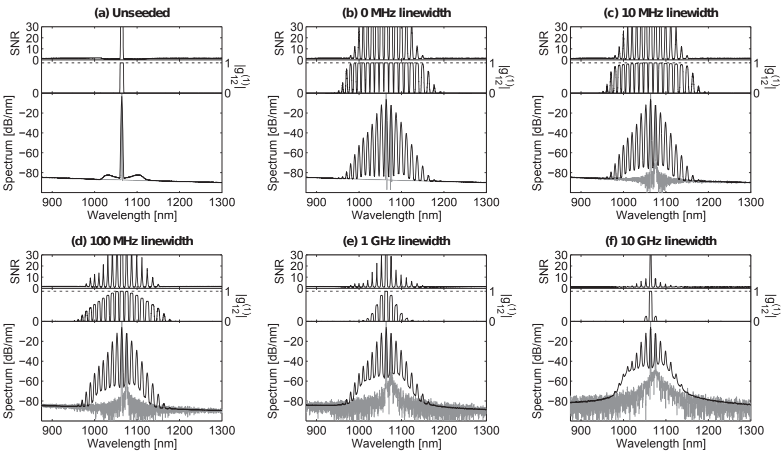

Fig. 4. Ensemble calculated spectra, coherence and SNR at a propagation distance of 1 m for (a) unseeded and (b)-(f) seeded SC generation with varying seed linewidth, $\Delta\nu_{\mathrm{FWHM}}$. The grey spectra show single shot input.

one photon per mode noise background, corresponding to Figs. 4(a) and 4(e). When the noise linewidth of the seed is increased, the fringe visibility of the comb is now seen to degrade much more severely and only the central fringe is generated with full coherence and high SNR. This is in sharp contrast to the effects of increasing the noise background, which leads us to conclude that the phase noise of the seed - and not the higher background noise level - is indeed the dominant effect responsible for the SC noise properties seen in Figs. 3-4.

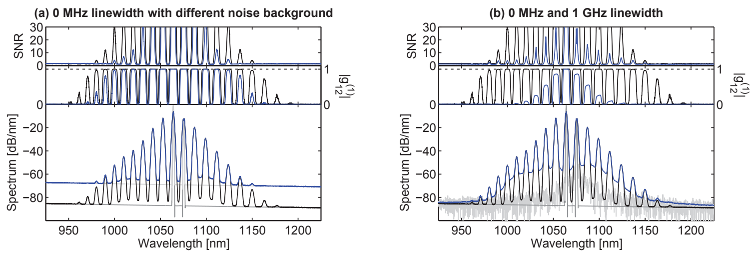

Fig. 5. Comparison of ensemble calculated spectra, coherence and SNR at a propagation distance of 1 m for (a) coherent seeding with normal (black) and raised (blue) background noise levels, and (b) seed linewidths of 0 MHz (black) and 1 GHz (blue) with a normal noise background. The grey spectra show single shot input.

The results are summarised in Fig. 6 by the overall coherence as a function of seed linewidth. We show the results of seeding for pump peak powers of 125, 250 and 500 W, respectively. The peak power of the seed was in all cases 5% of the pump. For the highest peak power only 250 simulations were carried out. As a further investigation, we also checked the results for a CW

#172872 - $15.00 USD Received 18 Jul 2012; revised 5 Sep 2012; accepted 16 Sep 2012; published 21 Sep 2012

seed. The CW field was approximated by a 10th order super-Gaussian with a 1/e width of 15 ps and a peak power of 1% of the pump, which gives a field that is constant seen by the pump pulse. In all cases, Fig. 6 clearly shows a decrease in the overall coherence with increasing seed linewidth. For the pulsed seed there is a major decrease in the overall coherence with increasing peak power. This is due to the increasingly turbulent dynamics caused by a higher number of solitons and spectra exceeding the MI gain bandwidth [11]: the spectral evolution after the pulse break-up is dominated by highly amplitude and phase-sensitive soliton collisions that significantly degrade the coherence. When the soliton number is increased there will be a corresponding increase in the number of such collisions and hence a decrease in the coherence of the generated spectrum. The seed linewidth at which the coherence is decreased by 25% relative to that of the coherent seed is marked with a black star. It is seen that the tolerance to phase noise on the seed is significantly decreased with increasing pump peak power, which again can be explained as a consequence of the increased number of solitons and collisions: when the number of collisions increases there will be a higher sensitivity to the initial shape and phase of the solitons, and hence to the phase noise of the seed that is responsible for the pulse break-up and soliton formation. For all peak powers there is however a clear decrease in overall coherence when the seed linewidth is increased above the MHz level. The same tendency is observed for the CW seed, which highlights the generality of the results: the phase noise of the seed must be weak in order for the pulse break-up and generated SC to be coherent.

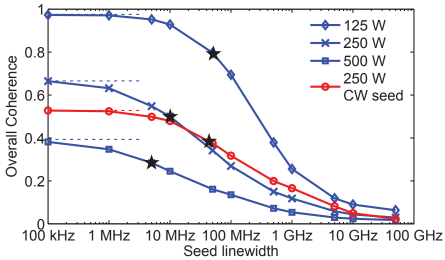

Fig. 6. Overall coherence as a function of seed linewidth, $\Delta\nu_{\mathrm{FWHM}}$, for pulsed and CW seeds at the fiber output (10 m). For the pulsed seed is shown results of pump peak powers of 125, 250 and 500 W, respectively. The pulsed seeds had 5% of the peak power of the pump and the CW seed had 1%. The horizontal dashed lines mark the overall coherence for a fully coherent seed and the black stars mark the seed linewidth at which the coherence is decreased by 25%.

The results presented so far were all calculated using a numerical resolution of 19.1 GHz, which is insufficient to resolve most of the relevant seed linewidths. To illustrate the implications of this, we show in Fig. 7(a) the overall coherence as a function of seed linewidth for various numerical frequency resolutions from 76.3 to 2.38 GHz and a peak power of 125 W. The frequency resolution was changed by fixing the temporal resolution and increasing the number of discretisation points from 2^{12} to 2^{17}, everything else was kept constant. For resolutions higher than 4.77 GHz (2^{16} points) only 250 simulations were carried out. The overall coherence is clearly observed to decrease with increasing frequency resolution. This tendency is even clearer in Fig. 7(b), where the overall coherence is shown as a function of frequency resolution down to 0.596 GHz (2^{19} points) for four fixed seed linewidths of 0.01, 0.1, 1 and 10 GHz, respectively. It is seen that the overall coherence converges when the frequency res-

#172872 - $15.00 USD Received 18 Jul 2012; revised 5 Sep 2012; accepted 16 Sep 2012; published 21 Sep 2012

olution approaches the seed linewidth, as expected. The 10 and 100 MHz seed linewidths can not be resolved and hence do not converge. Frequency resolutions smaller than ~1 GHz, which generally requires more than 2^{17} discretisation points, are computationally very intensive to simulate and it is therefore not possible to resolve noise linewidths much finer than 1 GHz. This also explains why it is not possible to use the Gaussian shaped noise model suggested in [14]: a Gaussian with a linewidth in the MHz is too narrow to be resolved numerically, whereas a long-tailed Loretzian spectrum falls off sufficiently slowly to be at least partially resolved.

We emphasize that the results presented in this paper are all *qualitatively* valid: when the seed linewidth is increased, the seed becomes increasingly incoherent with the pump as shown in Fig. 2. This results in an incoherent pulse break-up and correspondingly noisy and incoherent SC as seen in Figs. 3-4. These results clearly highlight the need for seeding with a seed that is at least partially coherent with the pump. However, one must be careful with making quantitative conclusions about noise and coherence based on the phase-diffusion model, unless the numerical resolution is at least comparable to the noise linewidth.

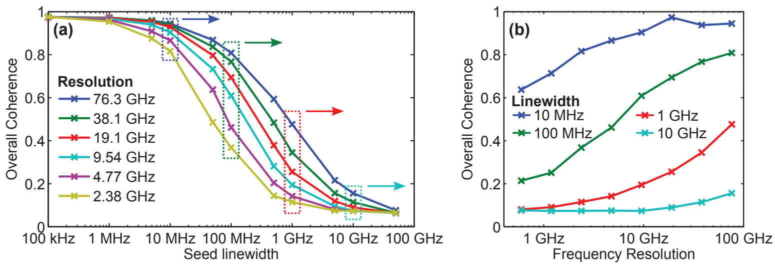

Fig. 7. (a) Overall coherence as a function of seed linewidth, $\Delta\nu_{\mathrm{FWHM}}$, for varying numerical frequency resolution. (b) Overall coherence as a function of numerical frequency resolution for the four seed linewidths marked by dotted boxes in (a). In all cases the pump peak power was 125 W.

The decrease in overall coherence with increasing numerical resolution shows that the maximum tolerable phase-noise of the seed is in fact quite small, although we can not accurately determine a quantitative value. Interestingly, Figs. 3-4 shows that the noise properties of the generated SC presented are deteriorated even when the linewidth of the seed is in the MHz range, although the seed is still coherent with the pump at the input ($\mathrm{CSD}(\lambda_{\mathrm{pump}}, \lambda_{\mathrm{seed}}) \approx 1$) as seen in Fig. 2. A linewidth of 100 MHz corresponds to just 0.4 pm, and since the actual tolerable seed linewidth will be smaller, this again clearly highlights the need for seeding coherently to achieve a coherent SC. Importantly, these results dictate which mechanisms can be used to generate the seed. It would be highly desirable to generate the seed by some frequency-shifting technique of the pump in an all-fiber design. A simple approach would be to use the Raman Stokes line as a seed. Unfortunately, a Raman amplified seed will generally not be coherent and have a significant noise linewidth. This exact approach was tested in [18], where no noise improvement was observed. However, a high peak power was used, which will by itself lead to noisy spectra due to chaotic solitonic dynamics irrespectively of the seed [11].

Finally, we would like to point out that FWM is a parametric and hence phase sensitive process. It was therefore to be expected that the amplification of a FWM comb eventually becomes noisy when the phase noise of the seed is increased. In the context of SC generation, the results presented in this work are nonetheless important, as they show just how sensitive

#172872 - $15.00 USD Received 18 Jul 2012; revised 5 Sep 2012; accepted 16 Sep 2012; published 21 Sep 2012

the seeding process is to the phase noise of the seed. In this paper we have only investigated the influence of phase noise on the seed for a single set of parameters of the pump and seed. In [11] it was found that seeding (under reasonable conditions) leads to the amplification of a number of FWM side-bands, and that the best noise improvement occurs for small pump-seed frequency offsets where a large number of FWM side-bands is coherently amplified. We have thus chosen the optimum seeding conditions as the starting point for this work. Seeding relies on the coherent amplification of FWM side-bands, which, as we have shown here, requires a seed that is at least partially coherent with the pump. Since FWM is a parametric process, we hence expect the results presented in this article to be valid for a wide range of parameters. A complete analysis of the exact dependence on, e.g., seed wavelength and power is beyond the scope of this manuscript.

4. Conclusions

In conclusion, we investigated the influence of the phase coherence of the seed on seeded SC generation. Numerical simulations were performed, in which the phase noise of the seed was modelled by a physically justified phase-diffusion model. For a coherent seed placed at the optimum near the pump, the pulse break-up is caused by a coherent amplification of a frequency comb through FWM. When phase noise is added to the seed, the pulse break-up and generated SC eventually become noisy. It was found that a coherent pulse break-up requires a nearly phase coherent seed, which limits the mechanisms that can be used to generate the seed. These tendencies were observed both for pulsed and CW seeding.

Acknowledgments

We thank the Danish Agency for Science, Technology and Innovation for financial support.

#172872 - $15.00 USD Received 18 Jul 2012; revised 5 Sep 2012; accepted 16 Sep 2012; published 21 Sep 2012

Paper VIII

Power dependence of supercontinuum noise in uniform and tapered PCFs

U. Møller, S. T. Sørensen, C. Jakobsen, J. Johansen, P. M. Moselund, C. L. Thomsen, and O. Bang
Opt. Express **20**, 2851-2857 (2012)

Abstract: We experimentally investigate the noise properties of picosecond supercontinuum spectra generated at different power levels in uniform and tapered photonic crystal fibers. We show that the noise at the spectral edges of the generated supercontinuum is at a constant level independent on the pump power in both tapered and uniform fibers. At high input power the spectral bandwidth is limited by the infrared loss edge, this however has no effect on the noise properties.

http://dx.doi.org/10.1364/OE.20.002851

Erratum

Opt. Express **20**, 23318-23319 (2012).

Abstract: An error was made in the calculation of the relative intensity noise (RIN) because of an incorrectly specified value of the photodetector DC transimpedance gain.

http://dx.doi.org/10.1364/OE.20.023318

Power dependence of supercontinuum noise in uniform and tapered PCFs

U. Møller,[1,*] **S. T. Sørensen,**[1] **C. Jakobsen,**[2] **J. Johansen,**[2]
P. M. Moselund,[2] **C. L. Thomsen,**[2] **and O. Bang**[1,2]

[1]*DTU Fotonik, Technical University of Denmark, DK-2800 Kgs. Lyngby, Denmark*
[2]*NKT Photonics A/S, Blokken 84, DK-3400 Birkerød, Denmark*
[*]*ufmo@fotonik.dtu.dk*

Abstract: We experimentally investigate the noise properties of picosecond supercontinuum spectra generated at different power levels in uniform and tapered photonic crystal fibers. We show that the noise at the spectral edges of the generated supercontinuum is at a constant level independent on the pump power in both tapered and uniform fibers. At high input power the spectral bandwidth is limited by the infrared loss edge, this however has no effect on the noise properties.

OCIS codes: (060.4370) Nonlinear optics, fibers; (060.5295) Photonic crystal fibers; (320.6629) Supercontinuum generation.

References and links

1. J. M. Dudley and J. R. Taylor, "Ten years of nonlinear optics in photonic crystal fibre," Nat. Photonics **3**, 85–90 (2009).
2. N. Savage, "Supercontinuum sources," Nat. Photonics **3**, 114–115 (2009).
3. W. Drexler, "Ultrahigh-resolution optical coherence tomography," J. Biomed. Opt. **9**, 47–74 (2004).
4. D. Wildanger, E. Rittweger, L. Kastrup, and S. W. Hell, "STED microscopy with a supercontinuum laser source," Opt. Express **16**, 9614–9621 (2008).
5. N. R. Newbury and W. C. Swann, "Low-noise fiber-laser frequency combs (Invited)," J. Opt. Soc. Am. B **24**, 1756–1770 (2007).
6. J. M. Dudley, G. Genty, and B. J. Eggleton, "Harnessing and control of optical rogue waves in supercontinuum generation." Opt. Express **16**, 3644–3651 (2008).
7. G. Genty, J. M. Dudley, and B. J. Eggleton, "Modulation control and spectral shaping of optical fiber supercontinuum generation in the picosecond regime," Appl. Phys. B **94**, 187–194 (2008).
8. D. R. Solli, C. Ropers, and B. Jalali, "Active control of rogue waves for stimulated supercontinuum generation," Phys. Rev. Lett. **101**, 18–21 (2008).
9. K. K. Y. Cheung, C. Zhang, Y. Zhou, K. K. Y. Wong, and K. K. Tsia, "Manipulating supercontinuum generation by minute continuous wave," Opt. Lett. **36**, 160–162 (2011).
10. Q. Li, F. Li, K. K. Y. Wong, A. Pak, T. Lau, and K. K. Tsia, "Investigating the influence of a weak continuous-wave-trigger on picosecond supercontinuum generation," Opt. Express **19**, 377–381 (2011).
11. P. M. Moselund, M. H. Frosz, C. L. Thomsen, and O. Bang, "Back-seeding of higher order gain processes in picosecond supercontinuum generation," Opt. Express **16**, 11954–11968 (2008).
12. P. Falk, M. Frosz, and O. Bang, "Supercontinuum generation in a photonic crystal fiber with two zero-dispersion wavelengths tapered to normal dispersion at all wavelengths," Opt. Express **13**, 7535–7540 (2005).
13. P. M. Moselund, "Long-pulse supercontinuum light sources," PhD thesis (Technical University of Denmark, Denmark, 2009).
14. A. Kudlinski, B. Barviau, A. Leray, C. Spriet, L. Héliot, and A. Mussot, "Control of pulse-to-pulse fluctuations in visible supercontinuum," Opt. Express **18**, 27445–27454 (2010).
15. D. Buccoliero, H. Steffensen, H. Ebendorff-Heidepriem, T. M. Monro, and O. Bang, "Midinfrared optical rogue waves in soft glass photonic crystal fiber," Opt. Express **19**, 17973–17978 (2011).
16. J. M. Dudley, G. Genty, and S. Coen, "Supercontinuum generation in photonic crystal fiber," Rev. Mod. Phys. **78**, 1135–1184 (2006).

#159492 - $15.00 USD   Received 7 Dec 2011; revised 3 Jan 2012; accepted 15 Jan 2012; published 23 Jan 2012

17. K. L. Corwin, N. R. Newbury, J. M. Dudley, S. Coen, S. A. Diddams, K. Weber, and R. S. Windeler, "Fundamental noise limitations to supercontinuum generation in microstructure fiber," Phys. Rev. Lett. **90**, 113904 (2003).
18. A. Hartung, A. M. Heidt, and H. Bartelt, "Design of all-normal dispersion microstructured optical fibers for pulse-preserving supercontinuum generation," Opt. Express **19**, 7742–7749 (2011).
19. O. Vanvincq, B. Barviau, A. Mussot, G. Bouwmans, Y. Quiquempois, and A. Kudlinski, "Significant reduction of power fluctuations at the long-wavelength edge of a supercontinuum generated in solid-core photonic bandgap fibers," Opt. Express **18**, 24352–24360 (2010).
20. C. Lafargue, J. Bolger, G. Genty, F. Dias, J. M. Dudley, and B. J. Eggleton, "Direct detection of optical rogue wave energy statistics in supercontinuum generation," Electron. Lett. **45**, 217–219 (2009).
21. D. R. Solli, C. Ropers, P. Koonath, and B. Jalali, "Optical rogue waves," Nature **450**, 1054–1057 (2007).
22. D. Derickson, ed., *Fiber Optic Test and Measurement* (Prentice Hall, 1998).
23. P. Beaud, W. Hodel, B. Zysset, and H. Weber, "Ultrashort pulse propagation, pulse breakup, and fundamental soliton formation in a single-mode optical fiber," IEEE J. Quantum Electron. **23**, 1938–1946 (1987).
24. F. Biancalana, D. V. Skryabin, and P. S. Russell, "Four-wave mixing instabilities in photonic-crystal and tapered fibers," Phys. Rev. E **68**, 046603 (2003).
25. A. V. Gorbach and D. V. Skryabin, "Light trapping in gravity-like potentials and expansion of supercontinuum spectra in photonic-crystal fibres," Nat. Photonics **1**, 653–657 (2007).
26. J. M. Stone and J. C. Knight, "Visibly 'white' light generation in uniform photonic crystal fiber using a microchip laser," Opt. Express **16**, 2670–2675 (2008).
27. J. C. Travers, "Blue extension of optical fibre supercontinuum generation," J. Opt. **12**, 113001 (2010).
28. S. Pricking and H. Giessen, "Tailoring the soliton and supercontinuum dynamics by engineering the profile of tapered fibers," Opt. Express **18**, 20151–20163 (2010).
29. S. T. Sørensen, A. Judge, C. L. Thomsen, and O. Bang, "Optimum fiber tapers for increasing the power in the blue edge of a supercontinuum-group-acceleration matching," Opt. Lett. **36**, 816–818 (2011).
30. N. R. Newbury, B. R. Washburn, K. L. Corwin, and R. S. Windeler, "Noise amplification during supercontinuum generation in microstructure fiber," Opt. Lett. **28**, 944–946 (2003).

1. Introduction

Supercontinuum generation (SCG) in photonic crystal fibers (PCFs) has drawn a lot of attention during the last decade [1]. The emergence of commercial fiber-based, long-pulsed supercontinuum (SC) sources has matured the technology [2], and the unique properties of SC light sources have made them ideal tools for a number of applications, including optical coherence tomography [3], fluorescence microscopy [4], and frequency combs [5]. However, SCG in commercial SC sources is initiated by modulation instability (MI) and thus, the SC is characterized by low coherence and high shot-to-shot fluctuations at the spectral edges. Several methods have been proposed to modify the spectrum and reduce the noise, including seeding by modulation of the input pulse [6, 7], seeding with minute pulsed and cw light [8–10], and back seeding [11]. Another approach to reduce the noise at a fixed wavelength has been to taper the PCF [12–14]. The influence of the material loss edge of soft glass PCFs has also been studied in the mid-IR [15].

Short-pulsed (femtosecond) SC is dominated by soliton fission processes and is fundamentally different from MI-initiated SCG and thus has different noise properties [6, 16, 17]. However, the higher complexity and lack of high average power makes these sources less attractive. Pumping in the normal dispersion regime will also drastically change the SC properties [18].

In this paper, we compare the noise properties of long-pulsed SC generated in a tapered and a uniform PCF, at different power levels. We investigate the full spectral region of 400-2400 nm. Recently, similar work has been done by Kudlinski *et al.* where they measured the shot-to-shot variations from a uniform and a tapered fiber for one fixed power level. They defined a noise measure given by the ratio $\sigma = 100 \cdot (V_{max} - V_{min})/(V_{max} + V_{min})$, where V_{max} and V_{min} are the maximum and minimum photodiode signal amplitudes, respectively, measured for at least 10 out of 10,000 recorded pulses, and showed that the noise was reduced in the tapered fiber when observing a fixed wavelength near the blue edge [14]. In this work we measure the relative intensity noise (RIN) in the whole parameter space of input power and wavelength, including the region of the silica material loss edge above 2 μm. RIN is a standard

#159492 - $15.00 USD Received 7 Dec 2011; revised 3 Jan 2012; accepted 15 Jan 2012; published 23 Jan 2012

measure for describing power fluctuations of lasers. Another article of Vanvincq *et al.* describes a significant reduction of power fluctuations at the long-wavelength edge of a SC generated in solid-core photonic bandgap (PBG) fibers [19]. There are three main reasons why this work is distinguished from the work of Vanvincq *et al.*. Firstly, the PBG fibers are less attractive from an application point of view, since the spectral bandwidth of SC generated in PBGs will be limited and thus not utilize the full potential of silica. Secondly, there is a fundamental difference of the guiding mechanisms and the soliton dynamics in PBG fibers compared to solid core PCFs. When a soliton is approaching the bandgap edge in a PBG fiber it will experience an asymptotic change of the group velocity dispersion (GVD). This change will cause the soliton to broaden in time and decrease in peak power adiabatically. It will never cross the bandgap edge due to the temporal broadening (and thereby reduction in redshift) arising from the increasing dispersion. Near the loss edge in a PCF the soliton will experience more or less the same GVD when redshifting, and the soliton energy will drop because of the gradually increasing material loss. However, it is still possible for the solitons to propagate into the loss region, with high-power solitons penetrating furthest. Since the soliton dynamics is different it is not obvious that the noise properties are the same for the two fibers. Thirdly, Vanvincq *et al.* investigated the noise properties at one power level where the spectrum was not limited by the material loss edge.

2. Experimental setup

For the experiments we used an ytterbium (Yb) fiber laser (NKT Photonics A/S) which delivers 10 ps pulses at 1064 nm at a repetition rate of 80 MHz. The laser delivery fiber was spliced to the PCFs to minimize coupling losses and instabilities. The PCF input power was 10 W, corresponding to a pulse energy of 125 nJ and a peak power of 11.7 kW when assuming Gaussian shaped pulses. The generated SC output was collimated and the spectra were measured with optical spectrum analyzers. The collimated SC output was guided through narrow-band pass filters (NBPs) of 10-30 nm full width at half maximum (450-1600 nm filters from Thorlabs and 1810-2310 nm from Multi-IR Optoelectronics Co., Ltd) and onto a photoreceiver (PR) (Newfocus 125 MHz Si and InGaAs photoreceivers for measurements in the 450-1000 and 1000-1600 nm range, respectively, and a Redwave Labs 100 MHz extended InGaAs photoreceiver for measurements in the 1600-2400 nm range). The photoreceiver was connected to an electrical spectrum analyzer (ESA) (sweeping for 30 s with a bandwidth of 10 kHz) and a voltmeter (V) to characterize the DC and AC voltage, respectively. A sketch of the experimental setup is shown in Fig. 1(a).

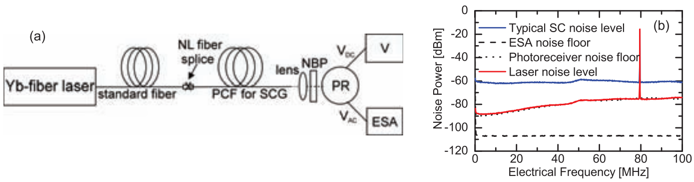

Fig. 1. (a) Experimental setup, see detailed description in text. (b) Noise power as a function of electrical frequency for a typical SC (blue line, 6.4 W input power at 1200 nm) and laser at 1064 nm (red line), respectively, and the noise floor for the electrical spectrum analyzer (dashed line) and the photoreceiver (dotted line), respectively.

Since the energy of the spectrally filtered pulses is proportional to their peak power, this measurement technique is adequate for measuring the shot-to-shot fluctuations [20, 21]. The RIN of the filtered wavelengths, i.e. the time series of power through the filters, were calculated

Received 7 Dec 2011; revised 3 Jan 2012; accepted 15 Jan 2012; published 23 Jan 2012

in the electrical frequency range of 20 kHz to 80 MHz. A full noise power spectrum is shown in Fig. 1(b). The dashed black line shows the noise floor of the electrical spectrum analyzer (ESA). The dotted line indicates the photoreceiver noise floor while the red line indicates the laser noise level. Note that the laser noise level and the photoreceiver noise floor in fact are indistinguishable, except at the carrier frequency of 80 MHz and thus it is not sensitive enough to resolve the real laser noise level. The blue line shows the noise power of a typical SC, which easily can be detected by the photoreceiver. When the DC photocurrent is simultaneously monitored, the noise properties of the SC can be quantified in terms of RIN as a function of wavelength and input power [22].

3. Results and discussion

3.1. Spectral characterization

A commercially available PCF (SC-5.0-1040, NKT Photonics A/S) with a total length of 10 m and a 4 m, asymmetric taper was fabricated directly on the draw-tower. This tapered fiber was compared to a uniform fiber of the same length. The output spectra for an input power of 10 W are depicted in Fig. 2(a) and profile of the tapered fiber is shown in the inset of Fig. 2(a). The fiber pitch was calculated from the continuous monitoring of the fiber diameter assuming that they are proportional. This was confirmed by several microscope images of the fiber cross section throughout the fiber. The tapered fiber is pumped from the fiber-end which gives most power in the blue edge according to the principle of group acceleration mismatch (GAM) [29]. The blue edge of the SC generated in the uniform fiber at a level of -10 dBm/nm is measured to

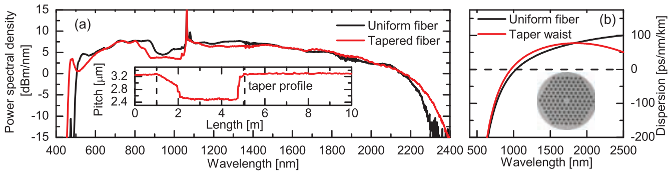

Fig. 2. (a) Spectra from a 10 m uniform PCF (black) and a 10 m PCF with a 4 m taper (red). Inset in (a): profile of the tapered fiber. (b) Calculated dispersion of the uniform fiber (black) and the taper waist (red). Inset in (b): microscope image of the fiber cross section.

be at 493 nm while it is 35 nm lower at 458 nm for the SC generated in the tapered fiber. The red edges of the SCs generated in the fibers are both limited by the IR material loss and at a -10 dBm/nm level they are measured to be at 2297 nm and 2342 nm for the uniform and tapered fiber, respectively. Figure 2(b) shows the calculated dispersion of the uniform fiber and at the taper waist, and the inset shows the cross sectional structure of the fiber.

The spectral edges of the SC are comprised by solitons and group-velocity (GV) matched dispersive waves [23–26]. The maximum spectral width and the position of the blue edge can hence be estimated from calculated GV curves. By tapering the fiber one can blueshift the blue edge [27–29]. For fibers with only one zero-dispersion wavelength (ZDW), such as the one we have here (see Fig. 2(b)), tapering will lead to an increased nonlinearity and thus in general to an increased redshift of solitons compared to a uniform fiber. For a given taper length and degree of tapering, the longer the downtapering the more power is in the dispersive waves trapped by the solitons due to reduced GAM [29].

#159492 - $15.00 USD Received 7 Dec 2011; revised 3 Jan 2012; accepted 15 Jan 2012; published 23 Jan 2012

3.2. Noise measurements

The noise in the SC process can be divided into two contributions: a low-frequency part originating from technical laser noise and a broadband frequency part originating from amplified quantum noise [17, 30]. We will here concentrate on the broadband frequency part. RIN is quantified by the noise power in a 1 Hz bandwidth normalized to the DC signal power, $RIN = (\Delta P)^2/P_{avg}^2$, where $(\Delta P)^2$ is the mean square intensity fluctuation spectral density and P_{avg} is the average optical power.

The SC noise in Fig. 1(b) is characterized by white noise in between dc and the pump frequency, which was observed for all measured SCs. Thus, the RIN is dependent on the wavelength and input power, but to a good approximation independent of the electrical frequency.

Figure 3 shows the RIN as a function of SC wavelength and average input power for the uniform and tapered fiber, respectively. The thick black line indicates the spectral edges of the

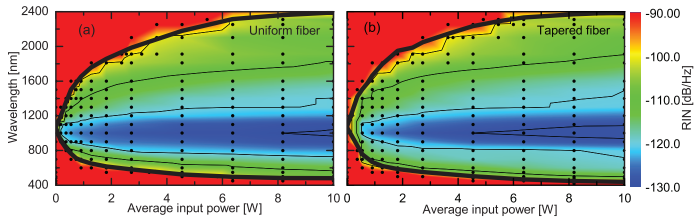

Fig. 3. RIN vs. input power and wavelength in (a) the uniform fiber and (b) the tapered fiber. The thick black line shows the spectral edges. The dots show the measurement points.

generated SC, defined at the -10 dBm/nm level, and the black dots indicate the actual measurement points, where the average RIN in the frequency region of 1-79 MHz has been measured. The noise properties of the SC generated in the two fibers are similar. At the spectral edge of the SC the RIN is about -100 dB/Hz. Generally, it decreases when the input power is increased (moving horizontally in Fig. 3) or the wavelength is chosen closer to the pump wavelength (moving vertically in Fig. 3). Thus, the minimum noise level of about -130 dB/Hz is observed close to the pump at a wavelength between 1000-1100 nm at the maximum input power level of 10 W. On the outer sides of the spectral edges the noise increases rapidly.

In Fig. 4(a) the RIN as a function of wavelength is compared for the uniform and the tapered fiber at two different power levels. The RIN of the tapered fiber is shown to be lower than the

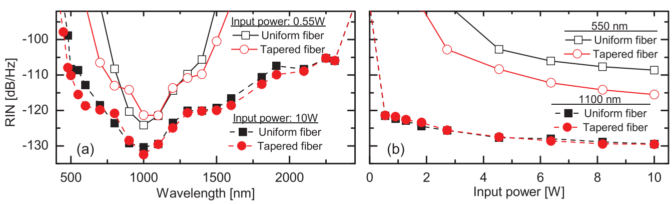

Fig. 4. RIN of the uniform (black squares) and the tapered fiber (red circles) (a) vs. wavelength at fixed input power of 0.55 W (open symbols) and 10 W (solid symbols) and (b) vs. input power at fixed wavelength of 550 nm (open symbols) and 1100 nm (solid symbols).

RIN of the uniform fiber for near-edge wavelengths. This is in good agreement with Kudlinski

#159492 - $15.00 USD Received 7 Dec 2011; revised 3 Jan 2012; accepted 15 Jan 2012; published 23 Jan 2012

et al. who have recently investigated the noise properties of tapered PCFs in the visible region [14]. They observed that the noise was reduced at the blue wavelength edge when the fiber was tapered and attributed it to a presumed increase of the spectral power density beyond 1750 nm. This increase will lead to increased probability to encounter solitons at the long wavelength side of the SC. Since the dispersive waves at the blue edge is group velocity matched to these solitons, the noise will also decrease in the blue edge of the SC. Our experiments show that for a *xed* wavelength near the spectral edge the noise will decrease when the fiber is tapered. This is, however, only due to the fact that the spectrum generated in a tapered fiber is broadened. Thus, looking at a near-edge wavelength *relative* to the spectral edge, e.g. 20 nm from the edge, of a SC generated in a uniform and a tapered fiber, respectively, will yield the same noise level.

Figure 4(b) shows the RIN as a function of input power for the uniform and the tapered fiber at a near-edge wavelength and at a central wavelength. It is clearly seen that the noise properties at a central wavelength for the two fibers are close to identical while the tapered fiber exhibit lower RIN for a fixed near-edge wavelength, which again is in good agreement with [14].

To further quantify the noise on the spectral edges of the SCs we have measured the RIN by adjusting the input power so that the spectral edge at a level of -10 dBm/nm is equivalent to the central wavelength of the narrow band filters. The RIN in the 1600-2400 nm range was not measured due to less well-defined filters and a noisier photoreceiver. In Fig. 5 it is clearly seen

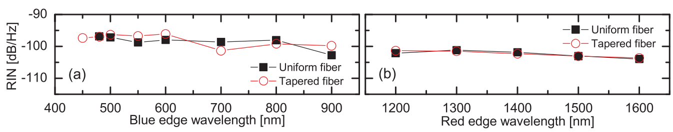

Fig. 5. RIN at the spectral (a) blue and (b) red edge of the uniform and tapered fiber, respectively, as a function of wavelength.

that the RIN level at the spectral edge is fixed at around -100 dB/Hz. The lower red edge noise level can be explained by the shape of the spectra. At the blue edge the spectrum is steep while it is more flat at the red edge. Since we have defined the edge to be at a level of -10 dBm/nm the the presence of a finite power spectral density (PSD) on the outer side of the red edge (below -10 dBm/nm) will lead to a reduction of the measured noise compared to the blue edge, where the is no PSD on the outer side of the blue edge because of the steep edge. Vanvincq *et al.* observed a significant reduction of power fluctuations at the long-wavelength edge of a SC generated in solid-core photonic bandgap fibers due to suppression of soliton self-frequency shift near the bandgap edge [19]. The dispersive waves below 550 nm in Fig. 5(a) will be matched to solitons above 2000 nm, i.e. solitons in the material loss region. Since we observe a nearly constant RIN in the blue edge, the materiel loss edge is thus not effecting the RIN.

4. Conclusion

We have experimentally investigated the RIN of picosecond SC generated at different power levels in uniform and tapered PCFs. When observing a fixed wavelength near the spectral edge the noise is reduced when the fiber is tapered. This reduction is however only due to the spectral shift of the spectrum. The noise at the spectral edge of a SC is constant independent of input power for both tapered and uniform fibers. An increase of power will generally lead to a decrease of noise for a fixed wavelength and the noise for a fixed power level will be lowest at the pump wavelength and highest at the spectral edges.

#159492 - $15.00 USD Received 7 Dec 2011; revised 3 Jan 2012; accepted 15 Jan 2012; published 23 Jan 2012

Acknowledgments

The authors acknowledge the H.C. Ørsted Foundation, Taumoses Legat, and the Danish Agency for Science, Technology and Innovation for the financial support of project no. 09-070566.

Power dependence of supercontinuum noise in uniform and tapered PCFs: erratum

Uffe Møller,[1,*] Simon T. Sørensen,[1] Christian Jakobsen,[2] Jeppe Johansen,[2] Peter M. Moselund,[2] Carsten L. Thomsen,[2] and Ole Bang[1,2]

[1] *DTU Fotonik, Department of Photonics Engineering, Technical University of Denmark, Ørsteds Plads, DK-2800 Kgs. Lyngby, Denmark*
[2] *NKT Photonics A/S, Blokken 84, DK-3400 Birkerød, Denmark*
[*] *ufmo@fotonik.dtu.dk*

Abstract: An error was made in the calculation of the relative intensity noise (RIN) because of an incorrectly specified value of the photodetector DC transimpedance gain.

OCIS codes: (060.4370) Nonlinear optics, fibers; (060.5295) Photonic crystal fibers; (320.6629) Supercontinuum generation.

References and links

1. U. Møller, S. T. Sørensen, C. Jakobsen, J. Johansen, P. M. Moselund, C. L. Thomsen, and O. Bang, "Power dependence of supercontinuum noise in uniform and tapered PCFs," Opt. Express **20**, 2851–2857 (2012).
2. U. Møller, S. T. Sørensen, C. Larsen, P. M. Moselund, C. Jakobsen, J. Johansen, C. L. Thomsen, and O. Bang, "Optimum PCF tapers for blue-enhanced supercontinuum sources," Opt. Fiber Technol. (2012), (article in press) http://dx.doi.org/10.1016/j.yofte.2012.07.010.

The DC transimpedance gain of the New Focus photodetectors used in [1] was mistakenly specified by the manufacturer to be $G_{DC} = 1\,V/mA$. The correct DC transimpedance gain is $G_{DC} = 10\,V/mA$ for an input impedance of 50 Ω and $G_{DC} = 20\,V/mA$ for an infinite input impedance. The AC transimpedance gain for a 50 Ω input impedance is as specified $G_{DC} = 40\,V/mA$. We have now measured these values and they have been confirmed by the manufacturer.

Since the relative intensity noise (RIN) is proportional to $[G_{DC}/G_{AC}]^2$ the RIN is increased by a factor of 400 corresponding to 26 dB. Below is shown Figs. 3–5 from [1] with the corrected RIN values. The corrected RIN measurements can also be found in [2].

The authors regret the error, but emphasize that it does not affect any of the conclusions presented in [1].

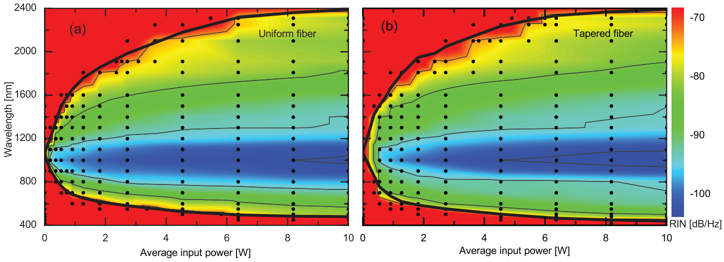

Fig. 3. RIN vs. input power and wavelength in (a) the uniform fiber and (b) the tapered fiber. The thick black line shows the spectral edges. The dots show the measurement points.

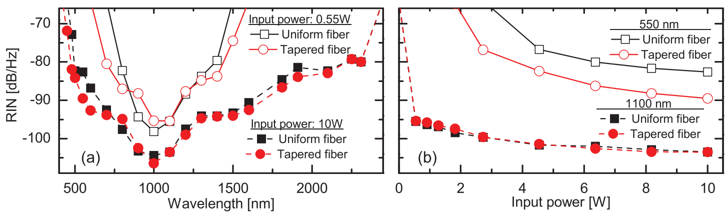

Fig. 4. RIN of the uniform (black squares) and the tapered fiber (red circles) (a) vs. wavelength at fixed input power of 0.55 W (open symbols) and 10 W (solid symbols) and (b) vs. input power at fixed wavelength of 550 nm (open symbols) and 1100 nm (solid symbols).

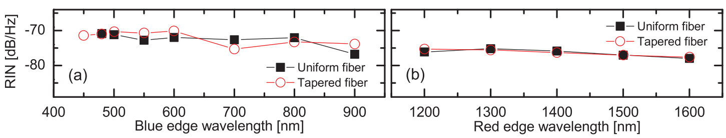

Fig. 5. RIN at the spectral (a) blue and (b) red edge of the uniform and tapered fiber, respectively, as a function of wavelength.

Bibliography

[1] J. M. Dudley, G. Genty, and S. Coen, "Supercontinuum generation in photonic crystal fiber," Rev. Mod. Phys. **78**, 1135–1184 (2006).

[2] J. M. Dudley and J. R. Taylor, "Ten years of nonlinear optics in photonic crystal fibre," Nat. Photon. **3**, 85–90 (2009).

[3] R. Alfano and S. Shapiro, "Observation of self-phase modulation and small-scale filaments in crystals and glasses," Phys. Rev. Lett. **24**, 592–594 (1970).

[4] R. Alfano and S. Shapiro, "Emission in the region 4000 to 7000 Åvia four-photon coupling in glass," Phys. Rev. Lett. **24**, 584–588 (1970).

[5] C. Lin and R. H. Stolen, "New nanosecond continuum for excited-state spectroscopy," Appl. Phys. Lett. **28**, 216 (1976).

[6] C. Lin, V. T. Nguyen, and W. G. French, "Wideband near-I.R. continuum (0.7-2.1 um) generated in low-loss optical fibres," Electron. Lett. **14**, 822–823 (1978).

[7] J. Knight, T. Birks, P. Russell, and D. Atkin, "All-silica single-mode optical fiber with photonic crystal cladding," Opt. Lett. **21**, 1547–1549 (1996).

[8] J. Knight, T. Birks, P. Russell, and D. Atkin, "All-silica single-mode optical fiber with photonic crystal cladding: errata," Opt. Lett. **22**, 484–485 (1997).

[9] J. Broeng, D. Mogilevstev, S. E. Barkou, and A. Bjarklev, "Photonic Crystal Fibers: A New Class of Optical Waveguides," Opt. Fiber Technol. **5**, 305–330 (1999).

[10] P. Russell, "Photonic crystal fibers," Science **299**, 358–62 (2003).

[11] P. S. J. Russell, "Photonic crystal fibers," J. Lightwave Technol. **24**, 4729–4749 (2006).

[12] J. Ranka, R. Windeler, and A. Stentz, "Visible continuum generation in air-silica microstructure optical fibers with anomalous dispersion at 800 nm," Opt. Lett. **25**, 25–27 (2000).

[13] J. M. Dudley, G. Genty, F. Dias, B. Kibler, and N. Akhmediev, "Modulation instability, Akhmediev Breathers and continuous wave supercontinuum generation," Opt. Express **17**, 21497–508 (2009).

[14] J. Herrmann, U. Griebner, N. Zhavoronkov, A. Husakou, D. Nickel, J. C. Knight, W. J. Wadsworth, P. S. J. Russell, and G. Korn, "Experimental Evidence for Supercontinuum Generation by Fission of Higher-Order Solitons in Photonic Fibers," Phys. Rev. Lett. **88**, 1–4 (2002).

[15] T. A. Birks, J. C. Knight, and P. S. Russell, "Endlessly single-mode photonic crystal fiber," Opt. Lett. **22**, 961–3 (1997).

[16] J. C. Knight, "Photonic crystal fibres," Nature **424**, 847–51 (2003).

[17] A. Hasegawa, "Generation of a train of soliton pulses by induced modulational instability in optical fibers," Opt. Lett. **9**, 288–90 (1984).

[18] K. Tai, A. Tomita, J. L. Jewell, and A. Hasegawa, "Generation of subpicosecond solitonlike optical pulses at 0.3 THz repetition rate by induced modulational instability," Appl. Phys. Lett. **49**, 236 (1986).

[19] M. Islam, G. Sucha, and I. Bar-Joseph, "Broad bandwidths from frequency-shifting solitons in fibers," Opt. Lett. **14**, 370–372 (1989).

[20] C. Y. Wang, P. L. Baldeck, Y. Budansky, and R. R. Alfano, "15-THz pulse generation arising from modulation instability oscillation in a colliding-pulse mode-locking dye laser." Opt. Lett. **14**, 497–9 (1989).

[21] E. J. Greer, D. M. Patrick, P. G. J. Wigley, and J. R. Taylor, "Generation of 2 THz repetition rare pulse trains through induced modulation instability," Electron. Lett. **25**, 1246–1248 (1989).

[22] E. M. Dianov, P. V. Mamyshev, A. M. Prokhorov, and S. V. Chernikov, "Generation of a train of fundamental solitons at a high repetition rate in optical fibers," Opt. Lett. **14**, 1008–10 (1989).

[23] P. Mamyshev and S. Chernikov, "Generation of a high-repetition-rate train of practically noninteracting solitons by using the induced modulational instability and Raman self-scattering effects," Opt. Lett. **15**, 1365–1367 (1990).

[24] V. Karpman and E. Krushkal, "Modulated waves in nonlinear dispersive media," Sov. Phys. JETP **28** (1969).

[25] N. Akhmediev and V. Korneev, "Modulation instability and periodic solutions of the nonlinear Schrödinger equation," Theor. Mat. Phys. **69** (1986).

[26] K. Tai, A. Hasegawa, and A. Tomita, "Observation of modulational instability in optical fibers," Phys. Rev. Lett. **56**, 0–4 (1986).

[27] D. R. Solli, C. Ropers, P. Koonath, and B. Jalali, "Optical rogue waves," Nature Lett. **450**, 1054–7 (2007).

[28] P. Müller, C. Garrett, and A. Osborne, "Rogue Waves - The fourteenth 'Aha Huliko'a Hawaiian Winter Workshop," Oceanography **18**, 66–75 (2005).

[29] N. Akhmediev, J. Soto-Crespo, and A. Ankiewicz, "Extreme waves that appear from nowhere: On the nature of rogue waves," Phys. Lett. A **373**, 2137–2145 (2009).

[30] N. Akhmediev, J. Soto-Crespo, and A. Ankiewicz, "Could rogue waves be used as efficient weapons against enemy ships?" Eur. Phys. J. **185**, 259–266 (2010).

[31] Y. Zhen-Ya, "Financial rogue waves," Commun. Theor. Phys. **54**, 947–949 (2010).

[32] O. Bang and M. Peyrard, “Generation of high-energy localized vibrational modes in nonlinear Klein-Gordon lattices,” Phys. Rev. E **53** (1996).

[33] A. Husakou and J. Herrmann, “Supercontinuum generation of higher-order solitons by fission in photonic crystal fibers,” Phys. Rev. Lett. **1**, 85–88 (2001).

[34] D. V. Skryabin, F. Luan, J. C. Knight, and P. S. J. Russell, “Soliton self-frequency shift cancellation in photonic crystal fibers,” Science **301**, 1705–8 (2003).

[35] P. Beaud, W. Hodel, B. Zysset, and H. P. Weber, “Ultrashort pulse propagation, pulse breakup, and fundamental soliton formation in a single-mode optical fiber,” IEEE J. Quantum Electron. **QE-23**, 1938–1946 (1987).

[36] A. V. Gorbach and D. V. Skryabin, “Theory of radiation trapping by the accelerating solitons in optical fibers,” Phys. Rev. A **76**, 1–10 (2007).

[37] A. V. Gorbach and D. V. Skryabin, “Light trapping in gravity-like potentials and expansion of supercontinuum spectra in photonic-crystal fibres,” Nat. Photon. **1**, 653–657 (2007).

[38] J. M. Stone and J. C. Knight, “Visibly ”white” light generation in uniform photonic crystal fiber using a microchip laser,” Opt. Express **16**, 2670–5 (2008).

[39] A. Kudlinski and G. Bouwmans, “Dispersion-engineered photonic crystal fibers for CW-pumped supercontinuum sources,” J. Lightwave Technol. **27**, 1556–1564 (2009).

[40] J. C. Travers, “Blue extension of optical fibre supercontinuum generation,” J. Opt. **12**, 113001 (2010).

[41] I. Hartl, X. D. Li, C. Chudoba, R. K. Ghanta, T. H. Ko, J. G. Fujimoto, J. K. Ranka, and R. S. Windeler, “Ultrahigh-resolution optical coherence tomography using continuum generation in an air-silica microstructure optical fiber.” Opt. Lett. **26**, 608–10 (2001).

[42] B. Povazay, K. Bizheva, A. Unterhuber, B. Hermann, H. Sattmann, A. F. Fercher, W. Drexler, A. Apolonski, W. J. Wadsworth, J. C. Knight, P. S. J. Russell, M. Vetterlein, and E. Scherzer, “Submicrometer axial resolution optical coherence tomography.” Opt. Lett. **27**, 1800–2 (2002).

[43] G. Humbert, W. Wadsworth, S. Leon-Saval, J. Knight, T. Birks, P. St J Russell, M. Lederer, D. Kopf, K. Wiesauer, E. Breuer, and D. Stifter, “Supercontinuum generation system for optical coherence tomography based on tapered photonic crystal fibre.” Opt. Express **14**, 1596–603 (2006).

[44] G. McConnell, “Confocal laser scanning fluorescence microscopy with a visible continuum source,” Opt. Express **12**, 2844–2850 (2004).

[45] J. Frank, A. Elder, J. Swartling, A. Venkitaraman, A. Jeyasekharan, and C. Kaminski, “A white light confocal microscope for spectrally resolved multidimensional imaging,” J. Microscopy **227**, 203–215 (2007).

[46] D. Jones, D. J. Jones, S. A. Diddams, J. K. Ranka, A. Stentz, R. S. Windeler, J. L. Hall, and S. T. Cundiff, “Carrier-envelope phase control of femtosecond mode-locked lasers and direct optical frequency synthesis,” Science **288**, 635–40 (2000).

[47] R. Holzwarth, T. Udem, T. Hansch, J. Knight, W. Wadsworth, and P. Russell, "Optical frequency synthesizer for precision spectroscopy," Phys. Rev. Lett. **85**, 2264–7 (2000).

[48] S. A. Diddams, T. Udem, J. C. Bergquist, E. A. Curtis, R. E. Drullinger, L. Hollberg, W. M. Itano, W. D. Lee, C. W. Oates, K. R. Vogel, and D. J. Wineland, "An optical clock based on a single trapped 199Hg+ ion," Science **293**, 825–8 (2001).

[49] T. Udem, R. Holzwarth, and T. W. Hänsch, "Optical frequency metrology." Nature **416**, 233–7 (2002).

[50] A. Ruehl, "Advances in Yb: Fiber Frequency Comb Technology," Opt. Photonics News pp. 30–35 (2012).

[51] M. Peach and M. Hatcher, "Supercontinuum sources make their presence felt," http://optics.org/news/4/2/7 (12 Feb. 2013) .

[52] A. Kudlinski, G. Bouwmans, O. Vanvincq, Y. Quiquempois, A. Le Rouge, L. Bigot, G. Mélin, and A. Mussot, "White-light cw-pumped supercontinuum generation in highly GeO(2)-doped-core photonic crystal fibers," Opt. Lett. **34**, 3631–3 (2009).

[53] C. Larsen, D. Noordegraaf, P. M. W. Skovgaard, K. P. Hansen, K. E. Mattsson, and O. Bang, "Gain-switched CW fiber laser for improved supercontinuum generation in a PCF," Opt. Express **19**, 3631–3633 (2011).

[54] A. Kudlinski and A. Mussot, "Optimization of continuous-wave supercontinuum generation," Opt. Fiber Technol. **18**, 322–326 (2012).

[55] M. Nakazawa, H. Kubota, and K. Tamura, "Random evolution and coherence degradation of a high-order optical soliton train in the presence of noise," Opt. Lett. **24**, 318–320 (1999).

[56] A. Heidt, "Pulse preserving flat-top supercontinuum generation in all-normal dispersion photonic crystal fibers," J. Opt. Soc. Am. B **27**, 550–559 (2010).

[57] A. M. Heidt, A. Hartung, G. W. Bosman, P. Krok, E. G. Rohwer, H. Schwoerer, and H. Bartelt, "Coherent octave spanning near-infrared and visible supercontinuum generation in all-normal dispersion photonic crystal fibers," Optics express **19**, 3775–87 (2011).

[58] A. M. Heidt, J. Rothhardt, A. Hartung, H. Bartelt, E. G. Rohwer, J. Limpert, and A. Tünnermann, "High quality sub-two cycle pulses from compression of supercontinuum generated in all-normal dispersion photonic crystal fiber," Optics Express **19**, 13873 (2011).

[59] A. Hartung, A. M. Heidt, and H. Bartelt, "Pulse-preserving broadband visible supercontinuum generation in all-normal dispersion tapered suspended-core optical fibers," Opt. Express **19**, 12275–12283 (2011).

[60] L. Hooper, P. Mosley, and A. Muir, "Coherent supercontinuum generation in photonic crystal fiber with all-normal group velocity dispersion," Opt. Express **19**, 4902–4907 (2011).

[61] A. Heidt, F. Poletti, J. Price, and D. J. Richardson, "Mid-IR coherent supercontinuum generation in all-solid step-index soft glass fibers," Specialty Optical Fibers, OSA **559**, paper STu3F.6 (2012).

[62] C. Xia, M. Kumar, O. P. Kulkarni, M. N. Islam, F. L. Terry, M. J. Freeman, M. Poulain, and G. Mazé, "Mid-infrared supercontinuum generation to 4.5 um in ZBLAN fluoride fibers by nanosecond diode pumping," Opt. Lett. **31**, 2553–2555 (2006).

[63] P. Domachuk, N. A. Wolchover, M. Cronin-Golomb, A. Wang, A. K. George, C. M. B. Cordeiro, J. C. Knight, and F. G. Omenetto, "Over 4000 nm bandwidth of mid-IR supercontinuum generation in sub-centimeter segments of highly nonlinear tellurite PCFs," Opt. Express **16**, 7161–8 (2008).

[64] G. Qin, X. Yan, C. Kito, M. Liao, C. Chaudhari, T. Suzuki, and Y. Ohishi, "Supercontinuum generation spanning over three octaves from UV to 3.85 microm in a fluoride fiber," Opt. Lett. **34**, 2015–7 (2009).

[65] C. Agger, C. Petersen, S. Dupont, H. Steffensen, J. K. Lyngsø, C. L. Thomsen, J. Thøgersen, S. R. Keiding, and O. Bang, "Supercontinuum generation in ZBLAN fibersdetailed comparison between measurement and simulation," J. Opt. Soc. Am. B **29** (2012).

[66] A. Kudlinski, A. K. George, J. C. Knight, J. C. Travers, A. B. Rulkov, S. V. Popov, and J. R. Taylor, "Zero-dispersion wavelength decreasing photonic crystal fibers for ultraviolet-extended supercontinuum generation," Opt. Express **14**, 5715 (2006).

[67] J. C. Travers, A. B. Rulkov, S. V. Popov, J. R. Taylor, A. Kudlinski, a. K. George, and J. C. Knight, "Multi-Watt Supercontinuum Generation from 0.3 to 2.4 um in PCF Tapers," in "Conference on Lasers and Electro-Optics," (IEEE, 2007), p. paper JTuB2.

[68] J. Stone and J. Knight, "From zero dispersion to group index matching: How tapering fibers offers the best of both worlds for visible supercontinuum generation," Opt. Fiber Technol. **18**, 315–321 (2012).

[69] S. P. Stark, J. C. Travers, and P. S. J. Russell, "Extreme supercontinuum generation to the deep UV," Opt. Lett. **37**, 770–772 (2012).

[70] A. Kudlinski, M. Lelek, B. Barviau, L. Audry, and A. Mussot, "Efficient blue conversion from a 1064 nm microchip laser in long photonic crystal fiber tapers for fluorescence microscopy," Opt. Express **18**, 16640–5 (2010).

[71] G. P. Agrawal, *Nonlinear Fiber Optics* (Academic Press, 2006), 4th ed.

[72] P. Kaiser and H. Astle, "Low-loss single-material fibers made from pure fused silica," Bell Syst. Tech. J. **53**, 1021–1039 (1974).

[73] T. Birks, P. Roberts, P. Russell, M. Atkin, and T. Shepherd, "Full 2-D photonic bandgaps in silica/air structures," IEEE Electron. Lett. **31**, 1941–1943 (1995).

[74] J. C. Knight, "Photonic Band Gap Guidance in Optical Fibers," Science **282**, 1476–1478 (1998).

[75] R. F. Cregan, B. J. Mangan, J. C. Knight, T. A. Birks, P. S. J. Russell, P. J. Roberts, and D. C. Allan, "Single-Mode Photonic Band Gap Guidance of Light in Air," Science **285**, 1537–1539 (1999).

[76] D. Mogilevtsev, T. Birks, and P. Russell, "Group-velocity dispersion in photonic crystal fibers," Opt. Lett. **23**, 1662–1664 (1998).

[77] O. Humbach, H. Fabian, and U. Grzesik, “Analysis of OH absorption bands in synthetic silica,” J. Non-Cryst. Sol. **203**, 19–26 (1996).

[78] S. Walker, “Rapid modeling and estimation of total spectral loss in optical fibers,” J. Lightwave Technol. **LT-4**, 1125–1131 (1986).

[79] P. Roberts, F. Couny, H. Sabert, B. Mangan, T. Birks, J. Knight, and P. Russell, “Loss in solid-core photonic crystal fibers due to interface roughness scattering,” Opt. Express **13**, 7779–93 (2005).

[80] M. Phan-Huy, J. Moison, J. A. Levenson, S. Richard, G. Mélin, M. Douay, and Y. Quiquempois, “Surface roughness and light scattering in a small effective area microstructured fiber,” J. Lightwave Technol. **27**, 1597–1604 (2009).

[81] W. Wadsworth, J. Knight, and T. Birks, “State-of-the-Art Photonic Crystal Fiber,” Opt. Photonics News pp. 24–31 (2012).

[82] I. Gris-Sánchez, B. Mangan, and J. Knight, “Reducing spectral attenuation in small-core photonic crystal fibers,” Opt. Mater. Express **1**, 179 (2011).

[83] K. J. Blow and D. Wood, “Theoretical Description of Transient Stimulated Raman Scattering in Optical Fibers,” IEEE J. Quantum Electron. **25**, 2665–2673 (1989).

[84] J. Lægsgaard, N. A. Mortensen, and A. Bjarklev, “Mode areas and field-energy distribution in honeycomb photonic bandgap fibers,” J. Opt. Soc. Am. B **20**, 2037 (2003).

[85] J. Lægsgaard, “Mode profile dispersion in the generalised nonlinear Schrödinger equation,” Opt. Express **15**, 337–342 (2007).

[86] J. Hult, “A Fourth-Order RungeKutta in the Interaction Picture Method for Simulating Supercontinuum Generation in Optical Fibers,” J. Lightwave Technol. **25**, 3770–3775 (2007).

[87] E. Treacy, “Measurement and interpretation of dynamic spectrograms of picosecond light pulses,” J. Appl. Phys. **42** (1971).

[88] R. Trebino, *Frequency-resolved optical gating: the measurement of ultrashort laser pulses* (Springer, 2000).

[89] E. P. Ippen, “Self-phase modulation of picosecond pulses in optical fibers,” Appl. Phys. Lett. **24**, 190 (1974).

[90] R. Stolen and C. Lin, “Self-phase-modulation in silica optical fibers,” Phys. Rev. A **17**, 1448–1453 (1978).

[91] A. Chraplyvy and J. Stone, “Measurement of crossphase modulation in coherent wavelength-division multiplexing using injection lasers,” Electron. Lett. **20**, 996–997 (1984).

[92] R. R. Alfano, Q. X. Li, T. Jimbo, J. T. Manassah, and P. P. Ho, “Induced spectral broadening of a weak picosecond pulse in glass produced by an intense picosecond pulse,” Opt. Lett. **11**, 626–8 (1986).

[93] M. Islam, L. Mollenauer, and R. Stolen, “Cross-phase modulation in optical fibers,” Opt. Lett. **12**, 625–627 (1987).

[94] R. Carman, R. Chiao, and P. Kelley, “Observation of degenerate stimulated four-photon interaction and four-wave parametric amplification,” Phys. Rev. Lett. **17**, 1281–1284 (1966).

[95] R. H. Stolen, "Phase-matched three-wave mixing in silica fiber optical waveguides," Appl. Phys. Lett. **24**, 308 (1974).

[96] R. Stolen, "Phase-matched-stimulated four-photon mixing in silica-fiber waveguides," IEEE J. Quantum Electron. **QE-11**, 100–103 (1975).

[97] T. Benjamin and J. Feir, "The disintegration of wave trains on deep water," J. Fluid Mech **27** (1967).

[98] K. Hammani, C. Finot, B. Kibler, and G. Millot, "Soliton Generation and Rogue-Wave-Like Behavior Through Fourth-Order Scalar Modulation Instability," IEEE Photon. J. **1**, 205–212 (2009).

[99] A. Hasegawa and W. Brinkman, "Tunable coherent IR and FIR sources utilizing modulational instability," IEEE J. Quantum Electron. **QE-16**, 694–697 (1980).

[100] C. Raman, "A new radiation," Indian J. Phys. **2**, 387–398 (1928).

[101] D. Hollenbeck and C. D. Cantrell, "Multiple-vibrational-mode model for fiber-optic Raman gain spectrum and response function," J. Opt. Soc. Am. B **19**, 2886 (2002).

[102] J. S. Russell, "Report on waves," in "14th meeting of the British Association for the Advancement of Science," (1844), pp. 311–390.

[103] A. Hasegawa, "Transmission of stationary nonlinear optical pulses in dispersive dielectric fibers. II. Normal dispersion," Appl. Phys. Lett. **23**, 171 (1973).

[104] L. Mollenauer, R. Stolen, and J. Gordon, "Experimental observation of picosecond pulse narrowing and solitons in optical fibers," Phys. Rev. Lett. **45** (1980).

[105] A. Hasegawa and Y. Kodama, "Amplification and reshaping of optical solitons in a glass fiber-I," Opt. Lett. **7**, 285–7 (1982).

[106] A. Hasegawa, "Amplification and reshaping of optical solitons in a glass fiber-IV: Use of the stimulated Raman process," Opt. Lett. **8**, 650–652 (1983).

[107] K. Blow, N. Doran, and D. Wood, "Generation and stabilization of short soliton pulses in the amplified nonlinear Schrödinger equation," J. Opt. Soc. Am. B **5**, 381–391 (1988).

[108] H. H. Kuehl and L. Angeles, "Solitons on an axially nonuniform optical fiber," J. Opt. Soc. Am. B **5**, 709–713 (1988).

[109] Y. Kodama and A. Hasegawa, "Amplification and reshaping of optical solitons in glass fiber-II," Opt. Lett. **7**, 339–341 (1982).

[110] Y. Kodama and A. Hasegawa, "Amplification and reshaping of optical solitons in glass fiber-III. Amplifiers with random gain," Optics Letters **8**, 342–344 (1983).

[111] E. Golovchenko and E. Dianov, "Decay of optical solitons," JETP Lett **42**, 74–77 (1985).

[112] E. M. Dianov, A. Y. Karasik, P. V. Mamyshev, A. M. Prokhorov, V. N. Serkin, M. F. Stel'makh, and A. A. Fomichev, "Stimulated-Raman conversion of multisoliton pulses in quartz optical fibers," JETP Lett **41**, 242–244 (1985).

[113] F. Mitschke and L. Mollenauer, "Discovery of the soliton self-frequency shift," Opt. Lett. **11**, 659–661 (1986).

[114] J. P. Gordon, "Theory of the soliton self-frequency shift," Opt. Lett. **11**, 662–4 (1986).

[115] P. K. Wai, C. R. Menyuk, Y. C. Lee, and H. H. Chen, "Nonlinear pulse propagation in the neighborhood of the zero-dispersion wavelength of monomode optical fibers," Opt. Lett. **11**, 464–6 (1986).

[116] N. Akhmediev and M. Karlsson, "Cherenkov radiation emitted by solitons in optical fibers," Phys. Rev. A **51** (1995).

[117] I. Cristiani, R. Tediosi, L. Tartara, and V. Degiorgio, "Dispersive wave generation by solitons in microstructured optical fibers," Opt. Express **12**, 124–35 (2004).

[118] M. Erkintalo, Y. Q. Xu, S. G. Murdoch, J. M. Dudley, and G. Genty, "Cascaded Phase Matching and Nonlinear Symmetry Breaking in Fiber Frequency Combs," Phys. Rev. Lett. **109**, 223904 (2012).

[119] K. E. Webb, Y. Q. Xu, M. Erkintalo, and S. G. Murdoch, "Generalized dispersive wave emission in nonlinear fiber optics," Opt. Lett. **38**, 151 (2013).

[120] D. Faccio, E. Rubino, S. C. Kehr, F. Belgiorno, D. Townsend, S. Rohr, C. E. Kuklewicz, U. Leonhardt, and F. König, "Negative frequency resonant radiation," Phys. Rev. Lett. **108**, 253901 (2012).

[121] F. Biancalana, "Negative Frequencies Get Real," Physics Online Journal **5** (2012).

[122] N. Nishizawa and T. Goto, "Pulse trapping by ultrashort soliton pulses in optical fibers across zero-dispersion wavelength," Opt. Lett. **27**, 152–4 (2002).

[123] N. Nishizawa and T. Goto, "Characteristics of pulse trapping by use of ultrashort soliton pulses in optical fibers across the zero-dispersion wavelength," Opt. Express **10**, 1151–1159 (2002).

[124] G. Genty, M. Lehtonen, and H. Ludvigsen, "Effect of cross-phase modulation on supercontinuum generated in microstructured fibers with sub-30 fs pulses," Opt. Express **12**, 4614–24 (2004).

[125] A. V. Gorbach, D. V. Skryabin, J. M. Stone, and J. C. Knight, "Four-wave mixing of solitons with radiation and quasi-nondispersive wave packets at the short-wavelength edge of a supercontinuum," Opt. Express **14**, 9854–63 (2006).

[126] S. Hill, C. E. Kuklewicz, U. Leonhardt, and F. König, "Evolution of light trapped by a soliton in a microstructured fiber," Opt. Express **17**, 13588–600 (2009).

[127] J. C. Travers and J. R. Taylor, "Soliton trapping of dispersive waves in tapered optical fibers," Opt. Lett. **34**, 115–7 (2009).

[128] M. Islam, G. Sucha, and I. Bar-Joseph, "Femtosecond distributed soliton spectrum in fibers," J. Opt. Soc. Am. B **6** (1989).

[129] N. Savage, "Supercontinuum sources," Nat. Photon. **3**, 114–115 (2009).

[130] M. H. Frosz, O. Bang, and A. Bjarklev, "Soliton collision and Raman gain regimes in continuous-wave pumped supercontinuum generation," Opt. Express **14**, 9391–407 (2006).

[131] F. Luan, D. V. Skryabin, A. V. Yulin, and J. C. Knight, “Energy exchange between colliding solitons in photonic crystal fibers,” Opt. Express **14**, 1479–1481 (2006).

[132] P. Falk, M. Frosz, O. Bang, and L. Thrane, “Broadband light generation at ˜1300 nm through spectrally recoiled solitons and dispersive waves,” Opt. Lett. **33**, 621–623 (2008).

[133] A. Kudlinski and A. Mussot, “Visible cw-pumped supercontinuum,” Opt. Lett. **33**, 2407–9 (2008).

[134] J. C. Travers, S. V. Popov, and J. R. Taylor, “Trapping of dispersive waves by solitons in long lengths of tapered PCF,” in “Conference on Lasers and Electro-Optics,” (Ieee, 2008), p. paper CThGG2.

[135] A. Mussot and A. Kudlinski, “19.5W CW-pumped supercontinuum source from 0.65 to 1.38 um,” Electron. Lett. **45**, 1–2 (2009).

[136] P. Moselund, “Long-pulse supercontinuum light sources,” Phd thesis, Technical University of Denmark (2009).

[137] A. Kudlinski, B. Barviau, A. Leray, and C. Spriet, “Control of pulse-to-pulse fluctuations in visible supercontinuum,” Opt. Express **18**, 2670–2675 (2010).

[138] T. A. Birks, W. J. Wadsworth, and P. S. Russell, “Supercontinuum generation in tapered fibers,” Opt. Lett. **25**, 1415–7 (2000).

[139] S. Leon-Saval, T. Birks, W. Wadsworth, P. St J Russell, and M. Mason, “Supercontinuum generation in submicron fibre waveguides,” Opt. Express **12**, 2864–9 (2004).

[140] F. Lu, Y. Deng, and W. H. Knox, “Generation of broadband femtosecond visible pulses in dispersion-micromanaged holey fibers,” Opt. Lett. **30**, 1566–8 (2005).

[141] P. Falk, M. Frosz, and O. Bang, “Supercontinuum generation in a photonic crystal fiber with two zero-dispersion wavelengths tapered to normal dispersion at all wavelengths,” Opt. Express **13**, 7535–40 (2005).

[142] S. Pricking and H. Giessen, “Tailoring the soliton and supercontinuum dynamics by engineering the profile of tapered fibers,” Opt. Express **18**, 5382–5387 (2010).

[143] J. Cascante-Vindas, A. Díez, J. Cruz, and M. Andrés, “White light supercontinuum generation in a Y-shaped microstructured tapered fiber pumped at 1064 nm,” Opt. Express **18**, 14535–14540 (2010).

[144] W. J. Wadsworth, A. Ortigosa-Blanch, J. C. Knight, T. a. Birks, T.-P. M. Man, and P. S. J. Russell, “Supercontinuum generation in photonic crystal fibers and optical fiber tapers: a novel light source,” J. Opt. Soc. Am. B **19**, 2148 (2002).

[145] M. Foster and A. Gaeta, “Ultra-low threshold supercontinuum generation in sub-wavelength waveguides,” Opt. Express **12**, 3137–43 (2004).

[146] J. Teipel, D. Türke, H. Giessen, A. Zintl, and B. Braun, “Compact multi-Watt picosecond coherent white light sources using multiple-taper fibers,” Opt. Express **13**, 1734–42 (2005).

[147] J. C. Travers, S. V. Popov, and J. R. Taylor, “Extended blue supercontinuum generation in cascaded holey fibers,” Opt. Lett. **30**, 3132–4 (2005).

[148] C. Xiong, A. Witkowska, S. G. Leon-Saval, T. A. Birks, and W. J. Wadsworth, "Enhanced visible continuum generation from a microchip 1064nm laser," Opt. Express **14**, 6188–93 (2006).

[149] J. Cascante-Vindas, A. Diez, J. Cruz, M. Andrés, E. Silvestre, J. Miret, and A. Ortigosa-Blanch, "Tapering photonic crystal fibres for supercontinuum generation with nanosecond pulses at 532nm," Opt. Commun. **281**, 433–438 (2008).

[150] S. P. Stark, A. Podlipensky, N. Y. Joly, and P. S. J. Russell, "Ultraviolet-enhanced supercontinuum generation in tapered photonic crystal fiber," J. Opt. Soc. Am. B **27**, 592 (2010).

[151] Y. Peiguang, W. Huifeng, R. Shuangchen, Z. Junqing, Z. Jian, S. Jie, and L. Jie, "Fabrication of a 145-m long microstructured optical fiber taper and its supercontinuum generation," Opt. Engineering **50**, 105003 (2011).

[152] H. Chen, Z. Chen, X. Zhou, and J. Hou, "Cascaded PCF tapers for flat broadband supercontinuum generation," Chin. Opt. Lett. **10**, 10–12 (2012).

[153] K. Tajima, "Compensation of soliton broadening in nonlinear optical fibers with loss," Opt. Lett. **12**, 54–56 (1987).

[154] E. Bordon and W. Anderson, "Dispersion-adapted monomode fiber for propagation of nonlinear pulses," J. Lightwave Technol. **7**, 353–357 (1989).

[155] S. V. Chernikov and P. V. Mamyshev, "Femtosecond soliton propagation in fibers with slowly decreasing dispersion," J. Opt. Soc. Am. B **8**, 1633 (1991).

[156] V. Bogatyrev and M. Bubnov, "A single-mode fiber with chromatic dispersion varying along the length," J. Lightwave Technol. **9**, 561–566 (1991).

[157] S. V. Chernikov, E. M. Dianov, D. J. Richardson, and D. N. Payne, "Soliton pulse compression in dispersion-decreasing fiber," Opt. Lett. **18**, 476–8 (1993).

[158] M. Nakazawa, K. Tamura, H. Kubota, and E. Yoshida, "Coherence degradation in the process of supercontinuum generation in an optical fiber," Opt. Fiber Technol. pp. 215–223 (1998).

[159] M. Tse and P. Horak, "Designing tapered holey fibers for soliton compression," IEEE J. Quantum Electron. **44**, 192–198 (2008).

[160] J. C. Travers, J. M. Stone, A. B. Rulkov, B. A. Cumberland, A. K. George, S. V. Popov, J. C. Knight, and J. R. Taylor, "Optical pulse compression in dispersion decreasing photonic crystal fiber," Opt. Express **15**, 13203–11 (2007).

[161] F. Gérôme, K. Cook, a. K. George, W. J. Wadsworth, and J. C. Knight, "Delivery of sub-100fs pulses through 8m of hollow-core fiber using soliton compression," Opt. Express **15**, 7126–31 (2007).

[162] A. Peacock, "Mid-IR soliton compression in silicon optical fibers and fiber tapers," Opt. Lett. **37**, 818–820 (2012).

[163] A. C. Judge, O. Bang, B. J. Eggleton, B. T. Kuhlmey, E. C. Mägi, R. Pant, and C. M. de Sterke, "Optimization of the soliton self-frequency shift in a tapered photonic crystal fiber," J. Opt. Soc. Am. B **26**, 2064 (2009).

[164] C. Milián, A. Ferrando, and D. Skryabin, "Polychromatic Cherenkov radiation and supercontinuum in tapered optical fibers," J. Opt. Soc. Am. B **29**, 589–593 (2012).

[165] A. Al-kadry and M. Rochette, "Mid-infrared sources based on the soliton self-frequency shift," J. Opt. Soc. Am. B **29**, 1347–1355 (2012).

[166] A. Al-kadry and M. Rochette, "Maximized Soliton Self-frequency Shift in Non-uniform Microwires by the Control of Third-order Dispersion Perturbation," J. Lightwave Technol. **31**, 1462–1467 (2013).

[167] S. P. Stark, A. Podlipensky, and P. S. J. Russell, "Soliton Blueshift in Tapered Photonic Crystal Fibers," Phys. Rev. Lett. **083903**, 1–4 (2011).

[168] P. Dumais, F. Gonthier, S. Lacroix, J. Bures, A. Villeneuve, P. G. J. Wigley, and G. I. Stegeman, "Enhanced self-phase modulation in tapered fibers," Opt. Lett. **18**, 1996–1998 (1993).

[169] X. Liu, C. Xu, W. H. Knox, J. K. Chandalia, B. J. Eggleton, S. G. Kosinski, and R. S. Windeler, "Soliton self-frequency shift in a short tapered air-silica microstructure fiber," Opt. Lett. **26**, 358–60 (2001).

[170] T. Man, T. Birks, W. Wadsworth, and P. S. J. Russell, "Fabrication of indefinitely long tapered fibres for supercontinuum generation," OSA Tech. Dig., Nonlinear Guided Waves and Their Applications pp. paper WB4–1 (2001).

[171] E. C. Mägi, L. B. Fu, H. C. Nguyen, M. R. Lamont, D. I. Yeom, and B. J. Eggleton, "Enhanced Kerr nonlinearity in sub-wavelength diameter As(2)Se(3) chalcogenide fiber tapers," Opt. Express **15**, 10324–9 (2007).

[172] D. Hudson, S. Dekker, and E. Mägi, "Octave spanning supercontinuum in an As2S3 taper using ultralow pump pulse energy," Opt. Lett. **36**, 1122–1124 (2011).

[173] M. Liao, X. Yan, W. Gao, Z. Duan, and G. Qin, "Five-order SRSs and supercontinuum generation from a tapered tellurite microstructured fiber with longitudinally varying dispersion," Opt. Express **19**, 15389–15396 (2011).

[174] A. Marandi, C. Rudy, N. C. Leindecker, V. G. Plotnichenko, E. M. Dianov, K. L. Vodopyanov, and R. L. Byer, "Mid-Infrared Supercontinuum Generation from 2.4 m to 4.6 m in Tapered Chalcogenide Fiber," in "Conference on Lasers and Electro-Optics," (2012), pp. 7–8.

[175] J. Chandalia, B. Eggleton, R. Windeler, S. Kosinski, X. Liu, and C. Xu, "Adiabatic coupling in tapered air-silica microstructured optical fiber," IEEE Photon. Technol. Lett. **13**, 52–54 (2001).

[176] R. Kenny, T. Birks, and K. Oakley, "Control of optical fibre taper shape," Electron. Lett. **27** (1991).

[177] T. A. Birks, G. Kakarantzasa, P. S. Russell, and D. F. Murphy, "Photonic crystal fibre devices," Proc. of SPIE **4943**, 142–151 (2003).

[178] H. C. Nguyen, B. T. Kuhlmey, E. C. Mägi, M. J. Steel, P. Domachuk, C. L. Smith, and B. J. Eggleton, "Tapered photonic crystal fibres: properties, characterisation and applications," Appl. Phys. B **81**, 377–387 (2005).

[179] N. Vukovic, N. G. R. Broderick, M. Petrovich, and G. Brambilla, "Novel Method for the Fabrication of Long Optical Fiber Tapers," IEEE Photon. Technol. Lett. **20**, 1264–1266 (2008).

[180] S. Pricking and H. Giessen, "Tapering fibers with complex shape," Opt. Express **18**, 3426–37 (2010).

[181] A. Felipe, G. Espíndola, H. J. Kalinowski, J. A. S. Lima, and A. S. Paterno, “Stepwise fabrication of arbitrary fiber optic tapers,” Opt. Express **20**, 19893–904 (2012).

[182] M. Liao, W. Gao, Z. Duan, and X. Yan, “Directly draw highly nonlinear tellurite microstructured fiber with diameter varying sharply in a short fiber length,” Opt. Express **20**, 1141–1150 (2012).

[183] C. Cordeiro and W. Wadsworth, “Engineering the dispersion of tapered fibers for supercontinuum generation with a 1064 nm pump laser,” Opt. Lett. **30**, 1980–1982 (2005).

[184] M. H. Frosz, P. M. Moselund, P. D. Rasmussen, C. L. Thomsen, and O. Bang, “Increasing the blue-shift of a supercontinuum by modifying the fiber glass composition,” Opt. Express **16**, 21076–86 (2008).

[185] B. Barviau, O. Vanvincq, and A. Mussot, “Enhanced soliton self-frequency shift and CW supercontinuum generation in GeO2-doped core photonic crystal fibers,” J. Opt. Soc. Am. B **28**, 1152–1160 (2011).

[186] X. Zhang, X. Zhu, R. Xing, X. Yang, F. Jiang, H. Li, J. Peng, N. Dai, and J. Li, “Microstructure core photonic crystal fiber for blue extension of supercontinuum generation,” Opt. Commun. **298-299**, 191–195 (2013).

[187] N. Vukovic and N. Broderick, “Method for improving the spectral flatness of the supercontinuum at 1.55 um in tapered microstructured optical fibers,” Phys. Rev. A **82**, 043840 (2010).

[188] Z. Chen, A. J. Taylor, and A. Efimov, “Soliton dynamics in non-uniform fiber tapers: analytical description through an improved moment method,” J. Opt. Soc. Am. B **27**, 1022 (2010).

[189] A. C. Judge, O. Bang, and C. Martijn de Sterke, “Theory of dispersive wave frequency shift via trapping by a soliton in an axially nonuniform optical fiber,” J. Opt. Soc. Am. B **27**, 2195 (2010).

[190] T. Schreiber, T. Andersen, D. Schimpf, J. Limpert, and A. Tünnermann, “Supercontinuum generation by femtosecond single and dual wavelength pumping in photonic crystal fibers with two zero dispersion wavelengths,” Opt. Express **13**, 9556–69 (2005).

[191] M. Koshiba and K. Saitoh, “Applicability of classical optical fiber theories to holey fibers,” Opt. Lett. **29**, 1739–1741 (2004).

[192] NKT Photonics A/S, “Application Note: Spectral Density Measurements,” www.nktphotonics.com (2011).

[193] W. Wadsworth, A. Witkowska, S. Leon-Saval, and T. Birks, “Hole inflation and tapering of stock photonic crystal fibres,” Opt. Express **13**, 6541–9 (2005).

[194] L. Skuja, “Optically active oxygen-deficiency-related centers in amorphous silicon dioxide,” J. Non-Cryst. Sol. **239**, 16–48 (1998).

[195] L. Skuja, K. Kajihara, M. Hirano, and H. Hosono, “Visible to vacuum-UV range optical absorption of oxygen dangling bonds in amorphous SiO_{2},” Phys. Rev. B **84**, 205206 (2011).

[196] J. C. Travers, W. Chang, J. Nold, N. Y. Joly, and P. St. J. Russell, “Ultrafast nonlinear optics in gas-filled hollow-core photonic crystal fibers [Invited],” J. Opt. Soc. Am. B **28**, A11 (2011).

[197] P. Hölzer, W. Chang, J. Travers, and A. Nazarkin, "Femtosecond nonlinear fiber optics in the ionization regime," Phys. Rev. Lett. **203901**, 1–5 (2011).

[198] Z. Sun and A. C. Ferrari, "Fibre sources in the deep ultraviolet," Nat. Photon. **5**, 446—-447 (2011).

[199] A. Gaeta, "Nonlinear propagation and continuum generation in microstructured optical fibers," Opt. Lett. **27**, 924–926 (2002).

[200] X. Gu, L. Xu, M. Kimmel, E. Zeek, P. O'Shea, A. P. Shreenath, R. Trebino, and R. S. Windeler, "Frequency-resolved optical gating and single-shot spectral measurements reveal fine structure in microstructure-fiber continuum," Opt. Lett. **27**, 1174–6 (2002).

[201] K. L. Corwin, N. R. Newbury, J. M. Dudley, S. Coen, S. a. Diddams, K. Weber, and R. S. Windeler, "Fundamental Noise Limitations to Supercontinuum Generation in Microstructure Fiber," Phys. Rev. Lett. **90**, 1–4 (2003).

[202] K. Corwin, N. Newbury, J. Dudley, S. Coen, S. Diddams, B. Washburn, K. Weber, and R. Windeler, "Fundamental amplitude noise limitations to supercontinuum spectra generated in a microstructured fiber," Appl. Phys. B **77**, 269–277 (2003).

[203] N. Newbury and B. Washburn, "Noise amplification during supercontinuum generation in microstructure fiber," Opt. Lett. **28**, 944–946 (2003).

[204] J. Dudley and S. Coen, "Numerical simulations and coherence properties of supercontinuum generation in photonic crystal and tapered optical fibers," IEEE J. Sel. Top. Quant. Electron. **8**, 651–659 (2002).

[205] G. Genty, C. M. D. Sterke, O. Bang, F. Dias, N. Akhmediev, and J. M. Dudley, "Collisions and turbulence in optical rogue wave formation," Phys. Lett. A **374**, 989–996 (2010).

[206] J. M. Dudley, G. Genty, and B. J. Eggleton, "Harnessing and control of optical rogue waves in supercontinuum generation," Opt. Express **16**, 3644–51 (2008).

[207] A. Mussot, A. Kudlinski, M. Kolobov, E. Louvergneaux, M. Douay, and M. Taki, "Observation of extreme temporal events in CW-pumped supercontinuum," Opt. Express **17**, 17010 (2009).

[208] N. Akhmediev, A. Ankiewicz, and M. Taki, "Waves that appear from nowhere and disappear without a trace," Phys. Lett. A **373**, 675–678 (2009).

[209] M. Erkintalo, G. Genty, and J. Dudley, "Giant dispersive wave generation through soliton collision," Opt. Lett. **35**, 658–660 (2010).

[210] M. Erkintalo, G. Genty, and J. Dudley, "On the statistical interpretation of optical rogue waves," Eur. Phys. J. **144**, 135–144 (2010).

[211] D. Buccoliero, H. Steffensen, H. Ebendorff-heidepriem, T. M. Monro, and O. Bang, "Midinfrared optical rogue waves in soft glass photonic crystal fiber," Opt. Express **19**, 17973–17978 (2011).

[212] B. Wetzel, K. J. Blow, S. K. Turitsyn, G. Millot, L. Larger, and J. M. Dudley, "Random walks and random numbers from supercontinuum generation," Opt. Express **20**, 11143–52 (2012).

[213] M. Bellini and T. Hänsch, "Phase-locked white-light continuum pulses: toward a universal optical frequency-comb synthesizer," Opt. Lett. **25**, 1049–1051 (2000).

[214] J. Dudley and S. Coen, "Coherence properties of supercontinuum spectra generated in photonic crystal and tapered optical fibers," Opt. Lett. **27**, 1180–1182 (2002).

[215] C. Lafargue, J. Bolger, G. Genty, F. Dias, J. M. Dudley, and B. J. Eggleton, "Direct detection of optical rogue wave energy statistics in supercontinuum generation," IEEE Electron. Lett. **45** (2009).

[216] B. Wetzel, A. Stefani, L. Larger, P. A. Lacourt, J. M. Merolla, T. Sylvestre, A. Kudlinski, A. Mussot, G. Genty, F. Dias, and J. M. Dudley, "Real-time full bandwidth measurement of spectral noise in supercontinuum generation," Sci. Rep. **2**, 882 (2012).

[217] D. Solli, C. Ropers, and B. Jalali, "Active control of rogue waves for stimulated supercontinuum generation," Phys. Rev. Lett. **233902**, 18–21 (2008).

[218] B. Kibler, J. Fatome, C. Finot, G. Millot, and F. Dias, "The Peregrine soliton in nonlinear fibre optics," Nature Phys. **6**, 790–795 (2010).

[219] M. Erkintalo, K. Hammani, B. Kibler, C. Finot, N. Akhmediev, J. M. Dudley, and G. Genty, "Higher-order modulation instability in nonlinear fiber optics," Phys. Rev. Lett. **253901**, 14–18 (2011).

[220] P. Moselund, M. Frosz, C. Thomsen, and O. Bang, "Back-seeding of higher order gain processes in picosecond supercontinuum generation," Opt. Express **16**, 1644–1646 (2008).

[221] G. Genty, J. M. Dudley, and B. J. Eggleton, "Modulation control and spectral shaping of optical fiber supercontinuum generation in the picosecond regime," Appl. Phys. B **94**, 187–194 (2009).

[222] G. Genty and J. Dudley, "Route to coherent supercontinuum generation in the long pulse regime," IEEE J. Quantum Electron. **45**, 1331–1335 (2009).

[223] D. Solli, B. Jalali, and C. Ropers, "Seeded supercontinuum generation with optical parametric down-conversion," Phys. Rev. Lett. **233902**, 1–4 (2010).

[224] K. Cheung, C. Zhang, and Y. Zhou, "Manipulating supercontinuum generation by minute continuous wave," Opt. Lett. **36**, 160–162 (2011).

[225] Q. Li, F. Li, K. Wong, and A. Lau, "Investigating the influence of a weak continuous-wave-trigger on picosecond supercontinuum generation," Opt. Express **19**, 377–381 (2011).

[226] M. Kues, N. Brauckmann, and T. Walbaum, "Nonlinear dynamics of femtosecond supercontinuum generation with feedback," Opt. Express **17**, 635–639 (2009).

[227] N. Brauckmann, M. Kues, T. Walbaum, and C. Fallnich, "Experimental investigations on nonlinear dynamics in supercontinuum generation with feedback," Opt. Express **18**, 233–237 (2010).

[228] N. Brauckmann, M. Kues, P. Groß, and C. Fallnich, "Adjustment of supercontinua via the optical feedback phasenumerical investigations," Opt. Express **18**, 20667–20672 (2010).

[229] N. Brauckmann, M. Kues, P. Groß, and C. Fallnich, "Adjustment of supercontinua via the optical feedback phaseexperimental verifications," Opt. Express **18**, 24611–24618 (2010).

[230] M. Kues, N. Brauckmann, P. Groß, and C. Fallnich, "Basic prerequisites for limit-cycle oscillations within a synchronously pumped passive optical nonlinear fiber-ring resonator," Phys. Rev. A **033833**, 1–10 (2011).

[231] N. Brauckmann, M. Kues, P. Groß, and C. Fallnich, "Noise reduction of supercontinua via optical feedback," Opt. Express **19**, 7914–7923 (2011).

[232] P. Groß, N. Haarlammert, M. Kues, T. Walbaum, and C. Fallnich, "Optical Fiber Technology Effects of optical feedback on femtosecond supercontinuum generation," Opt. Fiber Technol. **18**, 290–303 (2012).

[233] M. Schmidberger, W. Chang, P. S. J. Russell, and N. Y. Joly, "Influence of timing jitter on nonlinear dynamics of a photonic crystal fiber ring cavity," Opt. Lett. **37**, 3576–8 (2012).

[234] D. Solli, G. Herink, B. Jalali, and C. Ropers, "Fluctuations and correlations in modulation instability," Nat. Photon. **6**, 463–468 (2012).

[235] A. Mussot and A. Kudlinski, "Modulation instability: Loaded dice," Nat. Photon. **6** (2012).

[236] D. R. Solli, C. Ropers, and B. Jalali, "Measuring single-shot modulation instability and supercontinuum spectra at megahertz rates," Nonlinearity **26**, R85–R92 (2013).

[237] A. A. Rieznik, A. M. Heidt, G. König, V. A. Bettachini, and D. F. Grosz, "Optimum Integration Procedures for Supercontinuum Simulation," IEEE Photon. J. **4**, 552–560 (2012).

[238] O. Vanvincq, J. Travers, and A. Kudlinski, "Conservation of the photon number in the generalized nonlinear Schrödinger equation in axially varying optical fibers," Phys. Rev. A **84**, 1–7 (2011).

[239] J. Lægsgaard, "Modeling of nonlinear propagation in fiber tapers," J. Opt. Soc. Am. B **29**, 3183 (2012).

[240] A. Heidt, "Efficient adaptive step size method for the simulation of supercontinuum generation in optical fibers," J. Lightwave Technol. **27**, 3984–3991 (2009).

[241] G. Bosco, A. Carena, V. Curri, R. Gaudino, P. Poggiolini, and S. Benedetto, "Suppression of spurious tones induced by the split-step method in fiber systems simulation," IEEE Photon. Technol. Lett. **12**, 489–491 (2000).

[242] O. Sinkin, R. Holzlohner, J. Zweck, and C. Menyuk, "Optimization of the split-step fourier method in modeling optical-fiber communications systems," J. Lightwave Technol. **21**, 61–68 (2003).

[243] C. Shannon, "Communication in the presence of noise," Proc. of the IRE **37**, 10–21 (1949).

[244] M. H. Frosz, "Supercontinuum generation in photonic crystal fibres : Modelling and dispersion engineering for spectral shaping," Ph.D. thesis, Technical University of Denmark (2006).

[245] R. Smith, "Optical power handling capacity of low loss optical fibers as determined by stimulated Raman and Brillouin scattering," Appl. Opt. **11**, 2489–2494 (1972).

[246] M. H. Frosz, "Validation of input-noise model for simulations of supercontinuum generation and rogue waves," Opt. Express **18**, 14778–87 (2010).

[247] S. B. Cavalcanti and G. P. Agrawal, "Noise amplification in dispersive non-linear media," Phys. Rev. A **51**, 4086 (1995).

[248] A. Mussot, E. Lantz, H. Maillotte, T. Sylvestre, C. Finot, and S. Pitois, "Spectral broadening of a partially coherent CW laser beam in single-mode optical fibers," Opt. Express **12**, 2838–43 (2004).

[249] J. Gowar, *Optical communication systems* (Prentice-Hall, Inc., 1993), 2nd ed.

ISBN: 978-87-93089-00-6

Published by:
DTU Fotonik
Department of Photonics Engineering
Technical University of Denmark
Ørsteds Plads, building 343
DK-2800 Kgs. Lyngby

Simon Toft Sørensen was born 1984 in Aarhus, Denmark. He received the BSc degree in physics from Aarhus University in 2007. He then joined the Erasmus program and studied one year at Utrecht University, Netherlands. In 2010 he graduated with an MSc degree in physics and nanotechnology from the Technical University of Denmark, where he started his PhD immediately afterwards. The PhD work was focused on developing ultra-stable supercontinuum sources with high spectral densities in the deep-blue and was carried out in close collaboration with NKT Photonics A/S.

DTU Fotonik
Department of Photonics Engineering